ΕΘΝΙΚΟ ΜΕΤΣΟΒΙΟ ΠΟΛΥΤΕΧΝΕΙΟ

ΣΧΟΛΗ ΕΦΑΡΜΟΣΜΕΝΩΝ ΜΑΘΗΜΑΤΙΚΩΝ
ΚΑΙ ΦΥΣΙΚΩΝ ΕΠΙΣΤΗΜΩΝ

Διατμηματικό Πρόγραμμα Μεταπτυχιακών Σπουδών στην

Εφαρμοσμένη Μηχανική

Υπολογιστική μελέτη της θερμικής συμπεριφοράς των 2S ανιχνευτικών μονάδων για την αναβάθμιση στη φάση-2 του ανιχνευτή τροχιών του πειράματος CMS

MSc Διπλωματική Εργασία του
Αλέξανδρου Κολιάτου

Ακαδημαϊκός Επιβλέπων:
Ευστάθιος Ε. Θεοτόκογλου

Αθήνα, Οκτώβριος 2018

NATIONAL TECHNICAL UNIVERSITY OF ATHENS

SCHOOL OF APPLIED MATHEMATICS AND PHYSICS

Interdisciplinary Postgraduate Programme in

Applied Mechanics

Computational study of the thermal performance of the 2S detector modules for the CMS Tracker Phase-2 Upgrade

MSc Thesis of

Alexandros Koliatos

Academic Supervisor:

Efstathios E. Theotokoglou

Athens, Greece

October 2018

ΕΘΝΙΚΟ ΜΕΤΣΟΒΙΟ ΠΟΛΥΤΕΧΝΕΙΟ

ΣΧΟΛΗ ΕΦΑΡΜΟΣΜΕΝΩΝ ΜΑΘΗΜΑΤΙΚΩΝ ΚΑΙ ΦΥΣΙΚΩΝ ΕΠΙΣΤΗΜΩΝ

ΤΟΜΕΑΣ ΜΗΧΑΝΙΚΗΣ ΥΛΙΚΩΝ

Copyright ©–All rights reserved Alexandros Koliatos,

Με επιφύλαξη παντός δικαιώματος.

Απαγορεύεται η αντιγραφή, αποθήκευση και διανομή της παρούσας εργασίας, εξ' ολοκλήρου ή τμήματος αυτής, για εμπορικό σκοπό. Επιτρέπεται η ανατύπωση, αποθήκευση και διανομή για σκοπό μη κερδοσκοπικό, εκπαιδευτικής ή ερευνητικής φύσης, υπό την προϋπόθεση να αναφέρεται η πηγή προέλευσης και να διατηρείται το παρόν μήνυμα. Ερωτήματα που αφορούν τη χρήση της εργασίας για κερδοσκοπικό σκοπό πρέπει να απευθύνονται προς τον συγγραφέα.

Η εργασία εκπονήθηκε στο Ευρωπαϊκό Συμβούλιο Πυρηνικής Έρευνας (CERN) για το πείραμα Compact Muon Solenoid (CMS) σε συνεργασία του Τομέα Μηχανικής Υλικών της Σχολής Εφαρμοσμένων Μαθηματικών και Φυσικών Επιστημών του Εθνικού Μετσόβιου Πολυτεχνείου και του Εθνικού Κέντρου Έρευνας Φυσικών Επιστημών ‘Δημόκριτος΄, υπό την καθοδήγηση του επιβλέποντος Καθηγητή Ε.Ε Θεοτόκογλου και σε συνεργασία του Αν. Καθηγητή Α. Σιδερίδη. Μέρος της εργασίας έχει χρηματοδοτηθεί από το CERN.

ΕΘΝΙΚΟ ΚΕΝΤΡΟ ΕΡΕΥΝΑΣ
ΦΥΣΙΚΩΝ ΕΠΙΣΤΗΜΩΝ «ΔΗΜΟΚΡΙΤΟΣ»

Αθήνα, Οκτώβριος 2018

ΕΘΝΙΚΟ ΜΕΤΣΟΒΙΟ ΠΟΛΥΤΕΧΝΕΙΟ

ΣΧΟΛΗ ΕΦΑΡΜΟΣΜΕΝΩΝ ΜΑΘΗΜΑΤΙΚΩΝ ΚΑΙ ΦΥΣΙΚΩΝ ΕΠΙΣΤΗΜΩΝ

ΤΟΜΕΑΣ ΜΗΧΑΝΙΚΗΣ ΥΛΙΚΩΝ

Εγκρίθηκε από την ακόλουθη τριμελή εξεταστική επιτροπή στις 22 Οκτωβρίου 2018:

Ευστάθιος Ε. Θεοτόκογλου (Καθηγητής Ε.Μ.Π.)

Δημήτριος Μανωλάκος (Καθηγητής Ε.Μ.Π.)

Αιμίλιος Σιδερίδης (Αν. Καθηγητής Ε.Μ.Π.)

Abstract

For the LHC upgrade, the CMS detector needs to be substantially upgraded during LS3 in order to exploit the increase in luminosity, provided by the HL-LHC. This will increase the track density and rate within the particle detectors, which means that especially the CMS Tracker and its components have to meet stronger requirements regarding radiation hardness of the used materials and a sufficient cooling of the silicon sensor modules. This thesis work has been focused on the upgrade of the CMS Outer Tracker.

The new Tracker is composed of silicon sensor modules that will have an on-module p_T discrimination. The current concept of building silicon sensor modules for the new outer tracker of the CMS detector is based on advanced composite materials: carbon fiber reinforced aluminium (Al-CF) and carbon fiber reinforced polymers (CFRPs). The Tracker will be composed of two module types, called PS-Module and 2S-Module, differing in the granularity of their silicon sensors. The subject of this thesis was to study the thermal performance of the 2S Modules in terms of micromechanics and macromechanics.

In order to decrease the production cost and the mass of the 2S Modules, there is a need of comparison of different materials used for thermal management. The target was to predict the thermal conductivity of CFRPs using different micromechanical model and, according to macromechanical aspects, to study the thermal performance and the thermal runaway of the 2S Module. A comparative study was conducted using two different stacking sequences of carbon fiber reinforced polymers, comparing various carbon fiber systems, manufactured by the two leading companies in high performance carbon fibers: Mitsubishi Chemical Carbon Fiber & Composites and Nippon Graphite Fiber Corporation. The optimization of the thermal performance of the modules has provided important information about the appropriate selection of materials and stacking sequences of composite materials.

The analysis has been conducted using the following software packages: CATIA v5 for the 3D design of the module, ANSYS Thermal-Electric for the thermal analysis and Mathcad 15 for the thermal conductivity prediction, using different micromechanical models.

Περίληψη

Για την αναβάθμιση του LHC, ο ανιχνευτής CMS πρέπει να αναβαθμισθεί σημαντικά κατά τη διάρκεια του LS3 προκειμένου να ανταποκριθεί στην αύξηση της φωτεινότητας, που παρέχεται από το HL-LHC. Αυτό θα αυξήσει την πυκνότητα και το εύρος των τροχιών μέσα στους ανιχνευτές σωματιδίων, πράγμα που σημαίνει ότι ειδικά ο ανιχνευτής τροχιών του CMS και τα εξαρτήματά του πρέπει να πληρούν τις ισχυρότερες απαιτήσεις όσον αφορά την ανθεκτικότητα στην ακτινοβολία των χρησιμοποιούμενων υλικών και την επαρκή ψύξη των μονάδων αισθητήρα πυριτίου. Η εργασία αυτή έχει επικεντρωθεί στην αναβάθμιση του εξωτερικού ανιχνευτή τροχιών του CMS.

Ο νέος ανιχνευτής τροχιών θα αποτελείται από ανιχνευτικές μονάδες αισθητήρων πυριτίου, οι οποίες θα έχουν διακριτική ικανότητα αναγνώρισης της εγκάρσιας ορμής των σωματιδίων p_T. Η τρέχουσα ιδέα της κατασκευής ανιχνευτικών μονάδων αισθητήρων πυριτίου για τον νέο ανιχνευτή τροχιών του ανιχνευτή CMS, βασίζεται σε προηγμένα σύνθετα υλικά: αλουμίνιο με ενίσχυση από ίνες άνθρακα (Al-CF) και πολυμερή ενισχυμένα με ίνες άνθρακα (CFRPs). Ο ανιχνευτής τροχιών θα αποτελείται από δύο τύπους ανιχνευτικών μονάδων: τις ανιχνευτικές μονάδες PS και 2S, που διαφέρουν ως προς τον βαθμό ανάλυσης που παρουσιάζονται στους αισθητήρες πυριτίου. Το αντικείμενο της παρούσας εργασίας ήταν η μελέτη της θερμικής συμπεριφοράς των ανιχνευτικών μονάδων 2S υπό την σκοπιά της μικρο-μηχανικής και μακρο-μηχανικής.

Προκειμένου να μειωθεί το κόστος παραγωγής και το βάρος των μονάδων 2S, υπάρχει ανάγκη σύγκρισης διαφόρων υλικών που χρησιμοποιούνται για βέλτιστη θερμική συμπεριφορά. Ο στόχος ήταν η πρόβλεψη της θερμικής αγωγιμότητας των CFRPs, με τη χρήση διάφορων μοντέλων μικρο-μηχανικής και, σύμφωνα με πτυχές μακρο-μηχανικής, η μελέτη της θερμικής συμπεριφοράς και του φαινομένου ‘thermal runaway’ της μονάδας 2S. Έγινε μία συγκριτική μελέτη, χρησιμοποιώντας δύο διαφορετικές μορφές στρώσεων από πολυμερή υλικά ενισχυμένα με ίνες άνθρακα, συγκρίνοντας διάφορα είδη ινών άνθρακα από τις δύο κορυφαίες εταιρείες σε ίνες άνθρακα υψηλής απόδοσης: Mitsubishi Chemical Carbon Fiber & Composites και Nippon Graphite Fiber Corporation. Η βελτιστοποίηση της θερμικής απόδοσης των μονάδων έχει δώσει σημαντικές πληροφορίες σχετικά με την κατάλληλη επιλογή υλικών και το είδος της στρώσης των σύνθετων υλικών.

Η ανάλυση έγινε χρησιμοποιώντας τα παρακάτω λογισμικά πακέτα: CATIA v5 για τον τρισδιάστατο σχεδιασμό της μονάδας, ANSYS Thermal-Electric για τη θερμική ανάλυση και Mathcad 15 για την πρόβλεψη της θερμικής αγωγιμότητας, χρησιμοποιώντας διαφορετικά μικρομηχανικά μοντέλα.

Εκτενής Περίληψη

Σε πειράματα της φυσικής υψηλών ενεργειών σωματίδια όπως ηλεκτρόνια, πρωτόνια και ποζιτρόνια επιταχύνονται και συγκρούονται μεταξύ τους με ενέργειες GeV έως και TeV **[1]**. Από την αρχική αλληλεπίδραση των δύο σωματιδίων που συγκρούονται, δημιουργούνται δευτερεύοντα σωματίδια τα οποία με την σειρά τους μπορούν να αλληλεπιδράσουν και να διασπασθούν. Μελετώντας τις ιδιότητες των δευτερευόντων σωματιδίων όπως το είδος του σωματιδίου, το φορτίο, τη ενέργεια και τη γωνίας της διάσπασης μπορεί να γίνει πλήρης ανακατασκευή της αλληλεπίδρασης κάτι που οδηγεί σε συμπεράσματα για την φύση των σωματιδίων. Προφανώς όλες αυτές οι ιδιότητες δεν μπορούν να μετρηθούν από ένα μόνο ανιχνευτικό σύστημα. Για το λόγο αυτό, σε ένα πείραμα σύγκρουσης τοποθετούνται πολλοί ανιχνευτές διαφορετικού τύπου σε στρώματα με σχήμα κυλίνδρου γύρω από το σημείο που γίνεται οι αρχική σύγκρουση, καλύπτοντας μια στερεά γωνία 4π. Το κάθε στρώμα προορίζεται για έναν συγκεκριμένο σκοπό αποτελώντας έναν υπό-ανιχνευτή. Η παρούσα εργασία σχετίζεται με την αναβάθμιση του ανιχνευτή τροχιών του κύριου ανιχνευτή Compact Muon Solenoid (CMS) (Εικόνα 1) του μεγάλου επιταχυντή αδρονίων (LHC) του CERN. Ο ανιχνευτής τροχιών αποτελείται απο ανιχνευτές πυριτίου.

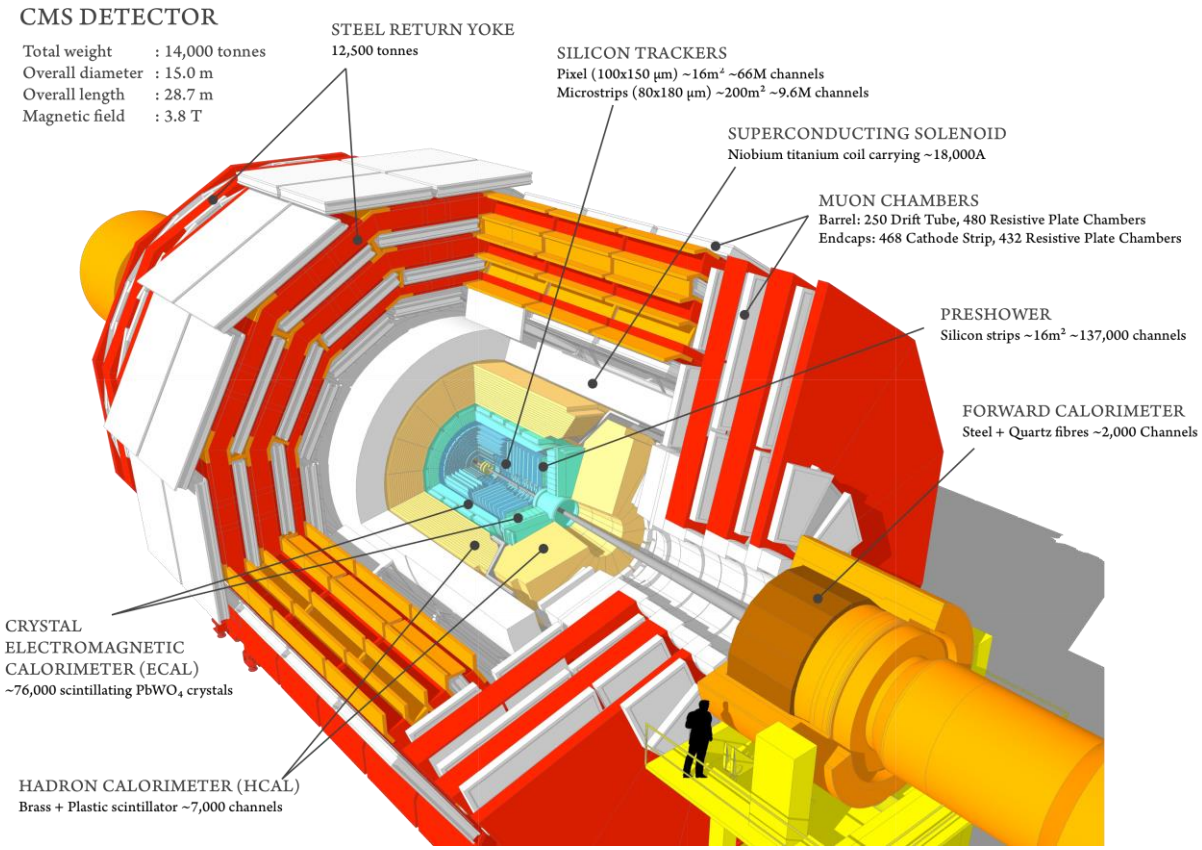

Εικόνα 1: Ανιχνευτής CMS. Τα διαφορετικά επίπεδα και οι βασικοί υπό-ανιχνευτές οι οποίοι συγκροτούν τον κύριο ανιχνευτή. Το επίπεδο το οποίο είναι κοντά στη αλληλεπίδραση αποτελεί τον ανιχνευτή τροχιών, ο οποίος αποτελείται από ανιχνευτές πυριτίου.

Ο πιο απλός τύπος ανιχνευτών πυριτίου είναι ο ανιχνευτής παράλληλων μικρο-λωρίδων (strip). Οι ανιχνευτές αυτοί είναι ικανοί να ανιχνεύουν την προβολή της τροχιάς ενός σωματιδίου. Μέτρηση δύο διαστάσεων μπορεί να γίνει με ανιχνευτές μικρο-λωρίδων, όταν υπάρχουν δύο παράλληλα στρώματα μικρο-λωρίδων τα οποία σχηματίζουν γωνία μεταξύ τους. Άλλος τύπος ανιχνευτών πυριτίου όπου παρέχονται ικανοποιητικές πληροφορίες στις δύο διαστάσεις είναι οι ανιχνευτές μικρο-πλακιδίων (pixel).

Ο ανιχνευτής CMS έχει συνεισφέρει σε πολλούς τομείς της σύγχρονης φυσικής όπως έρευνες για την ύπαρξη και τις ιδιότητες του μποζονίου Higgs, έρευνες για την ύπαρξη της σκοτεινής ύλης καθώς και μέτρηση των ιδιοτήτων των είδη γνωστών σωματιδίων με μεγάλη ακρίβεια. Ο ανιχνευτής αποτελείται από διάφορα μέλη κατασκευασμένα γύρω από ένα υπέρ-μαγνήτη σε σχήμα σωληνοειδούς. Το μαγνητικό πεδίο που παρέχει ο υπέρ-μαγνήτης είναι περίπου 4 Tesla 100.000 φορές ισχυρότερο από το μαγνητικό πεδίο της Γης. Τα υποσυστήματα του ανιχνευτή έχουν σχεδιασθεί ώστε να μετρούν την ενέργεια , την ορμή φωτονίων , ηλεκτρονίων , μιονίων και άλλων παραγόμενων από τις συγκρούσεις σωματιδίων.

Το εσωτερικό τμήμα το οποίο περικλείει το σημείο της σύγκρουσης είναι ο ανιχνευτής τροχιών πυριτίου (Εικόνα 2). Ο ανιχνευτής αυτός περικλείεται από κρυστάλλους σπινθηρισμών. Τον ανιχνευτή τροχιών περικλείει το ηλεκτρομαγνητικό καλορίμετρο το οποίο με την σειρά του περικλείεται από το αδρονικό καλορίμετρο. Ο ανιχνευτής τροχιών καθώς και τα καλαρίμετρα είναι τοποθετημένα στο εσωτερικό του σωληνοειδούς μαγνήτη. Εξωτερικά από τον μαγνήτη είναι τοποθετημένοι ανιχνευτές μιονίων.

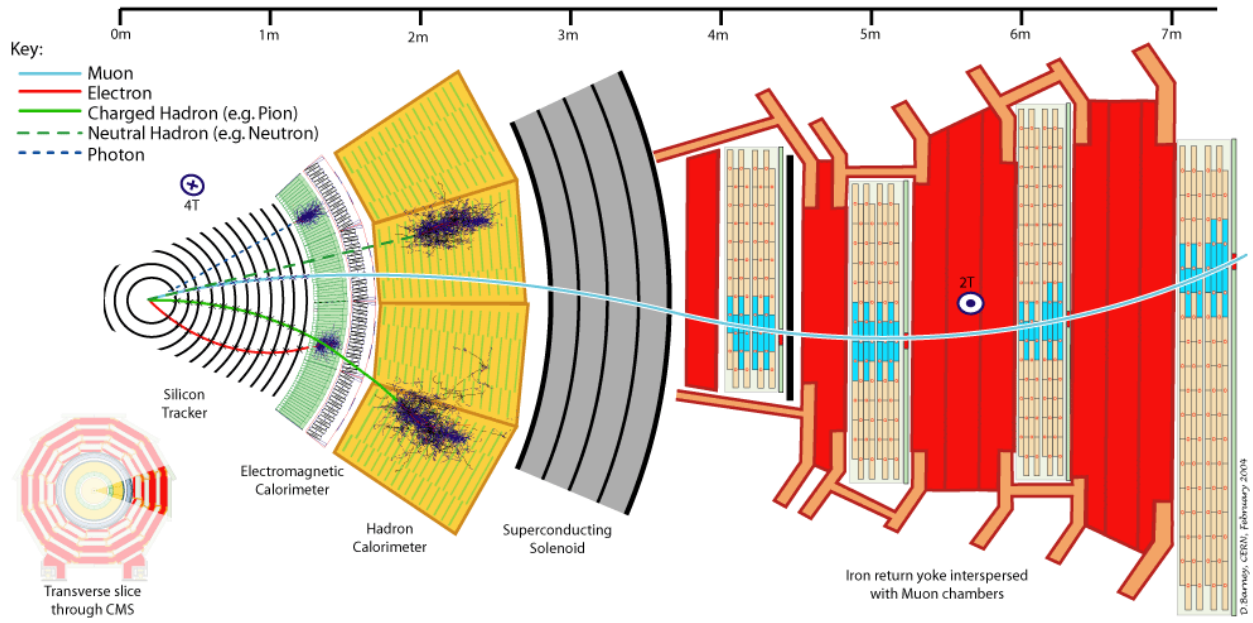

Εικόνα 2: Τα επιμέρους τμήματα του ανιχνευτή CMS. Στο εσωτερικό τμήμα είναι τοποθετημένος ο ανιχνευτής τροχιών με αισθητήρες πυριτίου. Εξωτερικά από τον ανιχνευτή τροχιών και πριν από τον υπεραγώγιμο μαγνήτη τοποθετούνται το ηλεκτρομαγνητικό και το αδρονικό καλορίμετρο. Εξωτερικά του υπεραγώγιμου μαγνήτη είναι τοποθετημένοι ανιχνευτές μιονίων.

Η παρούσα εργασία σχετίζεται με την αναβάθμιση του ανιχνευτή τροχιών ώστε να ανταποκριθεί στις αυξημένες απαιτήσεις του HL-LHC, όπου η φωτεινότητα αναμένεται στο εύρος από $5 \cdot 10^{34}$ $cm^2 s^{-1}$ εώς $7.5 \cdot 10^{34}$ $cm^2 s^{-1}$με τιμή ολική ολοκληρωμένης φωτεινότητας 3000 fb^{-1}. Η αναβάθμιση του LHC, ώστε να ανταποκρίνεται στις νέες συνθήκες, θα πραγματοποιηθεί κατά τη διάρκεια δύο μεγάλων παύσεων : του LS2 την περίοδο 2019-2020 και του LS3 την περίοδο 2024-2026. Η αναβάθμιση του ανιχνευτή τροχιών θα γίνει σε δύο διαφορετικές φάσεις. Σύμφωνα με το χρονοδιάγραμμα του LHC η εγκατάσταση του αναβαθμισμένου ανιχνευτή τροχιών αναμένεται να γίνει στο τέλος του 2024.

Προδιαγραφές αναβάθμισης του ανιχνευτή τροχιών:

- Αυξημένη ανοχή στην ακτινοβολία. Ο αναβαθμισμένος ανιχνευτής τροχιών θα πρέπει να λειτουργεί αποτελεσματικά στις αυξημένες απαιτήσεις του HL-LHC. Αυτές οι απαιτήσεις θα πρέπει να εκπληρωθούν χωρίς παρεμβάσεις συντήρησης για τον εξωτερικό ανιχνευτή τροχιών, ενώ ο εσωτερικός ανιχνευτής Pixel προβλέπεται να έχει ευκολότερη πρόσβαση προσφέροντας την δυνατότητα εργασιών συντήρησης, καθώς θα μπορούν να αντικατασταθούν ανιχνευτικές μονάδες στο εσωτερικότερο τμήμα του ανιχνευτή όπου η ροή σωματιδίων ανα επιφάνεια θα είναι και μεγαλύτερη.

- Μειωμένη ποσότητα υλικού. Η απόδοση του ανιχνευτή σχετίζεται άμεσα με την ποσότητα του υλικού. Από το υλικό του ανιχνευτή τροχιών επηρεάζεται επίσης και η απόδοση των εξωτερικών τμημάτων του ανιχνευτή όπως τα θερμιδόμετρα.

- Βελτιωμένο διαχωρισμό μεταξύ δύο τροχιών. Ο ανιχνευτής τροχιών πριν την αναβάθμιση είχε υποβαθμισμένη απόδοση ως προς τον διαχωρισμό δύο διαφορετικών γεγονότων με πολύ κοντινή τροχιά.

- Αυξημένος βαθμός ανάλυσης. Με σκοπό να εξασφαλιστεί επαρκής απόδοση στην ανίχνευση τροχιών σε καταστάσεις λειτουργίας υψηλής επιστοίβασης γεγονότων (pile-up). Η απασχόληση κάθε καναλιού από την συλλογή του φορτίου μέχρι την τελική ψηφιοποίηση του θα πρέπει να είναι αρκετά μικρή σε όλες τις περιοχές του ανιχνευτή. Αυτό απαιτεί υψηλή πυκνότητα καναλιών. Ως δείκτης αναφοράς έχει οριστεί μια μέση τιμή των 140 συγκρούσεων ανα διασταύρωση δέσμης.

- Ισχυρότερη διαδικασία αναγνώρισης προτύπων. Ο αναβαθμισμένος ανιχνευτής τροχιών θα πρέπει να επιτρέπει γρήγορη και αποδοτική ανίχνευση τροχιών. Κάθε σήμα από διαφορετικές ανιχνευτικές μονάδες θα πρέπει να κατανέμεται αποδοτικά και γρήγορα στην τροχιά που ανήκει επιτρέποντας την καλύτερη ανακατασκευή της τροχιάς του σωματιδίου.

- Μονάδες με λειτουργία triggering. Η επιλογή των γεγονότων που είναι ενδιαφέροντα από πλευρά φυσικής γίνεται ιδιαίτερα απαιτητική σε υψηλή φωτεινότητα όχι μόνο λόγω της αυξημένης ροής αλλά και επειδή οι αλγόριθμοι που είναι υπεύθυνοι για την διαδικασία της επιλογής γίνονται λιγότερο αποδοτικοί σε καταστάσεις υψηλής επιστοίβασης (pile-up). Προκειμένου να διατηρηθεί η απόδοση του CMS καλύπτοντας το φάσμα των γεγονότων που έχουν ενδιαφέρον από πλευράς της φυσικής θα πρέπει να γίνεται κατάλληλη επιλογή των γεγονότων στον ανιχνευτή τροχιών.

Η εργασία επικεντρώθηκε στην αναβάθμιση του εξωτερικού ανιχνευτή τροχιών. Στο τμήμα αυτό του ανιχνευτή θα γίνεται κατάλληλη επιλογή των γεγονότων, κρατώντας μόνο αυτά που μας ενδιαφέρουν από πλευράς φυσικής. Αυτό μπορεί να συμβεί με ανιχνευτικές μονάδες οι οποίες μπορούν να απορρίψουν το σήμα από ένα σωματίδιο για το οποίο η εγκάρσια ορμή είναι μικρότερη από μια συγκεκριμένη τιμή. Όταν φορτισμένα σωματίδια, όπως τα ηλεκτρόνια, κινούνται στο CMS, οι τροχιές τους καμπυλώνονται από το ισχυρό μαγνητικό πεδίο. Όσο μεγαλύτερη η ορμή (~ενέργεια) του, τόσο λιγότερο στρίβουν. Σωματίδια με μικρή εγκάρσια ορμή κάμπτονται περισσότερο από το μαγνητικό πεδίο. Τα σωματίδια παράγουν σήματα καθώς διαπερνούν τα τοποθετημένα με μεγάλη ακρίβεια (<10 μm) στρώματα των αισθητήρων πυριτίου που αποτελούν τον ανιχνευτή τροχιών. Κατόπιν υπολογιστικά προγράμματα «ενώνουν» τις τελείες από τα σήματα που συλλέχθηκαν και δίνουν τις ορμές των σωματιδίων (Εικόνα 3).

Οπότε μπορούμε να απορρίψουμε γεγονότα από σωματίδια τα οποία κάμπτονται περισσότερο από το κατώφλι που έχει ορισθεί. Η διαδικασία αυτή θα πρέπει να γίνεται στον ανιχνευτή έτσι ώστε ο συνολικός όγκος δεδομένων προς επεξεργασία να μην περιέχει ποσότητα πληροφορίας που δεν θα είναι χρήσιμη. Η κάθε ανιχνευτική μονάδα αποτελείται από δύο ανιχνευτές πυριτίου σε πολύ κοντινή απόσταση. Συλλέγεται το σήμα και από τους δύο ανιχνευτές και επιλέγονται τα ζευγάρια που αντιστοιχούν σε σωματίδιο με εγκάρσια ορμή (p_T) μεγαλύτερη από το κατώφλι που έχει ορισθεί. Το ισχυρό μαγνητικό πεδίο του CMS επιτρέπει να να υπάρξει επαρκής ευαισθησία στην μέτρηση της ορμής.

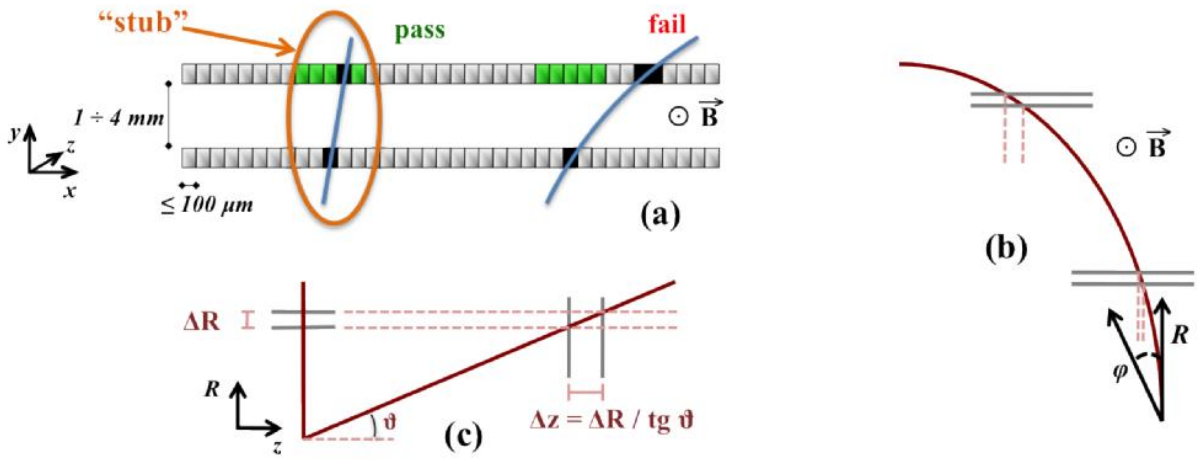

Εικόνα 3: Διαδικασία επιλογής γεγονότων. Σωματίδια τα οποία η εγκάρσια ορμή είναι μικρότερη από μία συγκεκριμένη τιμή δεν συλλέγονται, έτσι ώστε ο συνολικός όγκος δεδομένων να μην περιέχει πληροφορία που δεν είναι χρήσιμη.

Δύο τύποι ανιχνευτικών μονάδων είναι υπό μελέτη **[2]**:

- Ανιχνευτικές μονάδες 2S (Εικόνα 4) οι οποίες αποτελούνται από δύο ανιχνευτές πυριτίου τύπου strip διαστάσεων περίπου 10 × 10 cm με τα strips να είναι παράλληλα μεταξύ τους. Οι μονάδες αυτές τοποθετούνται στις εξωτερικές περιοχές σε ακτίνα περίπου $R \approx 60$ cm καλύπτοντας μια επιφάνεια 150 m^2. Για να είναι δυνατόν ο ανιχνευτής τροχιών να απορρίπτει

γεγονότα από σωματίδια με μικρή εγκάρσια ορμή κάθε ανιχνευτική μονάδα θα έχει διαφορετική απόσταση μεταξύ των λωρίδων καλύπτοντας ένα φάσμα από 1,8 έως 4,0 mm. Στην εικόνα φαίνεται σχηματικά η διάταξη ανιχνευτών τύπου 2S. Οι δύο ανιχνευτές με διατάξεις strip συνδέονται μεταξύ τους μέσω ενός υλικού το οποίο αποτελείται από νανο-ίνες άνθρακα AL-CF (carbon fibre aluminum reinforced) το οποίο λειτουργεί ως στήριξη , διαχωριστής και απαγωγός θερμότητας. Τα ηλεκτρονικά για την παροχή τάσης και την λήψη του σήματος τοποθετούνται εξωτερικά του ανιχνευτή και συνδέονται με τις δύο πλευρές του ανιχνευτή. Αντίστοιχα και στα εξωτερικά ηλεκτρονικά τοποθετείται AL-CF έτσι ώστε να επιτυγχάνεται απομόνωση των ανιχνευτών. Η δομή της ανιχνευτικής μονάδας 2S φαίνεται αριστέα της Εικόνας 5.

- Ανιχνευτικές μονάδες PS **[3, 4]** (Εικόνα 4) οι οποίες αποτελούνται από δύο ανιχνευτές συνολικής επιφάνειας $5 \times 10\ cm2$ σε πολύ κοντινή απόσταση ο ένας με τον άλλον. Ο ένας ανιχνευτής είναι τύπου strip και ο άλλος macro-pixel με αναλογία διαστάσεων pixel $100\ \mu m \times 1.5\ mm$. Οι μονάδες PS τοποθετούνται σε ακτίνα μεταξύ $R \approx 20\ cm$ και $R \approx 60\ cm$. Οι ανιχνευτές με διάταξη macro-pixel παρέχουν επαρκείς μετρήσεις στην κάθετη z συντεταγμένη για την ακριβή αποτύπωση της τροχιάς και επιτρέπουν την διάκριση πρωτογενών κορυφών διάσπασης σωματιδίων ενισχύοντας την αναγνώριση προτύπων με πιο αποτελεσματικό τρόπο από μια πιθανή επέκταση του εσωτερικού ανιχνευτή Pixel σε μεγαλύτερες ακτίνες. Στην Εικόνα 4 φαίνεται σχηματικά η διάταξη ανιχνευτών τύπου PS. Ο ανιχνευτής με διάταξη macro-pixel συνδέεται μέσω bump-bondings με τις πλακέτες των εξωτερικών ηλεκτρονικών ανάγνωσης MPA με αποτέλεσμα να μπορεί να χρησιμοποιηθεί σαν ενιαία μονάδα. Ο ανιχνευτής strip έπειτα συνδέεται με τα MPAs με την βοήθεια AL-CF. Τα ηλεκτρονικά για την παροχή τάσης και την λήψη του σήματος τοποθετούνται ξεχωριστά εκατέρωθεν του ανιχνευτή και συνδέονται και με τις δύο πλευρές. Η δομή της ανιχνευτικής μονάδας PS φαίνεται δεξιά στην Εικόνα 5.

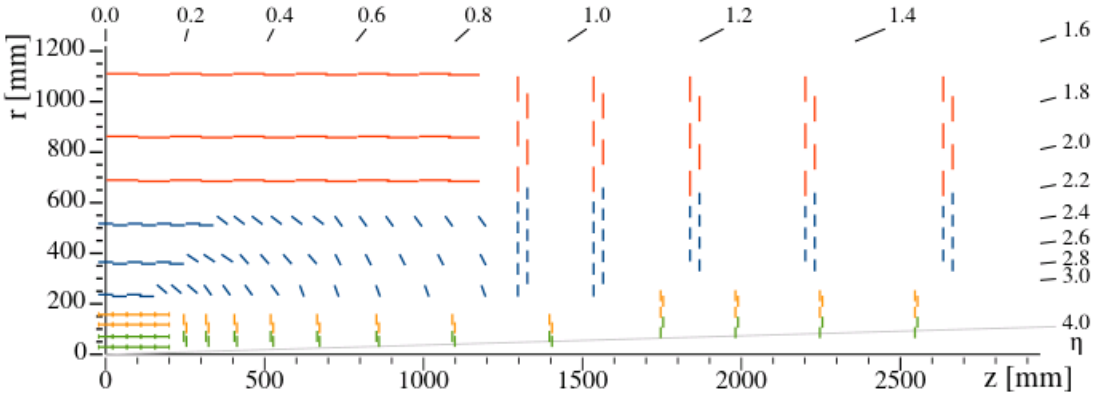

Εικόνα 4: Ο εξωτερικός ανιχνευτής τροχιών αποτελείται από PS ανιχνευτικές μονάδες (μπλε γραμμές) και από 2S ανιχνευτικές μονάδες (κόκκινες γραμμές). Τα επίπεδα του εσωτερικού ανιχνευτή σημειώνονται με πράσινες και κίτρινες γραμμές.

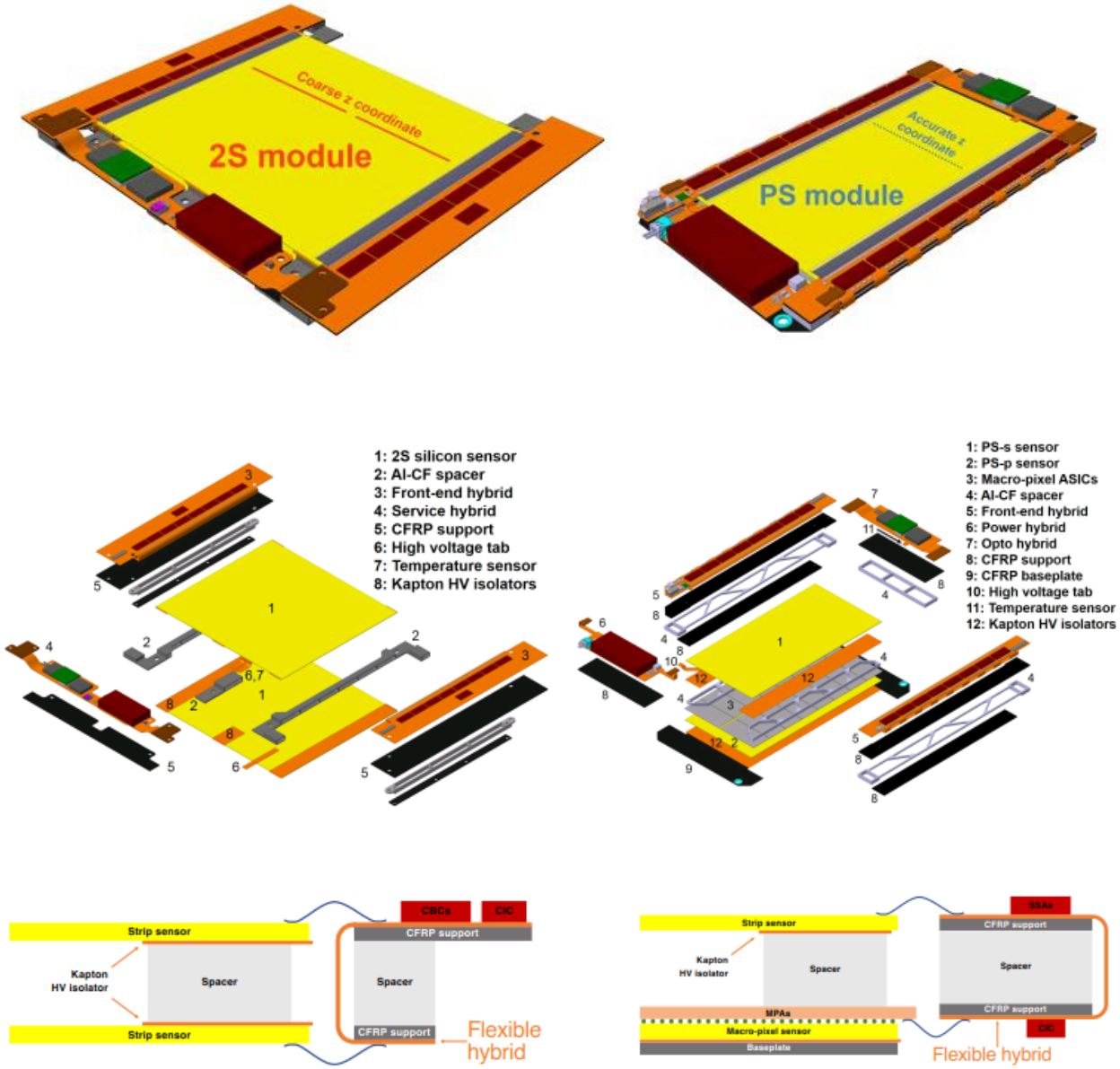

Εικόνα 5: 2S Ανιχνευτική μονάδα (αριστερά) και PS ανιχνευτική μονάδα (δεξιά) του εξωτερικού ανιχνευτή τροχιών. Στις εικόνες φαίνεται η συναρμολογημένη όψη (πάνω) και λεπτομέριες της δομής των ανιχνευτικών μονάδων.

Η απόσταση των αισθητήρων πυριτίου είναι 1.8 mm και 4 mm. Στην παρούσα εργασία, μελετήθηκε λεπτομερώς η δομή των ανιχνευτικών μονάδων 2S 1.8 mm στην περιοχή TEDD (Εικόνα 6). Ο εξωτερικός ανιχνευτής τροχιών περιέχει ανεξάρτητο σύστημα ψύξης. Η πιο σημαντική αλλαγή στα χαρακτηριστικά του ανιχνευτή λόγω ακτινοβολίας είναι η αύξηση του ρεύματος διαρροής το οποίο μπορεί να περιορισθεί σε ένα βαθμό μειώνοντας τη θερμοκρασία ψύξης. Σύμφωνα με μελέτες, η ψύξη της ανιχνευτικής μονάδας θα γίνει στους -35 ^{o}C. Το ρεύμα διαρροής ελέγχεται από το σύστημα ελέγχου του ανιχνευτή για κάθε μια ανιχνευτική μονάδα. Ο τρόπος με τον οποίο μεταβάλλεται το ρεύμα διαρροής σε σχέση με την προβλεπόμενη φωτεινότητα , την θέση και το μέγεθος κάθε ανιχνευτικής μονάδας μπορεί να προβλεφθεί από ακριβέστατα συστήματα προσομοίωσης συμπεριλαμβάνοντας διάφορα σενάρια θερμοκρασίας. Με αυτό τον τρόπο μπορεί να προβλεφθεί η μείωση της απόδοσης του ανιχνευτή λόγω του ρεύματος διαρροής.

Όπως διακρίνουμε στην Εικόνα 6, ο εξωτερικός ανιχνευτής τροχιών αποτελείται απο έξι κυλινδρικά στρώματα στην κεντρική περιοχή |z| < 1200 mm -σχηματίζοντας την μορφή ενός βαρελιού και από πέντε στρώματα διπλών δίσκων στα άκρα 1200 < |z| < 2700 mm. Οι ανιχνευτικές μονάδες τοποθετούνται μεταξύ r ≈ 21 cm και r ≈112 cm. Ο εξωτερικός ανιχνευτή τροχιών περιέχει τις παρακάτω τρεις περιοχές που αποτελούν τους υπο-ανιχνευτές: την TBPS: Tracker Barrel με PS ανιχνευτικές μονάδες, την TB2S: Tracker Barrel με 2S ανιχνευτικές μονάδες και την TEDD: Tracker Endcap Double-Discs, δίσκοι με PS ανιχνευτικές μονάδες και 2S ανιχνευτικές μονάδες.

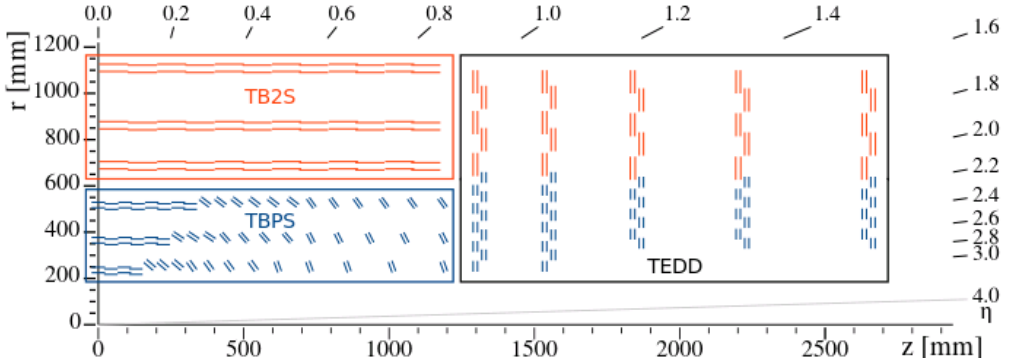

Εικόνα 6: Ένα τέταρτο του εξωτερικού ανιχνευτή τροχιών σε όψη r-z. Μπλε και κόκκινες γραμμές παρουσιάζουν την διάταξη των PS και 2S ανιχνευτικών μονάδων αντίστοιχα. Τρεις περιοχές υπο-ανιχνευτών: TBPS, TB2S και TEDD.

Οι ανιχνευτικές μονάδες 2S αποτελούνται από κατάλληλα υλικά για ελαφρές κατασκευές και παρουσιάζουν υψηλή αγωγιμότητα. Πιο συγκεκριμένα ο 2S 1.8 mm ανιχνευτής αποτελείται απο στρώματα σύνθετων υλικών με ίνες άνθρακα σε μήτρα εποξικής ρητίνης (CFRPs) και αλουμινίου (Al-CF). Τα υλικά αυτά πρέπει να διαχέουν κατάλληλα και αποδοτικά την θερμότητα των ηλεκτρονικών προς την περιοχή ψύξης. Ο μεχρι στιγμής σχεδιασμός του ανιχνευτή βασίζεται σε ενισχυτικές πλάκες CFRPs πάχους 0.5 mm με 5 στρώσεις μορφής 0/90/0/90/0 και αποτελούνται από 65% ίνες άνθρακα τύπου Mitsubishi K13D2U. Κατόπιν μέτρησης της θερμικής αγωγογιμότητας των ενισχυτικών πλάκων, τα αποτελέσματα παρουσίασαν σημαντικές διαφορές. Επίσης, η σύγκριση διάφορων ίνων άνθρακα και μορφών στρώσεων είναι απαραίτητη για την μείωση του κόστους και του ολικού βάρους της κατασκευής, προσδίδοντας την κατάλληλη θερμική συμπεριφορά σε αυτήν.

Η μελέτη εστιάστηκε στην πρόβλεψη της θερμικής αγωγιμότητας των CFRPs με χρήση διάφορων μοντέλων που αναπτύχθηκαν από πλευράς μικρομηχανικής καθώς επίσης και στην θερμική συμπεριφορά της ανιχνευτικής μονάδας 2S 1.8mm TEDD υπό ολοκληρωμένη φωτεινότητα 3000 fb^{-1} και ροής $2.2 \cdot 10^{14} n_{eq}/cm^2$. Έγινε σύγκριση της θερμικής συμπεριφοράς της ανιχνευτικής μονάδας με χρήση διαφορετικών CFRPs από τις εταιρείες Mitsubishi Chemical Carbon Fiber & Composites **[5]** και Nippon Graphite Fiber Corporation **[6]** υπό στρώσεις μορφής 0/90/0/90/0 και $[0/90]_s$. Η θερμική συμπεριφορά εξετάστηκε υπό τους παραγόντες της θερμοκρασιακής διαφοράς που παρατηρήθηκε στον ανιχνευτική μονάδα και στους δύο αισθητήρες πυριτίου αλλά και ως προς τον παράγοντα της διαφυγής θερμότητας (thermal runaway). Λόγω της συμπεριφοράς του αισθητήρα πυριτίου, με την αύξηση της θερμοκρασίας ψύξης το ρεύμα διαρροής αυξάνεται εκθετικά. Εξετάστηκε η τιμή της θερμοκρασίας κατά την οποία η ισχύς ψύξης γίνεται ανεπαρκής για την ψύξη της μονάδας και το ρεύμα διαρροής αυξάνεται σημαντικά.

Συμπεράσματα: Συγκρίνοντας τα αποτελέσματα της ανάλυσης (Εικόνες 7 και 8), παρατηρήθηκε ότι τα CFRPs με κατα μήκος θερμική αγωγιμότητα της ίνας άνθρακα από 500 W/mK εώς 800 W/mK παρουσιάζουν μικρές διαφορές, σχετικά με την μέγιστη θερμοκρασία της ανιχνευτικής μονάδας και της θερμοκρασιακής διαφοράς που παρατηρήθηκε στους αισθητήρες και της ανιχνευτικής μονάδας. Επίσης παρατηρήθηκε ότι η ανιχνευτική μονάδα με CFRPs στρώσης $[0/90]_s$ παρουσιάζει παρόμοια θερμική συμπεριφορά με τα CFRPs στρώσης 0/90/0/90/0.

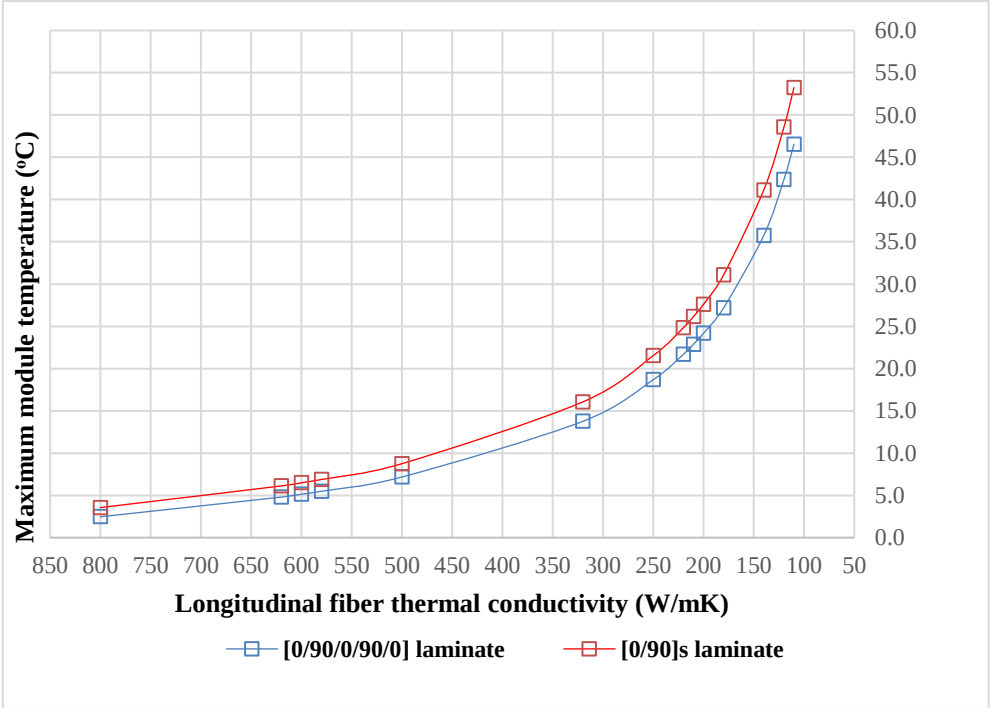

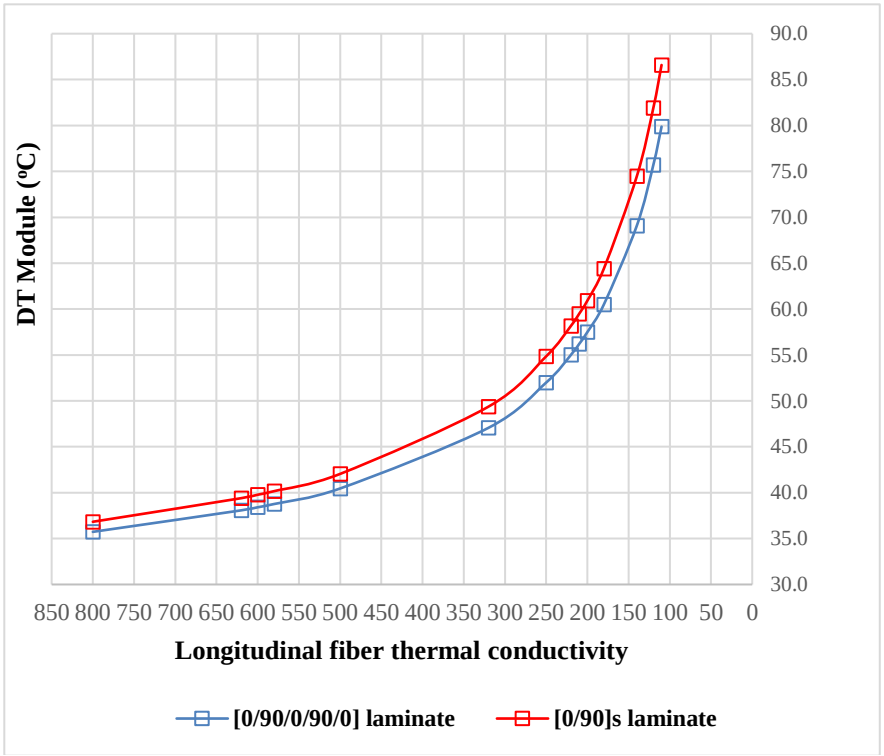

Εικόνα 7: Μέγιστη θερμοκρασία που παρατηρήθηκε στην ανιχνευτική μονάδα 2S 1.8 mm και η θερμοκρασιακή διαφορά σε σχέση της κατά μήκους θερμικής αγωγιμότητας των ινών άνθρακα και του είδους στρώσης.

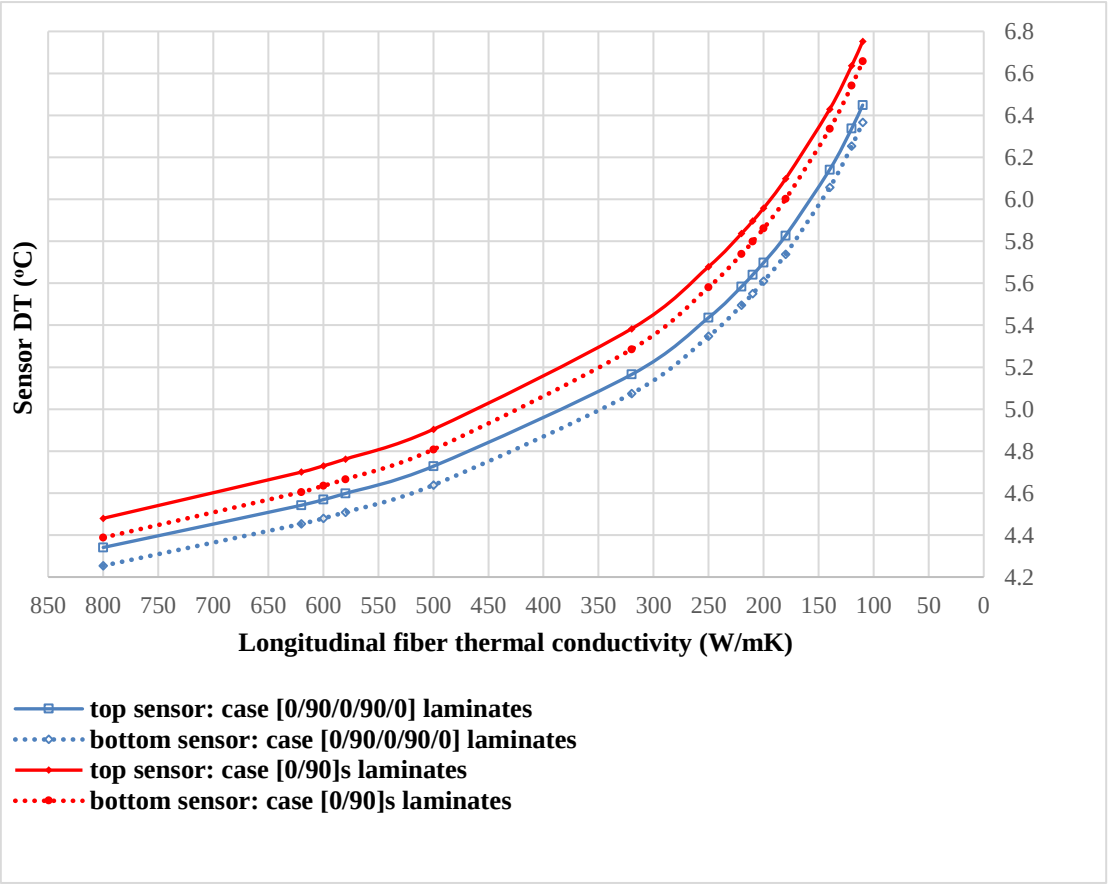

Εικόνα 8: Θερμοκρασιακή διαφορά που παρατηρήθηκε στους αισθητήρες πυριτίου σε σχέση με την κατά μήκους θερμικής αγωγιμότητας και του είδους στρώσης.

Επίσης, παρατηρήθηκε ότι η μέγιστη θερμοκρασία εμφανίζεται στην περιοχή που βρίσκεται ο μετατροπέας DC-DC και ότι ο αισθητήρας πυριτίου εμφανίζει συμμετρική κατανομή θερμοκρασίας ως προς τον άξονα Y (Εικόνες 9,10) σε όλες τις υπό εξέταση περιπτώσεις.

Η μελέτη έδειξε ότι χρησιμοποιώντας διάφορετικές ίνες άνθρακα, το thermal runaway εμφανίζεται σε τιμές άνω των 10 ^{o}C από την ελάχιστη θερμοκρασία της μονάδας ~ -33 ^{o}C. Το γεγονός αυτό είναι ιδιαίτερα ενθαρρυντικό, καθώς ένα περιθώριο 10 ^{o}C μπορεί να επιτευχθεί με χρήση και των δύο υπό εξέταση στρώσεων με τα διάφορα είδη ινών άνθρακα (Εικόνα 11). Συνεπώς, λαμβάνοντας υπόψιν τους παράγοντες της θερμικής συμπεριφοράς, του βάρους και της μείωσης κόστους κατασκευής, τα CFRPs με στρώση $[0,90]_s$ και ίνες άνθρακα που παρουσιάζουν θερμική αγωγιμότητα του εύρους 500-800 W/mK μπορούν να μεταδώσουν αποδοτικά την θερμότητα που εκλύεται από τα ηλεκτρονικά και τους αισθητήρες πυριτίου προς την ψύξη. Μία ομάδα με έξι διαφορετικούς τύπους ινών άνθρακα μπορούν να χρησιμοποιηθούν, δίνοντας περίπου τα ίδια αποτελέσματα, υπό των παραγόντων της θερμικής συμπεριφοράς και του thermal runaway. Αυτά είναι τα ακόλουθα: Mitsubishi K13D2U, K13C2U, K13C6U και Nippon YS-95, XN-90, YS-90A. Η καλύτερη θερμική συμπεριφορά παρατηρήθηκε με CFRPs και ίνες άνθρακα Mitsubishi K13D2U. Τα CFRPs με Mitsubishi K13C2U, K13C6U και Nippon YS-95 έδωσαν περίπου τα ίδια αποτελέσματα. Τα CFRPs με Nippon XN 90και YS-90A ήταν ελαφρώς διαφορετικά, παρουσιάζοντας την χειρότερη θερμική συμπεριφορά από την ομάδα

Εξαιτίας της θερμοκρασιακής διαφοράς που παρατηρήθηκε στους αισθητήρες πυριτίου και στην ανιχνευτική μονάδα, η κατασκευή θα παρουσιάσει θερμικές καταπονήσεις. Θερμικές παραμορφώσεις μπορούν να επηρεάσουν σημαντικά την συμπεριφορά των μονάδων. Συνεπώς, αναλυτικές μελέτες υπό την σκοπιά της θερμομηχανικής ανάλυσης είναι απαραίτητες για την κατασκευή μιας ανιχνευτικής μονάδας στιβαρής και ανθεκτικής στην ακτινοβολία.

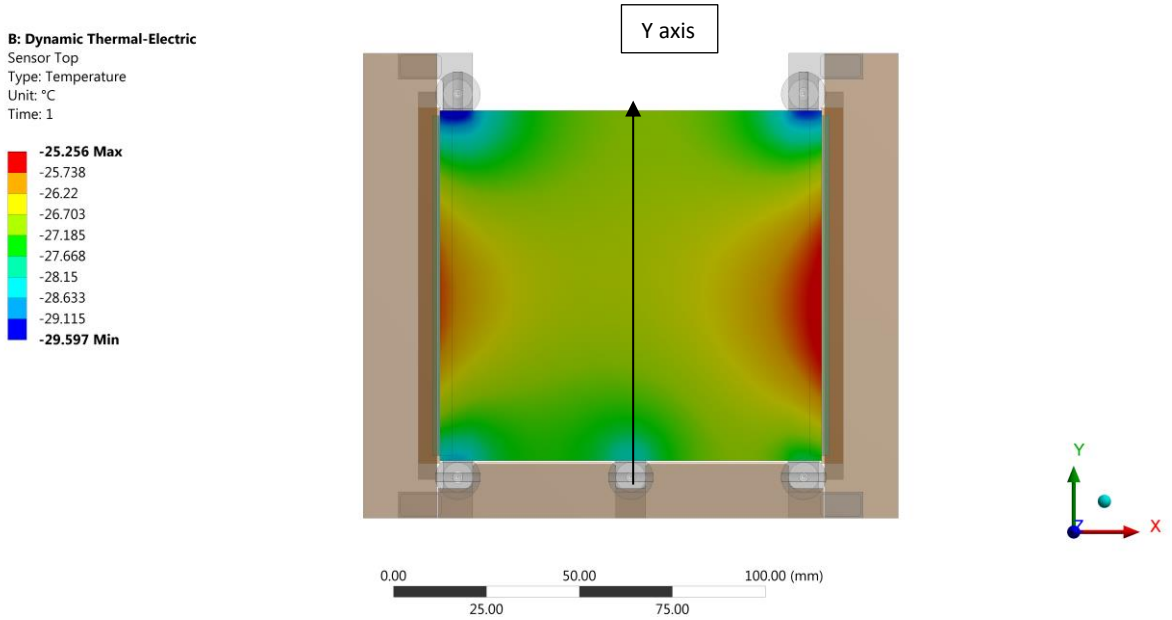

Εικόνα 9: Θερμοκρασιακή κατανομή του πάνω αισθητήρα πυριτίου με CFRPs στρώσης 0/90/0/90/0 και ίνες άνθρακα Mitsubishi K13D2U.

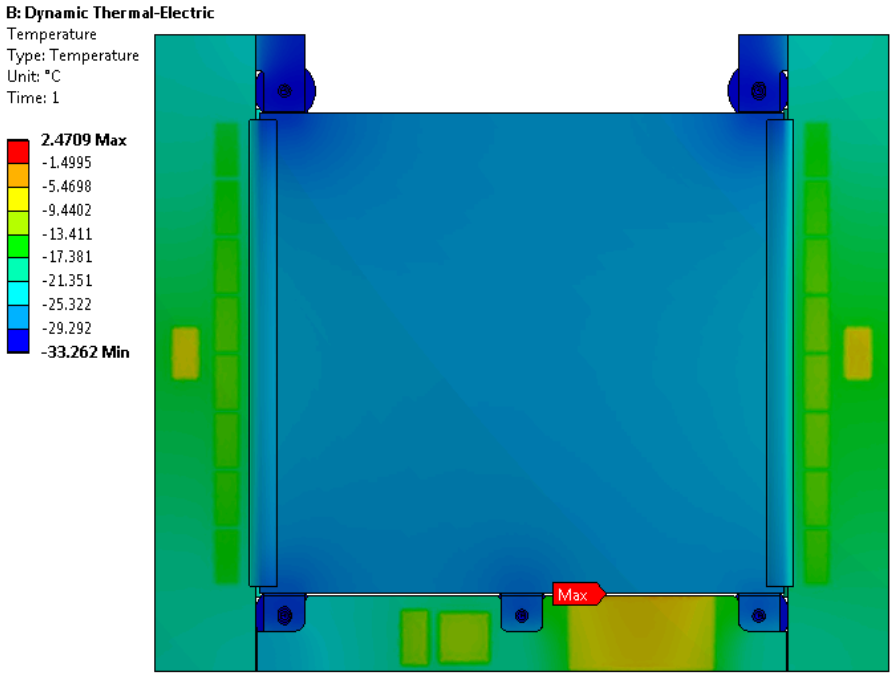

Εικόνα 10: Θερμοκρασιακή κατανομή της ανιχνευτική μονάδας με CFRPs στρώσης 0/90/0/90/0 και ίνες άνθρακα Mitsubishi K13D2U.

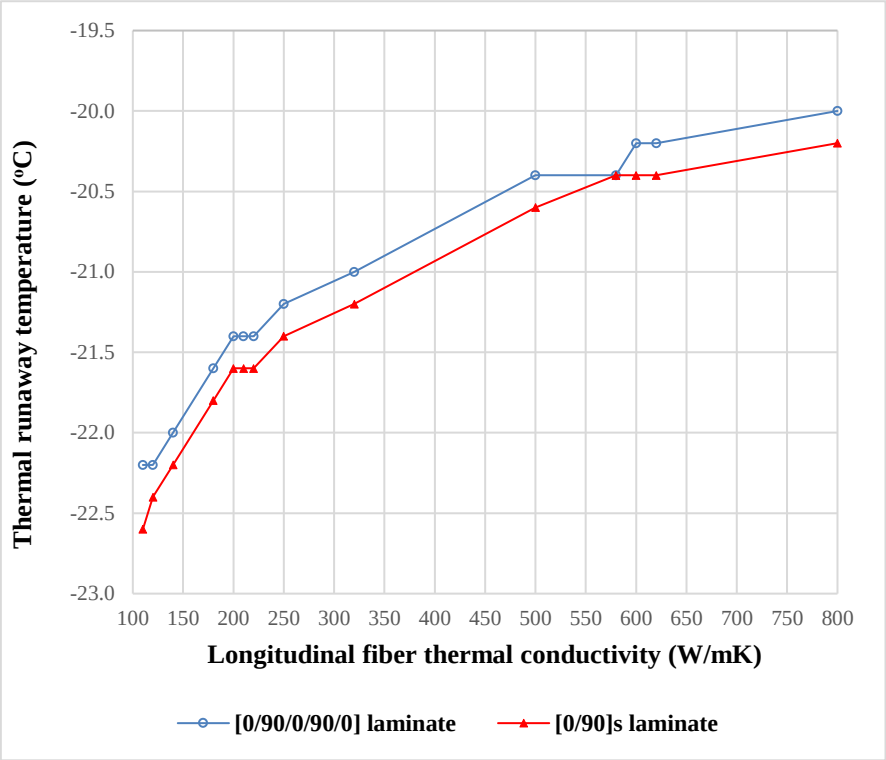

Εικόνα 11: Θερμοκρασίες που εμφανίζεται το thermal runaway της ανιχνευτικής μονάδας 2S 1.8 mm module σε σχέση με την κατά μήκος θερμική αγωγιμότητα ινών άνθρακα για τις δύο υπό εξέταση στρώσεις: 0/90/0/90/0 and [0/90]s.

Προτάσεις για περαιτέρω έρευνα:

- Θερμομηχανική ανάλυση της ανιχνευτικής μονάδας 2S 1.8 mm για τον προσδιορισμό των των τάσεων και των παραμορφώσεων.
- Ανάλυση κόστους για μαζική παραγωγή σύνθετων υλικών από ίνες άνθρακα (CFRPs).
- Συγκριτική μελέτη της θερμικής ανάλυσης με αλλαγή:
  - της διάταξης των ινών άνθρακα.
  - περιεκτικότητας των ινών.
- Σύγκριση της απόδοσης με χρήση άλλων ινών από διάφορες εταιρείες.
- Μελέτη μείωσης τους βάρους με χρήση διάφορων CFRPs.
- Προσδιορισμός της εποξικής ρητίνης ή της ρητίνης κυανικού εστέρα με υψηλή θερμική αγωγιμότητα.
- Μελέτη της απόδοσης με αλλαγή της δομής της ανιχνευτικής μονάδας με χρήση υλικών υψηλής θερμικής αγωγιμότητας.

Contents

Chapter 1
The HL-LHC and the CMS Phase-2 Upgrade

1.1 The Large Hadron Collider

The Large Hadron Collider (LHC) is the world's largest and most powerful particle accelerator. The LHC can accelerate protons and heavy ions, and has delivered collisions of protons, lead ions, and protons on lead ions: pp, PbPb, and pPb collisions.

Operation of the accelerator started in 2009. The 2010-2012 running period is referred to as Run 1. In 2010 and 2011 the LHC operated at a centre-of-mass energy, $\sqrt{s}$, of 7 TeV, and delivered to the CMS experiment data volumes of 45 pb^{-1} and 6.1 fb^{-1} of integrated luminosity, respectively. The centre-of-mass energy was increased to 8 TeV in 2012 and an integrated luminosity of 23.3 fb^{-1} was delivered to CMS during that year. Run 1 was followed by a two-year long shutdown, referred to as Long Shutdown 1 (LS1), during which the accelerator and the experiments were consolidated. This allowed starting Run 2 in 2015 at a centre-of-mass energy of 13 TeV. The integrated luminosities delivered to CMS were 4.2 fb^{-1} in 2015 and 41.1 fb^{-1} in 2016.

The collision rate of pp collisions increased steadily, with instantaneous luminosities of up to 2.1×10^{32} $cm^{-2}s^{-1}$ in 2010, 7.7×10^{33} $cm^{-2}s^{-1}$ in 2012, and 1.5×10^{34} $cm^{-2}s^{-1}$ in 2016, exceeding the LHC design value of 1.0×10^{34} $cm^{-2}s^{-1}$.

Thanks to the excellent performance of the LHC, the experiments (ATLAS, ALICE, CMS, and LHCb) have been able to achieve a plethora of highly relevant physics results, including the discovery of the Higgs boson by ATLAS and CMS in 2012, and the measurement of the branching ratios of the rare decays of the neutral Bs0 and B0 mesons to two muons by CMS and LHCb and more recently by ATLAS. Stringent limits have been placed on a large variety of new physics models. The top quark pair production cross section has been determined as a function of $\sqrt{s}$ and the top quark mass has been measured with unprecedented precision. Figure 1.1 shows an overview of the LHC planning from 2015 onwards. Run 2 will continue until the end of 2018, when the Long Shutdown 2 (LS2) will start. The LS2 will be followed by Run 3. It is expected that about 300 fb^{-1} will have been collected by 2024. The Long Shutdown 3 (LS3), scheduled to last from 2024 to mid 2026, will see the main preparation of the accelerator and of the experiments for the High Luminosity phase of the LHC (HL-LHC), while certain aspects of these upgrades (e.g. the upgrade of the LHC injector complex) will already happen during LS2.

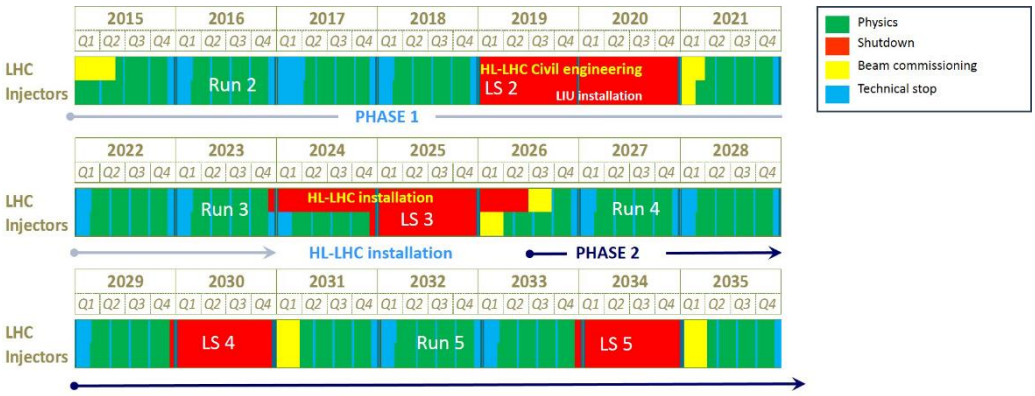

Figure 1: Overview of the LHC project planning from 2015 to 2035, indicating data taking phases (Runs) in green and long shutdowns, labelled LS, in red. Phases of beam commissioning (yellow) and technical stops (blue) are indicated as well. The planning is shown both for the LHC and its injectors.

1.2 The HL-LHC upgrade

During LS3 the accelerator will be upgraded to enable instantaneous peak luminosities of 5×10^{34} $cm^{-2}s^{-1}$, or even 7.5×10^{34} $cm^{-2}s^{-1}$ in the ultimate performance scenario (here and in the following, we quote expected operational performance numbers, not maximal performance numbers potentially achievable by the accelerator). This will allow ATLAS and CMS to collect integrated luminosities of the order of 300 fb^{-1} per year and up to 3000 fb^{-1} during the HL-LHC projected lifetime of ten years (up to 4000 fb^{-1} if the ultimate instantaneous luminosity can be achieved). The HL-LHC is expected to run at a centre-of-mass energy of 14 TeV and with a bunch spacing of 25 ns. The HL-LHC project was formally approved by CERN Council in June 2016. The HL-LHC upgrade and its full exploitation is considered a top priority effort by the European Strategy for Particle Physics (ESPP) and the US Particle Physics Project Prioritization Panel (P5), and is in the landmark list of the European Strategy Forum on Research Infrastructures (ESFRI) “Roadmap 2016” strategy report on large research infrastructures.

The increase of the instantaneous luminosity will be achieved by a variety of measures. Most importantly, the inner triplet quadrupole magnets in the insertion regions will be replaced with more radiation tolerant ones based on Nb3Sn technology. The new quadrupole magnets will provide a higher magnetic field strength and feature a larger aperture, allowing for a luminosity increase through a lower beam beta function, $\beta^{\star}$, in the collision region.

As a consequence, a number of new corrector magnets and separation dipoles will need to be installed, and the TAS (Target Absorber Secondary) absorbers need to be replaced. A lower $\beta^{\star}$ comes at the cost of a smaller geometrical luminosity reduction factor, due to a larger crossing angle of the beams. Superconducting radiofrequency crab cavities will be installed in the interaction regions, allowing rotation of the beams before collision so that the bunches collide head on.

The number of simultaneous pp collisions (pileup) happening during a single bunch crossing is proportional to the instantaneous luminosity. To limit the number of pileup events, it is foreseen to level

the luminosity during an LHC fill, i.e. to operate at a constant luminosity below the maximum achievable value.

While the mean number of pileup events reached 53 at the highest instantaneous luminosity in 2016, in a special high pileup run, about 140 pileup events on average are expected for an instantaneous luminosity of $5.0 \times 1034\ \mathrm{cm}^{-2}\mathrm{s}^{-1}$, increasing to 200 pileup events in the ultimate luminosity scenario. The radiation level will be unprecedented: for the design integrated luminosity of 3000 fb^{-1} a 1 MeV neutron equivalent fluence of $2.3 \times 1016\ \mathrm{n_{eq}/cm^2}$ and a total ionizing dose (TID) of 12 MGy (1.2 Grad) is expected at the centre of CMS, where the innermost silicon pixel tracking layers will be installed.

The HL-LHC upgrade is accompanied by an upgrade programme of the CMS experiment, to maintain the excellent performance of the detector and to allow us to fully profit from the HL-LHC capabilities, in spite of the challenging radiation levels and operating conditions.

1.3 The CMS Phase-2 Upgrade

The CMS detector needs to be substantially upgraded during LS3 in order to exploit the increase in luminosity provided by the HL-LHC. This upgrade is referred to as the CMS Phase-2 Upgrade **[2]**. The increase in radiation levels requires improved radiation hardness, while the larger pileup and associated increase in particle density requires higher detector granularity to reduce occupancy, increased bandwidth to accomodate higher data rates, and improved trigger capability to keep the trigger rate at an acceptable level while not compromising physics potential. It is foreseen upgrade procedures on the CMS trigger system, the muon chambers, the electromagnetic calorimeter (ECAL), the hadronic calorimeter (HCAL), the scintillator tiles close to the beam line and the entire tracking system.

This thesis is focused on the silicon tracking system, presently consisting of pixel and strip detectors. The new tracker will feature increased forward acceptance, increased radiation hardness, higher granularity, and compatibility with higher data rates and a longer trigger latency. In addition, the tracker will provide tracking information (on tracks above a configurable transverse momentum threshold) to the L1 trigger, information presently only available at the HLT. This will allow the trigger rates to be kept at a sustainable level without sacrificing physics potential.

The planned upgrade of the tracker will include an Inner Tracker based on silicon pixel modules and an Outer Tracker made from silicon modules with strip and macro-pixel sensors. CMS adopts a right-handed coordinate system. The origin is centred at the nominal collision point inside the experiment. The x axis points towards the centre of the LHC, and the y axis points vertically upwards. The z axis points along the beam direction. The azimuthal angle, ϕ, is measured from the x axis in the x-y plane, and the radial coordinate in this plane is denoted by r. The polar angle, ϑ, is measured from the z axis. The pseudorapidity, η, is defined as $\eta = -\ln\tan(\vartheta/2)$. The momentum and energy transverse to the beam direction, denoted by p_T and E_T, respectively, are computed from the x and y components.

Chapter 2
Overview of the Phase-2 Tracker Upgrade

2.1 Limitations of the present tracker

The present strip tracker was designed to operate with high efficiency at an instantaneous luminosity of $1.0 \times 10^{34}\,\mathrm{cm^{-2}s^{-1}}$, with an average pileup of 20–30 collisions per bunch crossing, and up to an integrated luminosity of 500 $\mathrm{fb^{-1}}$. The tracker is indeed performing very well at current instantaneous luminosities that are well above the design value. Performance will however degrade due to radiation damage beyond 500 $\mathrm{fb^{-1}}$. The original pixel detector has already been replaced with a new device, the "Phase-1" pixel detector, during the extended year-end technical stop (EYETS) 2016/2017. As the instantaneous luminosity exceeded the original design value and is projected to increase further prior to LS3, this upgrade was needed to address dynamic inefficiencies in the readout chip at high rates. One quarter of the layout of the Phase-1 tracker is shown in Fig. 2.1. The radial region below 200 mm is equipped with pixelated detectors. Beyond 200 mm, the present tracker features single-sided strip modules and double-sided modules composed of two back-to-back silicon strip detectors with a stereo angle of 100 mrad. Double-sided modules provide coarse measurements of the z and r coordinates in the barrel and endcaps, respectively. The tracking system was designed to provide coverage up to a pseudorapidity of $|\eta| \approx 2.4$.

Before the start of the HL-LHC both the strip tracker and the Phase-1 pixel detector will have to be replaced due to the significant damage and performance degradation they would suffer during operation at the HL-LHC, and to cope with the more demanding operational conditions. The performance degradation has been studied extensively and is documented in the Technical Proposal for the CMS Phase-2 Upgrade.

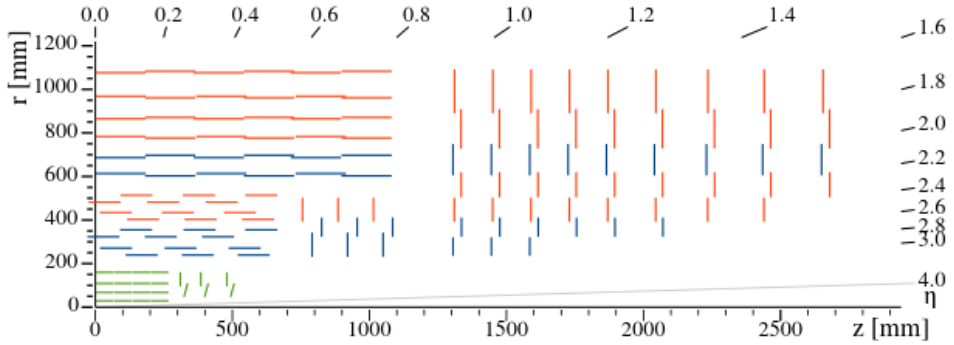

Figure 2-1: Sketch of one quarter of the Phase-1 CMS tracking system in r-z view. The pixel detector is shown in green, while single-sided and double-sided strip modules are depicted as red and blue segments, respectively.

Accumulated radiation damage in the pixel sensors reduces the charge collection efficiency as well as the Lorentz angle, leading initially to decreased charge sharing among neighbouring pixels and hence to deteriorated spatial resolution, and eventually to reduced hit efficiency. For the present strip tracker, the most prominent changes of detector properties with irradiation are the increase of the sensor depletion voltage and of the leakage current. The latter can be mitigated, up to a certain point,

by lowering the operating temperature of the cooling system, while the former cannot. It has been demonstrated that basically all double-sided strip modules cannot be operated anymore at the nominal cooling temperature already after 1000 fb^{-1}. Studies of the expected performance of the current tracking system as a function of integrated luminosity have shown unacceptable degradation beyond about 1000 fb^{-1}, including the deterioration of tracking and b tagging performance and a worsening of the impact parameter resolution. The physics programme would also be affected by limitations in readout bandwidth and trigger latency. The tracker must therefore be entirely replaced for the Phase-2 physics programme.

2.2 Requirements for the tracker upgrade

The Phase-2 tracker will consist of an Inner Tracker (IT) based on silicon pixel modules and an Outer Tracker (OT) made from silicon modules with strip and macro-pixel sensors. The thesis is focused on the Outer Tracker upgrade project. The main requirements for the tracker upgrade can be summarized as follows.

- *Radiation tolerance*. The upgraded tracker must be fully efficient up to a target integrated luminosity of 3000 fb−1, with appropriate margin. A margin of the order of 50% is tar-geted, to accommodate both uncertainties and the potential delivery of additional integrated luminosity, should the ultimate luminosity scenario be realized. This requirement must be fulfilled without any maintenance intervention for the Outer Tracker. For the Inner Tracker, where pixel detector modules are deployed, it is envisaged to keep the present concept of accessibility, allowing us to extract the Inner Tracker during regular shutdowns and offering the option to replace modules and other elements as they accumulate substantial radiation damage.

- *Increased granularity*. In order to ensure efficient tracking performance with a highlevel of pileup, the channel occupancy must be kept at around or below the per cent level (per mille level) in the Outer Tracker (Inner Tracker), which requires a high channel density. Target values of 140 and 200 collisions per bunch crossing are used to benchmark the performance of the detector.

- *Improved two-track separation.* The present tracker has limited track finding performance in highly energetic jets, due to hit merging in the pixel detector. In order to optimally exploit the large amounts of collision data that will be taken during high luminosity operation, two-track separation needs to be improved.

- *Reduced material in the tracking volume*. The exploitation of the high luminosity will greatly benefit from a lighter tracker. The performance of the current tracker is affected by the amount of material, which also influences the performance of the calorimeters and of the overall event reconstruction in CMS.

- *Robust pattern recognition*. Track finding under high pileup conditions becomes increasingly more difficult and time consuming. The design of the upgraded tracker should enable fast and efficient track finding, notably at the HLT.

- *Contribution to the level-1 trigger.* The selection of interesting physics events at the first trigger stage becomes extremely challenging at high luminosity, not only because of the rate increase, but also because selection algorithms become inefficient in high pileup conditions. The CMS trigger will operate with substantially increased latency and output rate and the tracker has to comply with those. In addition, in order to preserve and possibly enhance the performance in a wide spectrum of physics channels, CMS has chosen to use tracking information in the L1 event selection, anticipating part of the reconstruction presently performed in the HLT.

- *Extended tracking acceptance.* The overall CMS physics capabilities will greatly benefit from an extended acceptance of the tracker and calorimeters in the forward region. The upgraded tracking system will provide efficient tracking up to about $|\eta| = 4$.

The following section summarizes the main concepts and features of the upgraded tracking system. One quarter of the Phase-2 tracker layout can be seen in Fig. 2.2. The number of layers has been optimised to ensure robust tracking, i.e. basically unaffectedperformance when one detecting layer is lost in some parts of the rapidity acceptance. The six layers of the Outer Tracker are the minimum required to ensure robust track finding at the L1 trigger in the rapidity acceptance of $|\eta| < 2.4$. In the central region, the four layers of the Inner Tracker (the same number as already implemented in the Phase-1 upgrade) are the key for the pixel-based track seeding, which ensures good track finding performance with affordable computing time down to very low transverse momentum. The same number of layers as in the Phase-1 detector good performance is preserved also at the expected HL-LHC pileup levels, thanks to the smaller pixel size. In the forward part, the number of detection layers deployed ensures that particles originating from the luminous region traverse on average more than eight layers of active detector modules up to $|\eta| \approx 3.5$, and more than six up to $|\eta| \approx 4.0$.

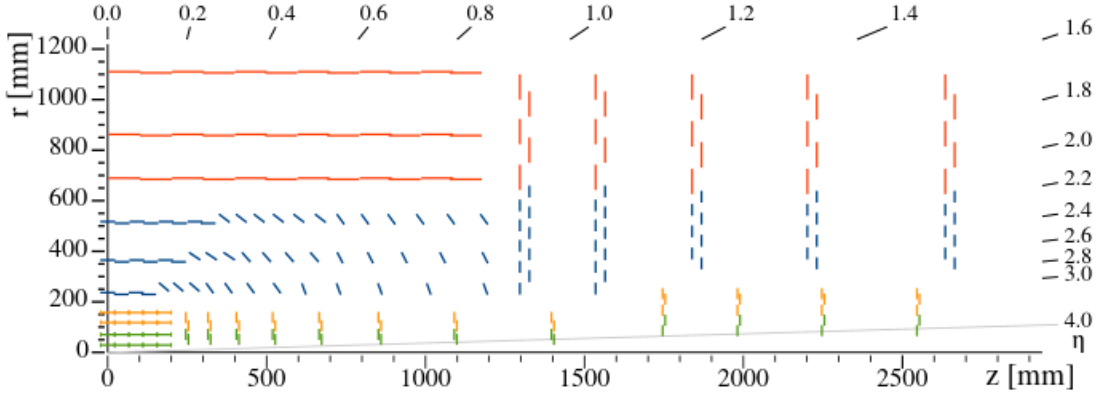

Figure 2-2: Sketch of one quarter of the tracker layout in r-z view. In the Inner Tracker the green lines correspond to pixel modules made of two readout chips and the yellow lines to pixel modules with four readout chips. In the Outer Tracker the blue and red lines represent the two types of modules described in the text.

2.3 The Outer Tracker

The Outer Tracker is populated with p_T modules, implementing the L1 trigger functionality. The p_T module concept relies on the fact that the strips of the top and bottom sensors of a module are parallel to each other. With the strip direction being parallel to the z axis in the barrel and nearly radial in the endcaps, this prevents the concept of stereo strips to be used to measure the z coordinate (r coordinate) in the barrel (endcaps).

For this reason two versions of p_T modules have been realized: modules with two strip sensors (2-strip or 2S modules) and modules with a strip and a macro-pixel sensor (pixel-strip or PS modules). The strips in the 2S modules have a length of about 5 cm, while those in the PS modules are about 2.4 cm long. In PS modules one of the two sensors is segmented into macro-pixels of about 1.5 mm length, providing the z (r) coordinate measurement in the barrel (endcaps). The PS modules are deployed in the first three layers of the Outer Tracker, in the radial region of 200–600 mm, i.e. down to radii at which the stub p_T resolution remains acceptable and the data reduction effective. The 2S modules are deployed in the outermost three layers, in the radial region above 600 mm. In the endcaps the modules are arranged in rings on disc-like structures, with the rings at low radii, up to about 700 mm, equipped with PS modules, while 2S modules are used at larger radii. The precision on the z coordinates provided by the three PS barrel layers constrain the origin of the trigger tracks to a portion of the luminous region of about 1 mm, which is sufficiently precise to partially discriminate particles coming from different vertices.

The p_T module concept implies that both the top and the bottom silicon sensors of a module must be connected to the readout electronics that performs stub finding. In order to implement the connectivity between the upper and lower sensors with reliable and affordable technologies, the two halves of each module are read out independently by front-end hybrids on the two ends, which prevents communication between the sensor halves and thus the reconstruction of stubs when particles cross the module near the centre with a large incident angle (Fig. 2.3). In a flat barrel layout such an effect translates into a geometrical inefficiency of stub finding, which is larger than 30% at the edge of the first barrel layer.

To overcome this limitation, CMS has developed an innovative layout where the first three barrel layers that are populated with PS modules feature progressively tilted modules, nearly perpendicular to incident particles over the entire barrel length (Fig. 2.2). In the outer three layers of the barrel the effect of stub finding inefficiency is much less severe because of the smaller incidence angles (the incidence angle is measured with respect to the sensor normal), the smaller sensor spacing at those radii, and the double length of the 2S modules along z.

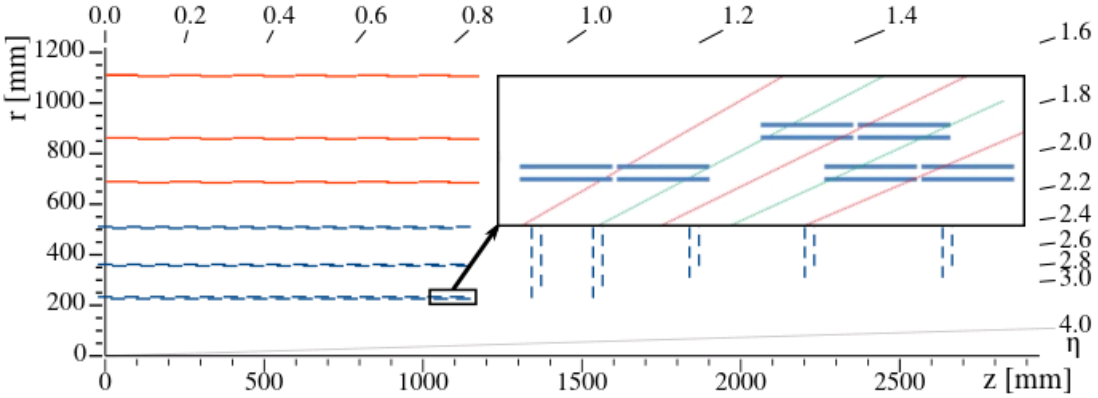

Figure 2-3: In a flat barrel layout the PS modules at the edge of the inner barrel layers would have a large geometrical inefficiency for on-module stub finding. This is illustrated in the zoom, where each blue thick line represents half of a sensor. The distance between sensors in r is of the order of millimetres. While the inefficiency at the edge of the modules can be compensated by implementing large overlaps between consecutive modules in z, the inefficiency between the two sensor halves (indicated by the red lines) is irrecoverable.

The Outer Tracker is composed of six cylindrical "barrel" layers in the central region, coveringthe region of $|z| < 1200$ mm, complemented on each side by five "endcap" double-discs, in the region of $1200 < |z| < 2700$ mm. Modules are installed between $r \approx 21$ cm and $r \approx 112$ cm. Three sub-detectors are distinguished, as illustrated in Fig. 2-4: the Tracker Barrel with PS modules, TBPS; the Tracker Barrel with 2S modules, TB2S; and the Tracker Endcap Double-Discs, TEDD. Hermeticity is provided for particles emerging from the luminous region $|z| < 70$ mm, so that at least six module layers are crossed by all particles in the rapidity range $|\eta| < 2.4$, except for a small gap in the transition from barrel to endcap at $|\eta| \approx 1$, where only five module layers are crossed on average. The chosen number of sensitive layers is the minimum that ensures sufficiently robust track finding performance for the L1 trigger. Extensive studies performed with different detector configurations have shown that with only five module layers the track finding performance for the L1 trigger would be heavily affected as soon as some parts of the detector become inefficient, while with six layers the performance is robust with respect to inefficiencies affecting one layer. A similar logic drives the choice of the number of layers populated with PS modules: at least two precise coordinates are needed to measure the polar angle of the track and provide some level of primary vertex discrimination, hence three macro-pixel layers are necessary to ensure adequate performance with minimal redundancy.

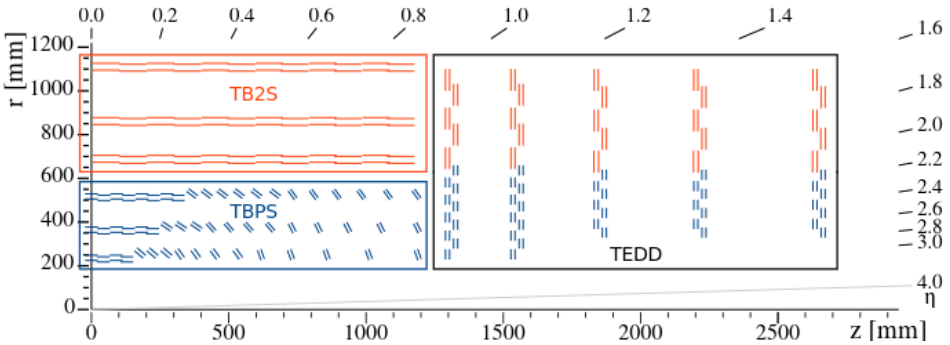

Figure 2-4: Sketch of one quarter of the Outer Tracker in r-z view. Blue (red) lines represent PS (2S) modules. The three sub-detectors, named TBPS, TB2S, and TEDD, are indicated.

2.4 Structure of 2S and PS modules

The main parameters of 2S and PS modules are summarized in Table 2-1. Images of the assembled modules, details of their components, and sketches of the connectivity between sensors and readout hybrid circuits are shown in Fig. 2-5. The strip sensors in 2S and PS modules have two rows of 5 cm and 2.4 cm long strips, respectively, with each row of strips read out from one module end, while the macro-pixel sensors of the PS modules have 32 rows of 1.5 mm long macro-pixels.

The size of the sensors of the 2S modules is defined to optimally fit in a 6" silicon wafer, while two PS sensors are obtained from one wafer. The reduced size of the PS modules is necessary to cover the surface of the pixelated sensor with two rows of Macro-Pixel ASICs (MPAs). At the same time, the shorter strips in the PS modules are appropriate for the higher track density in the inner regions of the Outer Tracker, keeping the occupancy at acceptable levels. The 90 µm and 100 µm strip pitch values, while allowing for excellent performance in terms of spatial resolution and p_T resolution for the L1 track finder, are driven by limitations in the line density on the readout hybrid for the 2S module and on the bump density of the C4 technology for the PS module. The strip sensors are wire bonded directly to the front-end hybrids, thus avoiding heavy pitch adapters.

In both modules the desired gap between the two sensors is achieved by gluing them onto spacers made of aluminium / carbon fibre composite (Al-CF). The spacers provide mechanical support and efficient heat removal, with a high thermal conductivity, in particular in-plane with the carbon fibres, and a coefficient of thermal expansion well matched to silicon.

The 2S modules are mounted on the supporting structures with small screws at the sides of the sensor spacers. These mounting points provide cooling to the entire module, including its readout electronics. In PS modules the large MPAs are thermally coupled to the pixelated sensor through the bumps, hence a large-surface cooling contact is required. For this reason the module is built on a baseplate made of carbon fibre reinforced polymer (CFRP). This baseplate is glued onto a cold surface on the supporting structure, in which the cooling pipe itself is embedded. The sensor spacers provide the thermal path from the strip sensor to the pixelated sensor, and the whole module is cooled through the baseplate.

The front-end hybrids are realized in a flexible (flex) technology and are laminated onto CFRP supports, also referred to as stiffeners. The hybrids are folded around spacers matching the thickness of the assembly of the two sensors, in order to minimize the length of the wirebonds between hybrids and sensors, or between hybrids and MPA periphery in the case of PS modules. One 2S front-end hybrid carries eight CMS Binary Chips (CBCs) reading out the strips of the top and bottom sensors at one sensor end, plus the Concentrator Integrated Circuit (CIC), which serves as interface between all the CBCs of the hybrid and the readout link. The role of the CIC is mainly to aggregate and serialize the data of the readout chips and to distribute clock, trigger, and control signals to them. One PS front-end hybrid houses eight Short Strip ASICs (SSAs) reading out the strip sensor, and the same CIC as used for 2S hybrids. All the front-end chips implement binary readout. In order to fully exploit the achievable hit position resolution in the on-module stub finding, which compares cluster positions, in both module types one extra bit is added to the hit address, such that in the case of clusters with an even number of fired channels the coordinate is set in the centre of the cluster, in between two channels ("half-strip resolution").

The auxiliary electronics for powering and optical readout is integrated on service hybrids realized in the same flex technology as the front-end hybrids. The service hybrids are also laminated onto stiffeners. In 2S modules one single service hybrid is located at one end of the sensor assembly. In PS modules, due to the reduced width of these modules, powering and readout functionalities are implemented in two separate circuits, located at the two ends of the sensor assembly.In all hybrids, the ASICs are bump-bonded onto the flex circuit. High p_T tracks are identified on-module by comparing the hit patterns in the top and bottom sensors of the module, in order to provide stub information to the L1 trigger at bunch crossing frequency. Different values of the gap between the two sensors of a module are needed, in addition to a programmable acceptance window in the front-end ASICs, in order to implement a coherent p_T filtering in the whole Outer Tracker volume. For this reason 2S modules are realized in two variants, with 1.8 and 4.0 mm gaps between the mid-planes of the active volumes of the sensors, and PS modules are realized in three variants, with 1.6, 2.6, and 4.0 mm gaps. Table 2-2 summarizes the number of modules per type and variant in the different sub-detectors.

The chip logic also implements an offset correction, separately programmable for eight groups of channels in each chip, in order to form an unbiased estimate of the particle transverse momentum in the front-end electronics. Such programmable parameter can also absorb possible small offsets in the relative positions of the two sensors originating from limited precision in the mechanical assembly. However, a relative tilt between the two sensors — with the strips in the upper sensor not being parallel to the strips (macro-pixels) in the lower sensor — cannot be corrected for in the chip logic, hence an optimal p_T estimate in the Outer Tracker modules translates into a requirement for the maximum angular tilt between the sensors.

.

2S module	PS module
$\sim 2 \times 90\ \text{cm}^2$ active area	$\sim 2 \times 45\ \text{cm}^2$ active area
2×1016 strips: $\sim 5\ \text{cm} \times 90\ \mu\text{m}$	2×960 strips: $\sim 2.4\ \text{cm} \times 100\ \mu\text{m}$
2×1016 strips: $\sim 5\ \text{cm} \times 90\ \mu\text{m}$	32×960 macro-pixels: $\sim 1.5\ \text{mm} \times 100\ \mu\text{m}$
Front-end power ~ 5 W	Front-end power ~ 8 W
Sensor power ($-20\,^\circ$C) ~ 1.0 W	Sensor power ($-20\,^\circ$C) ~ 1.4 W

Table 2-1: Main parameters of the 2S and the PS module of the CMS Tracker.

Module type and variant		TBPS	TB2S	TEDD	Total per variant	Total per type
2S	1.8 mm	0	4464	2792	7256	7680
	4.0 mm	0	0	424	424	
PS	1.6 mm	826	0	0	826	5616
	2.6 mm	1462	0	0	1462	
	4.0 mm	584	0	2744	3328	
Total		**2872**	**4464**	**5960**	**13296**	

Table 2-2: Number of modules in the Outer Tracker, by module type and variant.

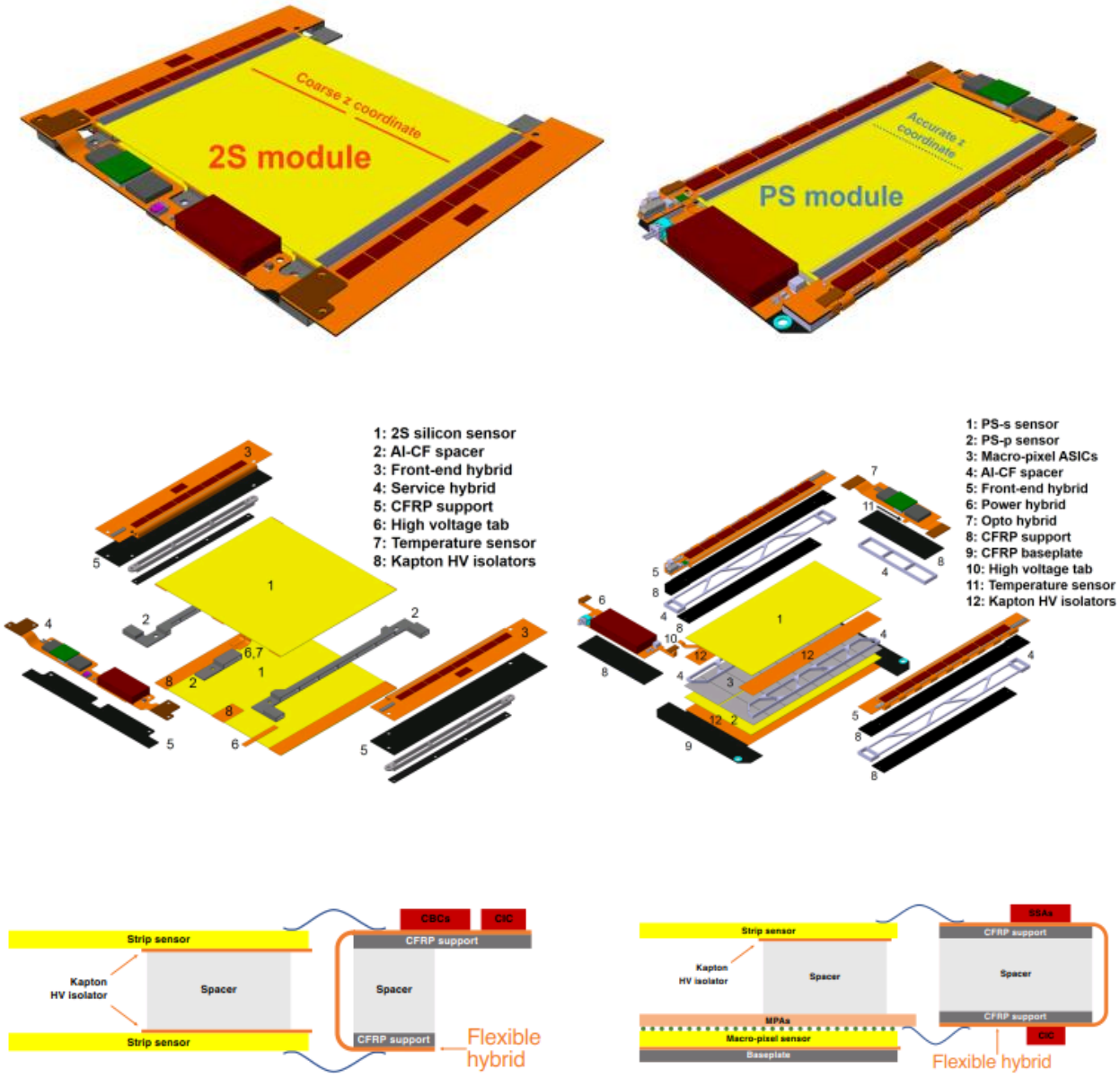

Figure 2-5: The 2S module (left) and PS module (right) of the Outer Tracker. Shown are views of the assembled modules (top), details of the module parts (centre) and sketches of the front-end hybrid folded assembly and connectivity (bottom).

2.5 Silicon sensors and operational aspects

Silicon strip and macro-pixel sensors are the detection devices of the CMS Outer Tracker. They have to provide sufficient spatial resolution at the right granularity to cope with the high density of particle tracks created in each collision. At the same time they have to be sufficiently radiation tolerant to withstand the HL-LHC environment for the projected lifetime of the detector.

The minimum operation voltage for the sensors shall be at least 10% above the full depletion voltage (V_{fd}) value of each sensor. Regardless of the final choice of sensor thickness and resistivity, the initial V_{fd} will be smaller than 300 V, therefore an operation voltage at the sensor backplane of −400 V will be sufficient during the first years of operation. Seed signals of about 12 000 and 8000 electrons can be extracted from 200 µm thick sensors at a depletion voltage of −600 V even after exposure to fluences of 6×10^{14} n_{eq}/cm^2 and 1.5×10^{15} n_{eq}/cm^2, respectively, corresponding to twice the fluence expected for 3000 fb^{-1} for 2S modules and 1.5 times the respective fluence for PS modules. The expected RMS noise is 1000 electrons for 2S sensors and 700 and 200 electrons for PS-s and PS-p sensors, respectively. Nevertheless, sensors, modules, and HV power supplies are specified to support a maximum operation voltage of −800 V, which allows for an additional boost in signal for the modules that are most affected by a reduction of the signal-to-noise ratio.

The reverse bias current that a sensor draws after exposure to irradiation is described using the current related damage factor α. For the end of the detector lifetime, with α equal to 6.16×10^{-17} A/cm (at +20 ◦C) is conservatively assumed, including a realistic annealing scenario. Using the maximum fluences of 3.0×10^{14} n_{eq}/cm^2 for 2S and 1.0×10^{15} n_{eq}/cm^2 for PS sensors, the maximum currents can be estimated. For PS (2S) sensors of an active thickness of 200 µm a maximum current of about 0.9 mA (0.6 mA) is expected for a sensor temperature of −20 °C. This results in a maximum power dissipation of approximately 0.7 W (0.5 W) per sensor, which has to be removed by cooling. No reverse annealing of the charge collection efficiency was observed in thin sensors. This would allow to exploit annealing of the leakage current without any loss of charge due to reverse annealing.

Chapter 3
Mechanics of 2S Modules

3.1 Module Mechanics

The module design was largely driven by the choice to make it self-contained, such that the power conversion, opto-components, and control electronics are all on-board and not shared with other modules. In addition, it was desirable to keep the 2S and PS module designs as similar as possible for the different sensor spacing versions, so that for each module type only a minor change in components is required for the different versions. Other general principles for the module design that apply to both 2S and PS modules include:

- Use of aluminium / carbon fibre (Al-CF) composite material as a spacer between sensors and for hybrid fold-over. This material has both high thermal conductivity and a low coefficient of thermal expansion (CTE) of 4 parts per million (ppm) per ^{o}C along two axes. This allows for good heat conduction from the sensor and hybrids as well as for low stress on the glue joints between sensors, spacers, and CFRP (carbon fibre reinforced polymer) parts.

- The use of high modulus and high thermal conductivity CFRP plates, mostly as flex hybrid stiffeners but also in the PS module baseplate.

- Employment of glue layers as thin as possible to permit good heat conduction while providing the necessary structural strength.

- Use of a flex hybrid circuit folded around a spacer allowing connection of sensors to the ASICs via wire bonding with optimal geometric conditions. In addition, the fold-over of the hybrids will be part of the hybrid assembly, done in industry.

- Direct sensor to hybrid wire bonding connections eliminating the need for pitch adapters. The bond pad pitch of the hybrid is identical to that of the sensor, simplifying the wire bonding. The electrical lines are routed further to the bump bond pads on the hybrid, to which the chips are connected via bump bonding.

- Use of high reliability connectors where possible between service hybrids and front-end hybrids as well as for connection to the backplane bias circuit. As a fall-back solution connectivity between hybrids would be realized through wire bonding.

- Encapsulation of all wire bonds to reduce risk of handling damage and damage due to possible resonant vibrations in the magnetic field.

- The HV isolation requirement is 1000 V between any conductive structures at high voltage and those at ground potential. This gives a safety margin of 400 V with respect to the nominal bias voltage of 600 V, and still 200 V margin with respect to the maximum sensor bias voltage of 800 V that is considered to be used in order to increase the signal, if that shall ever be required.

- Use of Kapton MT polyimide films **[7]** of 25 μm thickness for HV isolation between sensors and Al-CF spacers. This provides a reliable barrier and has good thermal conductivity.

- The HV bias connection to the 2S and PS strip sensors will use a small flex circuit glued to the back of the bare sensor before assembly. Then it will be wire bonded to the sensor back-plane and encapsulated to protect the wires. One thermistor, read out by the LpGBT, is also mounted on a Kapton flex circuit and will be glued to the top sensor in each module. Both the HV bias and thermistor circuit will have a connector tail so they can be connected to the service hybrid (temperature sensors and bias circuit in 2S modules) or the front-end hybrid (bias circuit in PS modules).

3.2 Mechanics of 2S Modules

An exploded view of the two variants of the 2S module (1.8 mm and 4.0 mm spacing) is shown in Fig. 3-1. The Al-CF spacers (referred to as bridges in the 2S module), besides providing the spacing between the sensors, also serve as the main structural element, the main cooling path, and the means of a precise (~ 100 μm) fixation of the modules in the mechanical support structures, using shoulder screws. There are three bridges in each module, two identical long bridges which span the full width of the sensors and one stump bridge which is a very short spacer penetrating only a small distance between the sensors. The stump bridge is located on the service hybrid side of the module, midway between the FE hybrids, and serves primarily as a means of heat transport from the service hybrid to the cooling system, although it does help to remove some heat from the sensors as well.

The main differences between the 1.8 mm and 4.0 mm 2S modules are the thickness and shape of the Al-CF spacers, as can be appreciated from Fig. 3.1. However, there are a few small differences in the FE hybrids and the service hybrid as well. In both variants, the support of the FE hybrid was designed to place the top and fold-over faces of the hybrid at the same height as the respective sensors for optimal wire bonding. The FE hybrid, which is laminated onto a CFRP stiffener, is glued directly onto the rectangular tabs of the Al-CF bridge. This represents the primary heat conduction path for cooling the hybrid. The fold-over part of the hybrid allows for optimal positioning for wire bonding between sensors and hybrids, provides adequate stiffness for wire bonding, minimizes material, and uses matched CTE structures so that the hybrid does not deform or undergo large stresses when at the cold operating temperatures.

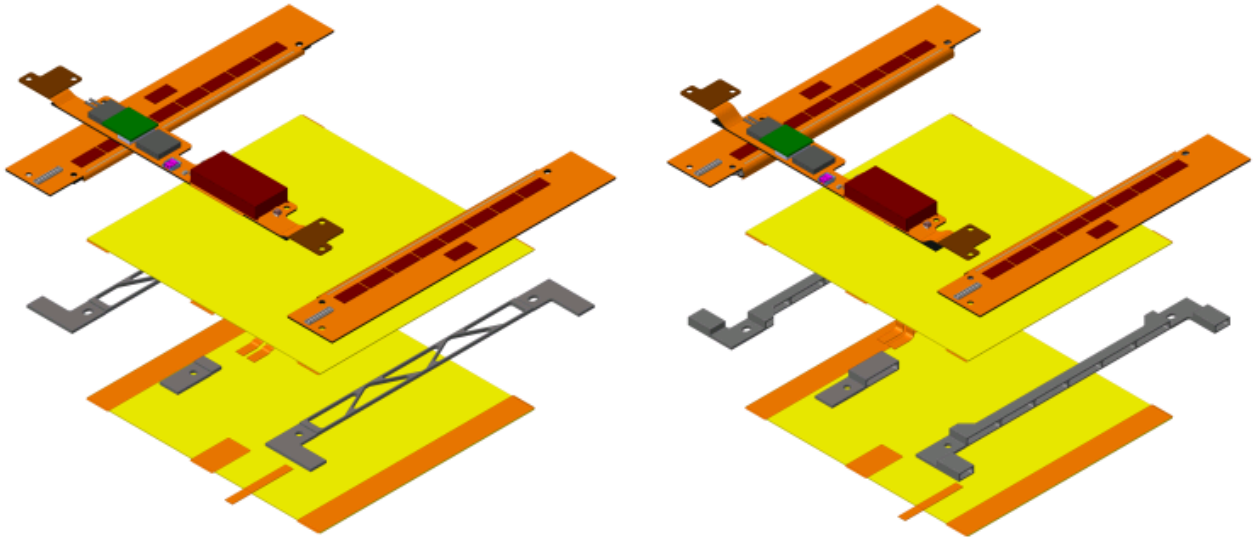

Figure 3-1: Exploded views of the 1.8 mm (left) and 4.0 mm (right) 2S module variants. From top to bottom the following components can be seen: the three hybrids, the top sensor, the three bridges, and the bottom sensor. The orange strips on the sensors are Kapton strips for HV isolation (below the bridges) and flex cables that deliver the bias voltage or carry a temperature sensor.

3.3 Module thermal performance aspects

The coefficients of thermal expansion of the main module components, namely the sensors, the bridges, and the carbon fibre stiffeners, are well matched, with CTE values of 3 ppm/◦C for silicon, 4 ppm/◦C for Al-CF, and 0 ppm/◦C for carbon fibre. For a temperature difference of 50 °C, corresponding to a temperature range spanning from −30 ◦C to +20 ◦C, differencial expansions of 5 µm between the Al-CF bridge and the sensor, and of 20 µm between the Al-CF hybrid spacer and the CF hybrid stiffener, are expected, for the full length of the respective glue joints. The front-end hybrids have a symmetric build-up, due to the fold-over of the flex circuit, limiting potential deformations. The thermal performance of 2S 1.8 mm was studied with finite element analyses (FEA). The studies were carried out using ANSYS by importing a CAD model of the module, removing features that are irrelevant for studying the thermal performance, and modelling simplified cooling structures, onto which the module was placed in the FEA model. The power consumptions of the front-end ASICs used in the calculations were estimated based on prototypes and simulations, whereas the sensor power consumption is calculated from the expected worst case fluence for a given module type and sub-detector, as obtained from FLUKA simulations. The thermal performance of the module and its corresponding cooling structure is characterised in terms of the temperature at which the module undergoes thermal runaway (i.e. a situation in which the cooling power is insufficient to cool the module and the sensor temperature rises in a positive feedback loop, since the leakage current increases exponentially with temperature) when the coolant temperature is increased. For this purpose a temperature dependency is introduced to the sensor power consumption by scaling the value calculated at room temperature and applying the resulting temperature dependent heat load to the individual sensor elements in the FEA model. The cooling system is designed such that the coolant at the first module in a cooling loop, corresponding to the warmest module along the loop, has a temperature of −33 °C. The 2S 1.8mm module has been studied after receiving 3000 $fb^{-1}$of integrated luminosity at the fluence of $2.2 \cdot 10^{14}$ n_{eq}/cm^2.

3.4 Cooling system

The total power dissipated in the tracking volume and due to heat leaks from the surroundings is expected to be about 100 kW for the Outer Tracker and about 50 kW for the Inner Tracker, including losses on cables inside the tracking volume and allowing for some margin. The cooling system must remove this heat load and maintain the silicon sensors at a temperature of −20 ◦C or lower. Two-phase CO_2 is chosen as the coolant. The cooling system will be designed for a nominal coolant operating temperature of −35 ◦C, resulting in a coolant temperature of about −33 ◦C at the location of the first silicon module, which is the warmest location along a cooling loop.

Like in the CMS pixel Phase-1 Upgrade the cooling of the Phase-2 tracker will be based on evaporative CO_2 in a liquid pumped cycle. A common system is designed to serve both the Outer Tracker and the Inner Tracker. The fluid properties of CO_2 make it an ideal medium for cooling of tracking detectors, in particular because of the ability of using smaller diameter, lower-mass tubing than is required with conventional refrigerants or liquid cooling applications. The main reason for this is that CO_2 evaporates at higher pressures than regular refrigerants. High pressure keeps the vapours compressed and therefore the circuit volume low. The boiling temperature is a function of the pressure and, since the dynamic pressure drop along a cooling pipe can be kept small compared to the high absolute pressure of the fluid, the change in the evaporation temperature along a cooling pipe is typically relatively small: two degrees between outlet and inlet coolant temperature is the target for the tracker pipe design. In addition the CO_2 has a high latent heat, translating into a smaller needed flow with respect to the one required with other refrigerants. As the viscosity of CO_2 is low, it allows the use of small diameter pipes with higher flow speeds, which increase the heat transfer coefficient from the pipe wall to the fluid. CO_2 is radiation hard, inexpensive, and environmentally friendly; in particular the global warming potential is orders of magnitude lower when compared to chlorofluorocarbons, such as C_6F_{14}, used in the present CMS strip tracker.

The drawback of CO_2 is the high pressure and the associated safety aspects. Nonetheless, the small pipe diameters sufficing lead to an overall stored energy, given by the product of volume and pressure, similar to that of low-pressure systems with larger volumes.

3.5 Differences between 2S modules variants

The main differences between the 1.8 mm and 4.0 mm 2S modules are the thickness and shape of the Al-CF spacers. In Fig. 3-1 one can see the long bridge and stump bridge for the 1.8 mm and 4.0 mm variants. The shape, size, and fibre orientation (since the good thermal conductivity and low CTE exists for only two of the three axes) of the bridges were optimised to have the necessary thermal and mechanical performance, but also to have the least mass possible. The 1.8 mm bridge has excess material removed by machining the faces that contact the sensors, whereas the 4.0 mm bridge has material removed from the faces that point toward the FE hybrids. The part of the bridge that supports the hybrids is quite different in the module variants because it was necessary to lower the height of the 4.0 mm service hybrid as much as possible with respect to the sensors for reasons of clearances between modules in the endcap (TEDD) region.

There are small differences in the 1.8 mm and 4 mm variants of the FE hybrids and the service hybrids as well. The differences between the 1.8 mm and 4.0 mm FE hybrids are the dimension of the fold-over part of the flex, which must accommodate different fold-over radii, and the spacer which defines the folded-over thickness. An Al-CF spacer is needed for the 4.0 mm version, whereas the 1.8 mm version uses a 0.5 mm thick CFRP (carbon fibre reinforced polymer) spacer.

The end region differs for the two variants of the service hybrid because the 4.0 mm version will have a longer flex tail that is free to bend upward so it can connect to the FE hybrid. In the case of the 1.8 mm module, the end regions of the FE and service hybrids are at the same height and are more easily connected. If a reliable connector solution is not found, then a wire bonding solution will be the fall-back, although this may require small differences in both the service hybrids and FE hybrids to accommodate the different mechanical requirements of wire bonding.

Chapter 4
Micromechanical models for the thermal conductivity prediction of CFRPs

4.1 Thermal conductivity of unidirectional composites

Taking into account the prediction of the thermal conductivity of unidirectional composites, it was assumed that **[8]**:

-The composite is free of voids and other irregularities.

-All fibers are uniformly distributed in a particular pattern in the matrix and are perfectly aligned.

-The interface between the fiber and matrix is perfectly bonded.

-The contact resistance between the plies is negligible. However, in real CFRPs, many bulk and interfacial defects would affect the thermal conductivities.

The thermal conductivity in the longitudinal direction k_1 and transverse direction k_2 are calculated according to rule of mixture and the transverse micromechanical model respectively:

$$\boldsymbol{k_1 = k_f V_f + k_m(1 - V_f)}[9]$$

The thermal conductivity of unidirectional composites in the axial or fibre direction k1 can be calculated using the axial rule of mixture (ROM). This model is widely acknowledged and requires the thermal conductivity of the constituent fibres k_f in the longitudinal direction, the thermal conductivity of the matrix km and the fibre volume fraction V_f.

$$\boldsymbol{k_2}\textbf{, according to the micromechanical model}$$

For individual ply **[10]**:

$$\boldsymbol{k_x = k_1 cos^2\theta + k_2 sin^2\theta}$$
$$\boldsymbol{k_y = k_1 sin^2\theta + k_2 cos^2\theta}$$
$$\boldsymbol{k_z = k_2}$$

If we assume that each individual ply has identical thickness, the following expressions can be obtained for the global thermal conductivity properties for the composite laminate **[8]**:

$$\mathbf{KX} = \frac{\mathbf{1}}{\mathbf{N}} \sum_{\mathbf{i=1}}^{\mathbf{N}} (\mathbf{k_x})_\mathbf{i}$$

$$KY = \frac{1}{N}\sum_{i=1}^{N}(k_y)_i$$

$$KZ = \frac{N}{\sum_{i=1}^{N}\frac{1}{(k_z)_i}}$$

4.2 Transverse thermal conductivity of unidirectional composites

Many analytical models exist for predicting the thermal conductivity of unidirectional composites in the in-plane direction transverse to the fibers k_2, which is the same as the through-thickness thermal conductivity for unidirectional composites. For all the thermal conductivity prediction models, the transverse fiber thermal conductivity k_{f2} is required. The simplest model for predicting k_2 is the transverse rule of mixture (ROM):

$$k_{2\,(ROM)} = \frac{k_{f2}k_m}{k_{f2}(1-V_f)+k_mV_f}$$

This model does not account for fibre geometry and fibre packing arrangement in the matrix, and generally underestimates the thermal conductivity **[11]**. Springer and Tsai identified the model as the lower bound for k_2 and the authors developed a semi-empirical model applicable to cylindrical or square filaments packed in a square array, based on a shear loading analogy for unidirectional composites. Equations for the case of cylindrical fibres are shown below **[12]**:

$$k_{2\,(Springer-Tsai)} = k_m\left[1-2\sqrt{\frac{V_f}{\pi}}+\frac{1}{B}\left(\pi-\frac{4}{\sqrt{1-(B^2V_f/\pi)}}tan^{-1}\left(\frac{\sqrt{1-(B^2V_f/\pi)}}{1+\sqrt{(B^2V_f/\pi)}}\right)\right)\right]$$

where:

$$\mathrm{B} = 2\cdot\left(\frac{k_m}{k_{f2}}-1\right)$$

Halpin and Tsai developed a model **[13]** accounting for the fibre geometry, for cylindrical fibres with ζ=1 the equations turn to the Hashin Model **[14]**:

$$k_2 = k_m\left[\frac{1+\zeta\eta V_f}{1-\eta V_f}\right]$$

with

$$\zeta = 1\ and\ \eta = \frac{\frac{k_{f2}}{k_m}-1}{\frac{k_{f2}}{k_m}+\zeta}$$

$$k_{2(Hashin)} = k_m + \left[\frac{V_f}{\frac{1}{k_{f2} - k_m} + \frac{1 - V_f}{2k_m}}\right]$$

According to Chawla **[10]**, the following model has been developed:

$$k_{2(Chawla)} = k_m \left[(1 - \sqrt{V_f}) + \frac{\sqrt{V_f}}{1 - \sqrt{V_f}(1 - \frac{k_m}{k_{f2}})}\right]$$

Clayton **[15]** developed a semi-empirical model validated by Dasgupta et al. **[16]** where thermal conductivity values vary following a power law trend as a function of V_f :

$$k_{2(Clayton)} = \frac{k_m}{4}\left[\sqrt{(1 - V_f)^2(\frac{k_{f2}}{k_m} - 1)^2 + 4\frac{k_{f2}}{k_m}} - (1 - V_f)\frac{k_{f2}}{k_m}\right]^2$$

Rayleigh **[17]** developed a model based on heat transfer calculations with square fiber packing, which was reviewed by Karol Pietrak et al. **[18]** and used on the study of Michael Zimmer et al. **[19]**:

$$k_{2(Rayleigh)} = k_m \left[1 - \frac{2V_f}{\mu + V_f - \frac{C_1}{\mu}{V_f}^4 - \frac{C_2}{\mu}{V_f}^8}\right]$$

With $C_1 = 0.3058, C_2 = 0.0134$ and

$$\mu = \frac{\frac{k_m}{k_{f2}} + 1}{\frac{k_m}{k_{f2}} - 1}$$

4.3 Definition of the transverse thermal conductivity of the fibers

A study comparing datasheets from Mitsubishi Chemical Carbon Fiber & Composites and Nippon Graphite Fiber Corporation was conducted **[5,6]**. The transverse thermal conductivity was not defined in the datasheets of the fibers. According to the European Cooperation for Space Standardization **ECSS-E-HB-32-20 Part 1A** (March 2011) **[20]**, the thermal properties of commonly used pitch based carbon fibers could be found on the following table. As it can been observed regarding the Thornel (Cytec) carbon fibers, the transverse thermal conductivity remains constant and equal to 2.4 W/mK, as the longitudinal fiber thermal conductivity varies from 185 W/mK to 1000 W/mK. Assuming a common behaviour for the fiber thermal conductivity of the Mitsubishi and Nippon fibers, a transverse thermal conductivity of 2.4 W/mK is assumed for the composite laminate studies.

Fibre (Manufacturer)	Tensile Strength (MPa)	Tensile Modulus (GPa)	CTE (1) (ppm)	Thermal (1) Conductivity (W/m.K)	Fibre Density (kg/m³)	Fibre Diameter (m)
T 300, 3k PAN fibre (Cytec)	3100	235	L 0.6 T +9.0	L 8.5 T 5.0	1750	7
Thornel (Cytec) (2):						
P 25 2k	1380	159	L T	L 22 T 10	1900	11
P 30X 2k	2760	201	L T	L 40 T 10	1990	11
P 55S 2k	1900	379	L 1.3 T	L 120 T 5	2000	10
P 75S 2k	2070	517	L 1.46 T +12.5	L 185 T 2.4	2050	10
P 100S 2k	2410	759	L 1.48 T +12.0	L 520 T 2.4	2150	10
P 120S 2k	2410	828	L 1.5 T +12.0	L 640 T 2.4	2180	10
P 1100S 2k	3100	931	L 1.5 T +12.0	L 1000 T 2.4	2200	10
DIALEAD (Mitsubishi) (3):						
K1352U 2k	3600	620		140	2120	
K1392U 2k	3700	760		210	2150	
K13C2U 2k	3800	900		620	2200	
K13D2U 2k	3700	935		800	2200	
K63712 10k 12k type	2600	640		140	2120	
GRANOC (NGF Nippon) (4)						
YSH 50A 1k,3k,6k	3830	520	1.4	120	2100	7
YSH 60A 1k,3k,6k	3830	630	1.4	180	2120	7
YSH 70A 1k,3k,6k	3630	720	1.5	250	2150	7
YS 80A 3k, 6k	3630	785	1.5	320	2150	7
YS 90A 3k, 6k	3530	880	1.5	500	2180	7
YS 95A 1.5k, 3k, 6k	3530	920	1.5	600	2190	7
XN 05 3k	1100	54	+1.4	7.4	1650	10
XN 06 3k	1700	110	0.1		1700	10
XN 07 3k	2400	155	0.8	6.3	1850	10

(1) L – longitudinal; T – transverse;

(2) Cytec Engineered Materials (USA), includes former BP Amoco products;

(3) Distributor Sumitomo Corporation Europe Ltd. (UK);

(4) Nippon Graphite Fibers (Japan) YSH A series high compressive strength for aerospace; YSA series UHM and high thermal conductivity; XN series low modulus, high elongation (1.5% to 2.0%).

Figure 4-1: Thermal properties of pitch based carbon fibers. A transverse thermal conductivity of 2.4 W/m·K is assumed for all the fibers.

4.4 Carbon fiber composites

The carbon fiber systems have been selected in comparison with those of two different companies, global leaders for the carbon fiber production, Mitsubishi Chemical Carbon Fibre and Composites [1] and Nippon Graphite Fibre Corporation.[2] The summary of the thermal conductivity and mechanical properties is listed below. As it can be observed, fibers with high thermal conductivity values are combined with high mechanical properties, in terms of tensile modulus and tensile strength.

Mitsubishi Carbon Fiber Type	**Thermal Conductivity (W/mK)**	**Density (g/cm^3)**	**Tensile Modulus (GPa)**	**Tensile Strength (MPa)**
K13D2U	800	2.20	935	3700
K13C2U	620	2.20	900	3800
K13C6U	580	2.18	900	3600
K63A12	220	2.15	790	2600
K1392U	210	2.15	760	3700
K13916	200	2.15	760	3200
K63712	140	2.12	640	2600
K1352U	140	2.12	620	3600
K13312	110	2.06	420	3200
Nippon Carbon Fiber Type	**Thermal Conductivity (W/mK)**	**Density (g/cm^3)**	**Tensile Modulus (GPa)**	**Tensile Strength (MPa)**
YS-95A	600	2.19	920	3530
YS 90A	500	2.18	880	3530
XN 90	500	2.19	860	3430
YS 80A	320	2.17	785	3630
XN 80	320	2.17	780	3430
YSH-70A	250	2.15	720	3630
YSH-60A	180	2.12	630	3830
XN 60	180	2.12	620	3430
YSH-50A	120	2.10	520	3830

Table 4-1: Thermal conductivity and mechanical properties of Mitsubishi and Nippon Carbon Fibers.

[1] The carbon fibre properties are given from the Mitsubishi Chemical Carbon Fiber and Composites Website: http://mccfc.com/pitch-fiber/.

[2] The carbon fibre properties are given from the Nippon Graphite Fibre Corporation Website: http://www.ngfworld.com/.

4.5 Selection of the resin system

Regarding the resin selection of the prepreg, this should satisfy the process regarding the hybrid production and the production of the carbon fiber stiffeners for a 2S 1.8mm hybrid. This process will involve:

- Gluing of the carbon fiber stiffeners on the flex: After the flex panel is made, the carbon fiber stiffeners are glued to the flex by means of a jig that uses the alignment pins in the flex and the stiffener. The glue used is a contact adhesive which can take the solder reflow temperatures. This work is done by the flex manufacturer.

- Shipping of the flex: The flex is shipped to the assembly company.

- The assembly company bakes out the circuits at between 100-125 ^{o}C for about 8 hours, before starting the loading sequence.

- Hybrid Fold-over: Folding over the flex in a jig which can also hold the CF spacer in place for gluing. However, before this gluing is done, the flex and stiffeners are heated to about 150 ^{o}C and a pre-folding lasting a few minutes is done to remove the stress in the fold-over. Then the glue is applied on both sides of the CF spacer and it is glued in place on the jig. The curing temperature is 60-80 ^{o}C for 2-4 hours. The fold-over is now complete.

- The solder paste is applied to the circuit and then the SMD components and CBC chips are placed.

- The hybrid is then put in the reflow oven where it will have a heat cycle that could go up to 280 ^{o}C for a few minutes. In the case of the 2S hybrid only one solder cycle is done. In the case of the PS hybrids, two solder cycles are needed (one for the components on the top side, one for the components on the bottom side). In order to perform an efficient fold-over step, the epoxy resin of the prepreg should have a sufficient glass transition temperature. Optimization studies to define lower temperature heat cycles are in process.

According to the properties below of Granoc epoxy resin systems (Nippon), this is satisfied only by using cyanate resins or high glass transition temperature type of epoxy resins. The two available resins from Nippon that could satisfy the requirements are: NM31 (polycyanate resin) and NM35 (epoxy resin). The glass transition temperature of the epoxy and cyanate resins are summarised at the following table.

Granoc Prepreg Resin System (Nippon Graphite)	Tg (^{o}C)
25R	125
25T	108
35T-2	181
NM31	246
NM35	234

Table 4-2: Glass transition temperature of Nippon epoxy and cyanate resins.

The thermal conductivities are not defined by the manufacturer and on the following studies, it is assumed that the thermal conductivity of the resins is 0.2 W/m·K. Regarding the current 2S 1.8mm module design baseline, the epoxy EX-1515 is used. TenCate's EX-1515 cyanate ester resin system **[21]** is unique in the industry in that it is able to achieve an extremely high level of cure conversion after a 250°F (121°C) cure. This level of conversion provides optimal mechanical properties, high radiation resistance, low moisture absorption/low outgassing while retaining unparalleled toughness, a low 244°F (118°C), stress-free temperature and long out time. The resin system excels in its ability to resist microcracking, even when subjected to thermal cycling and high levels of radiation exposure. EX-1515 also displays low dielectric/low loss values similar to other cyanate esters which allow its use in radome and antenna applications. TenCate's EX-1515 can be post cured, free-standing, to increase its thermal performance for temperature critical structures.

Regardless the epoxy system is used, the value of 0.2 W/m·K is assumed for all the epoxy/cyanate resin's thermal conductivities. The use of cyanate ester resin is highly recommended for high precision detectors by the study of Susan Robitaille et al. **[22]**.

4.6 Thermal conductivity results for CFRP laminate 0/90/0/90/0

Using the above micromechanical models, the thermal conductivity of the laminate 0/90/0/90/0 has been defined as an average of the 6 micro-mechanical models. The thermal conductivity studies were conducted using the software Mathcad 15 **[23]**. For this study, the following assumption has been made:

- Volume fraction of the fiber $V_f = 0.65$
- Transverse thermal conductivity of the fiber $k_{f2} = 2.4\ W/m \cdot K$
- Epoxy/polycyanate resin thermal conductity, $k_m = 0.2\ W/m \cdot K$

Manufacturer	Carbon Fiber Name	Longitudinal Thermal Conductivity (W/mK)
Mitsubishi	K13D2U	800
	K13C2U	620
	K13C6U	580
	K63A12	220
	K1392U	210
	K13916	200
	K63712/ K1352U	140
	K13312	110
Nippon (NGF)	YS-95A	600
	XN 90/ YS 90A	500
	XN 80/YS 80A	320
	YSH-70A	250
	XN 60/YSH-60A	180
	YSH-50A	120

Table 4-3: Longitudinal thermal conductivity of Mitsubishi and Nippon carbon fibers.

Carbon Fiber type	Thermal Conductivity	ROM	Hashin	Chawla	Rayleigh	Clayton	Springer-Tsai
Mitsubishi K13D2U	**Fiber: 800 W/mK**						
	Longitudinal	312.24	312.32	312.31	312.34	312.32	312.39
	Transverse	208.33	208.44	208.42	208.47	208.45	208.55
	Through thickness	0.50	0.69	0.66	0.74	0.69	0.87

	Thermal Conductivity	Average	Std Dev	CV (%)
	Longitudinal	**312.32**	0.05	0.02
	Transverse	**208.44**	0.07	0.04
	Through thickness	**0.69**	0.12	17.66

Table 4-4: Thermal conductivity (W/mK) prediction of the laminate 0/90/0/90/0 by using Mitsubish K13D2U carbon fiber, according to the different micromechanical models.

Carbon Fiber type	Thermal Conductivity	ROM	Hashin	Chawla	Rayleigh	Clayton	Springer-Tsai
Mitsubishi K13C2U	**Fiber: 620 W/mK**						
	Longitudinal	242.04	242.12	242.11	242.14	242.12	242.19
	Transverse	161.53	161.64	161.62	161.67	161.65	161.75
	Through thickness	0.50	0.69	0.66	0.74	0.69	0.87

	Thermal Conductivity	Average	Std Dev	CV (%)
	Longitudinal	**242.12**	0.05	0.02
	Transverse	**161.64**	0.07	0.05
	Through thickness	**0.69**	0.12	17.66

Table 4-5: Thermal conductivity (W/mK) prediction of the laminate 0/90/0/90/0 by using Mitsubish K13C2U carbon fiber, according to the different micromechanical models.

Carbon Fiber type	Thermal Conductivity	ROM	Hashin	Chawla	Rayleigh	Clayton	Springer-Tsai
Mitsubishi K13C6U	**Fiber: 580 W/mK**						
	Longitudinal	226.44	226.52	226.51	226.54	226.52	226.59
	Transverse	151.13	151.24	151.22	151.27	151.25	151.35
	Through thickness	0.50	0.69	0.66	0.74	0.69	0.87

	Thermal Conductivity	Average	Std Dev	CV (%)
	Longitudinal	**226.52**	0.05	0.02
	Transverse	**151.24**	0.07	0.05
	Through thickness	**0.69**	0.12	17.66

Table 4-6: Thermal conductivity (W/mK) prediction of the laminate 0/90/0/90/0 by using Mitsubish K13C6U carbon fiber, according to the different micromechanical models.

Carbon Fiber type	Thermal Conductivity	ROM	Hashin	Chawla	Rayleigh	Clayton	Springer-Tsai
Mitsubishi K63A12	**Fiber: 220 W/mK**						
	Longitudinal	86.04	86.12	86.11	86.14	86.12	86.19
	Transverse	57.53	57.64	57.62	57.67	57.65	57.75
	Through thickness	0.50	0.69	0.66	0.74	0.69	0.87

	Thermal Conductivity	Average	Std Dev	CV (%)
	Longitudinal	**86.12**	0.05	0.06
	Transverse	**57.64**	0.07	0.13
	Through thickness	**0.69**	0.12	17.66

Table 4-7: Thermal conductivity (W/mK) prediction of the laminate 0/90/0/90/0 by using Mitsubish K63A12 carbon fiber, according to the different micromechanical models.

Carbon Fiber type	Thermal Conductivity	ROM	Hashin	Chawla	Rayleigh	Clayton	Springer-Tsai
Mitsubishi K1392U	**Fiber: 210 W/mK**						
	Longitudinal	82.14	82.22	82.21	82.24	82.22	82.29
	Transverse	54.93	55.04	55.02	55.07	55.05	55.15
	Through thickness	0.50	0.69	0.66	0.74	0.69	0.87

	Thermal Conductivity	Average	Std Dev	CV (%)
	Longitudinal	**82.22**	0.05	0.06
	Transverse	**55.04**	0.07	0.13
	Through thickness	**0.69**	0.12	17.66

Table 4-8: Thermal conductivity (W/mK) prediction of the laminate 0/90/0/90/0 by using Mitsubish K1392U carbon fiber, according to the different micromechanical models.

Carbon Fiber type	Thermal Conductivity	ROM	Hashin	Chawla	Rayleigh	Clayton	Springer-Tsai
Mitsubishi K13916	**Fiber: 200 W/mK**						
	Longitudinal	78.24	78.32	78.31	78.34	78.32	78.39
	Transverse	52.33	52.44	52.42	52.47	52.45	52.55
	Through thickness	0.50	0.69	0.66	0.74	0.69	0.87

	Thermal Conductivity	Average	Std Dev	CV (%)
	Longitudinal	**78.32**	0.05	0.06
	Transverse	**52.44**	0.07	0.14
	Through thickness	**0.69**	0.12	17.66

Table 4-9: Thermal conductivity (W/mK) prediction of the laminate 0/90/0/90/0 by using Mitsubish K13916 carbon fiber, according to the different micromechanical models.

Carbon Fiber type	Thermal Conductivity	ROM	Hashin	Chawla	Rayleigh	Clayton	Springer-Tsai
Mitsubishi K63712 or K1352U	**Fiber: 140 W/mK**						
	Longitudinal	54.84	54.92	54.91	54.94	54.92	54.99
	Transverse	36.73	36.84	36.82	36.87	36.85	36.95
	Through thickness	0.50	0.69	0.66	0.74	0.69	0.87
	Thermal Conductivity	**Average**		**Std Dev**	**CV (%)**		
	Longitudinal	**54.92**		0.05	0.09		
	Transverse	**36.84**		0.07	0.20		
	Through thickness	**0.69**		0.12	17.66		

Table 4-10: Thermal conductivity (W/mK) prediction of the laminate 0/90/0/90/0 by using Mitsubish K63712 or K1352U carbon fiber, according to the different micromechanical models.

Carbon Fiber type	Thermal Conductivity	ROM	Hashin	Chawla	Rayleigh	Clayton	Springer-Tsai
Mitsubishi K13312	**Fiber: 110 W/mK**						
	Longitudinal	43.14	43.22	43.21	43.24	43.22	43.29
	Transverse	28.93	29.04	29.02	29.07	29.05	29.15
	Through thickness	0.50	0.69	0.66	0.74	0.69	0.87
	Thermal Conductivity	**Average**	**Std Dev**	**CV (%)**			
	Longitudinal	**43.22**	0.05	0.11			
	Transverse	**29.04**	0.07	0.25			
	Through thickness	**0.69**	0.12	17.66			

Table 4-11: Thermal conductivity (W/mK) prediction of the laminate 0/90/0/90/0 by using Mitsubish K13312 carbon fiber, according to the different micromechanical models.

Carbon Fiber type	Thermal Conductivity	ROM	Hashin	Chawla	Rayleigh	Clayton	Springer-Tsai
Nippon YS-95A	**Fiber: 600 W/mK**						
	Longitudinal	234.24	234.32	234.31	234.34	234.32	234.39
	Transverse	156.33	156.44	156.42	156.47	156.45	156.55
	Through thickness	0.50	0.69	0.66	0.74	0.69	0.87
	Thermal Conductivity	**Average**	**Std Dev**	**CV (%)**			
	Longitudinal	**234.32**	0.05	0.02			
	Transverse	**156.44**	0.07	0.05			
	Through thickness	**0.69**	0.12	17.66			

Table 4-12: Thermal conductivity (W/mK) prediction of the laminate 0/90/0/90/0 by using Nippon YS-95A carbon fiber, according to the different micromechanical models.

Carbon Fiber type	Thermal Conductivity	ROM	Hashin	Chawla	Rayleigh	Clayton	Springer-Tsai
Nippon XN-90 or YS-90A	**Fiber: 500 W/mK**						
	Longitudinal	195.24	195.32	195.31	195.34	195.32	195.39
	Transverse	130.33	130.44	130.42	130.47	130.45	130.55
	Through thickness	0.50	0.69	0.66	0.74	0.69	0.87

	Thermal Conductivity	Average	Std Dev	CV (%)
	Longitudinal	**195.32**	0.05	0.02
	Transverse	**130.44**	0.07	0.06
	Through thickness	**0.69**	0.12	17.66

Table 4-13: Thermal conductivity (W/mK) prediction of the laminate 0/90/0/90/0 by using Nippon XN-90 or YS-90A carbon fiber, according to the different micromechanical models.

Carbon Fiber type	Thermal Conductivity	ROM	Hashin	Chawla	Rayleigh	Clayton	Springer-Tsai
Nippon XN-80 or YS-80A	**Fiber: 320 W/mK**						
	Longitudinal	125.04	125.12	125.11	125.14	125.12	125.19
	Transverse	83.53	83.64	83.62	83.67	83.65	83.75
	Through thickness	0.50	0.69	0.66	0.74	0.69	0.87

	Thermal Conductivity	Average	Std Dev	CV (%)
	Longitudinal	**125.12**	0.05	0.04
	Transverse	**83.64**	0.07	0.09
	Through thickness	**0.69**	0.12	17.66

Table 4-14: Thermal conductivity (W/mK) prediction of the laminate 0/90/0/90/0 by using Nippon XN-80 or YS-80A carbon fiber, according to the different micromechanical models.

Carbon Fiber type	Thermal Conductivity	ROM	Hashin	Chawla	Rayleigh	Clayton	Springer-Tsai
Nippon YSH-70A	**Fiber: 250 W/mK**						
	Longitudinal	97.74	97.82	97.81	97.84	97.82	97.89
	Transverse	65.33	65.44	65.42	65.47	65.45	65.55
	Through thickness	0.50	0.69	0.66	0.74	0.69	0.87

	Thermal Conductivity	Average	Std Dev	CV (%)
	Longitudinal	**97.82**	0.05	0.05
	Transverse	**65.44**	0.07	0.11
	Through thickness	**0.69**	0.12	17.66

Table 4-15: Thermal conductivity (W/mK) prediction of the laminate 0/90/0/90/0 by using Nippon YSH-70A carbon fiber, according to the different micromechanical models.

Carbon Fiber type	Thermal Conductivity	ROM	Hashin	Chawla	Rayleigh	Clayton	Springer-Tsai
Nippon XN-60 or YSH-60A	**Fiber: 180 W/mK**						
	Longitudinal	70.44	70.52	70.51	70.54	70.52	70.59
	Transverse	47.13	47.24	47.22	47.27	47.25	47.35
	Through thickness	0.50	0.69	0.66	0.74	0.69	0.87

	Thermal Conductivity	Average	Std Dev	CV (%)
	Longitudinal	**70.52**	0.05	0.07
	Transverse	**47.24**	0.07	0.15
	Through thickness	**0.69**	0.12	17.66

Table 4-16: Thermal conductivity (W/mK) prediction of the laminate 0/90/0/90/0 by using Nippon XN-60 or YSH-60A carbon fiber, according to the different micromechanical models.

Carbon Fiber type	Thermal Conductivity	ROM	Hashin	Chawla	Rayleigh	Clayton	Springer-Tsai
Nippon YSH-50A	**Fiber: 120 W/mK**						
	Longitudinal	47.04	47.12	47.11	47.14	47.12	47.19
	Transverse	31.53	31.64	31.62	31.67	31.65	31.75
	Through thickness	0.50	0.69	0.66	0.74	0.69	0.87

	Thermal Conductivity	Average	Std Dev	CV (%)
	Longitudinal	**47.12**	0.05	0.10
	Transverse	**31.64**	0.07	0.23
	Through thickness	**0.69**	0.12	17.66

Table 4-17: Thermal conductivity (W/mK) prediction of the laminate 0/90/0/90/0 by using Nippon YSH-50A carbon fiber, according to the different micromechanical models.

4.7 Thermal conductivity results for CFRP laminate $[0/90]_s$

As in the case of 0/90/0/90/0, the same assumptions using the 6 micro-mechanical models have been made also for the $[0/90]_s$ laminate (stacking sequence: 0/90/90/0):

- Volume fraction of the fiber $V_f = 0.65$
- Transverse thermal conductivity of the fiber $k_{f2} = 2.4\ W/m \cdot K$
- Epoxy/polycyanate resin thermal conductity, $k_m = 0.2\ W/m \cdot K$

Carbon Fiber type	Thermal Conductivity	ROM	Hashin	Chawla	Rayleigh	Clayton	Springer-Tsai
Mitsubishi K13D2U	**Fiber: 800 W/mK**						
	Longitudinal	260.28	260.38	260.36	260.40	260.38	260.47
	Transverse	260.28	260.38	260.36	260.40	260.38	260.47
	Through thickness	0.50	0.69	0.66	0.74	0.69	0.87
	Thermal Conductivity	**Average**	**Std Dev**	**CV (%)**			
	Longitudinal	**260.38**	0.06	0.02			
	Transverse	**260.38**	0.06	0.02			
	Through thickness	**0.69**	0.12	17.66			

Table 4-18: Thermal conductivity (W/mK) prediction of the laminate 0/90/90/0 by using Mitsubishi K13D2U carbon fiber, according to the different micromechanical models.

Carbon Fiber type	Thermal Conductivity	ROM	Hashin	Chawla	Rayleigh	Clayton	Springer-Tsai
Mitsubishi K13C2U	**Fiber: 620 W/mK**						
	Longitudinal	201.78	201.88	201.86	201.90	201.88	201.97
	Transverse	201.78	201.88	201.86	201.90	201.88	201.97
	Through thickness	0.50	0.69	0.66	0.74	0.69	0.87
	Thermal Conductivity	**Average**	**Std Dev**	**CV (%)**			
	Longitudinal	**201.88**	0.06	0.03			
	Transverse	**201.88**	0.06	0.03			
	Through thickness	**0.69**	0.12	17.66			

Table 4-19: Thermal conductivity prediction (W/mK) of the laminate 0/90/90/0 by using Mitsubishi K13C2U carbon fiber, according to the different micromechanical models.

Carbon Fiber type	Thermal Conductivity	ROM	Hashin	Chawla	Rayleigh	Clayton	Springer-Tsai
Mitsubishi K13C6U	**Fiber: 580 W/mK**						
	Longitudinal	188.78	188.88	188.86	188.90	188.88	188.97
	Transverse	188.78	188.88	188.86	188.90	188.88	188.97
	Through thickness	0.50	0.69	0.66	0.74	0.69	0.87

	Thermal Conductivity	Average	Std Dev	CV (%)
	Longitudinal	**188.88**	0.06	0.03
	Transverse	**188.88**	0.06	0.03
	Through thickness	**0.69**	0.12	17.66

Table 4-20: Thermal conductivity prediction (W/mK) of the laminate 0/90/90/0 by using Mitsubishi K13C6U carbon fiber, according to the different micromechanical models.

Carbon Fiber type	Thermal Conductivity	ROM	Hashin	Chawla	Rayleigh	Clayton	Springer-Tsai
Mitsubishi K63A12	**Fiber: 220 W/mK**						
	Longitudinal	71.78	71.88	71.86	71.90	71.88	71.97
	Transverse	71.78	71.88	71.86	71.90	71.88	71.97
	Through thickness	0.50	0.69	0.66	0.74	0.69	0.87

	Thermal Conductivity	Average	Std Dev	CV (%)
	Longitudinal	**71.88**	0.06	0.09
	Transverse	**71.88**	0.06	0.09
	Through thickness	**0.69**	0.12	17.66

Table 4-21: Thermal conductivity prediction (W/mK) of the laminate 0/90/90/0 by using Mitsubishi K63A12 carbon fiber, according to the different micromechanical models.

Carbon Fiber type	Thermal Conductivity	ROM	Hashin	Chawla	Rayleigh	Clayton	Springer-Tsai
Mitsubishi K1392U	**Fiber: 210 W/mK**						
	Longitudinal	68.53	68.63	68.61	68.65	68.63	68.72
	Transverse	68.53	68.63	68.61	68.65	68.63	68.72
	Through thickness	0.50	0.69	0.66	0.74	0.69	0.87

	Thermal Conductivity	Average	Std Dev	CV (%)
	Longitudinal	**68.63**	0.06	0.09
	Transverse	**68.63**	0.06	0.09
	Through thickness	**0.69**	0.12	17.66

Table 4-22: Thermal conductivity prediction (W/mK) of the laminate 0/90/90/0 by using Mitsubishi K1392U carbon fiber, according to the different micromechanical models.

Carbon Fiber type	Thermal Conductivity	ROM	Hashin	Chawla	Rayleigh	Clayton	Springer-Tsai
Mitsubishi K13916	**Fiber: 200 W/mK**						
	Longitudinal	65.28	65.38	65.36	65.40	65.38	65.47
	Transverse	65.28	65.38	65.36	65.40	65.38	65.47
	Through thickness	0.50	0.69	0.66	0.74	0.69	0.87

	Thermal Conductivity	Average	Std Dev	CV (%)
	Longitudinal	**65.38**	0.06	0.09
	Transverse	**65.38**	0.06	0.09
	Through thickness	**0.69**	0.12	17.66

Table 4-23: Thermal conductivity prediction (W/mK) of the laminate 0/90/90/0 by using Mitsubishi K13916 carbon fiber, according to the different micromechanical models.

Carbon Fiber type	Thermal Conductivity	ROM	Hashin	Chawla	Rayleigh	Clayton	Springer-Tsai
Mitsubishi K63712 or K1352U	**Fiber: 140 W/mK**						
	Longitudinal	45.78	45.88	45.86	45.90	45.88	45.97
	Transverse	45.78	45.88	45.86	45.90	45.88	45.97
	Through thickness	0.50	0.69	0.66	0.74	0.69	0.87

	Thermal Conductivity	Average	Std Dev	CV (%)
	Longitudinal	**45.88**	0.06	0.13
	Transverse	**45.88**	0.06	0.13
	Through thickness	**0.69**	0.12	17.66

Table 4-24: Thermal conductivity prediction (W/mK) of the laminate 0/90/90/0 by using Mitsubishi K63712 or K1352U carbon fiber, according to the different micromechanical models.

Carbon Fiber type	Thermal Conductivity	ROM	Hashin	Chawla	Rayleigh	Clayton	Springer-Tsai
Mitsubishi K13312	**Fiber: 110 W/mK**						
	Longitudinal	36.03	36.13	36.11	36.15	36.13	36.22
	Transverse	36.03	36.13	36.11	36.15	36.13	36.22
	Through thickness	0.50	0.69	0.66	0.74	0.69	0.87

	Thermal Conductivity	Average	Std Dev	CV (%)
	Longitudinal	**36.13**	0.06	0.17
	Transverse	**36.13**	0.06	0.17
	Through thickness	**0.69**	0.12	17.66

Table 4-25: Thermal conductivity prediction (W/mK) of the laminate 0/90/90/0 by using Mitsubishi K13312 carbon fiber, according to the different micromechanical models.

Carbon Fiber type	Thermal Conductivity	ROM	Hashin	Chawla	Rayleigh	Clayton	Springer-Tsai
Nippon YS-95A	**Fiber: 600 W/mK**						
	Longitudinal	195.28	195.38	195.36	195.40	195.38	195.47
	Transverse	195.28	195.38	195.36	195.40	195.38	195.47
	Through thickness	0.50	0.69	0.66	0.74	0.69	0.87

	Thermal Conductivity	Average	Std Dev	CV (%)
	Longitudinal	**195.38**	0.06	0.03
	Transverse	**195.38**	0.06	0.03
	Through thickness	**0.69**	0.12	17.66

Table 4-26: Thermal conductivity prediction (W/mK) of the laminate 0/90/90/0 by using Nippon YS-95A carbon fiber, according to the different micromechanical models.

Carbon Fiber type	Thermal Conductivity	ROM	Hashin	Chawla	Rayleigh	Clayton	Springer-Tsai
Nippon XN-90 or YS-90A	**Fiber: 500 W/mK**						
	Longitudinal	162.78	162.88	162.86	162.90	162.88	162.97
	Transverse	162.78	162.88	162.86	162.90	162.88	162.97
	Through thickness	0.50	0.69	0.66	0.74	0.69	0.87

	Thermal Conductivity	Average	Std Dev	CV (%)
	Longitudinal	**162.88**	0.06	0.04
	Transverse	**162.88**	0.06	0.04
	Through thickness	**0.69**	0.12	17.66

Table 4-27: Thermal conductivity prediction (W/mK) of the laminate 0/90/90/0 by using Nippon XN-90 or YS-90A carbon fiber, according to the different micromechanical models.

Carbon Fiber type	Thermal Conductivity	ROM	Hashin	Chawla	Rayleigh	Clayton	Springer-Tsai
Nippon XN-80 or YS-80A	**Fiber: 320 W/mK**						
	Longitudinal	104.28	104.38	104.36	104.40	104.38	104.47
	Transverse	104.28	104.38	104.36	104.40	104.38	104.47
	Through thickness	0.50	0.69	0.66	0.74	0.69	0.87

	Thermal Conductivity	Average	Std Dev	CV (%)
	Longitudinal	**104.38**	0.06	0.06
	Transverse	**104.38**	0.06	0.06
	Through thickness	**0.69**	0.12	17.66

Table 4-28: Thermal conductivity prediction (W/mK) of the laminate 0/90/90/0 by using Nippon XN-80 or YS-80A carbon fiber, according to the different micromechanical models.

Carbon Fiber type	Thermal Conductivity	ROM	Hashin	Chawla	Rayleigh	Clayton	Springer-Tsai
Nippon YSH-70A	**Fiber: 250 W/mK**						
	Longitudinal	81.53	81.63	81.61	81.65	81.63	81.72
	Transverse	81.53	81.63	81.61	81.65	81.63	81.72
	Through thickness	0.50	0.69	0.66	0.74	0.69	0.87

	Thermal Conductivity	Average	Std Dev	CV (%)
	Longitudinal	**81.63**	0.06	0.07
	Transverse	**81.63**	0.06	0.07
	Through thickness	**0.69**	0.12	17.66

Table 4-29: Thermal conductivity prediction (W/mK) of the laminate 0/90/90/0 by using Nippon YSH-70A carbon fiber, according to the different micromechanical models.

Carbon Fiber type	Thermal Conductivity	ROM	Hashin	Chawla	Rayleigh	Clayton	Springer-Tsai
Nippon XN-60 or YSH-60A	**Fiber: 180 W/mK**						
	Longitudinal	58.78	58.88	58.86	58.90	58.88	58.97
	Transverse	58.78	58.88	58.86	58.90	58.88	58.97
	Through thickness	0.50	0.69	0.66	0.74	0.69	0.87

	Thermal Conductivity	Average	Std Dev	CV (%)
	Longitudinal	**58.88**	0.06	0.10
	Transverse	**58.88**	0.06	0.10
	Through thickness	**0.69**	0.12	17.66

Table 4-30: Thermal conductivity prediction (W/mK) of the laminate 0/90/90/0 by using Nippon XN-60 or YS-60A carbon fiber, according to the different micromechanical models.

Carbon Fiber type	Thermal Conductivity	ROM	Hashin	Chawla	Rayleigh	Clayton	Springer-Tsai
Nippon YSH-50A	**Fiber: 120 W/mK**						
	Longitudinal	39.28	39.38	39.36	39.40	39.38	39.47
	Transverse	39.28	39.38	39.36	39.40	39.38	39.47
	Through thickness	0.50	0.69	0.66	0.74	0.69	0.87

	Thermal Conductivity	Average	Std Dev	CV (%)
	Longitudinal	**39.38**	0.06	0.16
	Transverse	**39.38**	0.06	0.16
	Through thickness	**0.69**	0.12	17.66

Table 4-31: Thermal conductivity prediction (W/mK) of the laminate 0/90/90/0 by using Nippon YSH-50A carbon fiber, according to the different micromechanical models.

Chapter 5
Module thermal performance

5.1 The Tracker Endcap Double-Discs (TEDD)

The TEDD uses exactly the same rectangular 2S and PS modules **[2]** that are used in the barrel sections of the Outer Tracker. The modules are mounted on discs, which for assembly reasons are split in half-discs, or "dees" (Fig. 5-1, left). Two discs are grouped to form one double-disc, which provides one hermetic detector plane. Ten double-disc units will be produced, five for each endcap (Fig. 5-1). To accommodate the change in diameter of the Inner Tracker support tube, the TEDD discs need to be of two different inner radii.

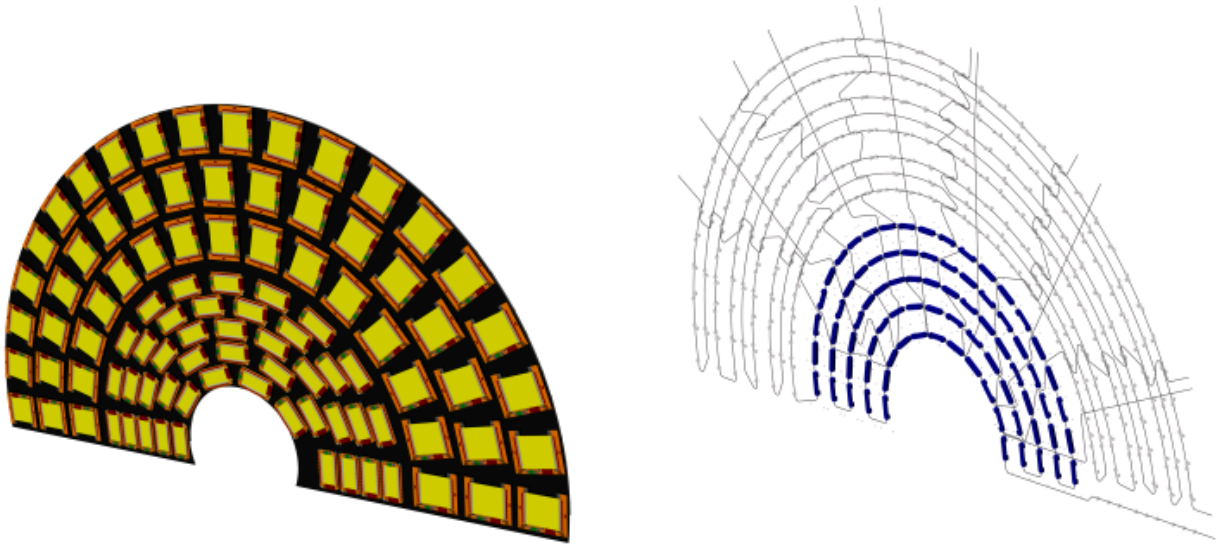

Figure 5-1: A fully assembled dee (left) and the seven cooling circuits of one dee (right), along with cooling inserts and carbon foam blocks (blue).

The cooling pipes run inside the sandwich structure of each dee. There are seven cooling circuits in each dee (Fig. 5-1, right). The cooling circuits are arranged in ϕ sectors, with each pipe passing in a "zig-zag" way along the module rings and thus reaching all cooling contacts in the sector. The cooling contacts are realized in different ways for PS and 2S modules. Carbon foam blocks are inserted in the PS module part of the dee to provide thermal connection between the dee skins and the cooling pipe. The PS modules, located in the low radius regions, are thus attached directly to the cooled surfaces of the dee. Aluminium inserts are used to provide thermal contacts between the 2S modules, located in larger radius regions, and the cooling pipes. These inserts are sticking out of the dee surface, and represent at the same time the precision mounting points for the 2S modules. Where no thermal connection is needed a lighter and cheaper polyetherimide foam (e.g. Airex R82) is used. To obtain a flat dee, the different foam sections are machined to even levels. The module support inserts are guided to their positions using a precision assembly table. After the gluing of the dee, the inserts both on the top and on the bottom side are machined to obtain the final module support and guide surfaces.

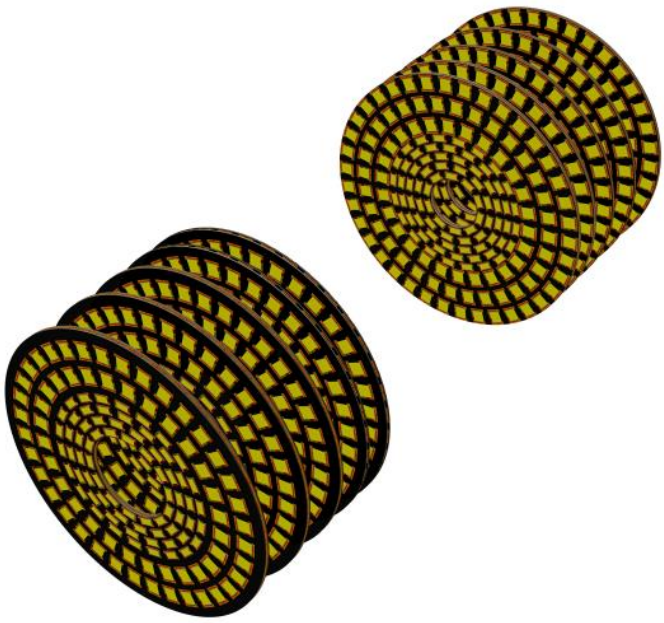

Figure 5-2: The two identical TEDD units, each consisiting of five double-discs. Each double-disc consists of four dees.

Power wires and optical fibres are routed radially outwards, above and between the modules, to the outer periphery of each dee. Thin protection frames are used to constrain the services and protect the modules. The transition from individual wires and fibres to multi-wire cables and 24-fibre bundles, respectively, takes place at the dee periphery. In the complete TEDD assembly of five double-discs the cables and fibre bundles run to the end of the TEDD and have there sufficiently long pigtails to reach the tracker patch panels (PP1) in CMS.

Each TEDD unit is installed into the tracker support tube as one package. The two TEDD units are identical.

5.1.1 TEDD mechanics and cooling

The TEDD dees comprise both 2S and PS modules. The cooling circuitry is made in sectors, each pipe serving both 2S and PS modules. The cooling pipes are up to 8 m long and have many bends in order to reach every module in the sector. Carbon foam blocks and aluminium inserts are used to provide thermal contacts between the modules and the cooling pipes, as shown in Fig. 5.3.

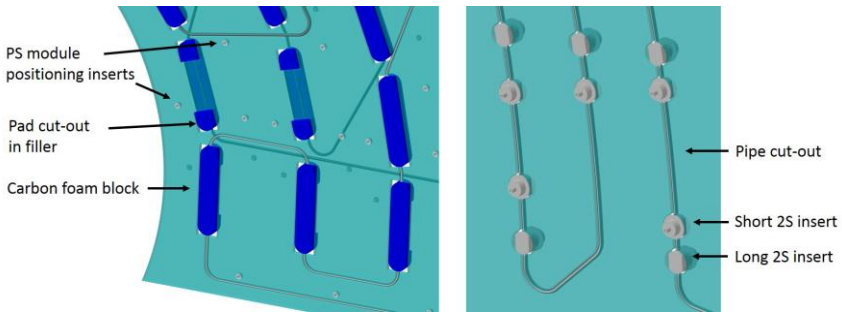

Figure 5-3: Carbon foam blocks (left) and aluminium inserts (right), used to provide thermal contacts between the modules and the cooling pipes.

The different layers (Fig. 5-4, left) of the dee (carbon fibre skins, two Airex foam filler layers, cooling pipes) are produced independently. The pipes for the seven different cooling sectors are bent using dedicated jigs. Expertise for this operation has been gained in-house and successful results have also been obtained using an external company. The carbon fibre skins are cut to shape and populated with holes for the cooling inserts by milling. Similarly, milling is used to cut the Airex filler layers to shape, to adjust them to the correct thickness, and to add holes for the inserts and grooves for the cooling pipes. The dee is then assembled in the order of the layers: "lower" carbon fibre skin, "lower" filler layer, first cooling pipe layers, "upper" filler layer, second cooling pipe layers, "upper" carbon fibre skin, with an appropriate glue layer at each of the interfaces. The module cooling and alignment inserts are positioned using a precision jig during the gluing phase, as shown in Fig. 5-5 (left). Production of the carbon fibre and filler layers, as well as the final assembly and gluing, will be subcontracted to an external company; promising candidates have been identified during prototyping.

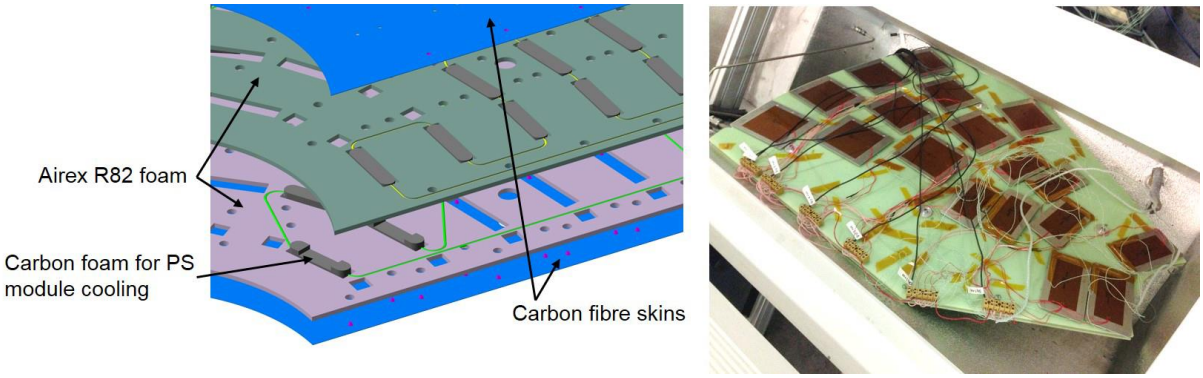

Figure 5-4: The TEDD cooling pipes are embedded into the sandwich structure of the dees and are routed to the 2S and PS module inserts (left). A thermal test setup consisting of two neighbouring cooling circuits inside the sandwich structure and dummy heat loads (right).

Figure 5-5 (right) shows a prototype spanning two cooling sectors of a dee. For this prototype the bending of the pipes and the gluing of the inserts and foam blocks to the pipes was done in-house, while the actual dee assembly was done in industry using an autoclave.

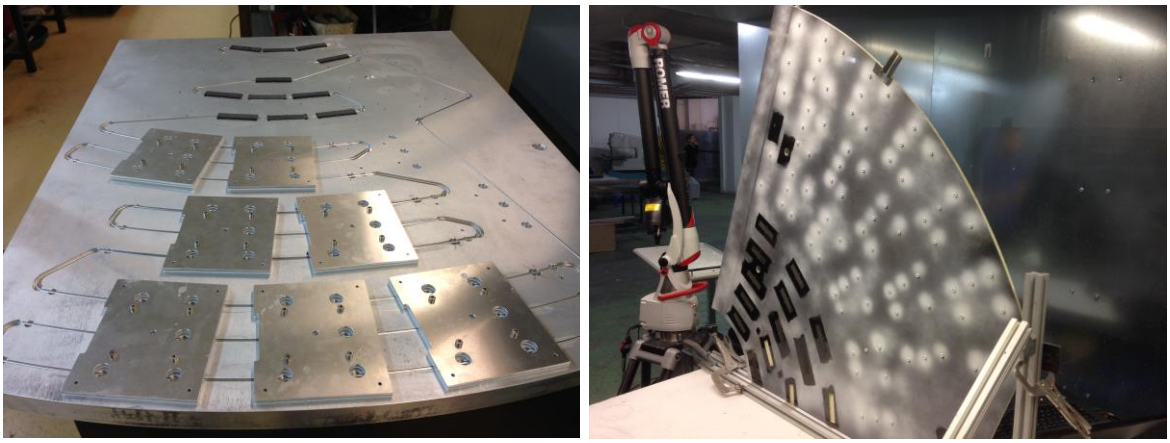

Figure 5-5: Photo of the jig used to glue the 2S cooling inserts and the carbon foam blocks to the cooling pipe (left), and photo of the prototype dee (spanning two cooling sectors) during optical metrology. Powder was used to reduce the reflectivity of the surface for that measurement.

5.2 2S 1.8 mm TEDD module thermal performance

To study the thermal performance of the 2S 1.8 mm TEDD module, different CFRPs have been compared using two laminates with stacking sequence of $[0/90]_s$ and 0/90/0/90/0. For all the cases, the CFRP laminates have been studied with volume fraction of 0.65, transverse thermal conductivity of the fiber (k_{f2}) of 2.4 W/m·K and epoxy/polycyanate resin thermal conductivity with the value of 0.2 W/m·K. The values for the thermal conductivity of the CFRPs are taken from the tables of the chapters 4.6 and 4.7.

The thermal performance of the 2S 1.8 TEDD designs, according to different thermal conductivities and fiber orientation, was studied with finite element analyses (FEA). The studies were carried out using ANSYS **[24]** by importing a CAD model of the module **[25]**, removing features that are irrelevant for studying the thermal performance (e.g. passive SMD components and connectors), and modelling simplified cooling structures onto which the module was placed in the FEA model. The simplified FEA model geometries is shown in Figure 5-6.

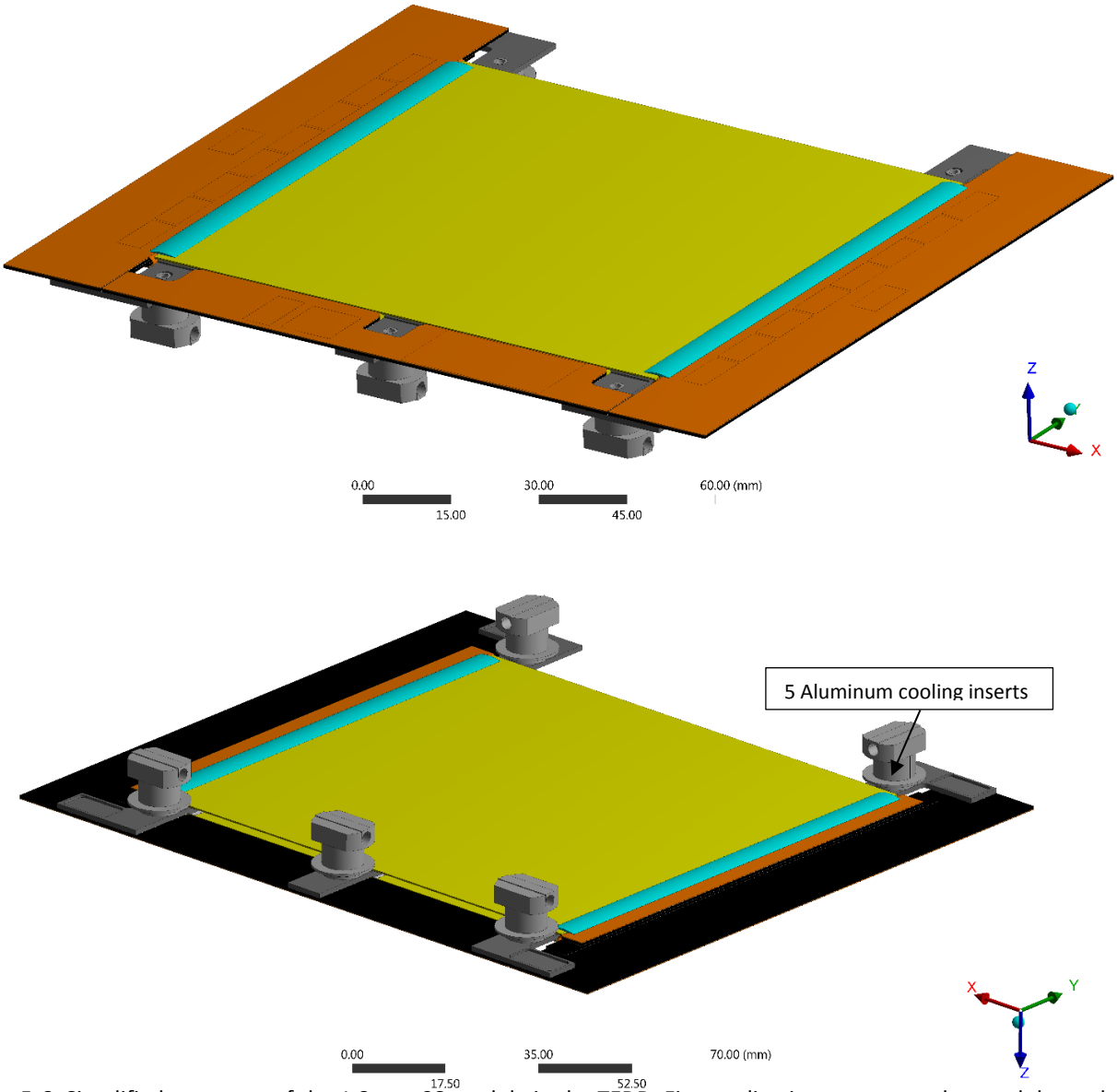

Figure 5-6: Simplified geometry of the 1.8 mm 2S module in the TEDD. Five cooling inserts are used to cool down the module.

5.2.1 Geometry specification

The 2S 1.8 mm Module (TEDD) consists of the following main structures:

- The 2S silicon sensors.
- The Al-CF (aluminum carbon fiber) composite bridges.
- The readout hybrids and their CFRP (carbon fiber reinforced polymer) stiffeners.
- The service hybrid and its CFRP (carbon fiber reinforced polymer) stiffeners.

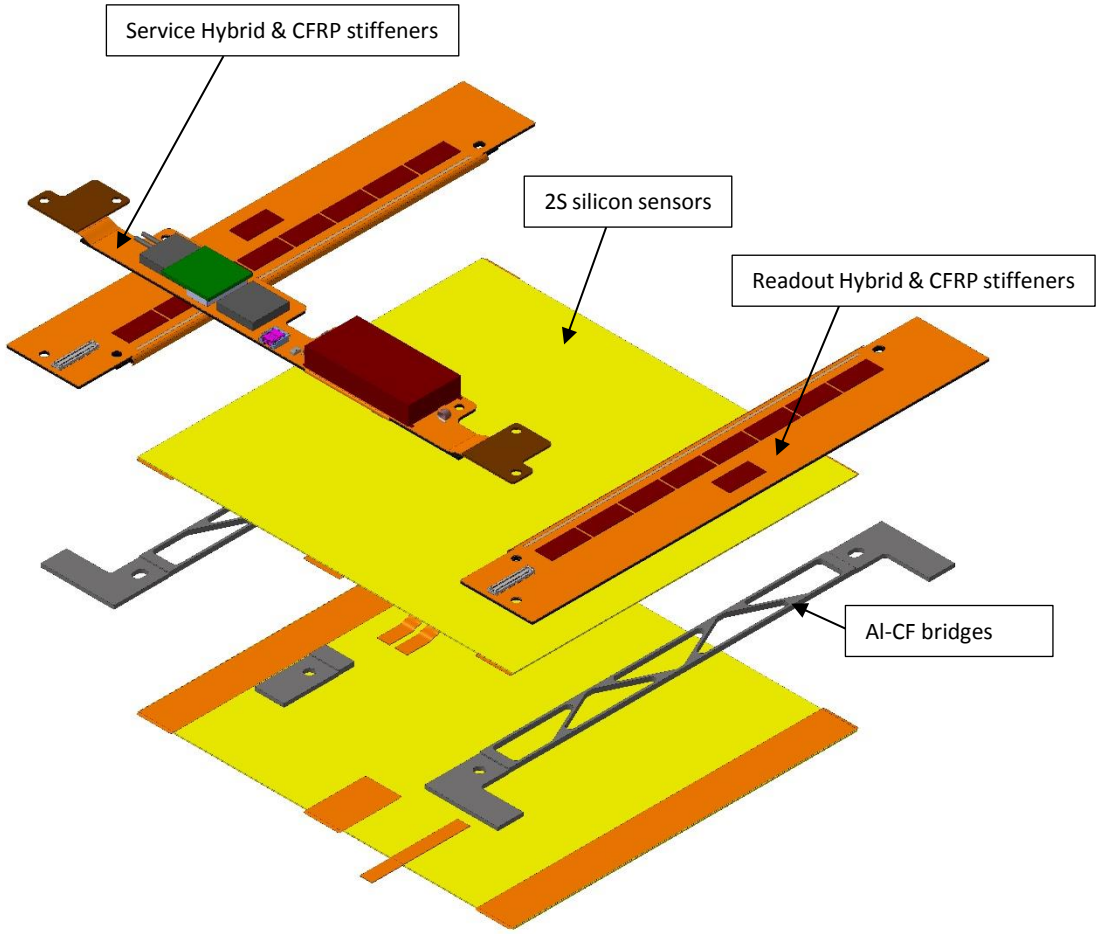

Figure 5-7: Exploded view of the 1.8 mm 2S Module. From top to bottom the following components can be seen: the three hybrids, the top sensor, the three bridges and the bottom sensor. The orange strips of the sensor are Kapton strips for the HV isolation (below the bridges) and flex cables that deliver the bias voltage or carry a temperature sensor.

The expected fluence for 3000 fb^{-1} of integrated luminosity is $2.2 \cdot 10^{14}\, n_{eq}/cm^2$. Under this fluence,the detector performance has been studied and evaluated. The thermal performance of a module and its corresponding cooling structure is characterised in terms of the temperature at which the module undergoes thermal runaway. For this purpose a temperature dependency is introduced to the sensor power consumption by scaling the value calculated at room temperature and applying the resulting temperature dependent heat load to the individual sensor elements in the FEA model. The cooling

system will be designed such that the coolant temperature at the first, and warmest, module in a cooling loop will be −33°C.

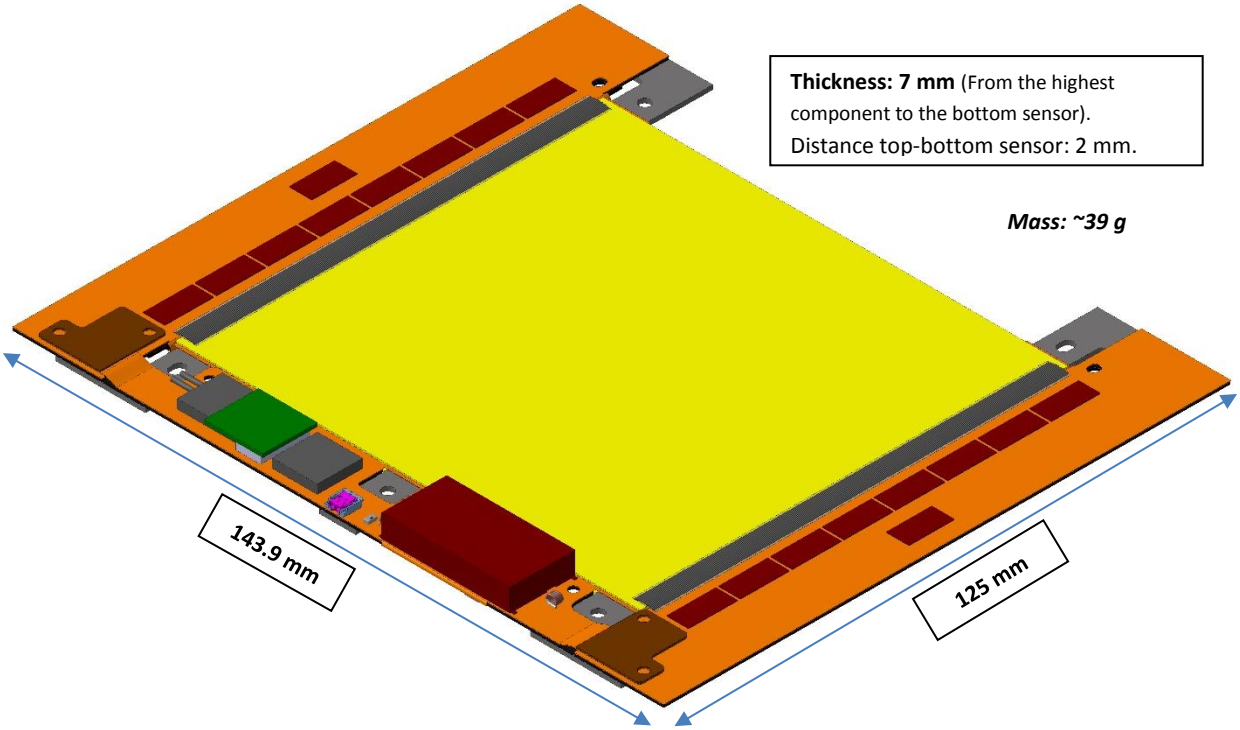

Figure 5-8: Perspective view with all the components and the total dimensions of the 2S 1.8mm Module.

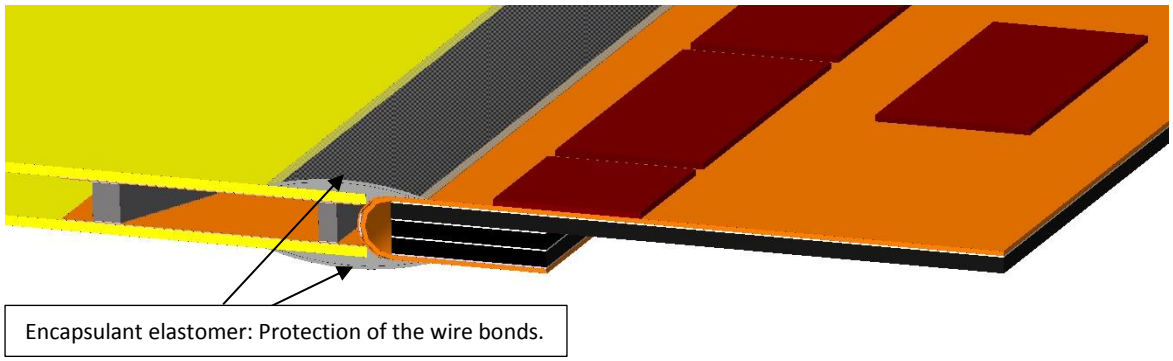

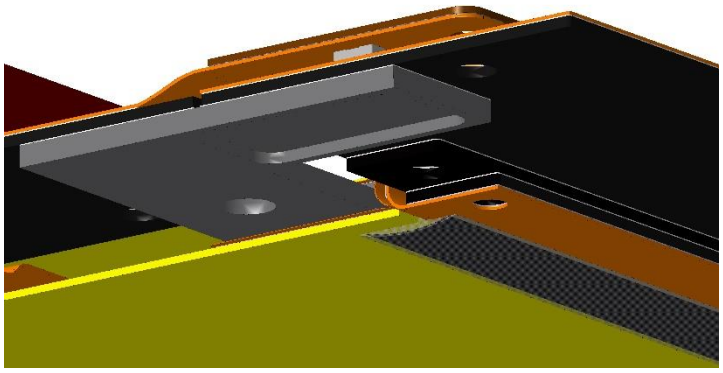

Figure 5-9: The CFRP stiffeners used for thermal dissipation and structural purposes. The three stiffeners of the readout hybrid are glued with each other. All the stiffeners are glued to the Al-CF bridges, creating the thermal path through the cooling inserts. Encapsulant elastomer is used for the protection of wire bonds.

5.2.2 Materials and thermal conductivities

The detector module has been simulated with the following thermal conductivities of the materials:

Material	Thermal Conductivity in X-direction (W/m·K)	Thermal Conductivity in Y-direction (W/m·K)	Thermal Conductivity in Z-direction (W/m·K)
Aluminum	240	240	240
Aluminum Carbon Fiber Composite	230	230	120
Epoxy Glue	0.45	0.45	0.45
Kapton (Hybrid)	0.12	0.12	0.12
Silicon	148	148	148
Kapton MT	0.46	0.46	0.46
Encapsulant Elastomer	2.55	2.55	2.55

Since the definition of the epoxy glue and the encapsulant elastomeris under study, it was assumed a thermal conductivity of 0.45 W/mK and 2.55 W/mK, respectively. The CFRP laminate thermal conductivity is defined according to the micromechanical models and the different fiber orientations. In all the cases, the laminate thickness is assumed stable at 0.5 mm.

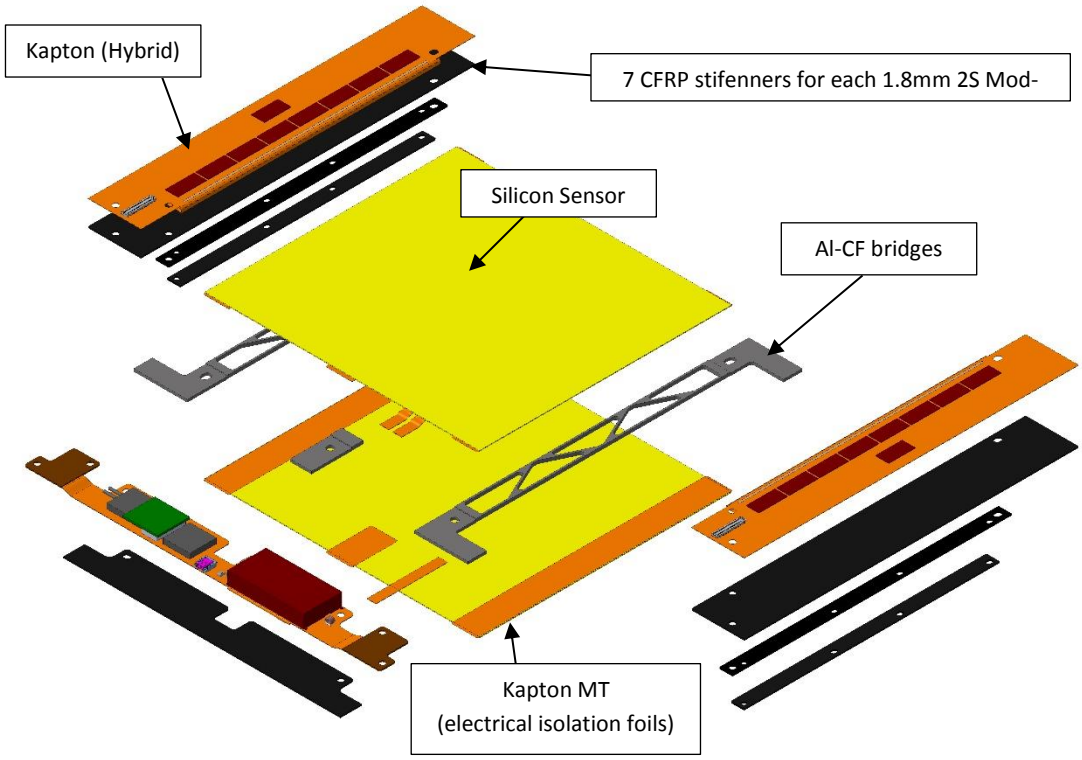

Figure 5-10: Exploded view of the 1.8 mm 2S Module. CFRP stiffeners (with black colour) located below the electronics, are used for thermal and structural purposes.

5.2.3 FEA Silicon sensor

In the FEA model, the silicon sensor has been treated as a resistor. The sensor resistor value is a strong function of the temperature and therefore a temperature dependency has been introduced to the sensor power consumption by applying the resulting temperature dependent heat load to the individual sensor elements. The value of the resistivity after 3000 fb^{-1} of integrated luminosity and at the fluence of $2.2 \cdot 10^{14}$ n_{eq}/cm^2 is a function of temperature : decreases linearly from 2136932.2 ohm·m at -80 ºC to 2870.8 ohm·m at -40 ºC and exponentially by increasing the temperature. In the following figure, the exponential behaviour of the silicon sensor can be observed for values of temperature from -40 ºC to 20 ºC.

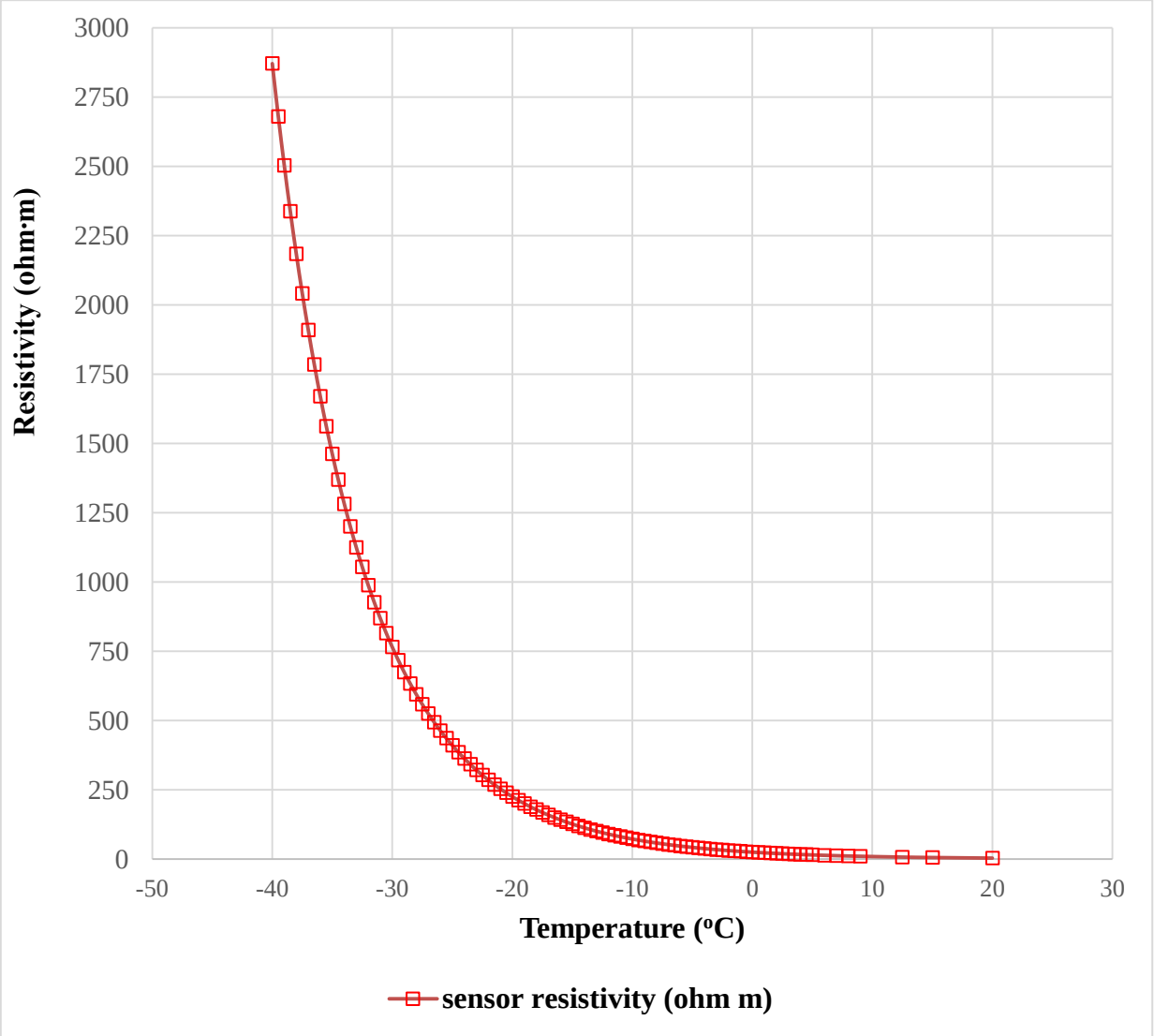

Figure 5-11: Exponential decrease of the resistivity values of the sensor (at the fluence of $2.2 \cdot 10^{14}$ n_{eq}/cm^2) by temperature increase.

5.2.4 Coordinate systems of composite materials

The following coordinate systems have been selected to define properly the thermal conductivites of the composite materials, used for the Al-CF bridges and the CFRP stiffeners of the readout and service hybrids.

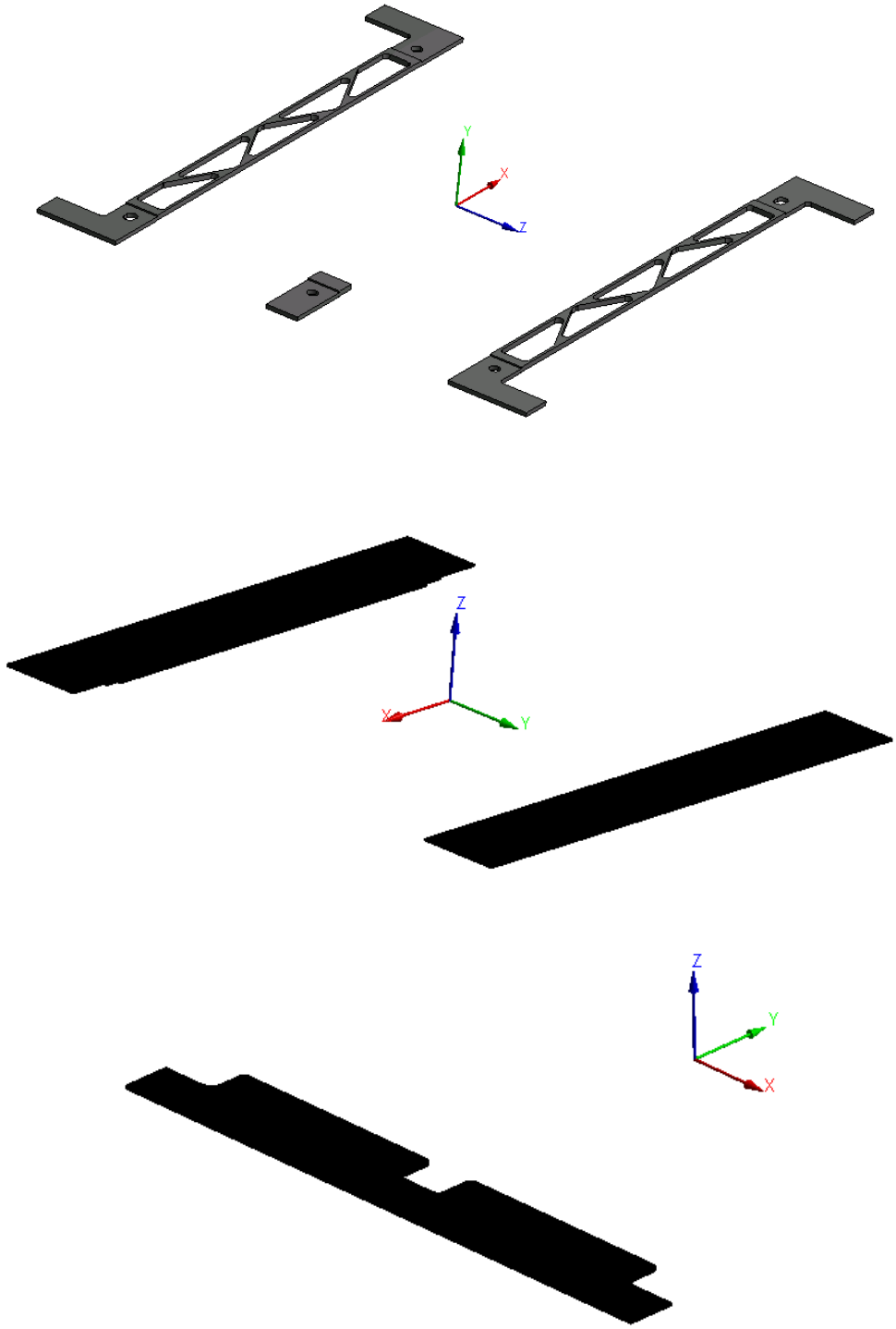

Figure 5-12: Coordinate systems of the composite materials: Al-CF bridges, CFRP stiffeners for the readout hybrids and CFRP stiffener for the service hybrid.

5.2.5 Finite Element Method Mesh

The mesh of the Finite Element model of the 2S 1.8mm TEDD module was realised by using 214788 elements and 780722 nodes. The global mesh with dense element distribution was customised to a maximum element size of 1 mm. Body sizing method with element size of 0.75 mm was applied to the wirebonds, the Al-CF bridges and the cooling inserts, achieving localized mesh refinement and a mesh convergence solution.

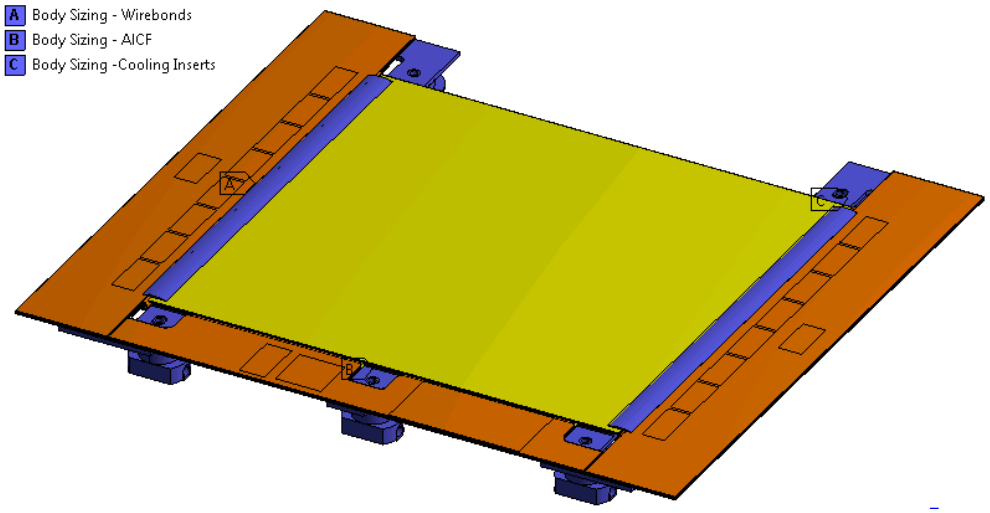

Figure 5-13: Body sizing method with element size of 0.75 mm.

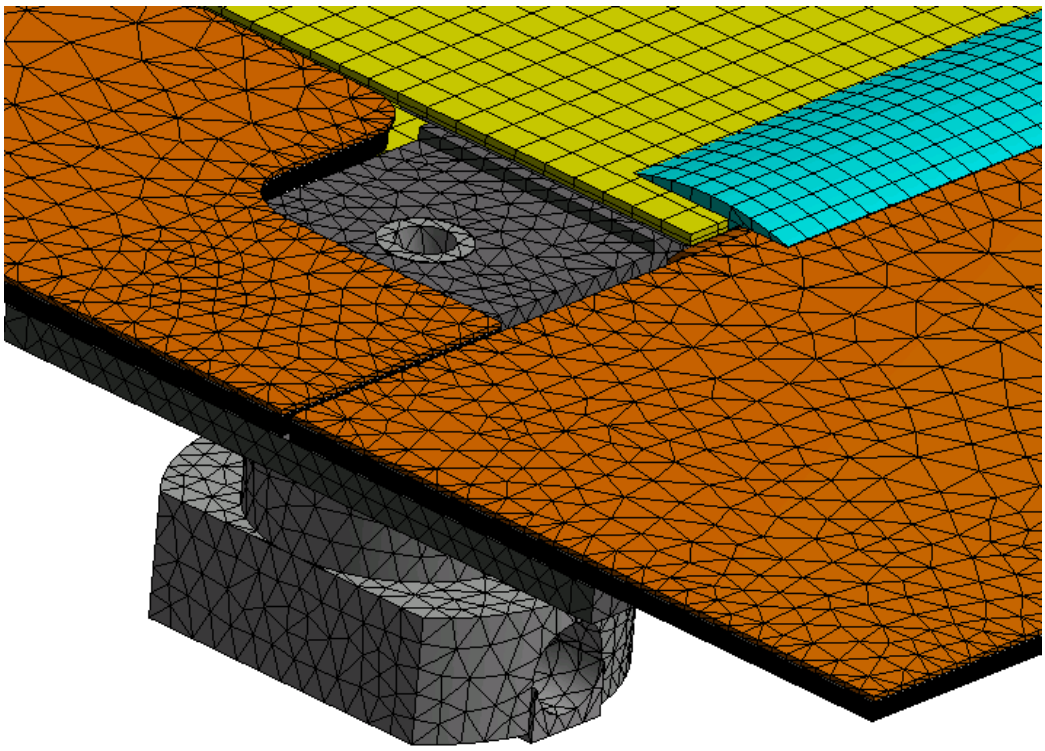

Figure 5-14: Detailed view of the FEM mesh.

5.2.6 Boundary conditions and thermal runaway

The thermal performance of the 1.8 mm 2S module design has been studied using ANSYS Thermal-Electric. The five cooling contacts should provide adequate cooling. A sufficient margin of 10 ^{o}C should be satisfied from the temperature of -33 ^{o}C, by using different types of CFRPs. The thermal performance of a module and its corresponding cooling structure is characterized in terms of temperature at which the module undergoes thermal runaway when the coolant temperature is increased. Thermal runaway is a situation in which:

- The cooling power is insufficient to cool the module
- The sensor temperature rises in a positive feedback loop, since the leakage current increases exponentially with the temperature.

The heat loads modelled in the thermal FEA of the 2S module are summarized on the following table:

Component	Power consumption (mW)
2x 8 CBCs	2187.5
2 CICs	625
LpGBT	500
VTRx+	306
DC-DC converter	1770
TOTAL	**5388.5**

`

A heat transfer coefficient of 5000 W/m^{2}K is assumed for the heat transfer from the cooling pipe inner wall to the CO_2, with actual boiling of the coolant not being modelled. A temperature dependent heat load has been applied to the silicon sensors. To study the thermal runaway, the starting temperature has been set to -42.5 ^{o}C. Multiple iterations have been performed to define the thermal runaway temperature. The temperature has been increased with a step of 0.5 ^{o}C at each run and close to the thermal runaway was set to 0.2 ^{o}C.

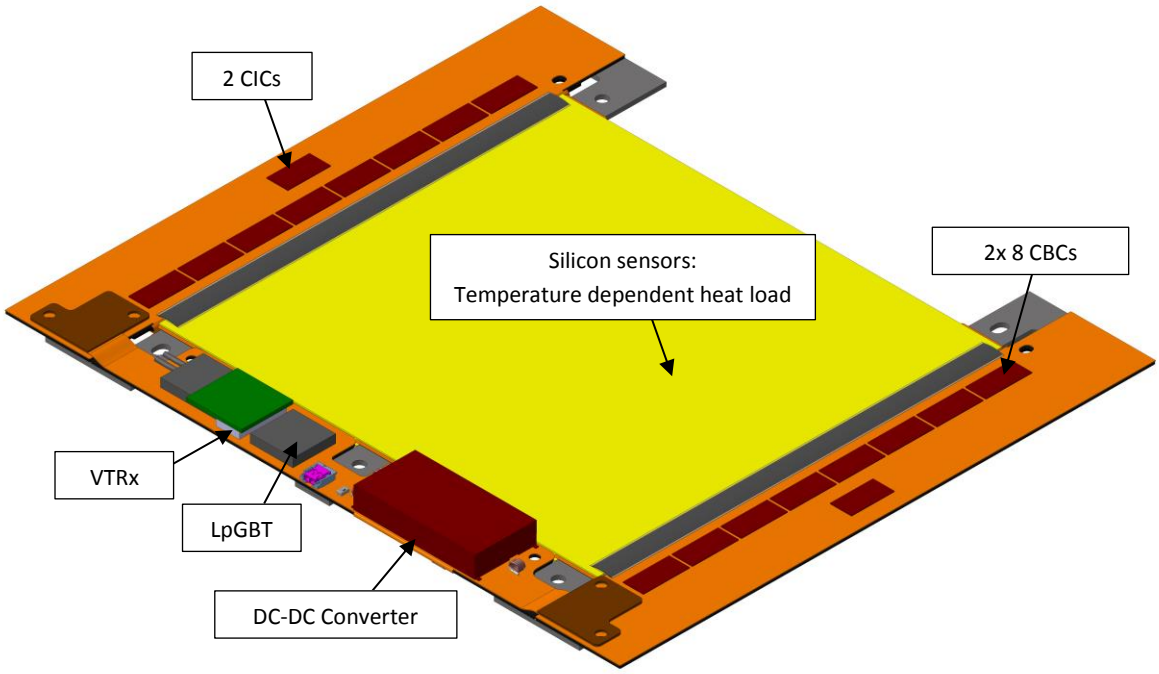

Figure 5-15: Location of the electronic components as heat loads.

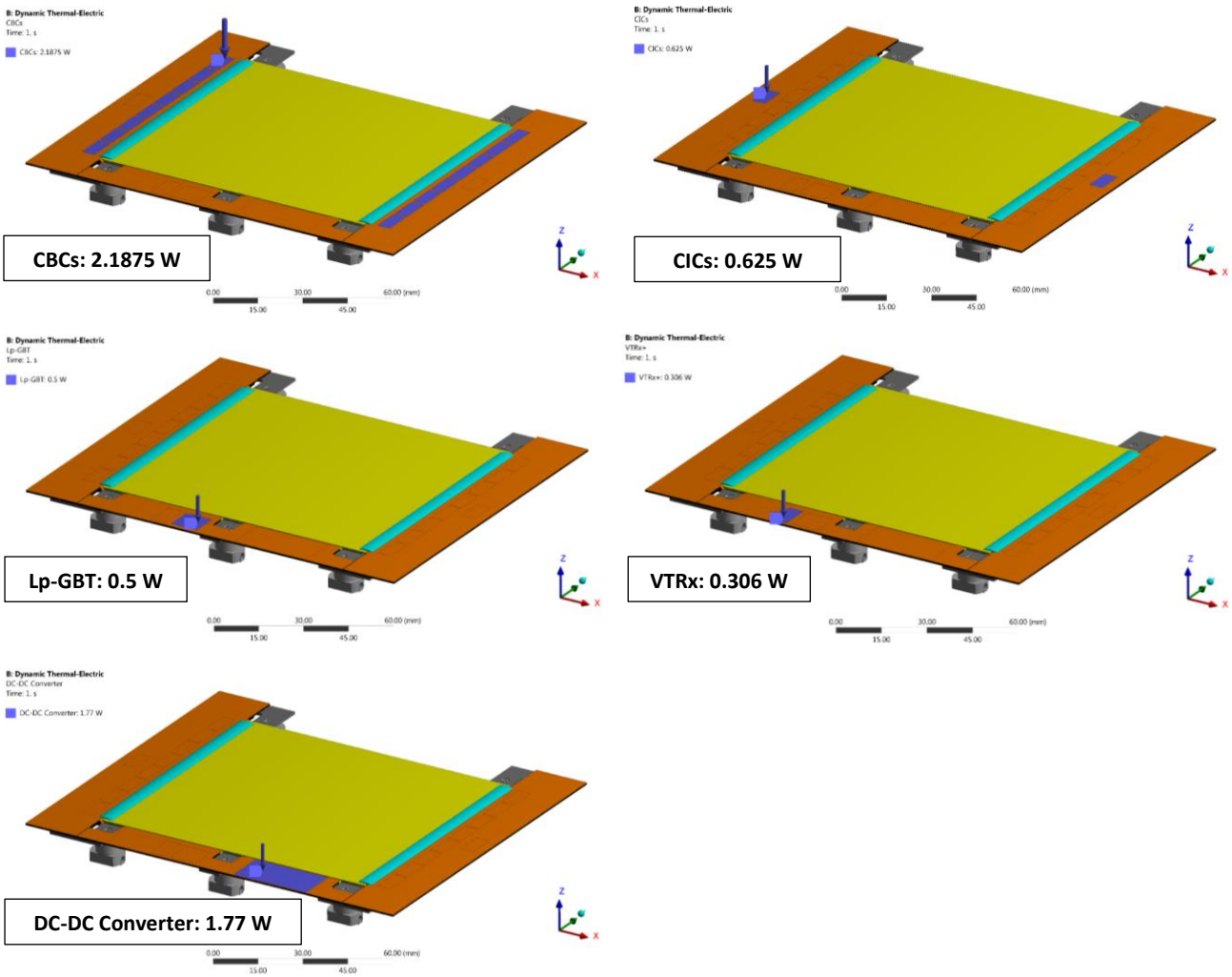

Figure 5-16: Boundary conditions of the heat loads of the 1.8 mm 2S Module.

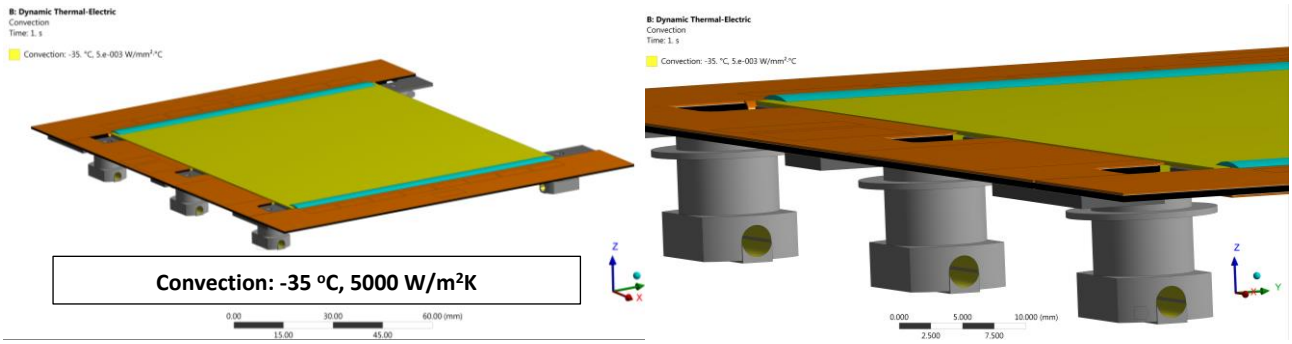

Figure 5-17: Boundary condition of convection on the cooling pipe inner wall.

Chapter 6 Results

6.1 Thermal performance results

As it was mentioned, the cooling system will be designed for a nominal coolant operating temperature of −35 ◦C, resulting in a coolant temperature of about −33 ◦C of the silicon module. A thermal study was conducted for a nominal coolant temperature at -35 ^{o}C, investigating the maximum temperatures on the module and the sensors as well as the temperature difference of them, according to various types of carbon fibers and the two types of laminates with stacking sequence: 0/90/0/90/0 and $[0/90]_s$.

Longitudinal fiber thermal conductivity (W/mK)	Carbon Fiber Type	Max. Temperature on the module with 0/90/0/90/0 laminates (^{o}C)	Max. Temperature on the module with $[0/90]_s$ laminates (^{o}C)	DT (^{o}C)
800	K13D2U	2.5	3.6	1.1
620	K13C2U	4.8	6.1	1.3
600	YS-95	5.1	6.5	1.4
580	K13C6U	5.5	6.9	1.4
500	XN 90/ YS 90A	7.2	8.8	1.6
320	XN 80/YS 80A	13.8	16.1	2.3
250	YSH-70A	18.7	21.5	2.9
220	K63A12	21.7	24.8	3.2
210	K1392U	22.9	26.2	3.3
200	K13916	24.2	27.6	3.4
180	XN 60/YSH-60A	27.2	31.1	3.9
140	K63712/ K1352U	35.8	41.1	5.4
120	YSH-50A	42.4	48.6	6.2
110	K13312	46.5	53.2	6.7

Table 6-1: Maximum temperature on the module with laminates 0/90/0/90/0 and [0/90]s and the temperature difference of them, according to different longitudinal thermal conductivities of carbon fibers. Green-Mitsubishi Carbon Fibers, Blue-Nippon Carbon Fibers.

Table 6-1 provides summarized results concerning the comparison of the laminates with different carbon fiber systems and the laminates. As it can be seen, the difference of the maximum temperature on the module varies from 1.1 ^{o}C to 1.6 ^{o}C, for values of thermal conductivity from 500 W/mK to 800 W/mK, comparing the two cases of the laminates. According to Figure 6-1, the slope of the graph is too small when considering values of thermal conductivity from 800 W/mK to 500 W/mK, whereas as the thermal conductivity is decreasing, the maximum module temperature increases with an exponential growth. In Figures 6-1 and 6-2, there is a linear portion with a small increase rate, for the decreased values of the longitudinal fiber thermal conductivity from 800 W/mK to 500 W/mK, after

which the slope increases in an abrupt manner. In Figures 5-6 − 5-10, there is an analytical view of the module's structure with all the components.

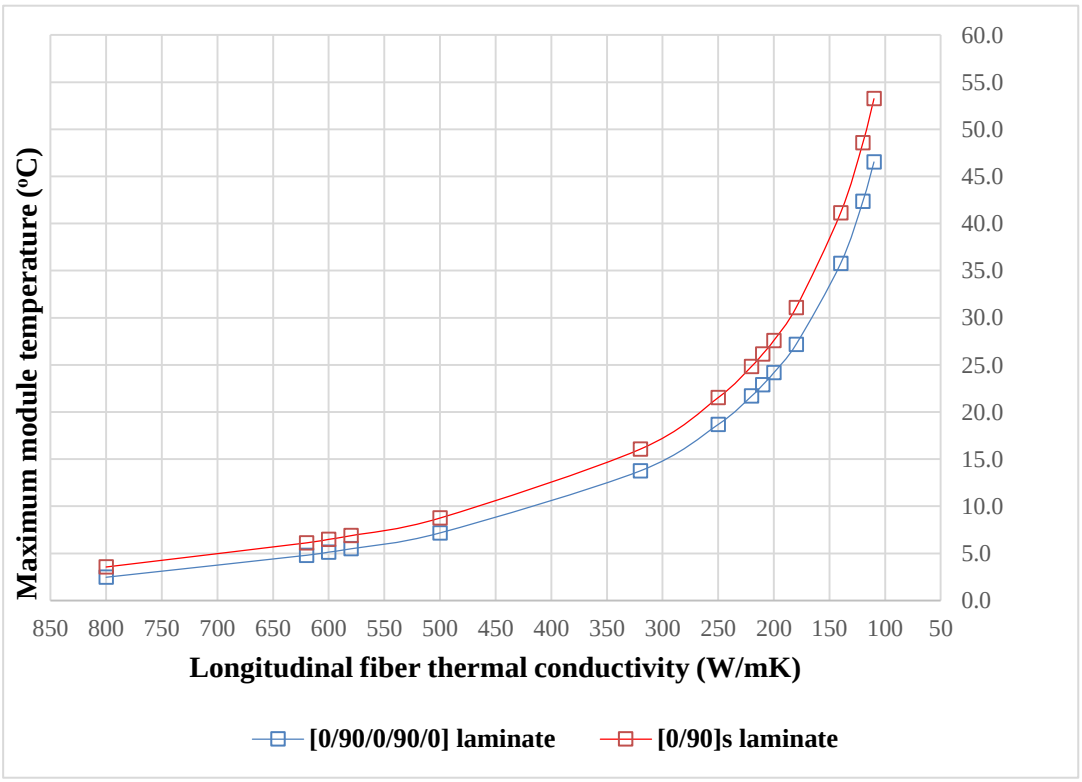

Figure 6-1: Maximum module temperature (°C) for the different values of the longitudinal thermal conductivity of carbon fiber.

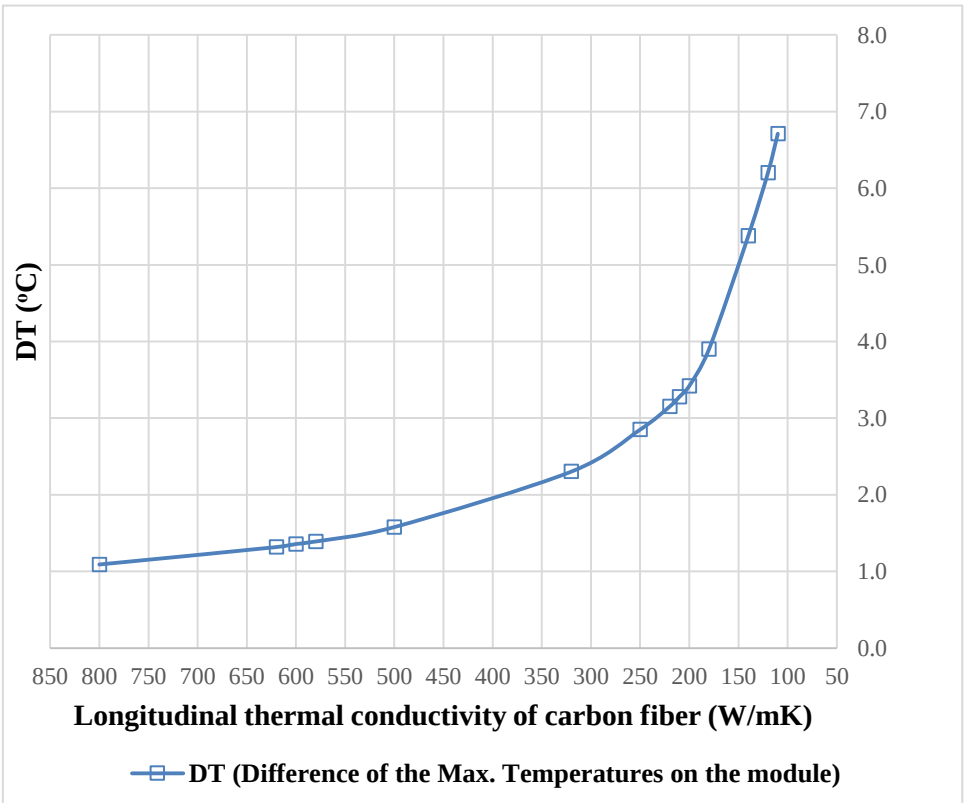

Figure 6-2: Temperature difference (°C) of the maximum temperatures on the module in comparison with the two laminates 0/90/0/90/0 and $[0,90]_s$ for the different values of the longitudinal thermal conductivity of carbon fiber.

Longitudinal fiber thermal conductivity (W/mK)	DT (°C) top sensor Case: 0/90/0/90/0 laminates	DT (°C) bottom sensor , Case: 0/90/0/90/0 laminates	DT (°C) Module Case: 0/90/0/90/0 laminates
800	4.34	4.25	35.73
620	4.54	4.45	38.08
600	4.57	4.48	38.41
580	4.60	4.51	38.77
500	4.73	4.64	40.46
320	5.17	5.07	47.07
250	5.44	5.35	52.00
220	5.58	5.50	55.01
210	5.64	5.55	56.20
200	5.70	5.61	57.50
180	5.83	5.74	60.50
140	6.14	6.06	69.09
120	6.34	6.25	75.70
110	6.45	6.37	79.87

Table 6-2: Temperature differences of the top sensor, bottom sensor and module, for the case of using laminates with stacking sequence 0/90/0/90/0, according to different longitudinal thermal conductivities of carbon fibers.

Longitudinal thermal conductivity of the fiber (W/mK)	DT (°C) top sensor Case: $[0/90]_s$ laminates	DT (°C) bottom sensor , Case: $[0/90]_s$ laminates	DT (°C) Module Case: $[0/90]_s$ laminates
800	4.48	4.39	36.83
620	4.70	4.61	39.40
600	4.73	4.64	39.78
580	4.76	4.67	40.17
500	4.90	4.81	42.05
320	5.38	5.29	49.38
250	5.68	5.58	54.86
220	5.84	5.74	58.17
210	5.90	5.80	59.48
200	5.96	5.86	60.92
180	6.10	6.00	64.41
140	6.43	6.34	74.47
120	6.64	6.54	81.90
110	6.75	6.66	86.59

Table 6-3: Temperature differences of the top sensor, bottom sensor and module, for the case of using laminates with stacking sequence $[0/90]_s$, according to different longitudinal thermal conductivities of carbon fibers.

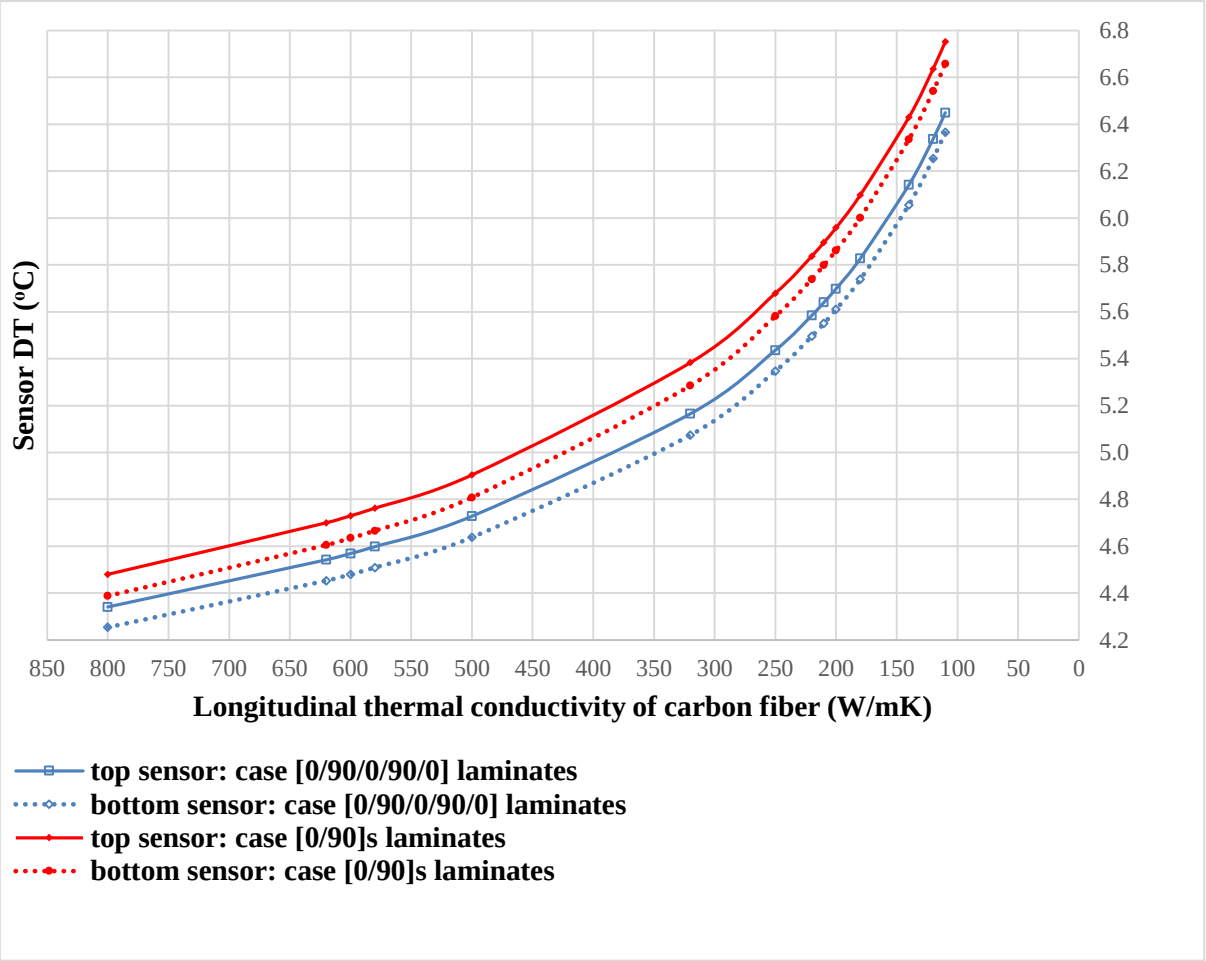

Figure 6-3: Temperature difference (ºC) of the sensors in comparison with the two laminates 0/90/0/90/0 and $[0,90]_s$ for the different values of the longitudinal thermal conductivity of carbon fiber.

Summarized results for the temperature differences of the top and bottom sensor, as well as for the module, are shown on the Tables 6-2 and 6-3, concerning the comparison with the different carbon fiber systems and the laminates. Regarding the temperature differences, the DT top sensor is the difference of the maximum with the minimum temperature observed on the top sensor. Correspondingly, the DT bottom sensor describes the temperature difference of the bottom sensor and the total structure of the 2S 1.8mm module. The results are shown on the Figures 6-3, 6-4. It should be noted that both graphs show the same behaviour. The part of the graph for the values of thermal conductivity from 800 W/mK to 500 W/mK can be considered linear with a small slope. After that value of 500 W/mK, the slope increases significantly and for the values of 320 W/mK and less, the tendency of the graph is not gradual, showing an abrupt behaviour.

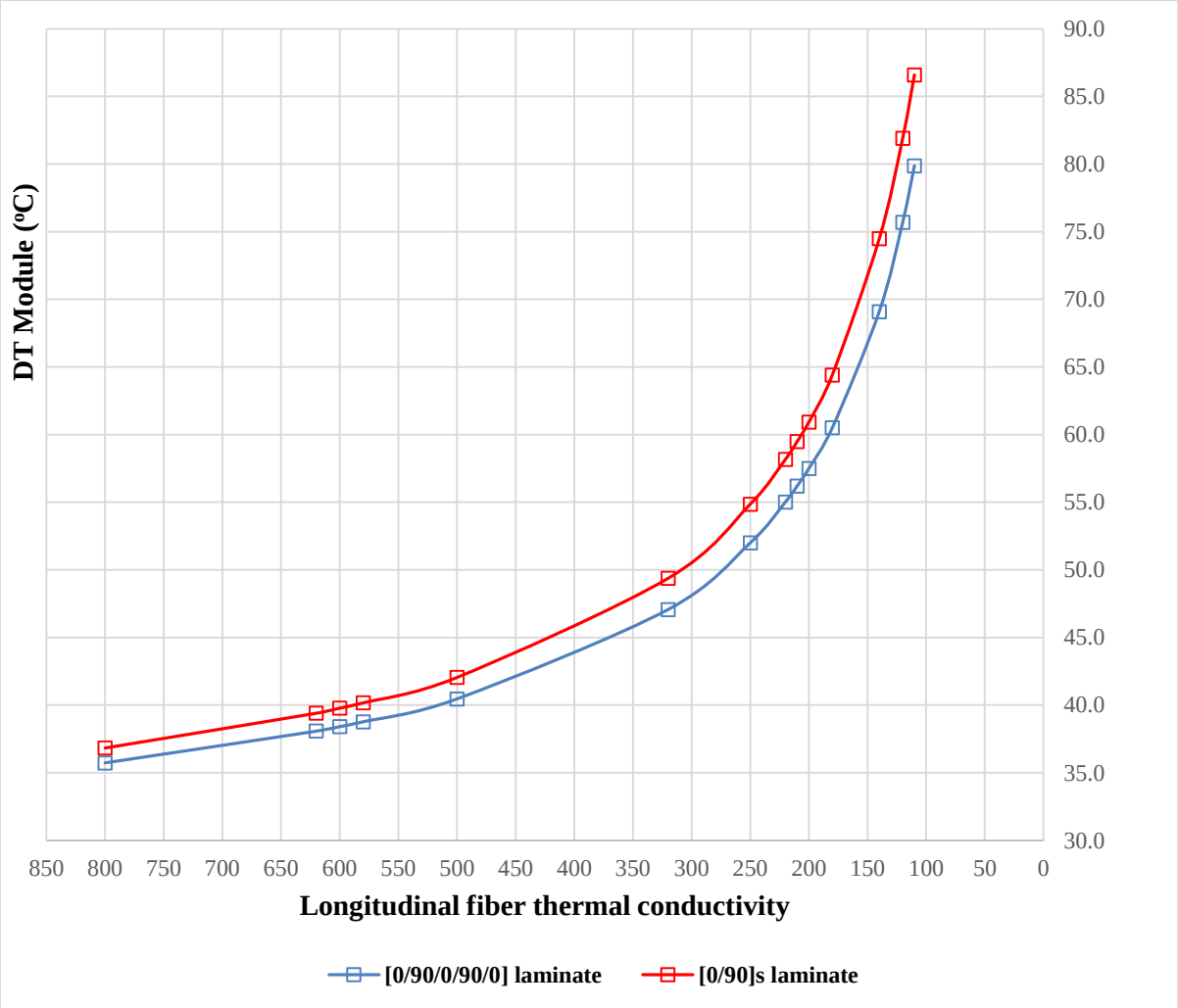

Figure 6-4: Temperature difference (ºC) of the 2S 1.8 mm Module in comparison with the two laminates 0/90/0/90/0 and $[0,90]_s$ for the different values of the longitudinal thermal conductivity of carbon fiber.

Comparing the two case-studies, from Table 6-2 and 6-3, the percentage diference of the DT on the sensors shows values from 3.1 % to 3.7% and from 4.2% to 4.7%, for thermal conductivities of the range 800-500 W/mK and 320-110 W/mK, respectively. Taking into account the percentage difference of the DT on the module, this varies from 3.1% to 3.9% for the range 800-500 W/mK, whereas it increases significantly for the lower values, varying from 4.9% to 8.4%. Therefore, the impact of changing the baseline laminate from 0/90/0/90/0 to $[0,90]_s$ is considerably important, by considering values of longitudinal fiber thermal conductivity lower than 500 W/mK. Taking into account the Figures 6-1 – 6-4, three distinct areas were observed:

- from 800 to 500 W/mK: there is a linear portion with a slight increase.
- from 500 to 320 W/mK: there is a transition area with a sharp increase.
- from 320 to 110 W/mk: the graph changes considerably and there is an abrupt increase in a certain manner with an hyperbolic behaviour.

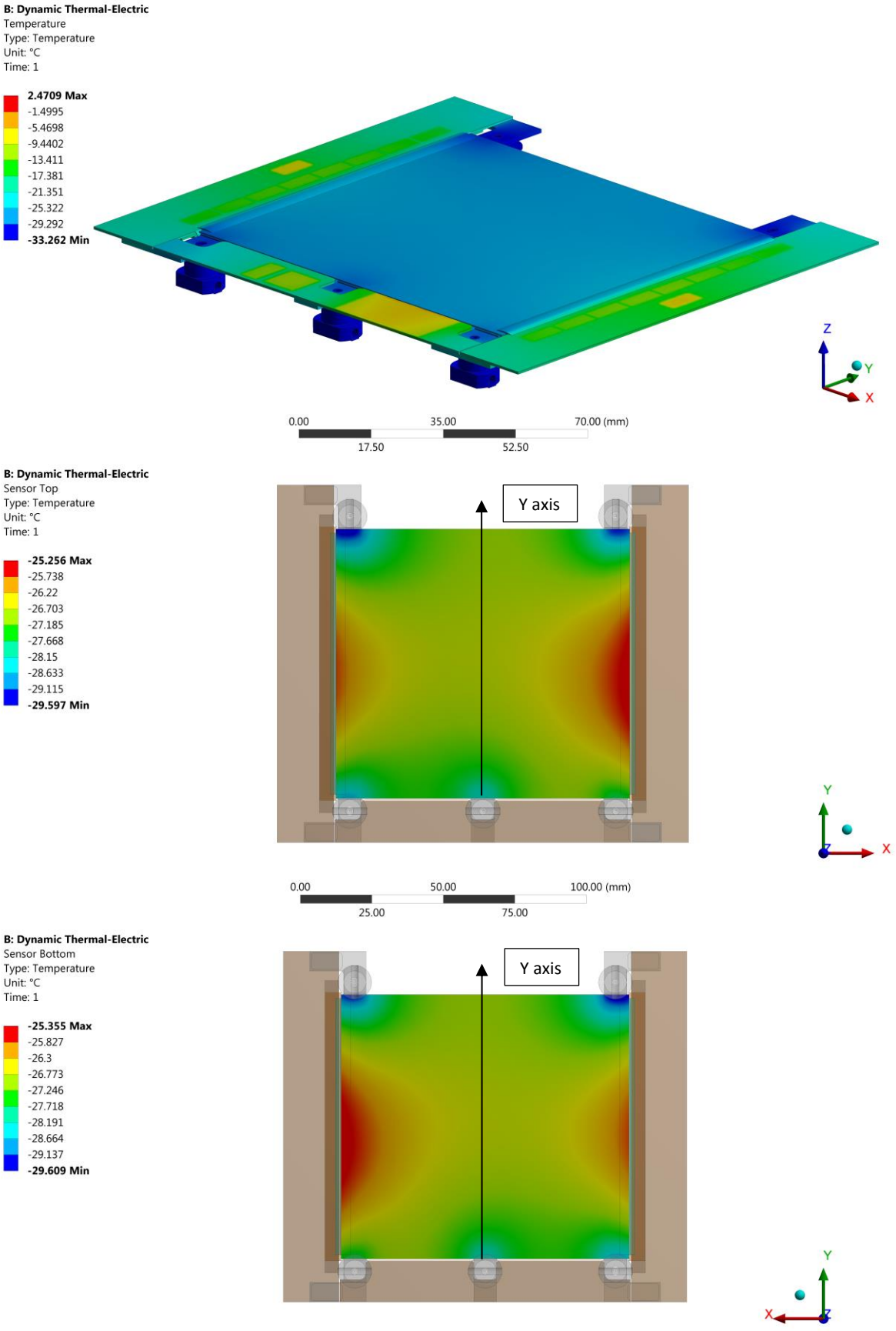

Figure 6-5: Temperature distribution (°C) on the total structure of the 2S 1.8mm Module and on the sensors, using laminates with the best case scenario: 0/90/0/90/0 and carbon fiber K13D2U.

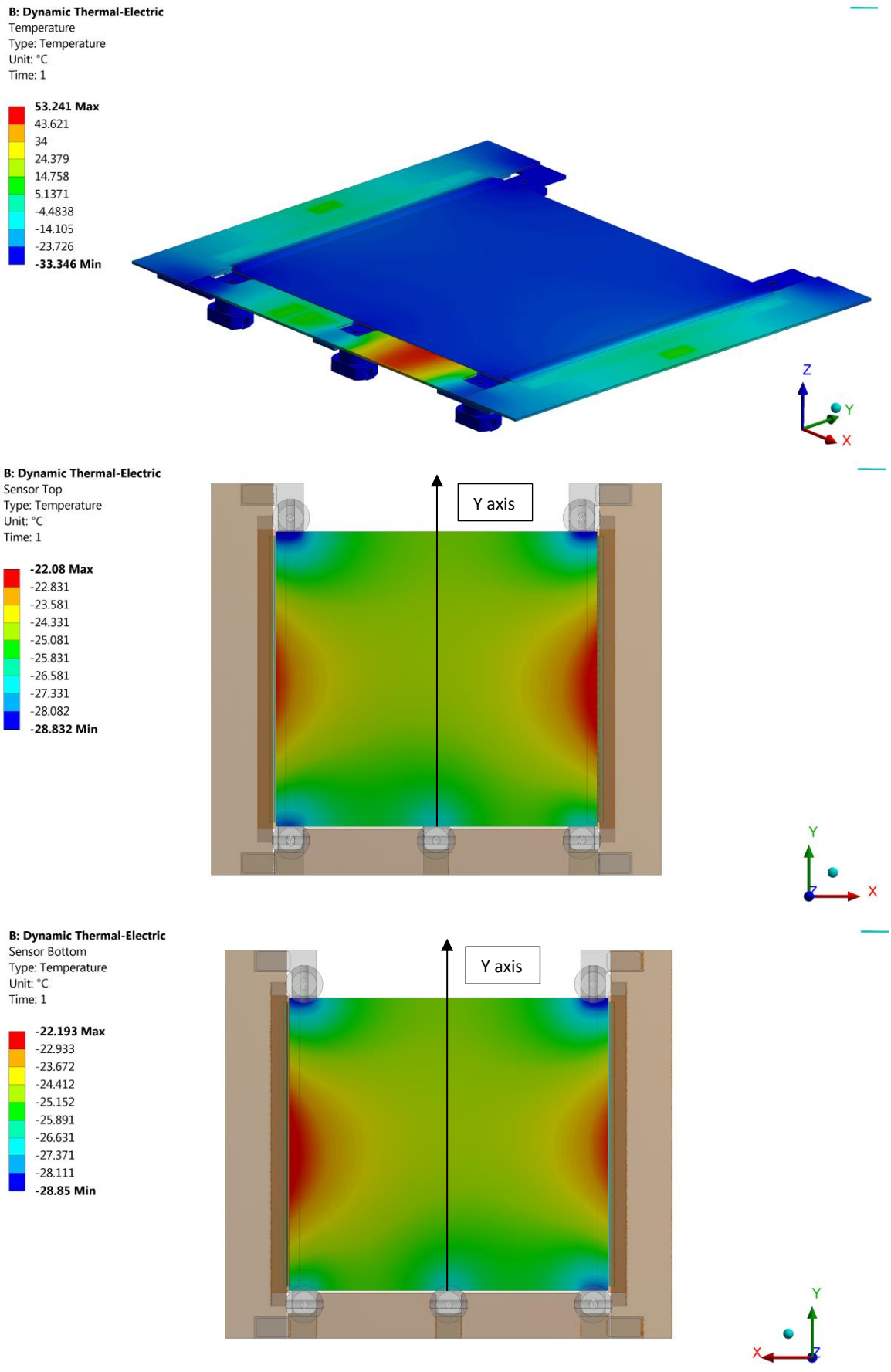

Figure 6-6: Temperature distribution (°C) on the total structure of the 2S 1.8mm Module and on the sensors, using laminates with the worst case scenario: $[0/90]_s$ and carbon fiber K13312.

Figures 6-5 and 6-6 show the results (obtained by Finite Element Analysis using ANSYS) for the best and the worst case scenario. Considering the 2S 1.8mm Module as total structure, the maximum temperature is observed on the service hybrid, where the DC-DC converter is located (Fig.5-15). As it is expected, the minimum temperature ~ -33 ºC is observed on the cooling inserts. The maximum value of the module for the best case scenario was 2.5 ºC, whereas a considerably higher value of 53.2 ºC was noticed for the worst case. For the sensors, a symmetric behaviour of the temperature distribution was observed on Y axis, with the lower values occurring close to the cooling areas and the higher ones in the middle close to the readout hybrids. For the best case and the worst scenario, the highest value was -25.3 ºC and -22.1 ºC respectively, both observed on the top sensor. This can be noticed in the following pictures.

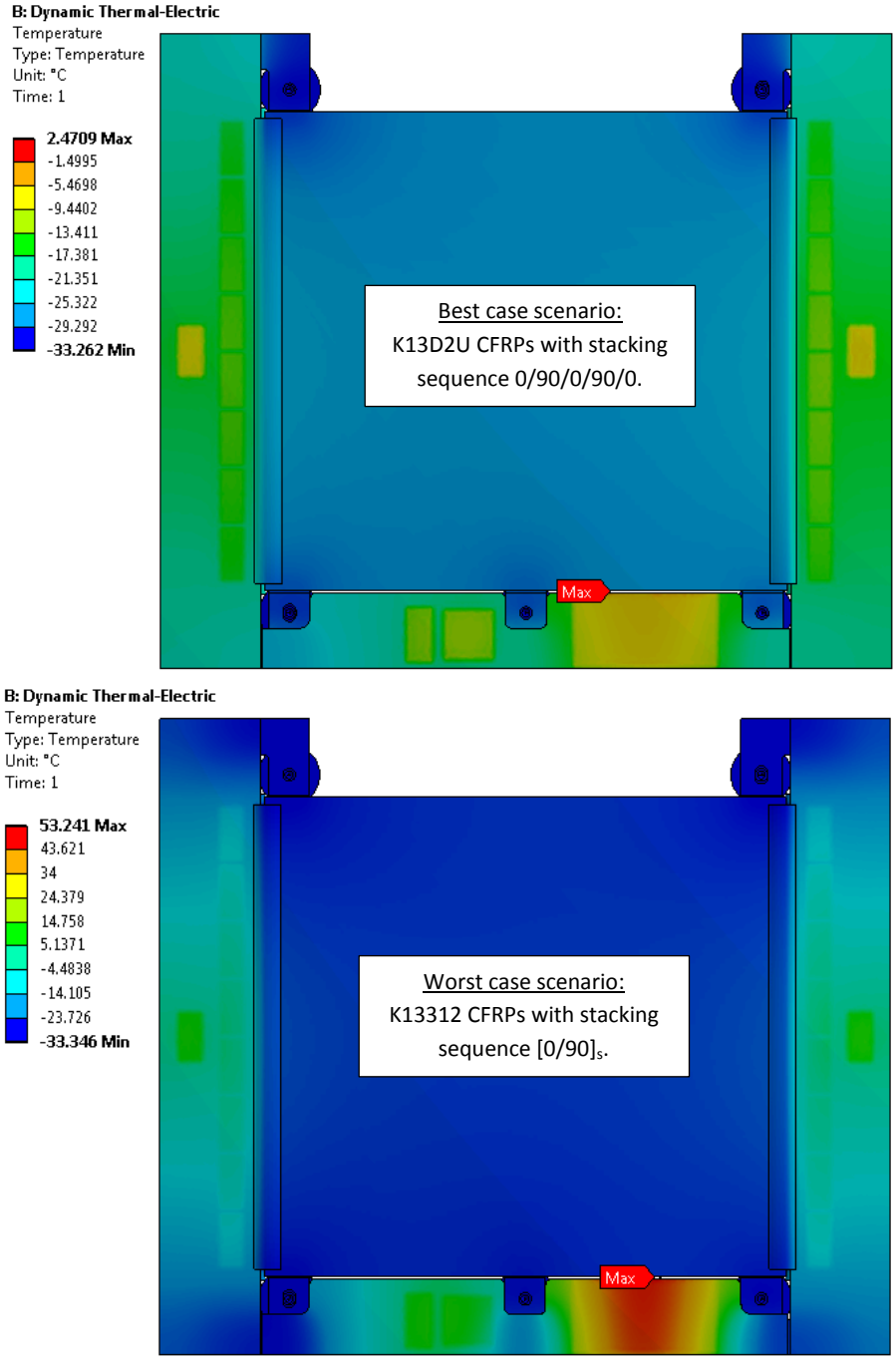

Figure 6-7: Detailed view of the maximum temperature observed on the module.

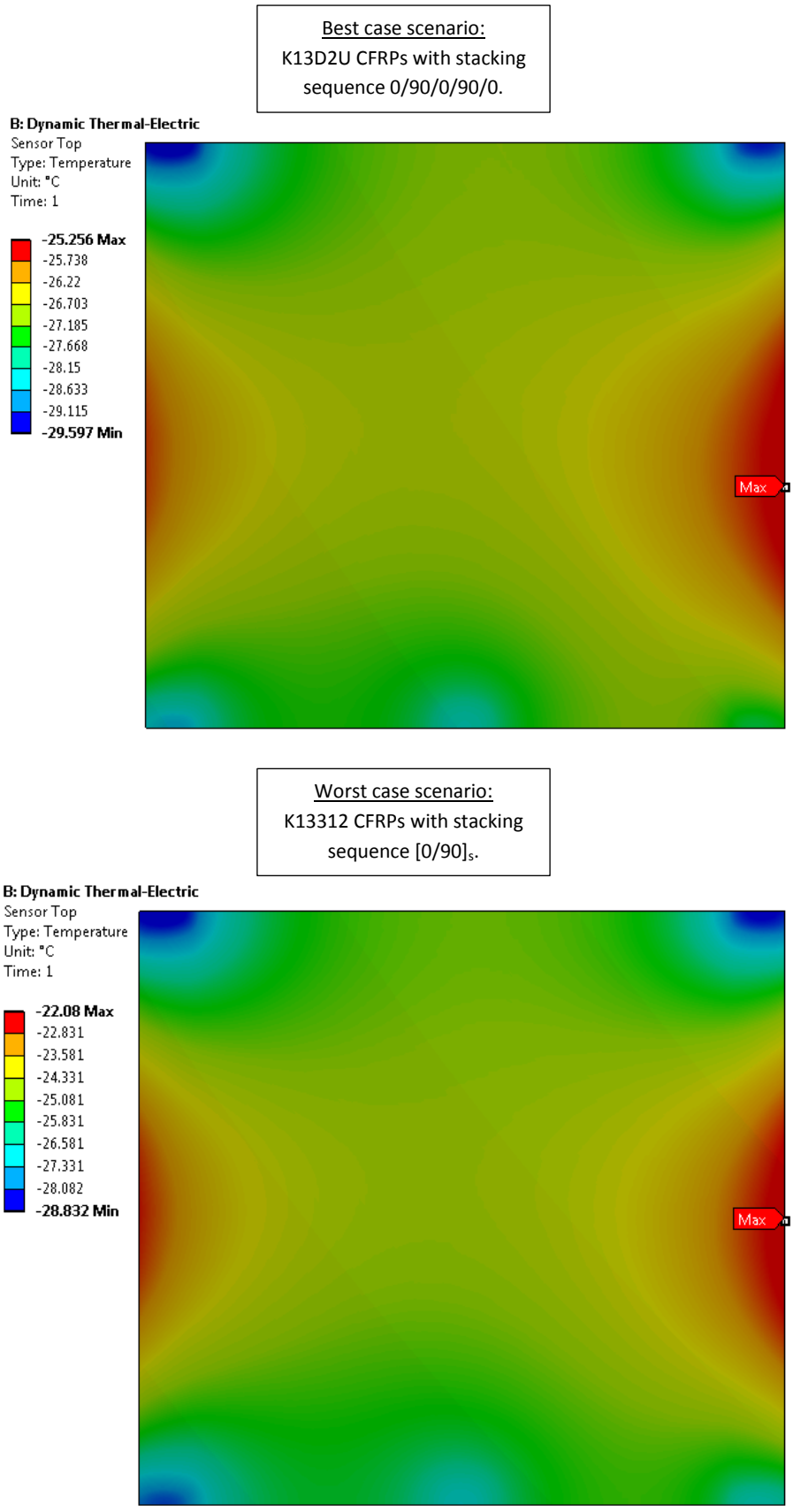

Figure 6-8: Detailed view of the maximum temperature observed on the top sensor.

Best case scenario:
K13D2U CFRPs with stacking sequence 0/90/0/90/0.

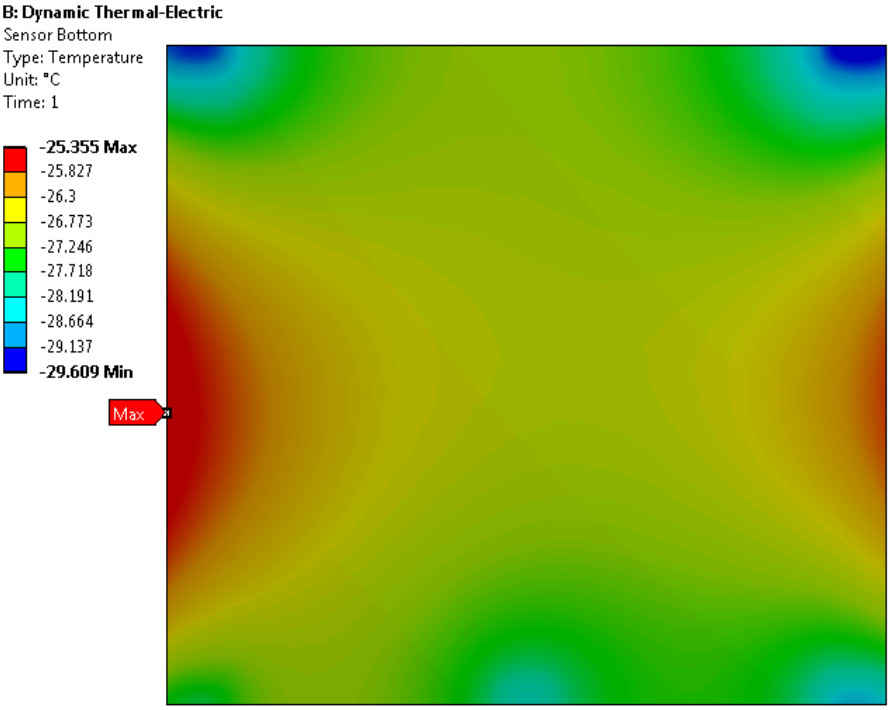

Worst case scenario:
K13312 CFRPs with stacking sequence $[0/90]_s$.

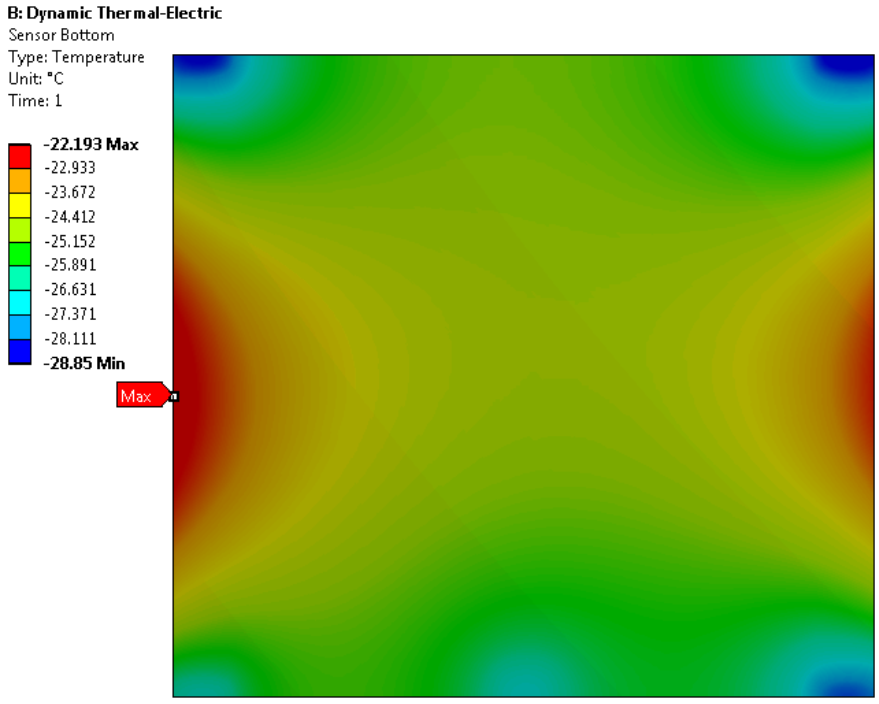

Figure 6-9: Detailed view of the maximum temperature observed on the bottom sensor.

6.2 Thermal runaway results

The thermal runaway performance of the 2S 1.8 mm module has been studied, concerning the various carbon fiber types and the laminates with stacking sequence $[0/90]_s$ and 0/90/0/90/0. Performing many iterations with ANSYS, while increasing the temperature from -42.5 ^oC with a step of 0.5 ^oC, the thermal runaway temperature was defined. In order to get a precision of 0.2 ^oC, the step was changed to 0.2 ^oC when the temperature reached the thermal runawaway. According to the results, the thermal runaway turn-on temperature (T.R.T) is expected to occur at temperatures at least 10 ^oC above the coolant temperature of the module. Therefore, as it can be observed from the following table (Table 6-4), a sufficient margin of 10 ^oC can be satisfied by using all the types of carbon fibers.

Manufacturer	Carbon Fiber Name	Longitudinal Thermal Conductivity (W/mK)	T.R.T (^oC) 0/90/0/90/0	T.R.T (^oC) $[0/90]_s$
Mitsubishi	**K13D2U**	**800**	-20	-20.2
	K13C2U	**620**	-20.2	-20.4
	K13C6U	**580**	-20.4	-20.4
	K63A12	**220**	-21.4	-21.6
	K1392U	**210**	-21.4	-21.6
	K13916	**200**	-21.4	-21.6
	K63712/ K1352U	**140**	-22	-22.2
	K13312	**110**	-22.2	-22.6
Nippon (NGF)	**YS-95**	**600**	-20.2	-20.4
	XN 90/ YS 90A	**500**	-20.4	-20.6
	XN 80/YS 80A	**320**	-21	-21.2
	YSH-70A	**250**	-21.2	-21.4
	XN 60/YSH-60A	**180**	-21.6	-21.8
	YSH-50A	**120**	-22.2	-22.4

Table 6-4: Thermal runaway temperatures (T.R.T) for different carbon fiber systems of the laminates 0/90/0/90/0 and [0/90]s with fiber volume ftaction 0.65.

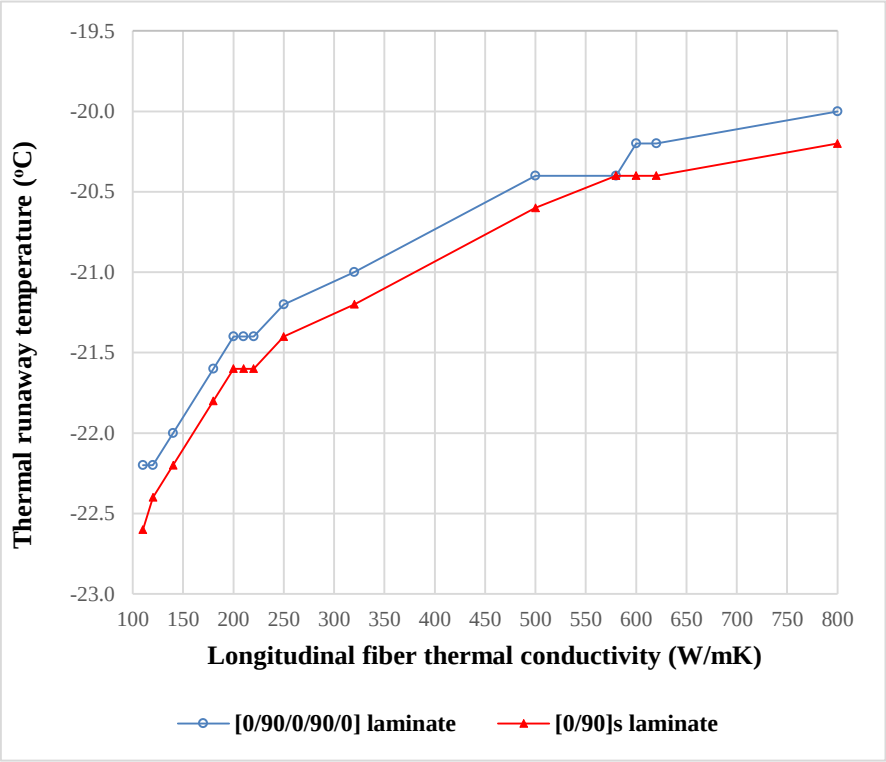

Figure 6-10: Thermal runaway temperatures of the 2S 1.8 mm module VS longitudinal fiber thermal conductivity for the two types of laminates: 0/90/0/90/0 and [0/90]s.

The foregoing results indicate that there is a slight difference between the two laminates showing only 0.2 ºC of variation. Comparing the two laminates and considering the case of using the K13C6U fiber, the thermal runaway temperature seems to have the same value. This means that the thermal runaway temperature for the two cases is close to each other with a value of difference less than 0.2 ºC. The effect of changing the carbon fiber type on the module's thermal runaway temperature is reported in Figure 6-10. It can be seen that the slope of the line is decreased for the cases of using carbon fibers with longitudinal thermal conductivity more than 500 W/mK. Six carbon fiber systems can be used showing approximately the same thermal runaway performance showing a difference of 0.4 ºC for the two laminate stacking sequences (considering the fibers with the highest and lowest value of longitundinal thermal conductivity): Mitsubishi K13D2U, K13C2U, K13C6U and Nippon YS-95, XN 90, YS-90A. As it was mentioned in previous chapter, it has been assumed that the laminates have the same thickness for all the investigated cases. However, in reality the laminate $[0,90]_s$ can lead to important mass savings, since with four layers, the thermal runaway performance of the module differs less than 1% from a 5-layer laminate. Figures 6-11−6-16 provide the thermal runaway results regarding the best-worst case scenario. The graphs show the temperature difference of the maximum temperature occured on the sensors (top and bottom) and the coolant temperature (Delta T), the maximum sensor temperature and the heat generation of the sensor, according to the different values of the coolant temperature. It can be noted that the module design with the laminates 0/90/0/90/0 and Mitsubishi K13D2U carbon fiber (800 W/mK) can be considered the best case, whereas that with laminates $[0,90]_s$ and Mitsubishi K13312 carbon fiber as the worst case (110 W/mK).

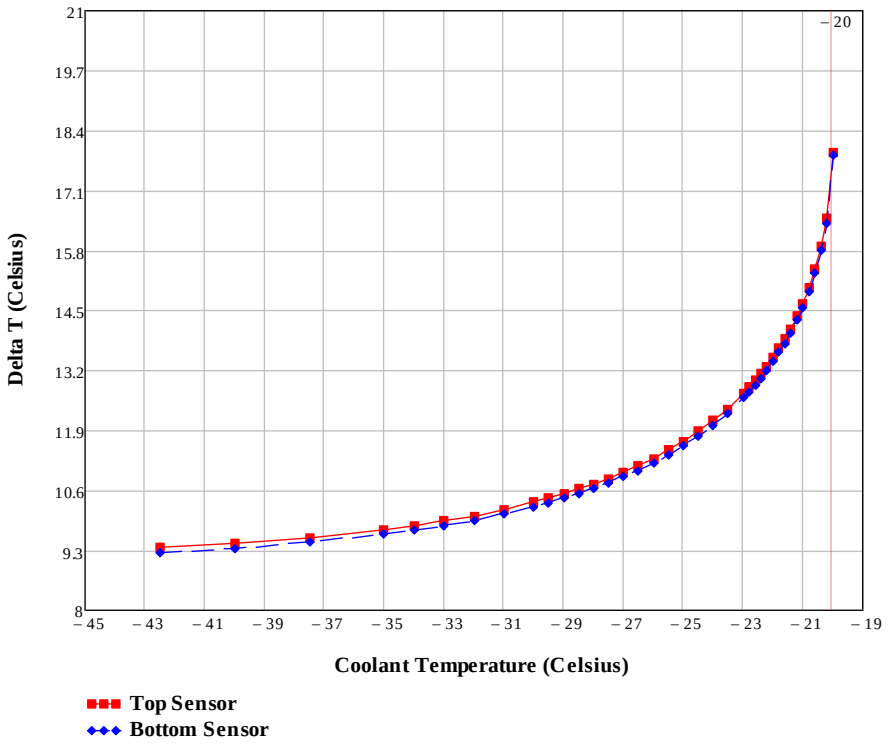

Figure 6-11: Temperature difference Vs Coolant temperature by using Mitsubishi K13D2U carbon fiber with 0/90/0/90/0 laminates.

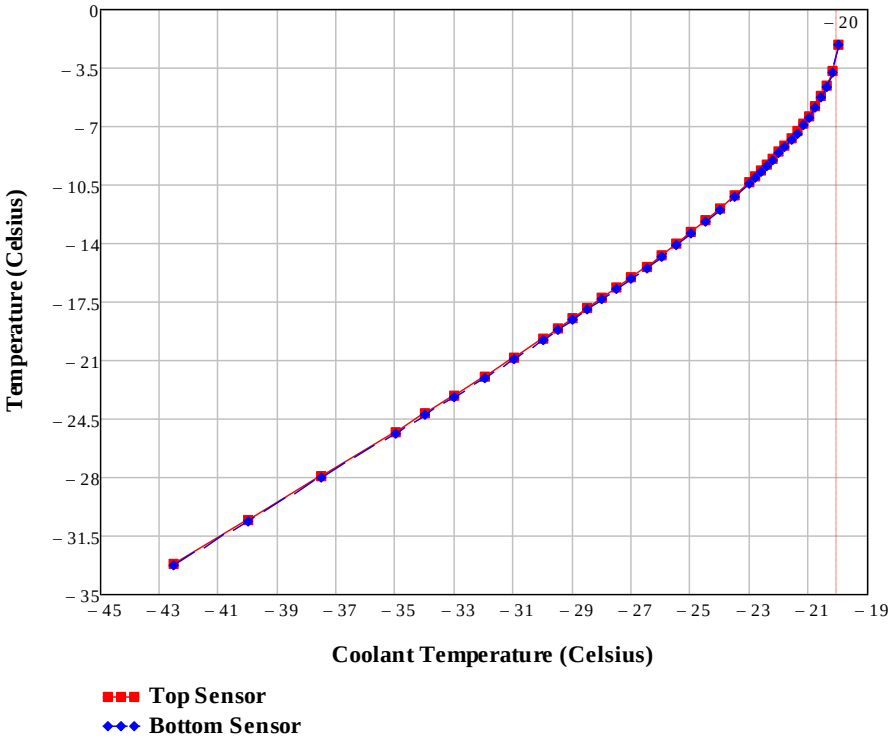

Figure 6-12: Maximum sensor temperature Vs Coolant temperature by using Mitsubishi K13D2U carbon fiber with 0/90/0/90/0 laminates.

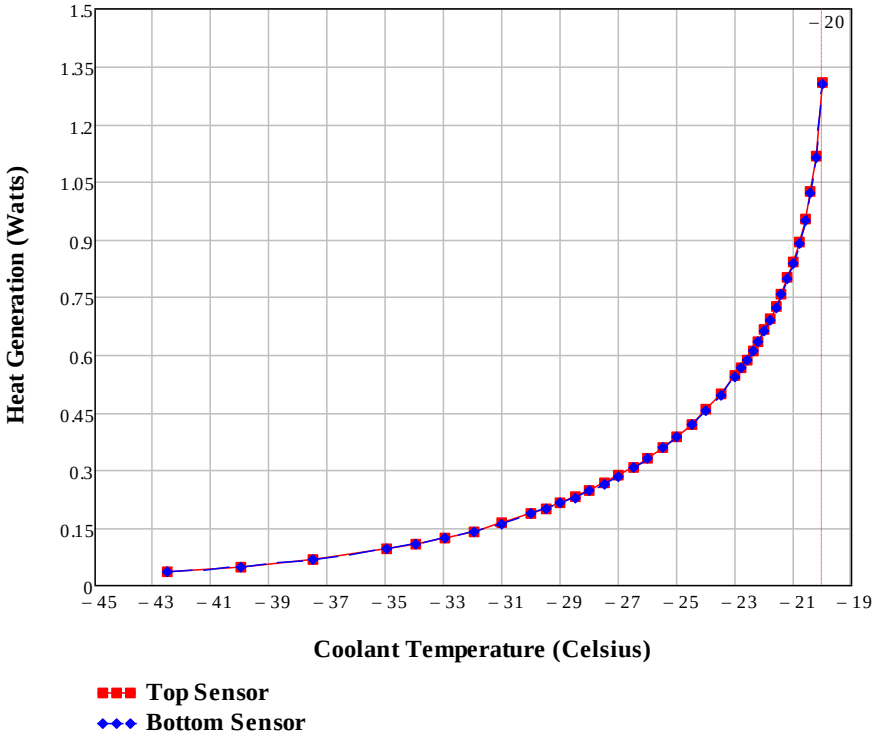

Figure 6-13: Heat generation of the sensors Vs Coolant temperature by using Mitsubishi K13D2U carbon fiber with 0/90/0/90/0 laminates.

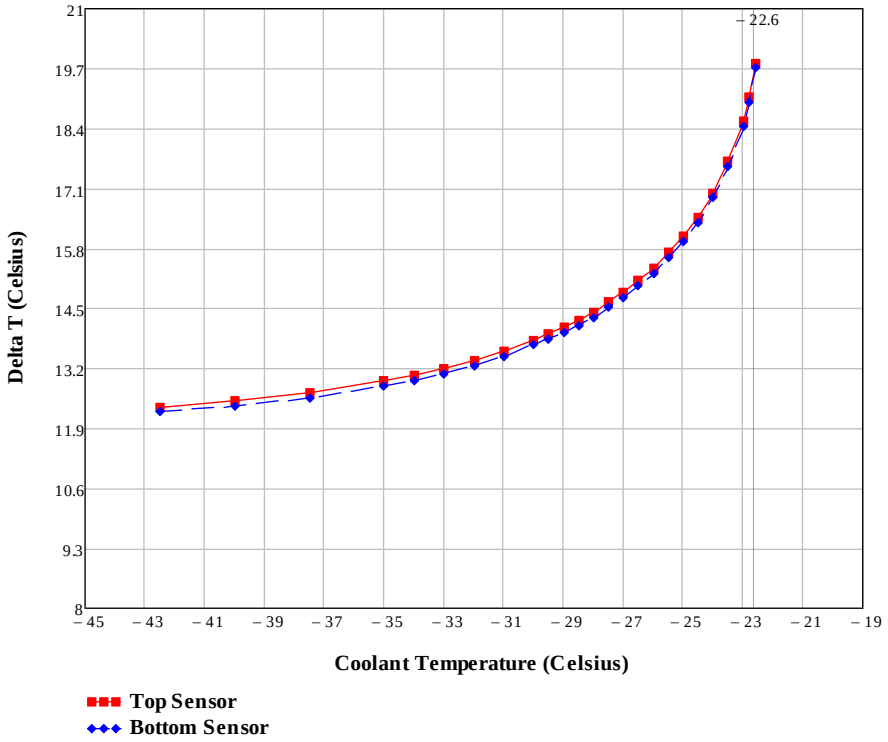

Figure 6-14: Temperature difference Vs Coolant temperature by using Mitsubishi K13312 carbon fiber with $[0/90]_s$ laminates.

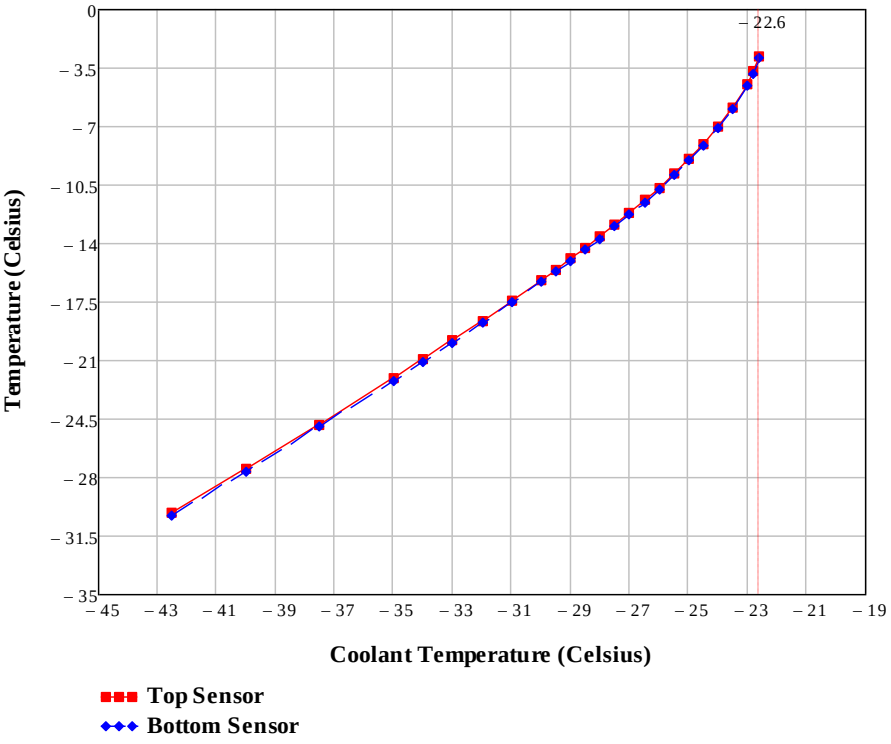

Figure 6-15: Maximum sensor temperature Vs Coolant temperature by using Mitsubishi K13312 carbon fiber with $[0/90]_s$ laminates.

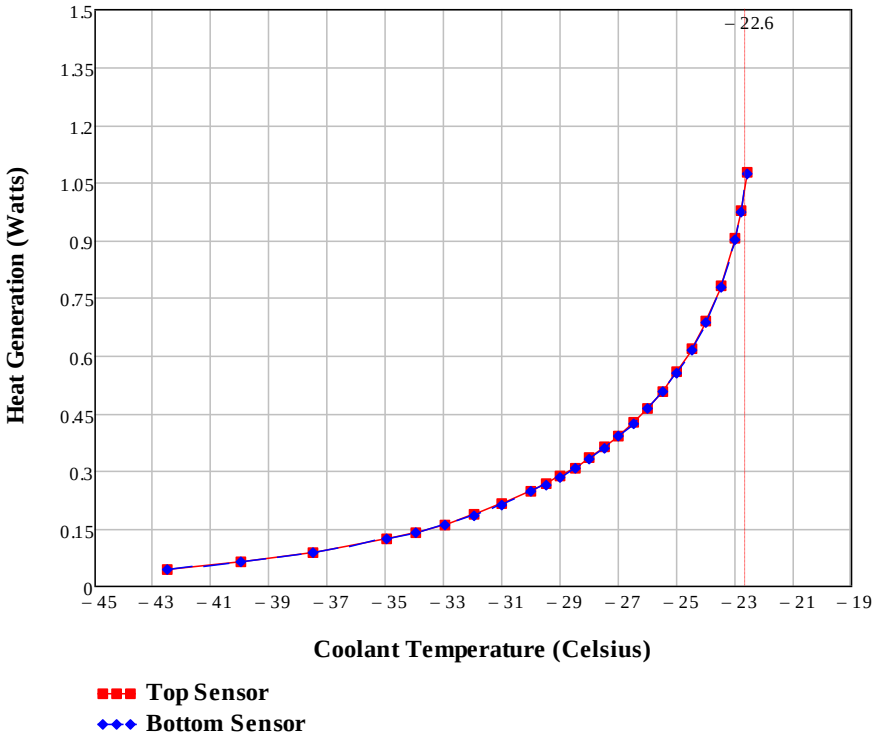

Figure 6-16: Heat generation of the sensors Vs Coolant temperature by using Mitsubishi K13312 carbon fiber with $[0/90]_s$ laminates.

It was observed that both sensors behave at the same way (reporting small differences). Moreover the temperature difference, as well as the heat generation of the sensor, increase exponentially, when the coolant temperature is increased. The plots concerning the maximum temperature on the sensor for the different values of coolant temperature increase linearly and a small exponential curve was observed when the coolant temperature reaches the thermal runaway (Figures 6-12 and 6-15). As the temperature increases and due to the thermal characteristics of a silicon sensor, the module becomes thermally unstable, the heat generated in the sensors exceeds the cooling capacity of the system and the leakage current is increasing more and more. The increased leakage currents which strongly depend on temperature can lead to the thermal runaway and hence to the failure of the silicon sensors and the module structure. A difference of 2.6 ^{o}C was observed taking into account the best-worst case scenario. In Figures 6-12 and 6-15, the variation of maximum sensor temperature according to the different values of coolant temperature presents a large linear portion at the main part of the graph. Then, this variation has the form of a curve, the slope of which does not increase in an abrupt manner. This behaviour does not appear in Figures 6-11, 6-13, 6-14 and 6-16, where there is an abrupt increase of the slope. The use of the laminate $[0,90]_s$ instead of 0/90/0/90/0 seems not to present significant difference in the form of the graphs, as it can be observed comparing the cases of the best-worst case scenario.

6.3 Conclusion

For the LHC upgrade, the CMS detector needs to be substantially upgraded during LS3 in order to exploit the increase in luminosity, provided by the HL-LHC. During LS3 the accelerator will be upgraded to enable instantaneous peak of luminosities of $5 \cdot 10^{34}$ cm^2s^{-1}, or even $7.5 \cdot 10^{34}$ cm^2s^{-1} in the ultimate performance scenario. This will increase the track density and rate within the particle detectors, which means that especially the tracker and its components have to meet stronger requirements regarding radiation hardness of the used materials and a sufficient cooling of the silicon sensor modules. In addition to this, the outer tracker should be able to support the first level of the CMS trigger system by providing high p_T tracks. Therefore, it is planned to fully remove the silicon tracker of the CMS detector. The new tracker is composed of silicon sensor modules that will have an on-module p_T discrimination. The current concept of building silicon sensor modules for the new outer tracker of the CMS detector is based on advanced composite materials: carbon fiber reinforced aluminium and carbon fiber reinforced polymers (CFRPs). The tracker will composed of two module types, called PS-Module and 2S-Module, differing in the granularity of their silicon sensors.

A lightweight design of the tracker and its components is essential to minimize photon conversion and multiple scattering in it. Due to the properties of the silicon sensors, a sufficient cooling of each silicon sensor has to be ensured. CFRPs with high thermal conductivity is of great interest in the construction of tracking mechanics. In this thesis, the thermal performance and the thermal runaway of the 2S TEDD 1.8mm Module, using two different CFRP laminates with stacking sequence of 0/90/0/90/0 and $[0,90]_s$ with different carbon fiber systems manufactured the two leading companies Mitsubishi Chemical Carbon Fiber & Composites and Nippon Graphite Fiber Corporation, have been studied and the results have been extensively compared. The module thermal behaviour has been studied according to two different studies: the thermal performance concerns the temperature difference observed on the silicon sensors and the module as a total structure and the thermal runaway temperature, meaning the maximum temperature after which the temperature and leakage current is increasing more and more and thermal instabilities are observed.

In figures and tables of chapter 6.1, three distinct plot areas could be observed. It was found that CFRPs with longitudinal fiber thermal conductivity of values between 500 W/mK and 800 W/mK show small differences, regarding the maximum temperature value of the module and the temperature difference of the sensors and the module. Moreover, by comparing the results of the two laminates for the aforementioned range, a slight difference has been observed. Concerning the chapter 6.2, considerably ambitious results were noticed for the thermal runaway performance showing that a sufficient margin of 10 ^oC can be satisfied by using all the investigated types of carbon fibers. Therefore, taking into account the aspects of thermal performance, mass and cost savings, CFRPs with laminate stacking sequence $[0,90]_s$ and carbon fiber type with longitudinal thermal conductivity from the range 500-800 W/mK, can be considered as an ideal heat spreader. Such laminates can efficiently transport the heat generated by the electronics and the silicon sensors to the cooling. A group of six carbon fiber systems can be used, yielding approximately the same results, when considering the thermal performance and thermal runaway.

This group concern the following carbon fiber systems: Mitsubishi K13D2U, K13C2U, K13C6U and Nippon YS-95, XN-90, YS-90A. The best thermal performance of the module was observed with CFRPs of Mitsubishi K13D2U. CFRPs with Mitsubishi K13C2U, K13C6U and Nippon YS-95 yield approximately the same values and the results with Nippon XN 90 and YS-90A were slightly different, showing the worst thermal performance from this group.

Due to the temperature difference on the sensor and the module, thermal stresses will arise. Thermal deformations can affect significantly the performance of the module. Therefore, an analytical thermo-mechanical study will reveal the CFRP laminate which is appropriate for a robust and radiation hard module.

Next developments:

- Thermo-mechanical studies to define the deformations and stresses.
- Cost analysis for a massive production of CFRP laminates.
- Comparative study of the thermal analysis by changing:
  - the stacking sequence of the CFRPs.
  - the fiber volume fraction.
- Comparative study of the performance using different carbon fibers from various alternative companies.
- Study of decreasing the mass by using different CFRPs.
- Definition of the epoxy or cyanate ester resin with high thermal conductivity.
- Study of the performance by changing the structure of the module using high thermal conductive materials.

Appendix

CASE STUDY WITH 0/90/0/90/0 LAMINATES

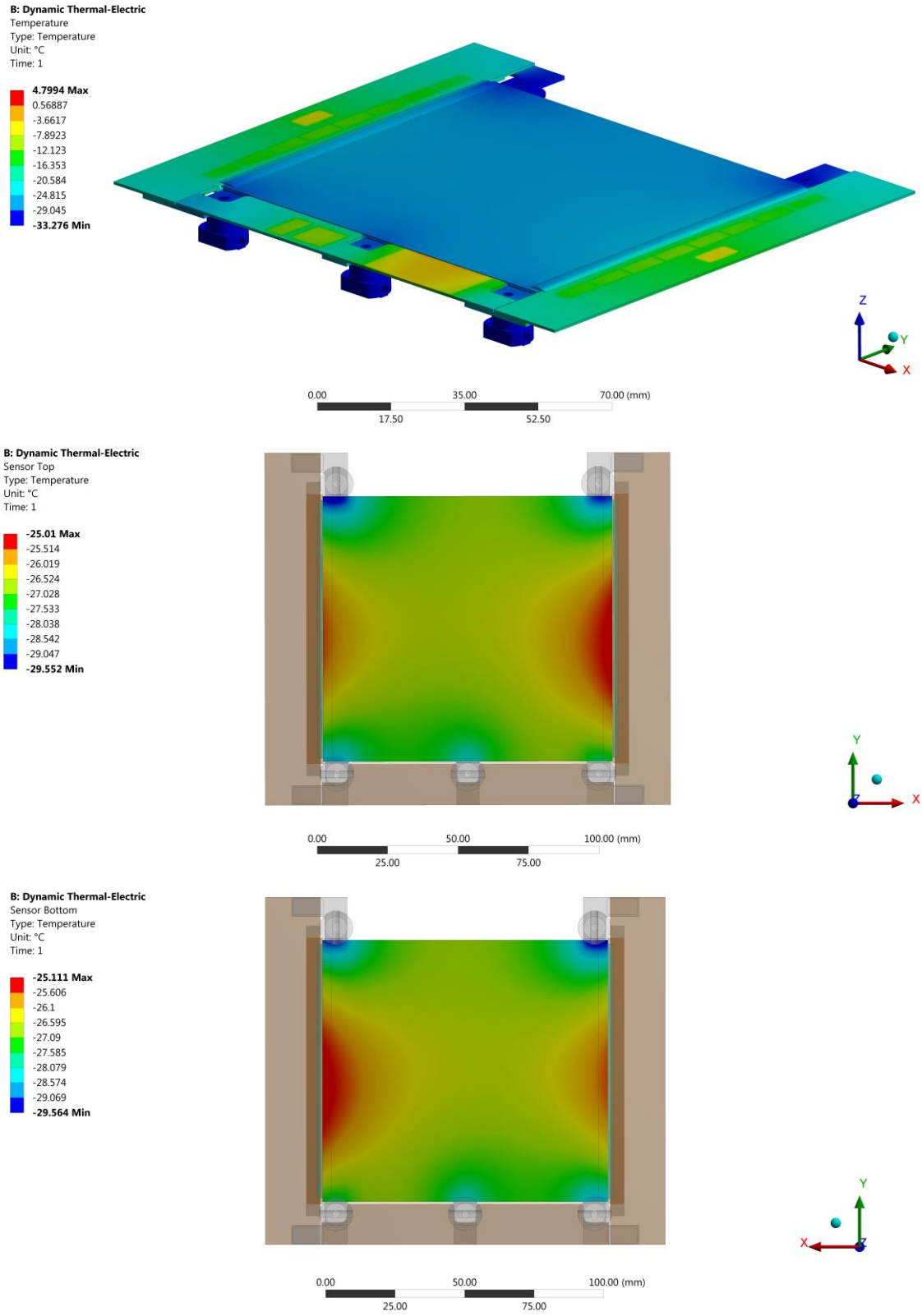

Appendix Figure 1: Temperature distribution (°C) on the total structure of the 2S 1.8mm Module and on the sensors, using laminates with stacking sequence 0/90/0/90/0 and carbon fiber Mitsubishi K13C2U.

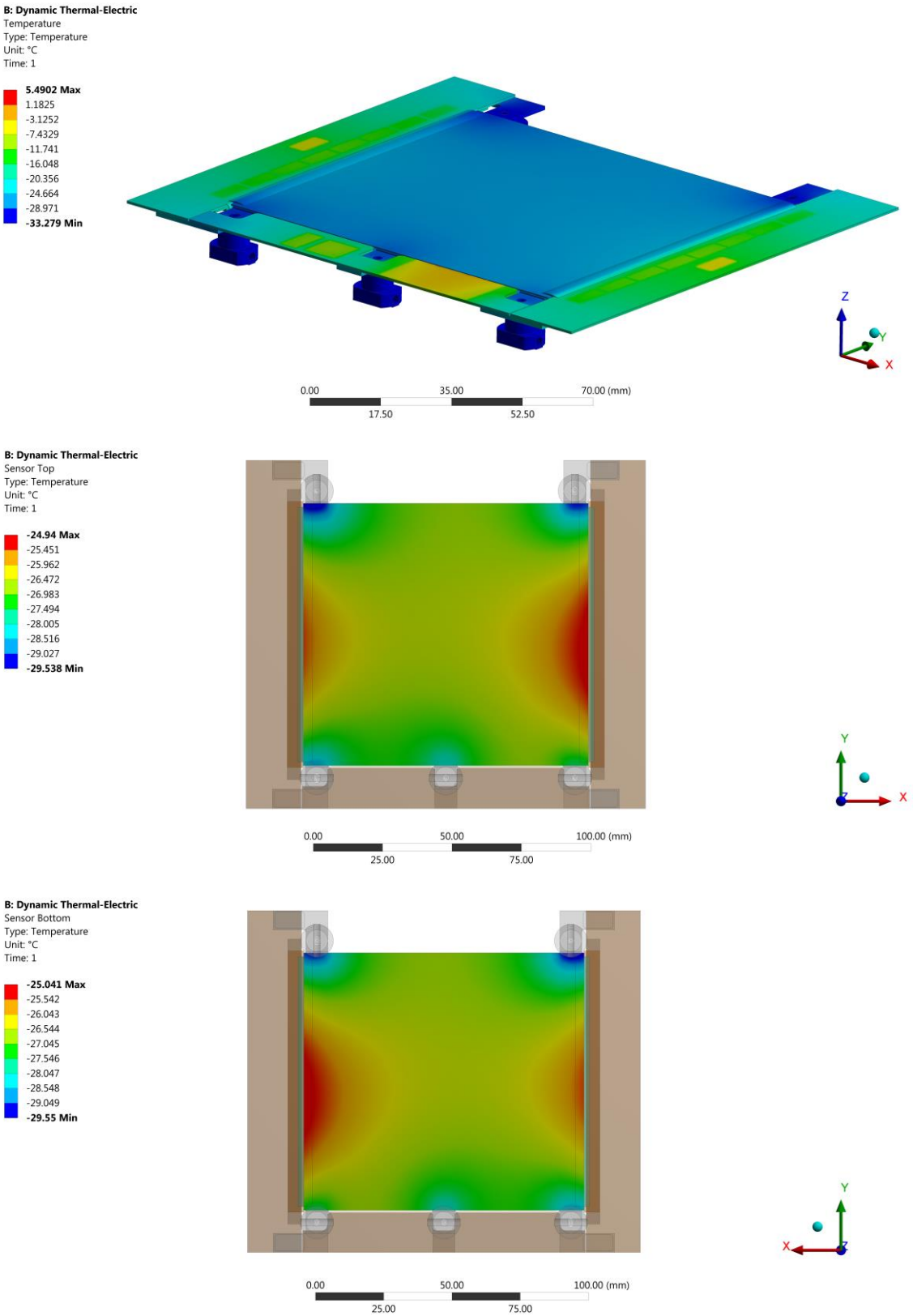

Appendix Figure 2: Temperature distribution (°C) on the total structure of the 2S 1.8mm Module and on the sensors, using laminates with stacking sequence 0/90/0/90/0 and carbon fiber Mitsubishi K13C6U.

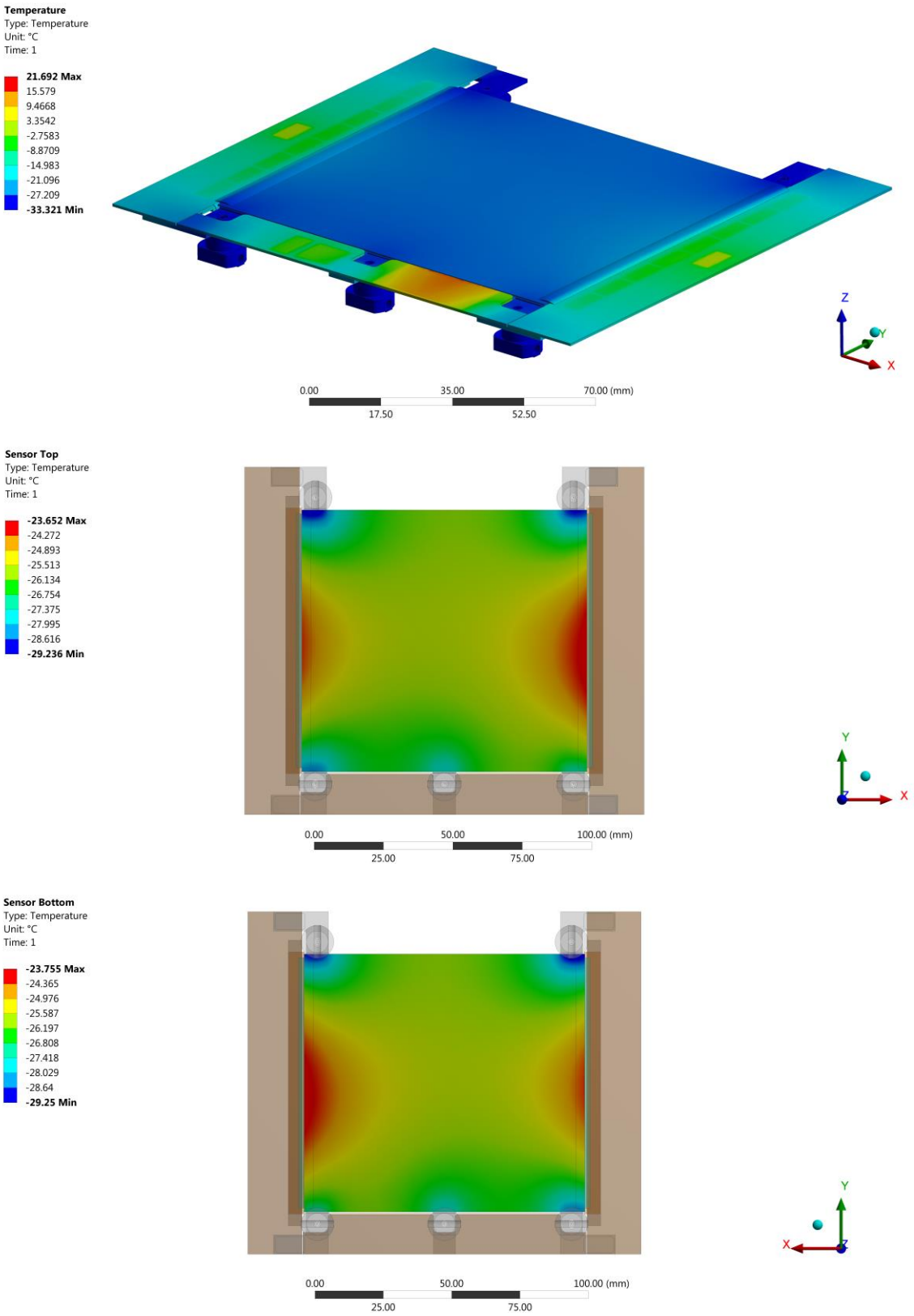

Appendix Figure 3: Temperature distribution (°C) on the total structure of the 2S 1.8mm Module and on the sensors, using laminates with stacking sequence 0/90/0/90/0 and carbon fiber Mitsubishi K63A12.

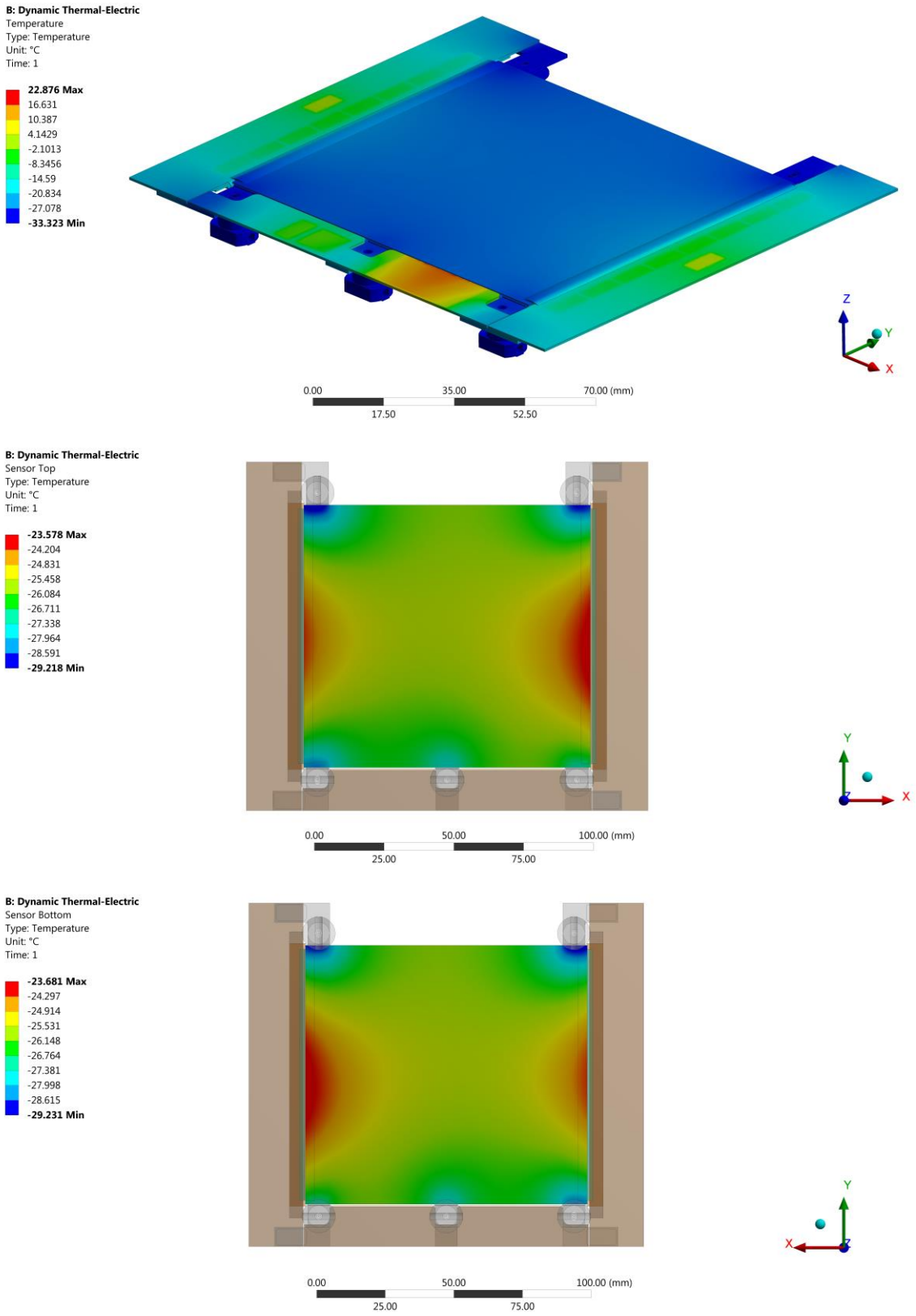

Appendix Figure 4: Temperature distribution (°C) on the total structure of the 2S 1.8mm Module and on the sensors, using laminates with stacking sequence 0/90/0/90/0 and carbon fiber Mitsubishi 1392U.

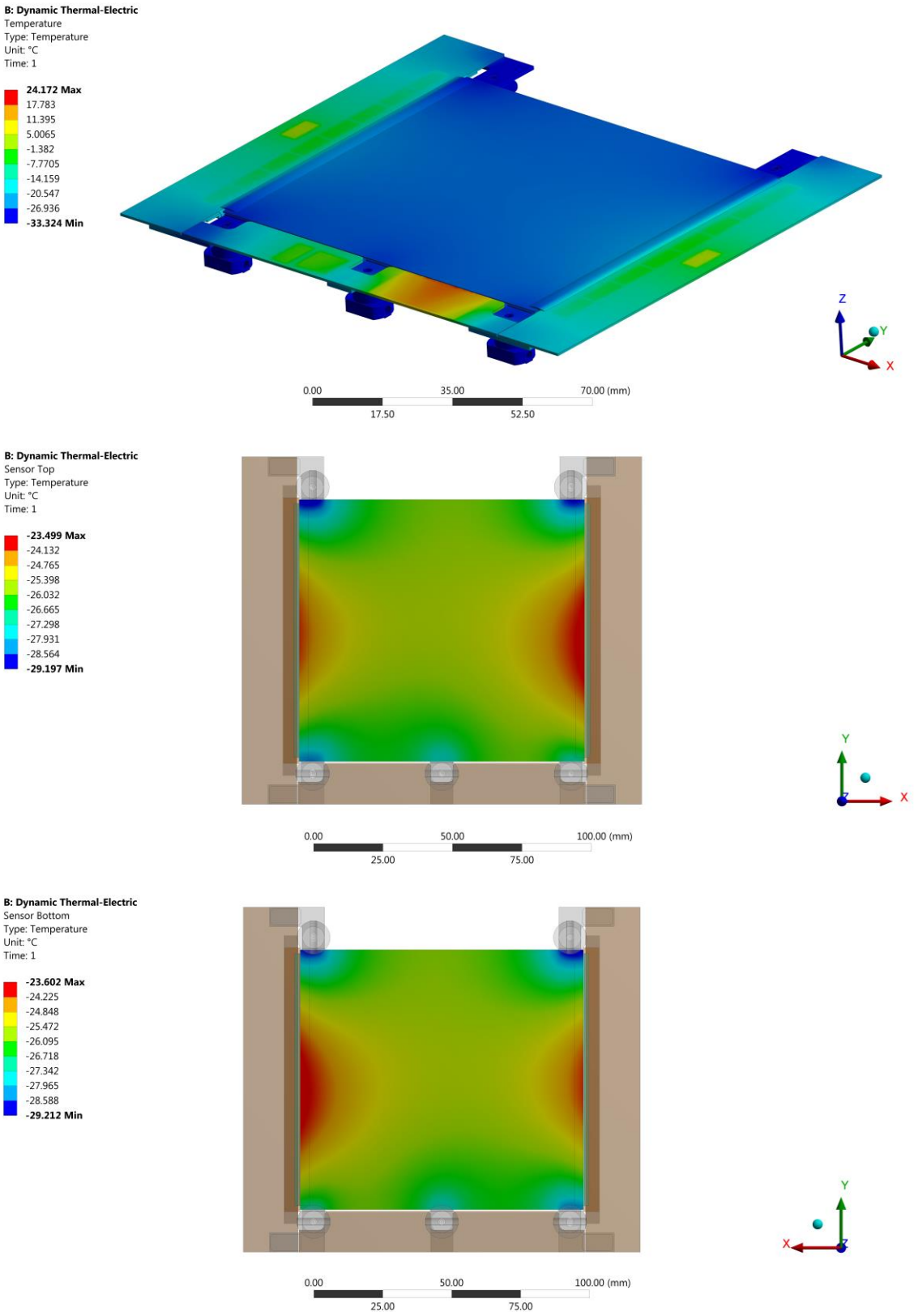

Appendix Figure 5: Temperature distribution (ºC) on the total structure of the 2S 1.8mm Module and on the sensors, using laminates with stacking sequence 0/90/0/90/0 and carbon fiber Mitsubishi 13916.

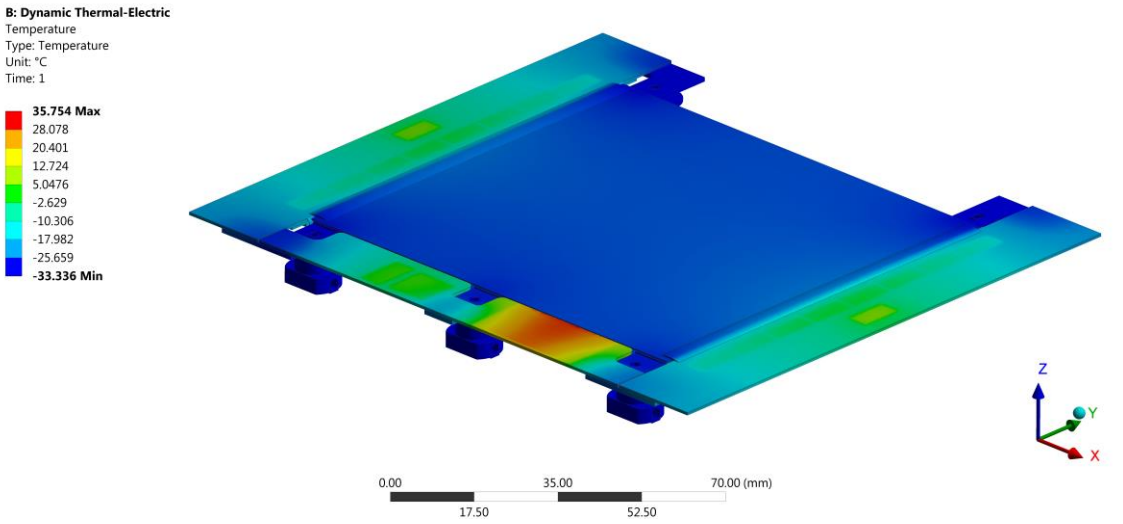

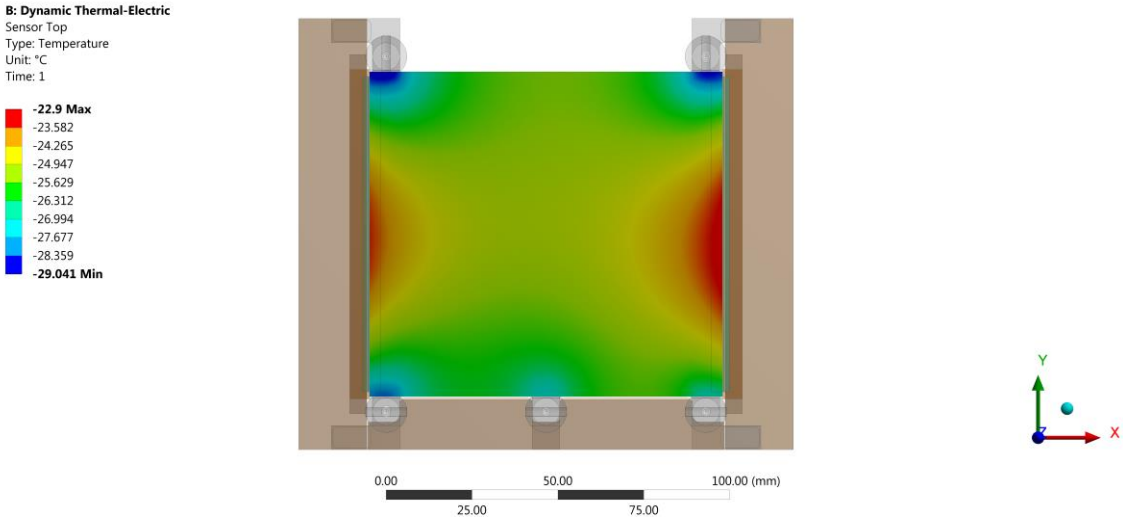

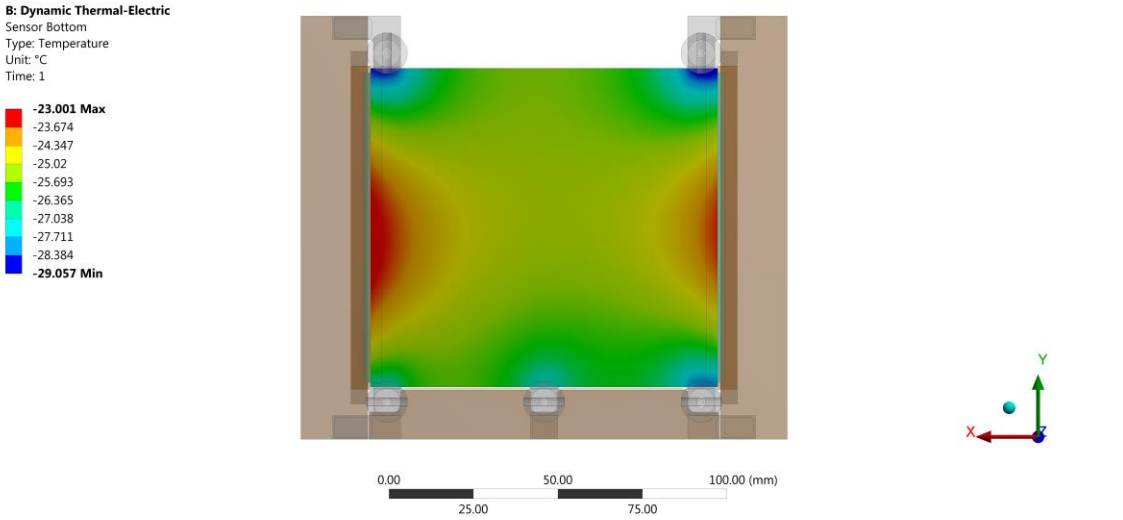

Appendix Figure 6: Temperature distribution (°C) on the total structure of the 2S 1.8mm Module and on the sensors, using laminates with stacking sequence 0/90/0/90/0 and carbon fiber Mitsubishi K63712 / K1352U.

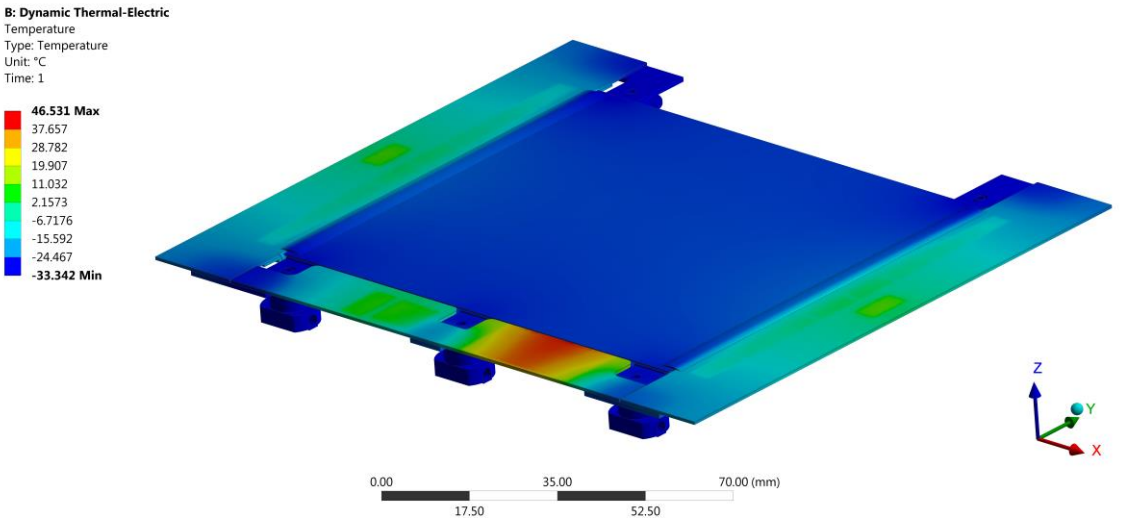

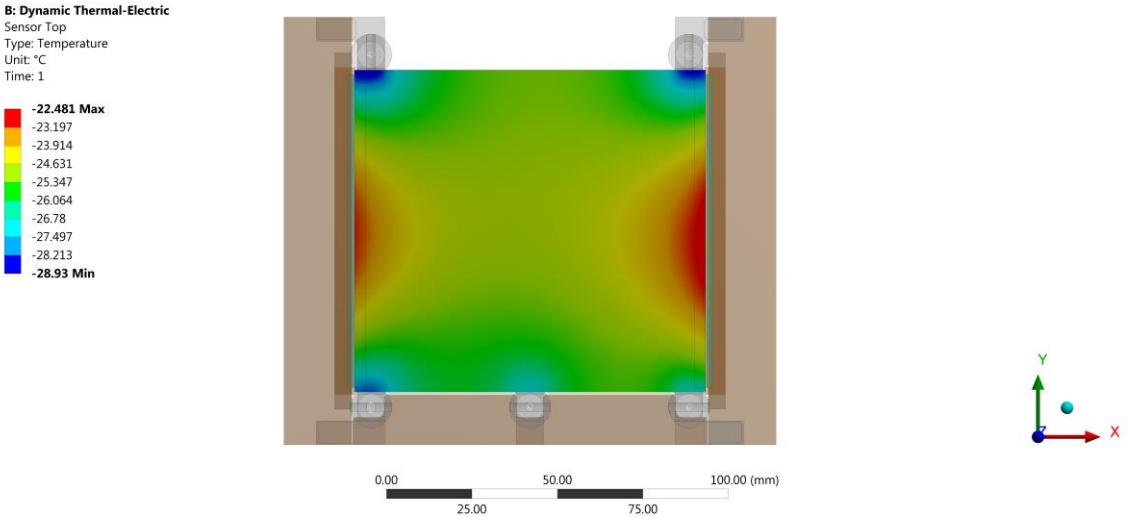

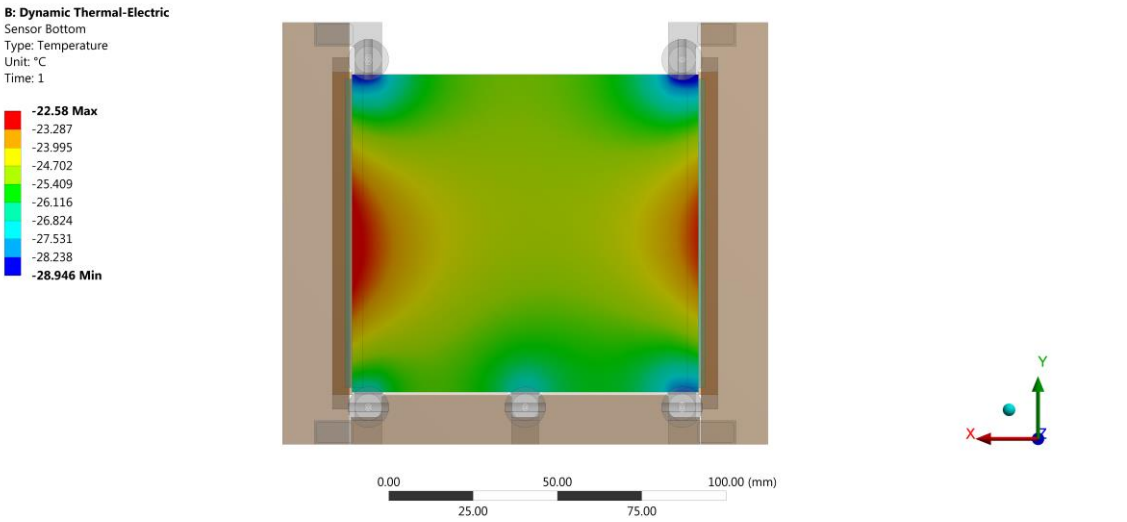

Appendix Figure 7: Temperature distribution (oC) on the total structure of the 2S 1.8mm Module and on the sensors, using laminates with stacking sequence 0/90/0/90/0 and carbon fiber Mitsubishi K13312.

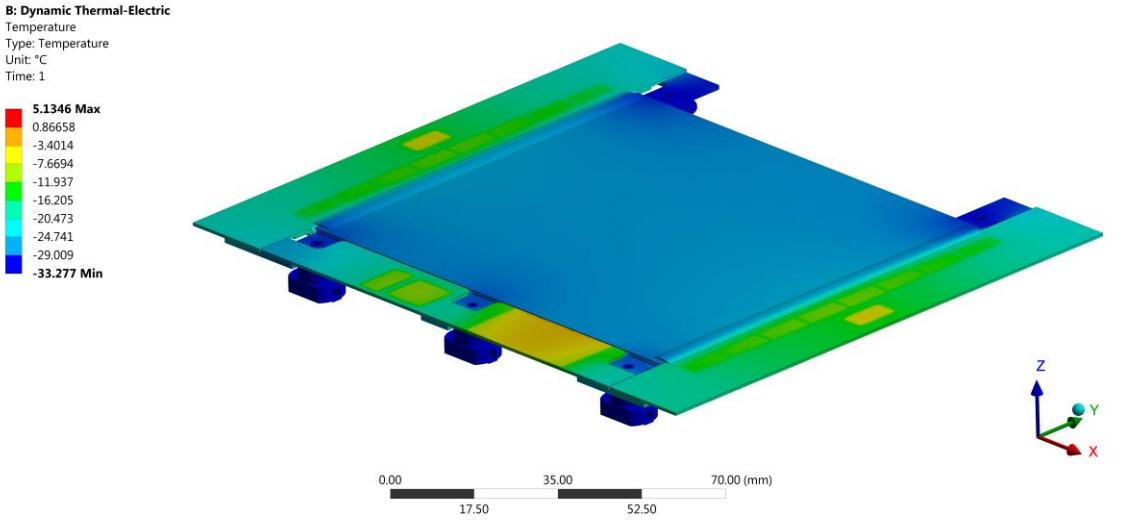

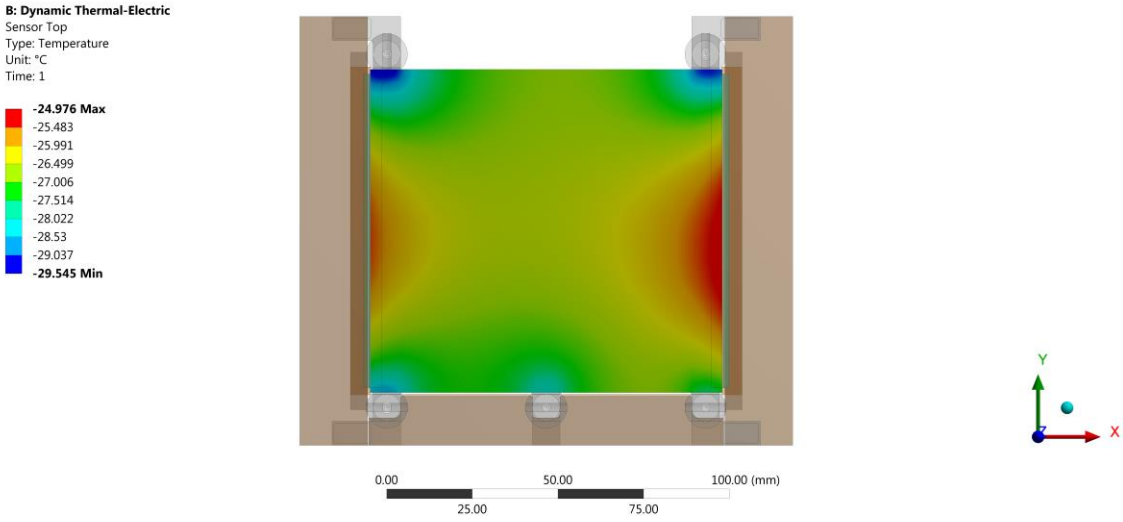

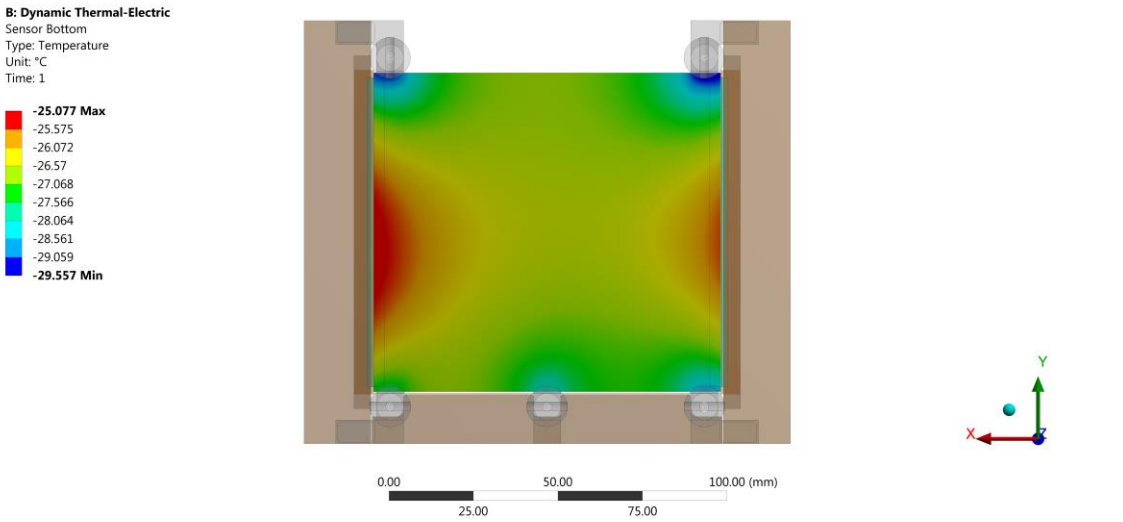

Appendix Figure 8: Temperature distribution (°C) on the total structure of the 2S 1.8mm Module and on the sensors, using laminates with stacking sequence 0/90/0/90/0 and carbon fiber Nippon YS 95A.

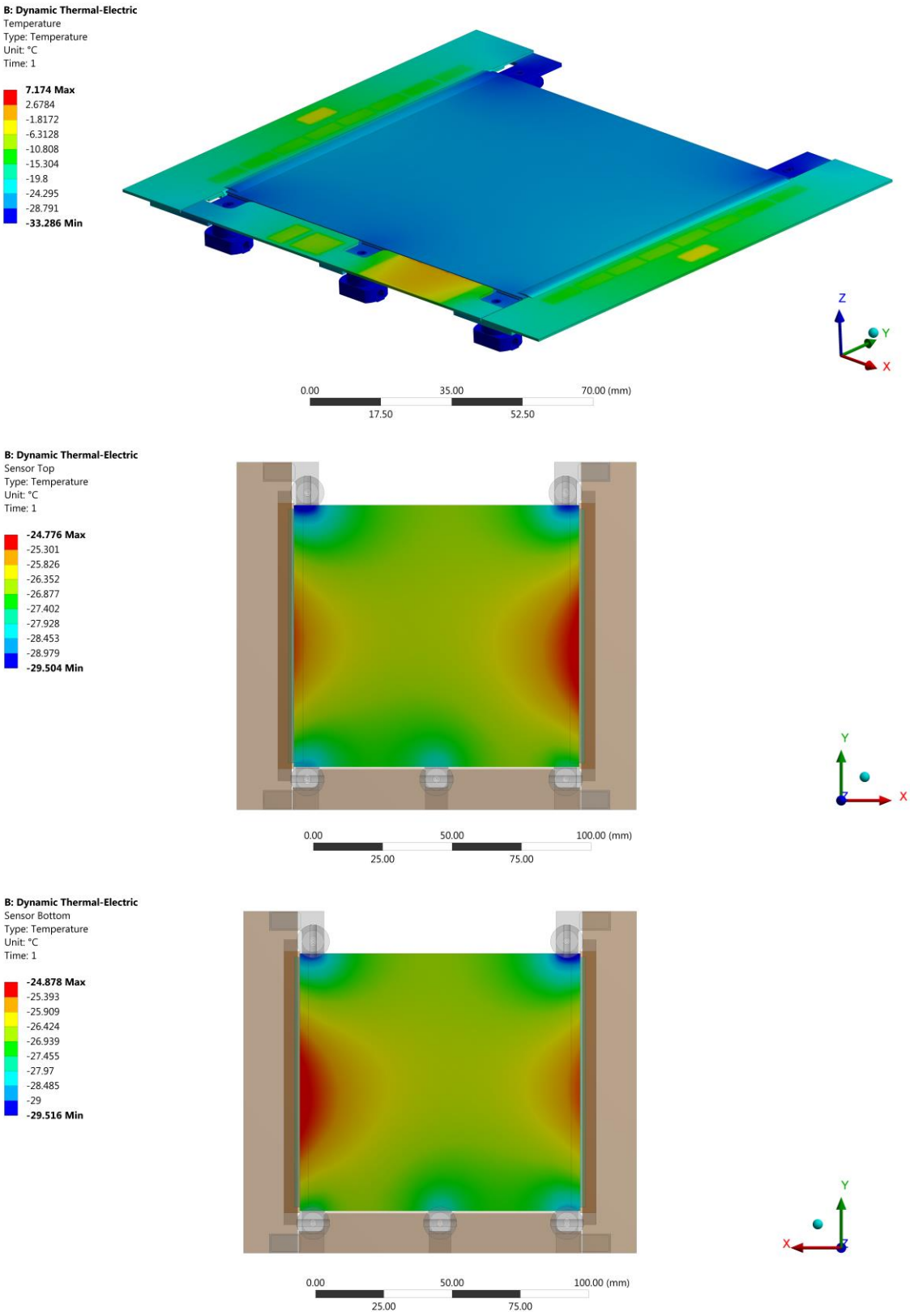

Appendix Figure 9: Temperature distribution (°C) on the total structure of the 2S 1.8mm Module and on the sensors, using laminates with stacking sequence 0/90/0/90/0 and carbon fiber Nippon XN 90/ YS 90A.

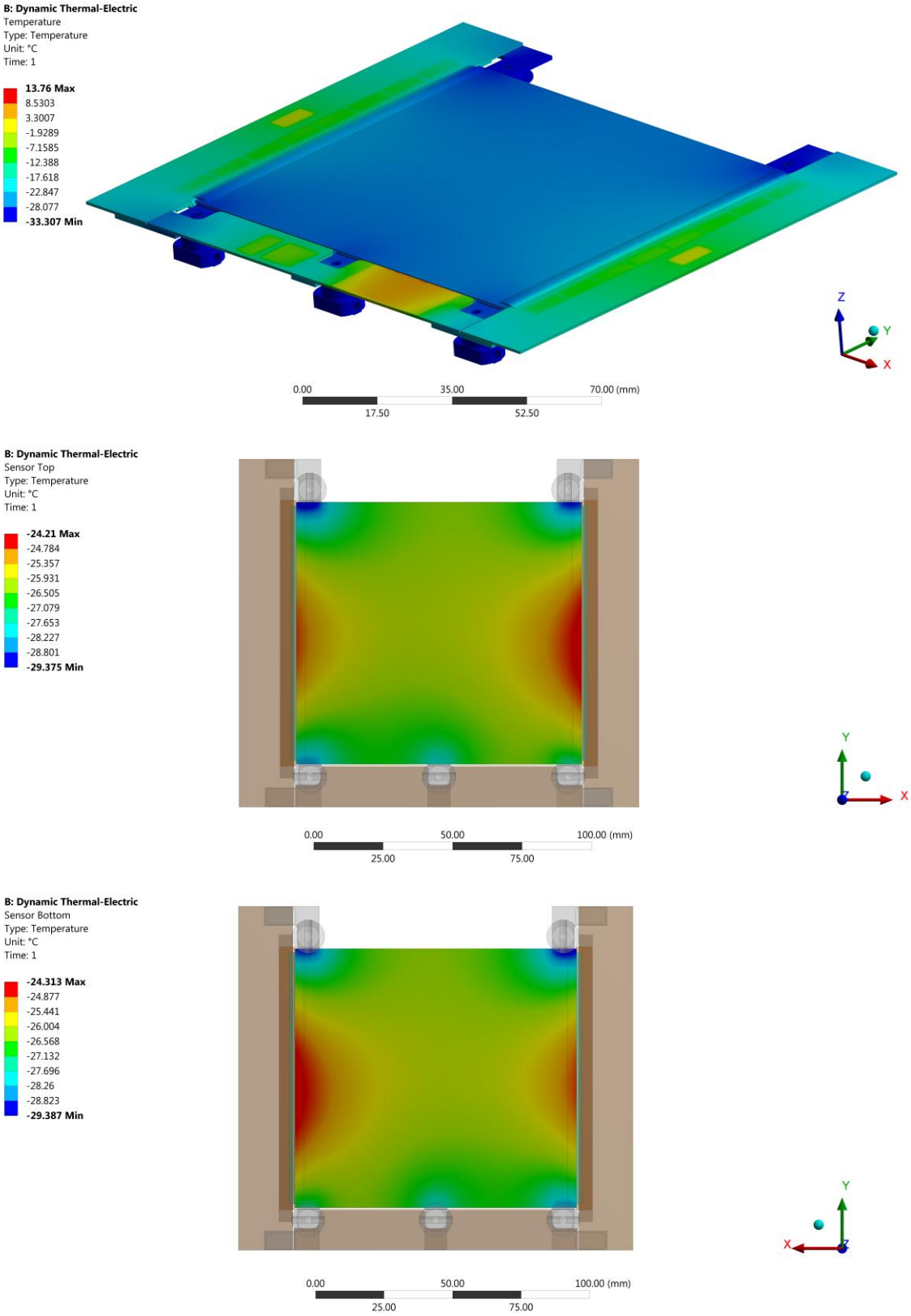

Appendix Figure 10: Temperature distribution (°C) on the total structure of the 2S 1.8mm Module and on the sensors, using laminates with stacking sequence 0/90/0/90/0 and carbon fiber Nippon XN 80/ YS 80A.

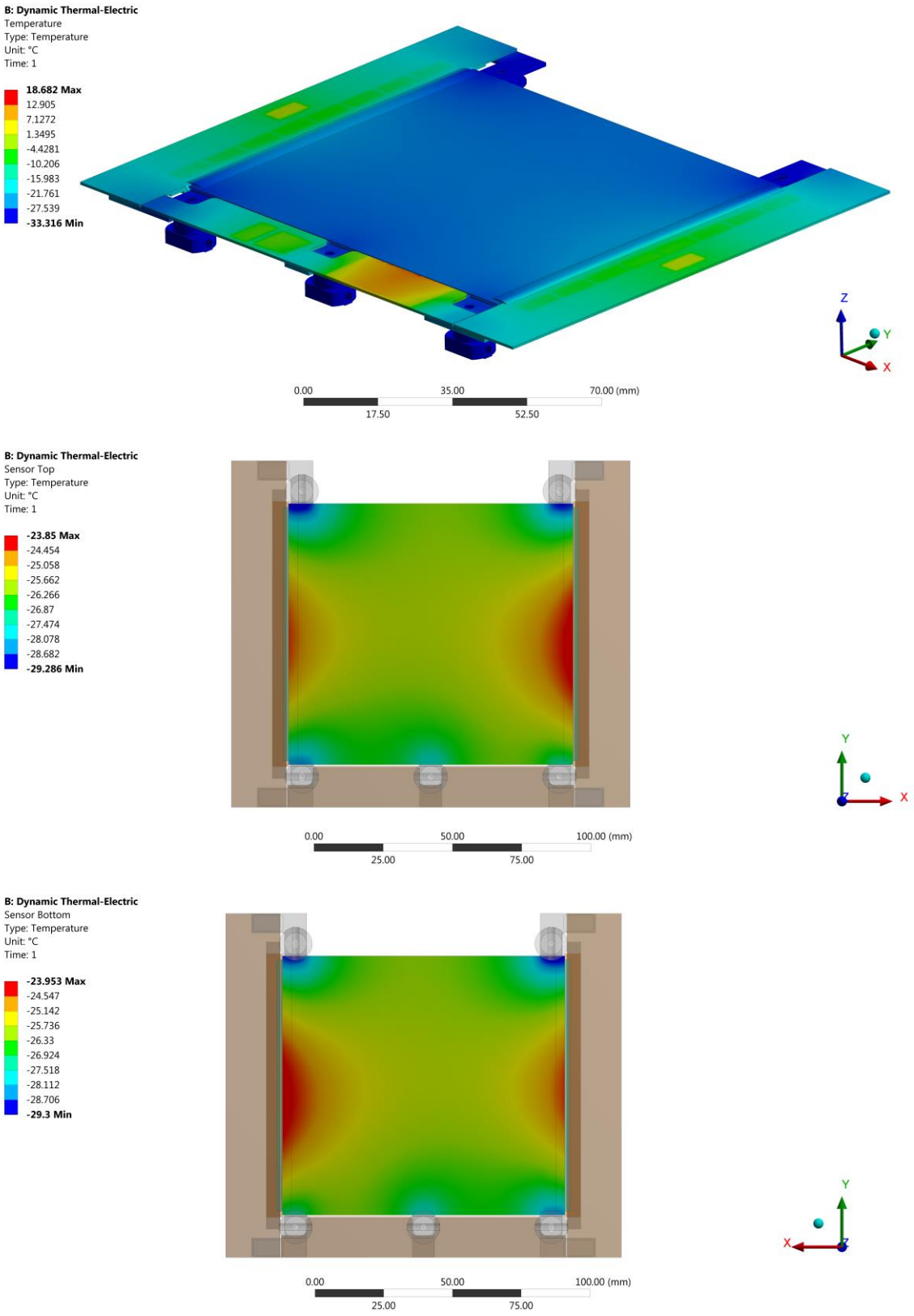

Appendix Figure 11: Temperature distribution (°C) on the total structure of the 2S 1.8mm Module and on the sensors, using laminates with stacking sequence 0/90/0/90/0 and carbon fiber Nippon YSH 70A.

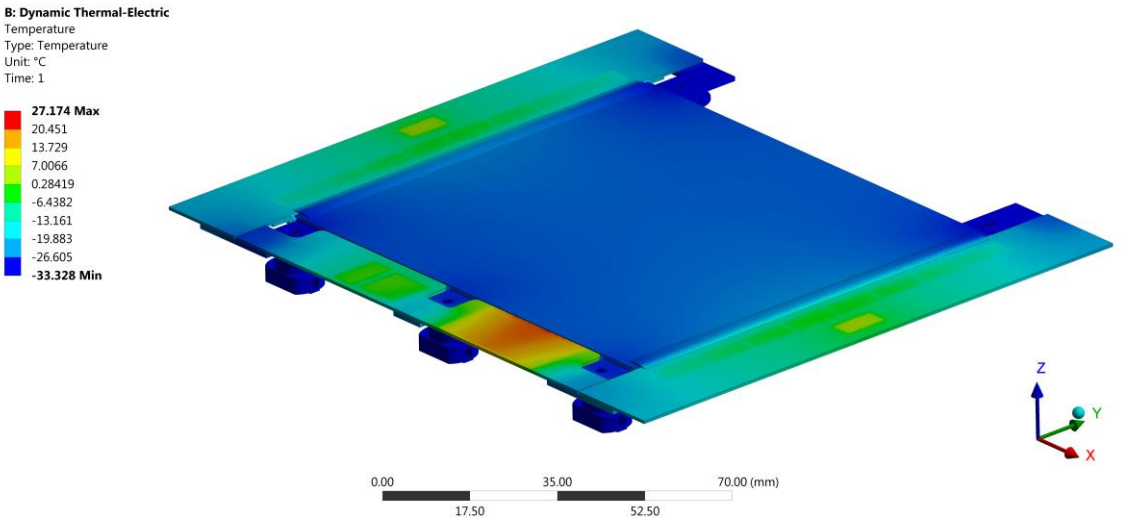

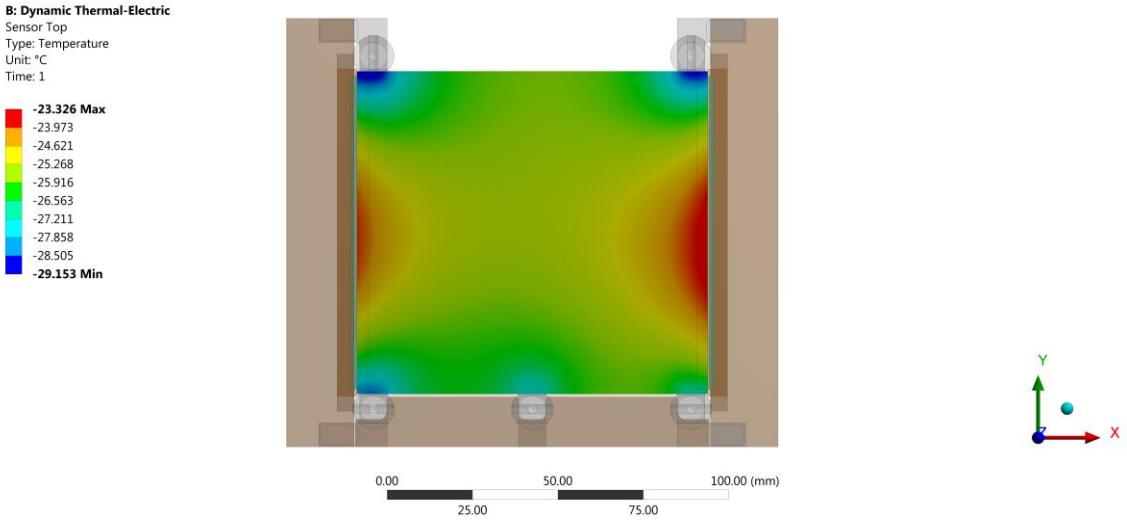

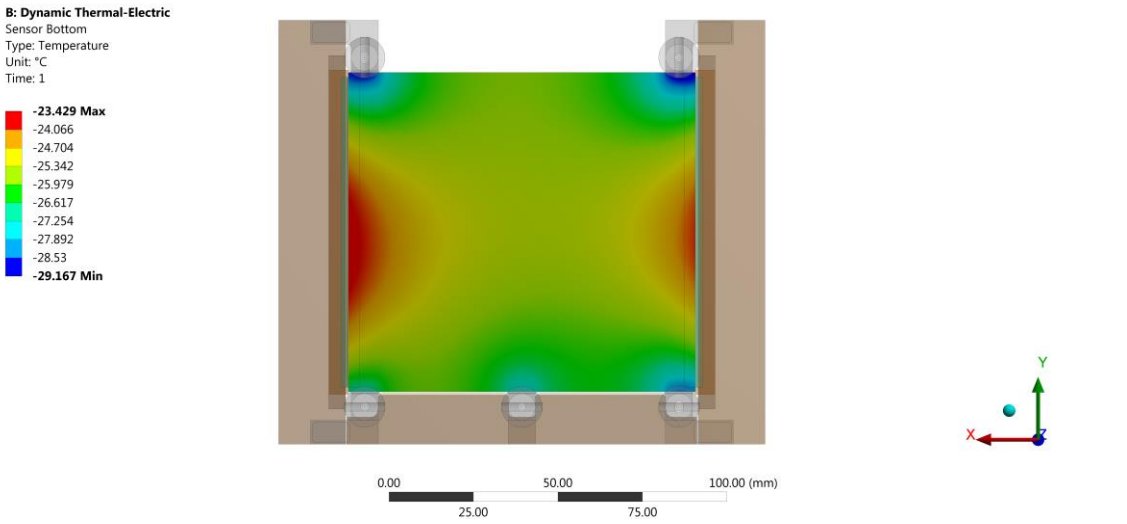

Appendix Figure 12: Temperature distribution (ºC) on the total structure of the 2S 1.8mm Module and on the sensors, using laminates with stacking sequence 0/90/0/90/0 and carbon fiber Nippon XN 60/ YSH 60A.

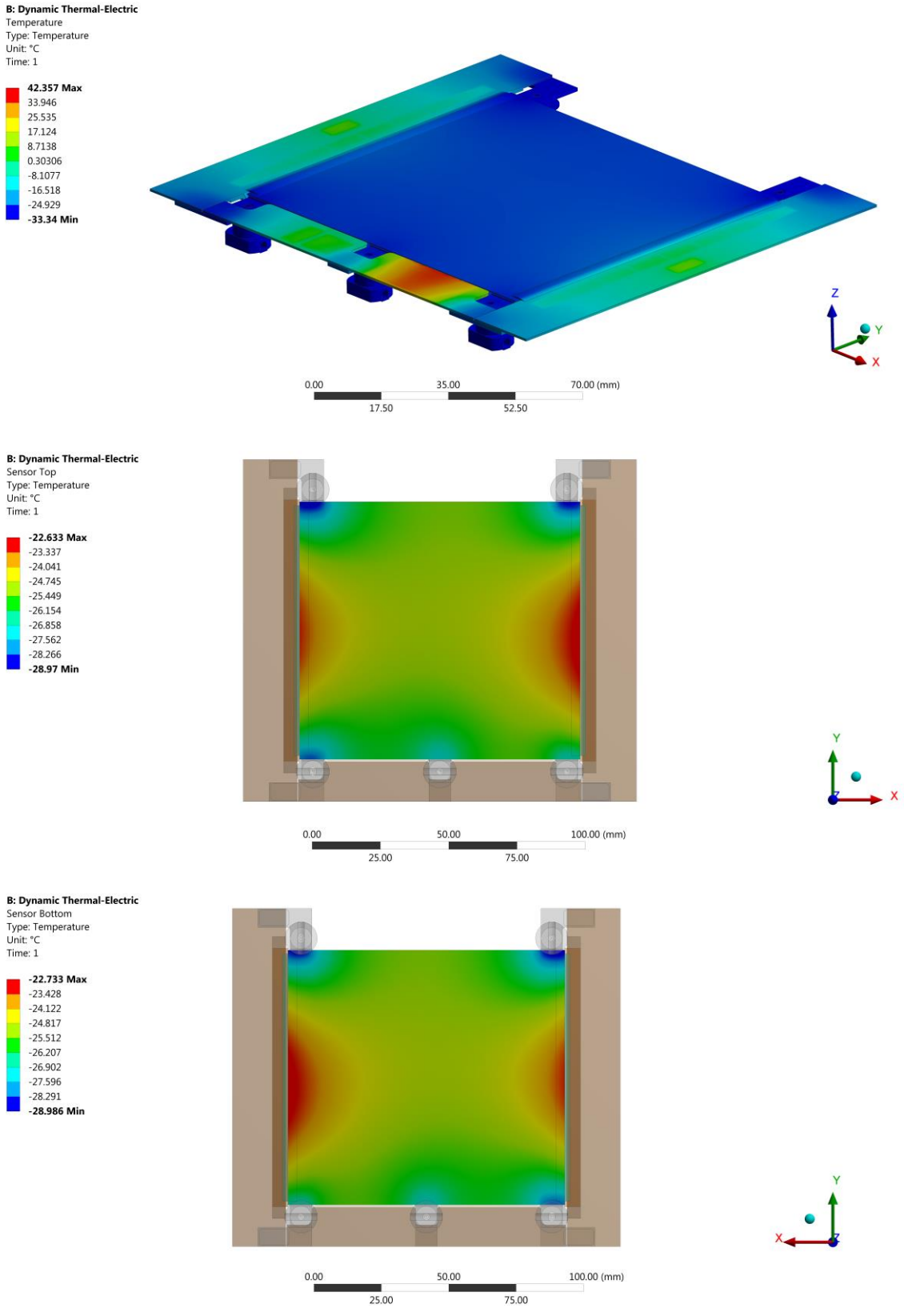

Appendix Figure 13: Temperature distribution (°C) on the total structure of the 2S 1.8mm Module and on the sensors, using laminates with stacking sequence 0/90/0/90/0 and carbon fiber Nippon YSH 50A.

CASE STUDY WITH $[0/90]_s$ LAMINATES

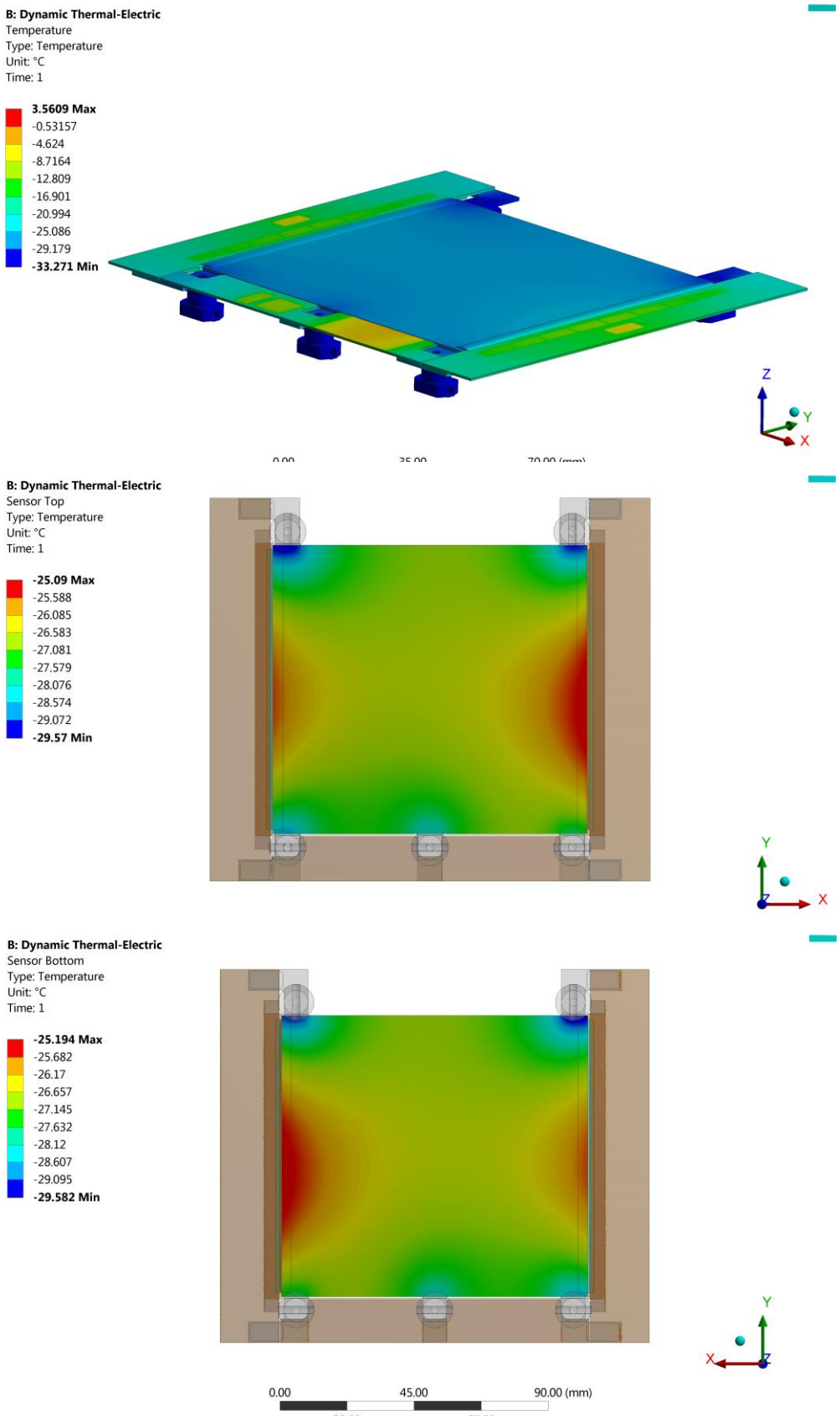

Appendix Figure 14: Temperature distribution (°C) on the total structure of the 2S 1.8mm Module and on the sensors, using laminates with stacking sequence [0,90]s and carbon fiber Mitsubishi K13D2U.

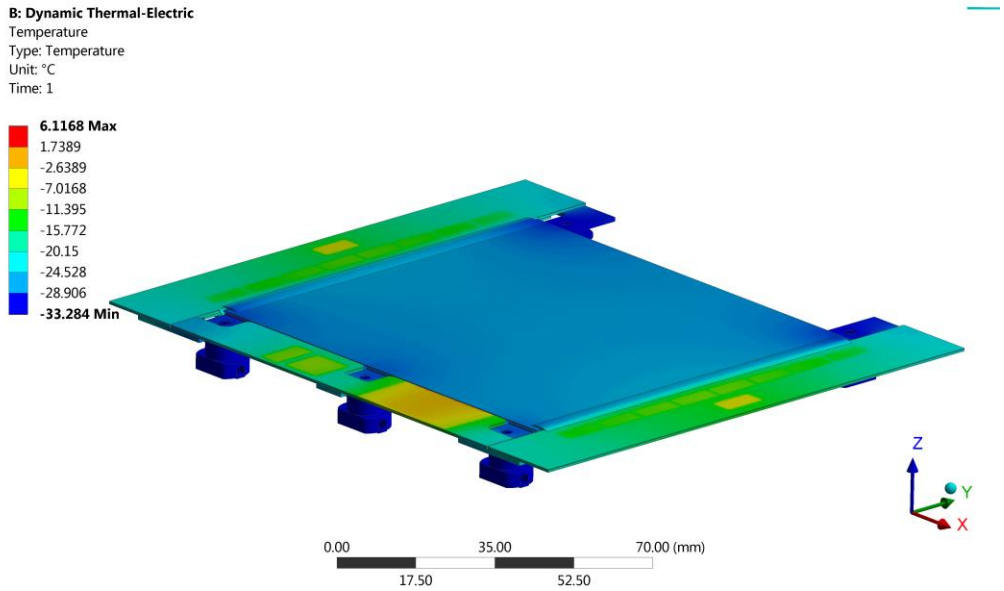

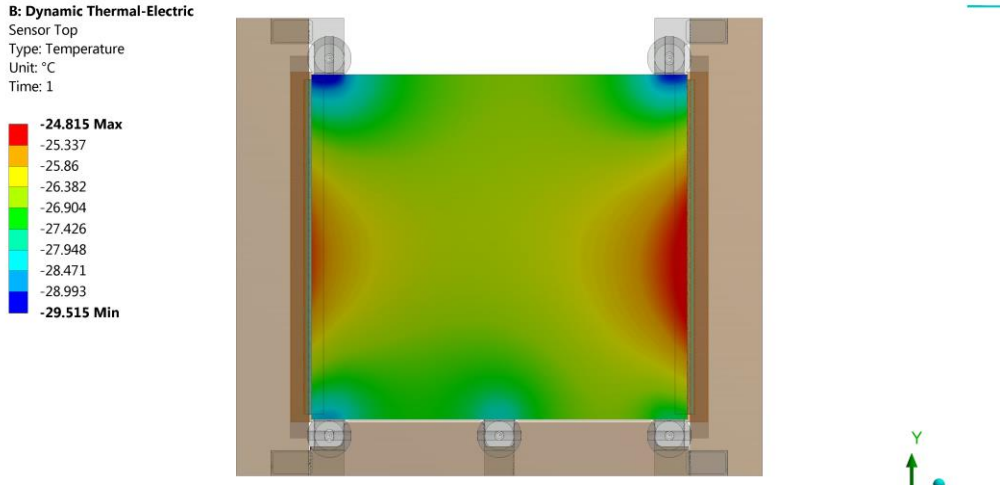

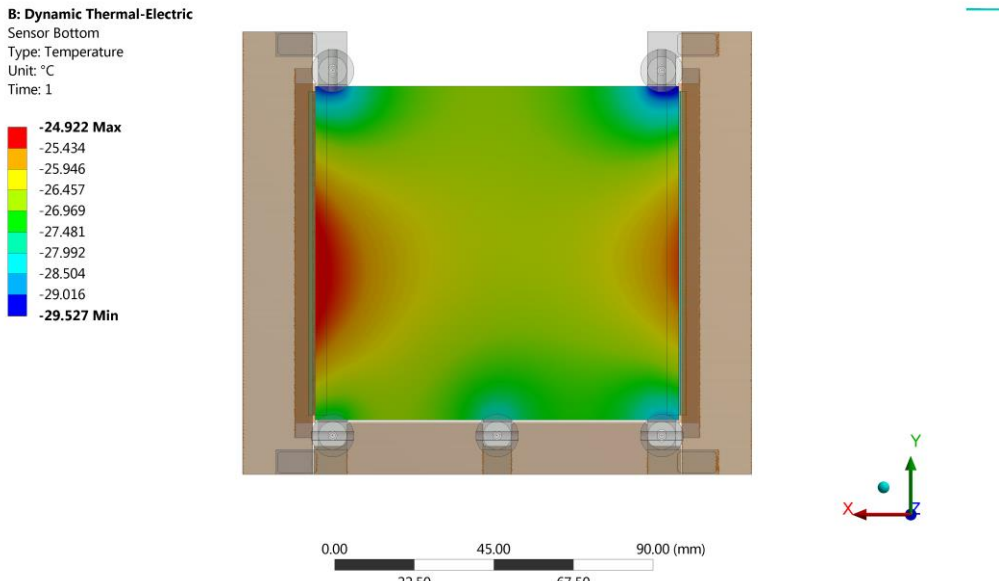

Appendix Figure 15: Temperature distribution (ºC) on the total structure of the 2S 1.8mm Module and on the sensors, using laminates with stacking sequence [0,90]s and carbon fiber Mitsubishi K13C2U.

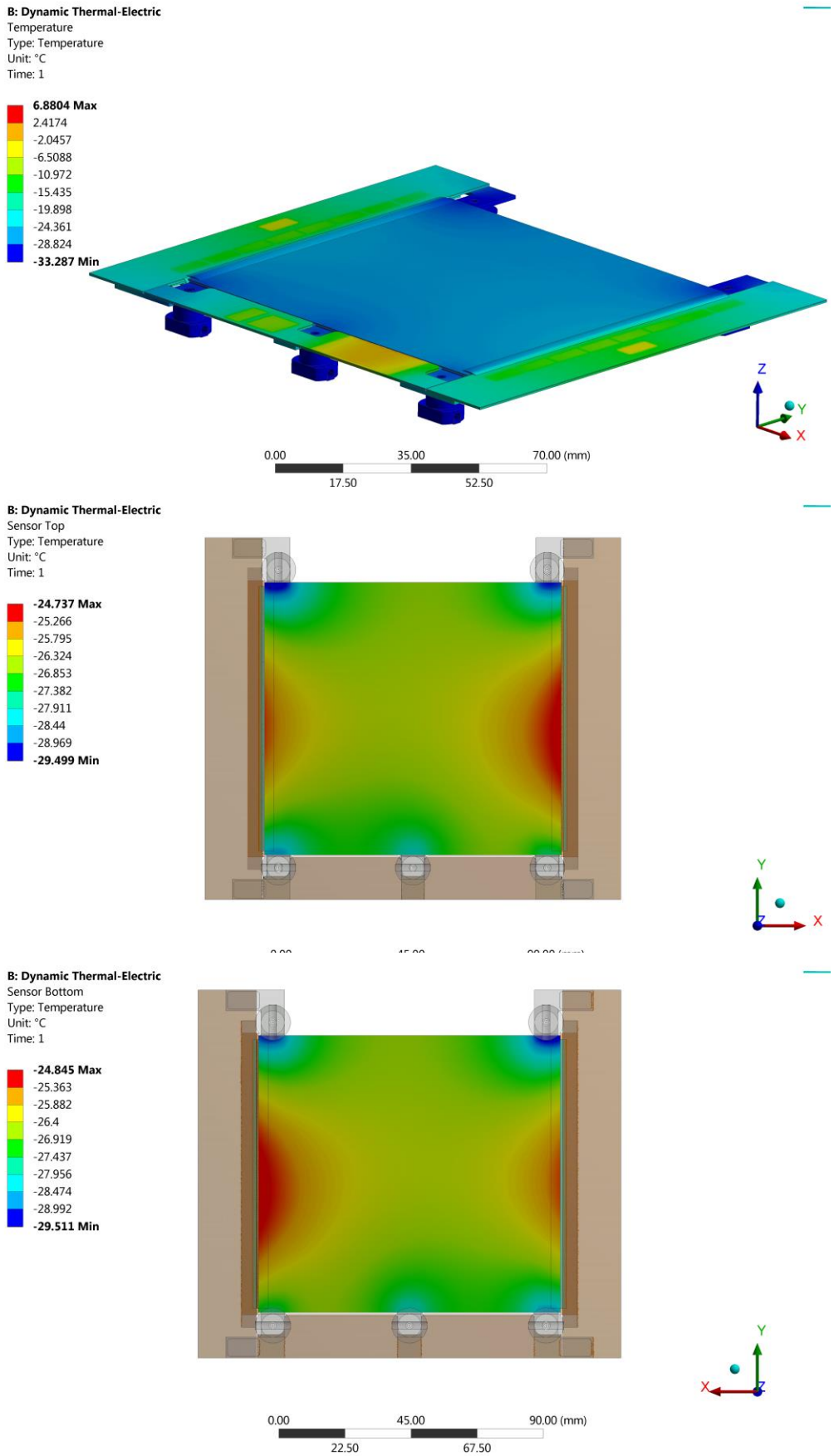

Appendix Figure 16: Temperature distribution (ºC) on the total structure of the 2S 1.8mm Module and on the sen-sors, using laminates with stacking sequence [0,90]s and carbon fiber Mitsubishi K13C6U.

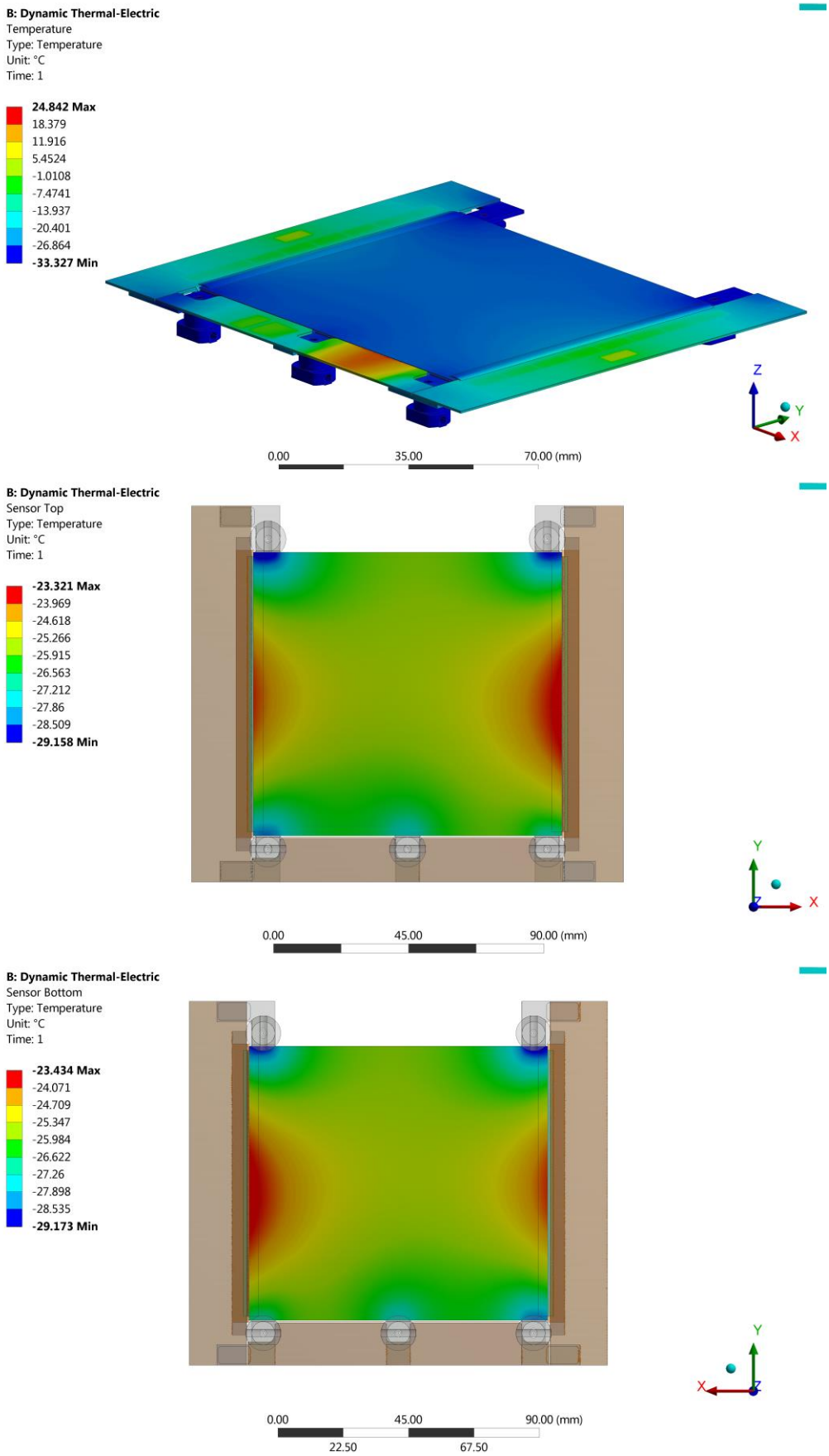

Appendix Figure 17: Temperature distribution (oC) on the total structure of the 2S 1.8mm Module and on the sen-sors, using laminates with stacking sequence [0,90]s and carbon fiber Mitsubishi K63A12.

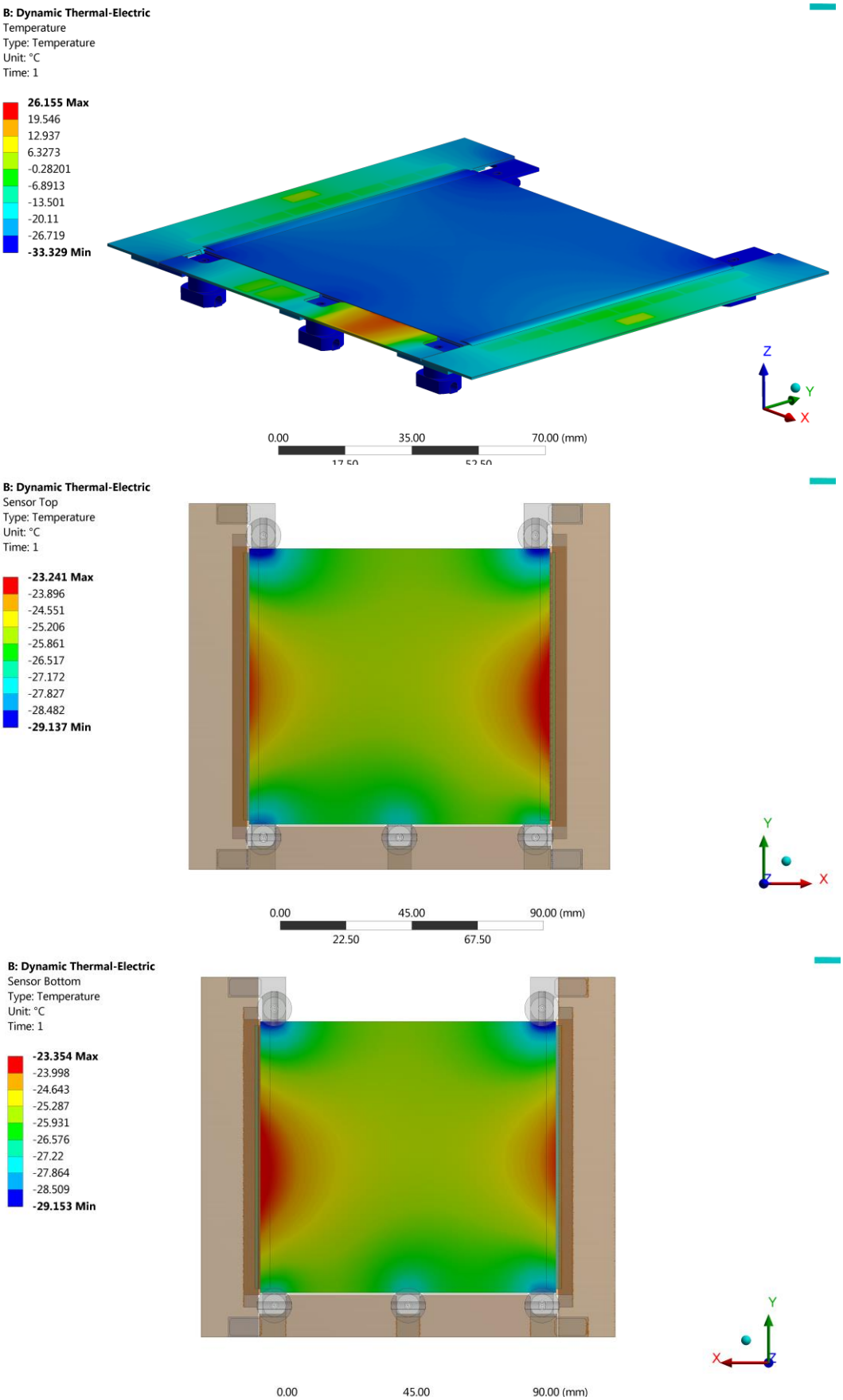

Appendix Figure 18: Temperature distribution (oC) on the total structure of the 2S 1.8mm Module and on the sensors, using laminates with stacking sequence [0,90]s and carbon fiber Mitsubishi K1392U.

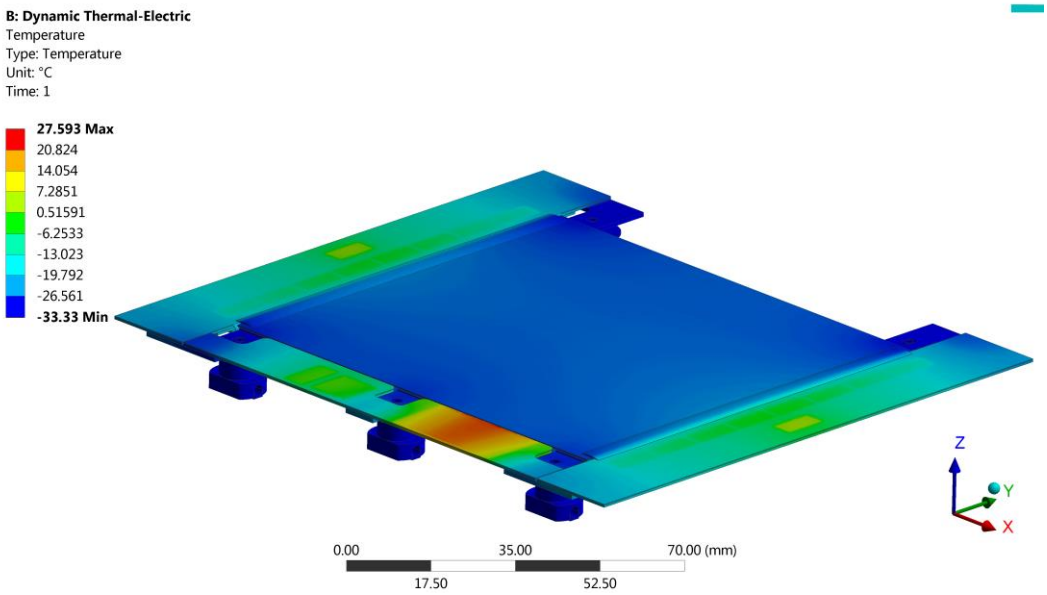

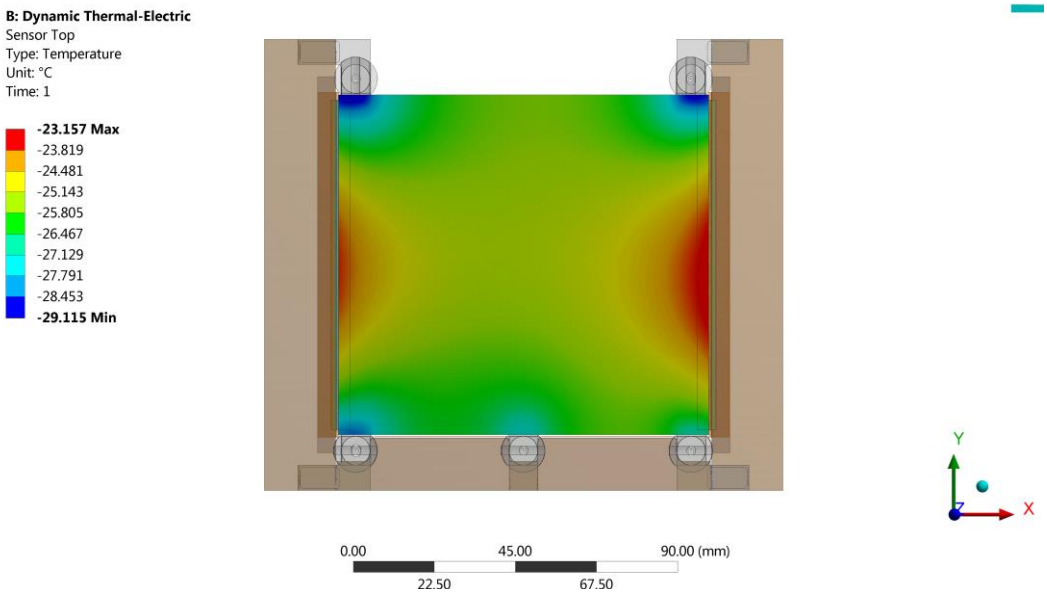

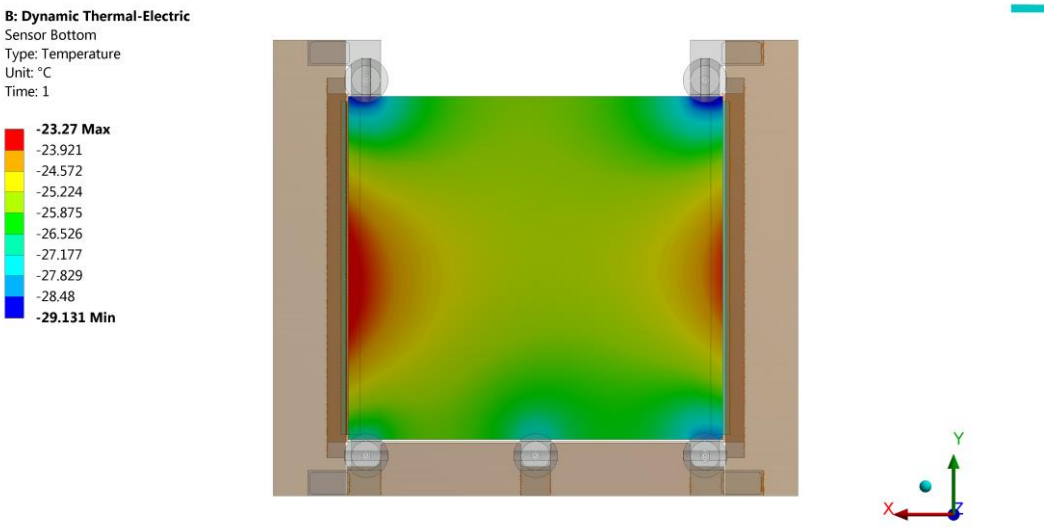

Appendix Figure 19: Temperature distribution (oC) on the total structure of the 2S 1.8mm Module and on the sensors, using laminates with stacking sequence [0,90]s and carbon fiber Mitsubishi K13916.

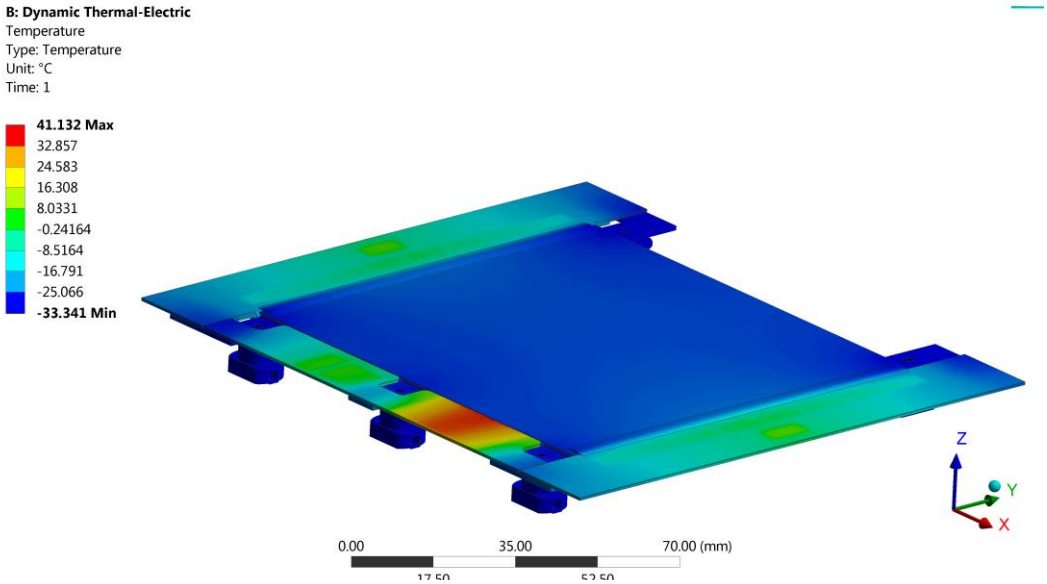

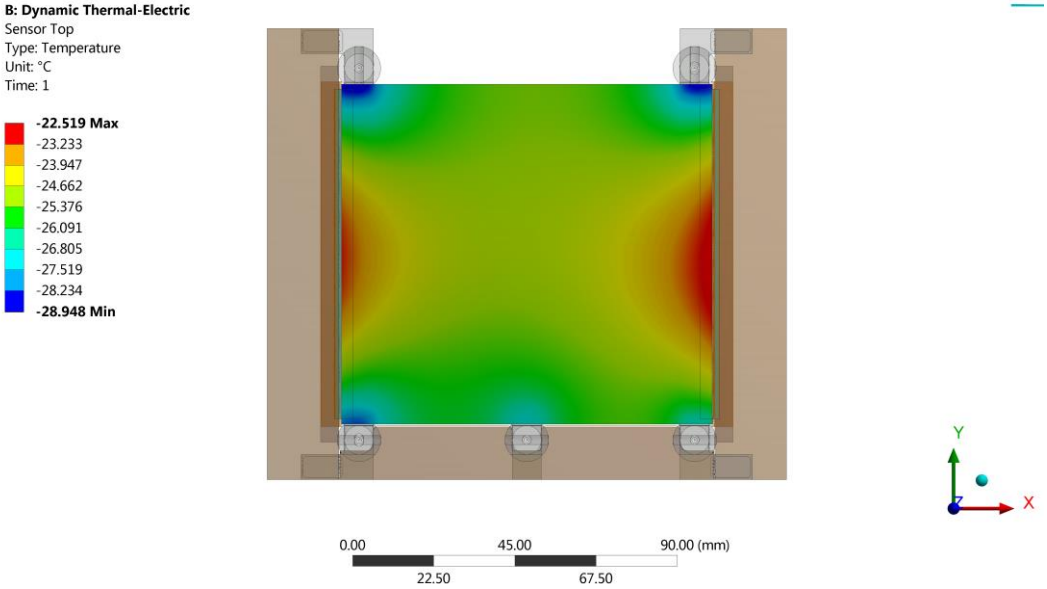

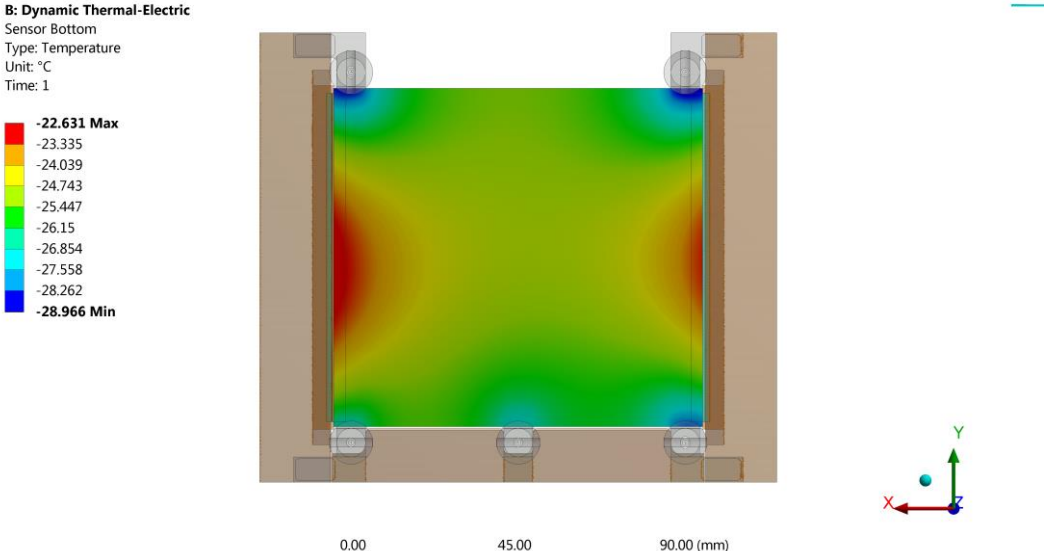

Appendix Figure 20: Temperature distribution (oC) on the total structure of the 2S 1.8mm Module and on the sensors, using laminates with stacking sequence [0,90]s and carbon fiber Mitsubishi K63712/K1352U.

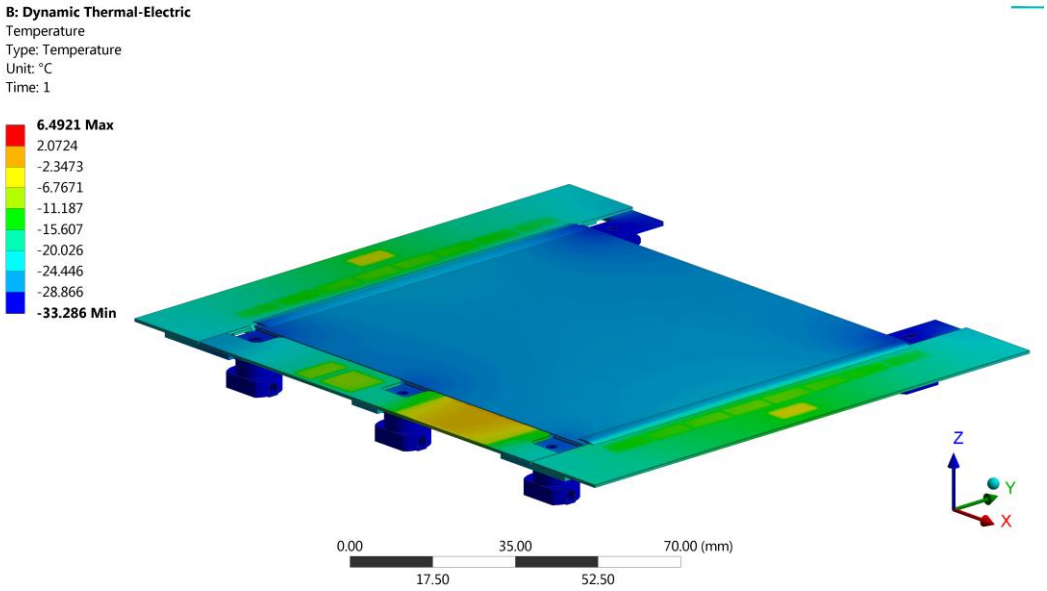

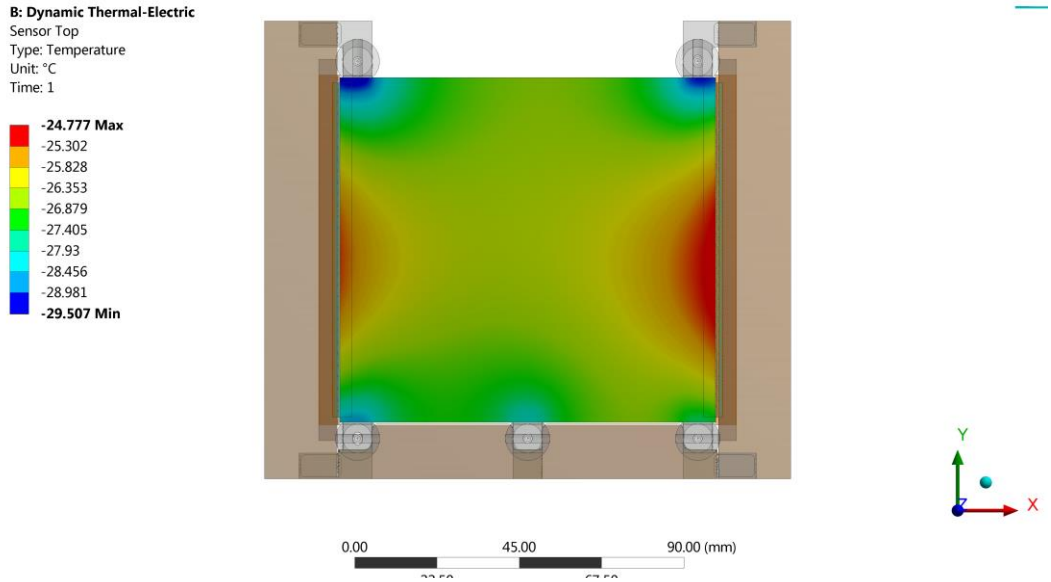

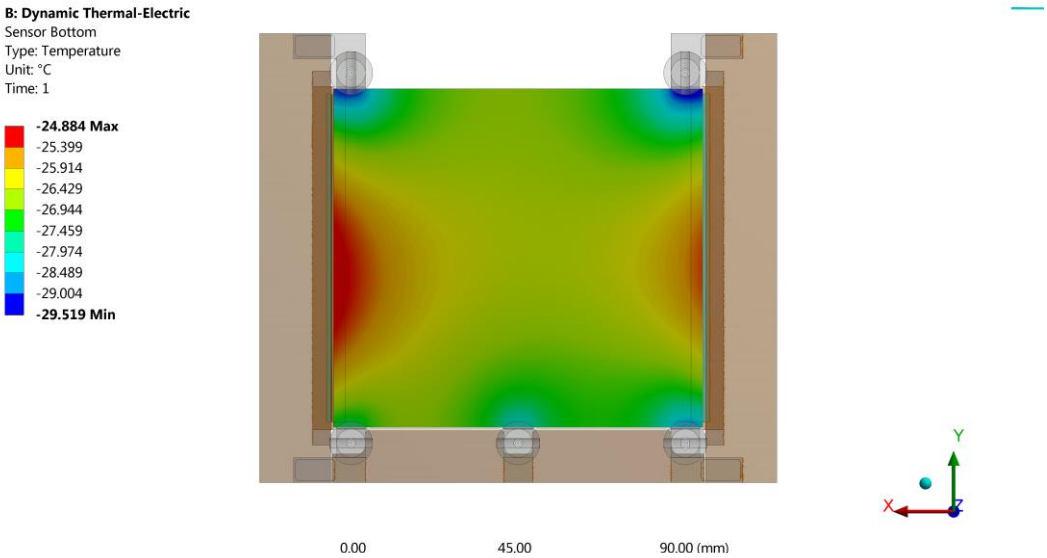

Appendix Figure 21: Temperature distribution (oC) on the total structure of the 2S 1.8mm Module and on the sensors, using laminates with stacking sequence [0,90]s and carbon fiber Nippon YS 95A.

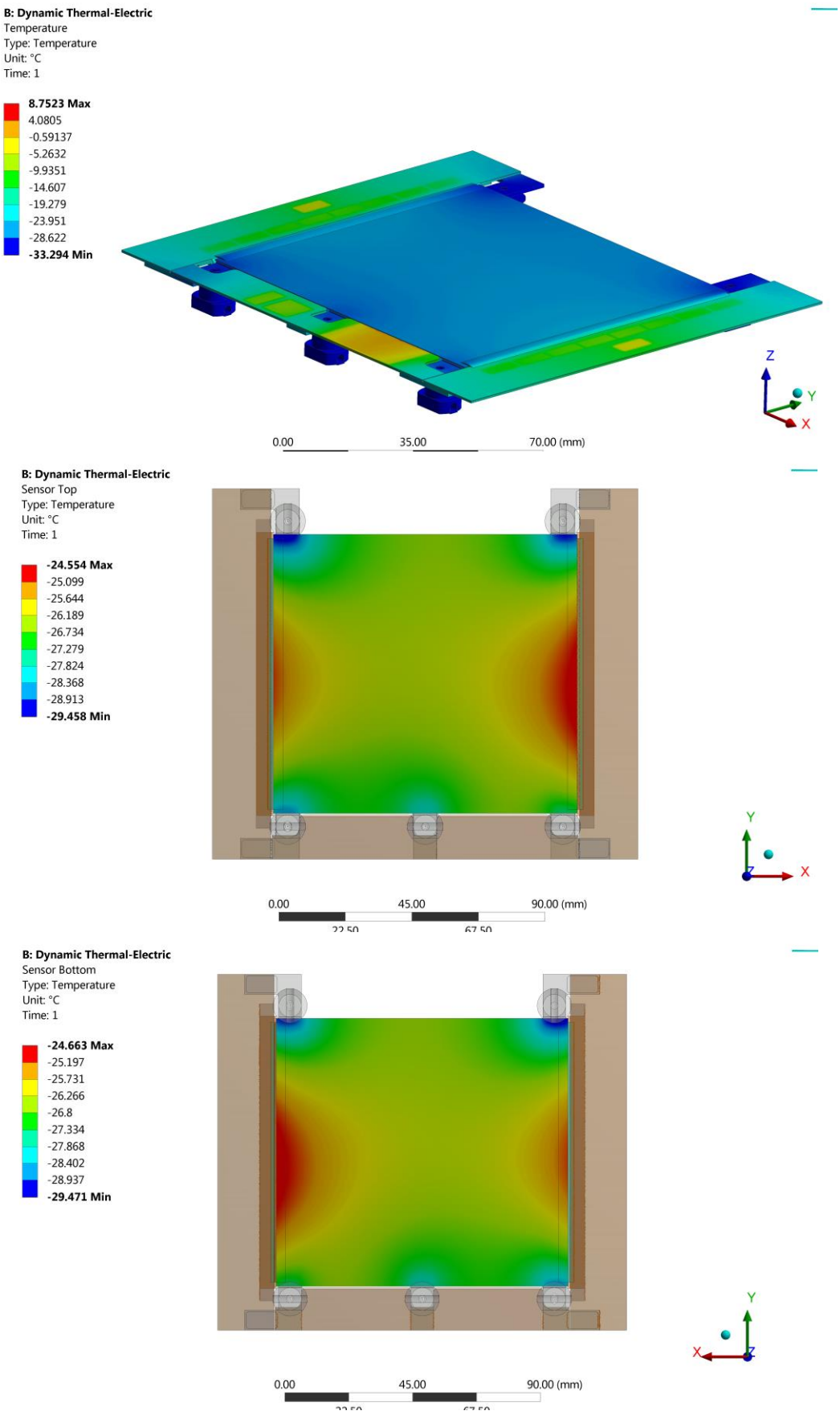

Appendix Figure 22: Temperature distribution (oC) on the total structure of the 2S 1.8mm Module and on the sensors, using laminates with stacking sequence [0,90]s and carbon fiber Nippon XN 90/ YS 90A.

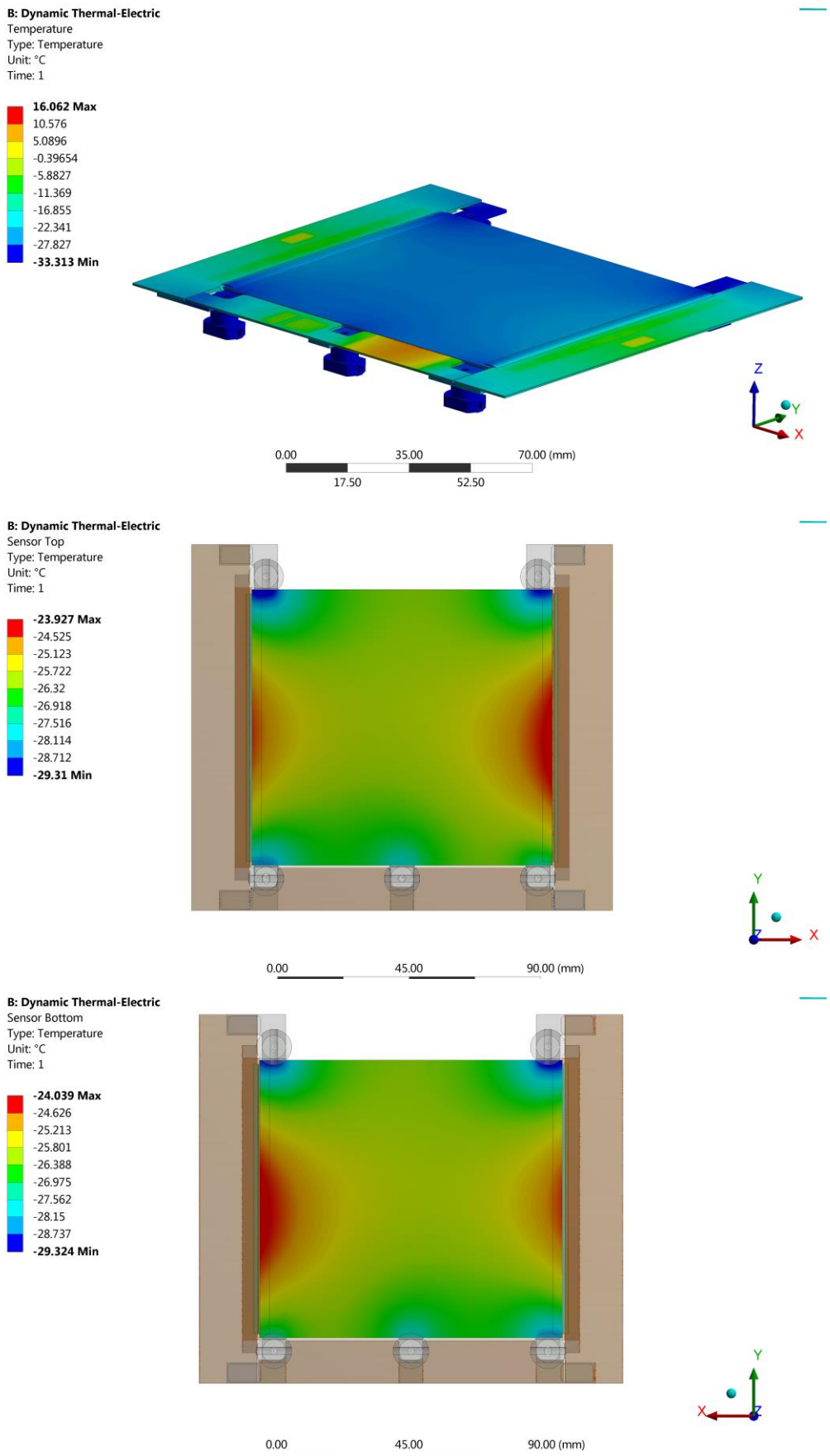

Appendix Figure 23: Temperature distribution (oC) on the total structure of the 2S 1.8mm Module and on the sensors, using laminates with stacking sequence [0,90]s and carbon fiber Nippon XN 80/ YS 80A.

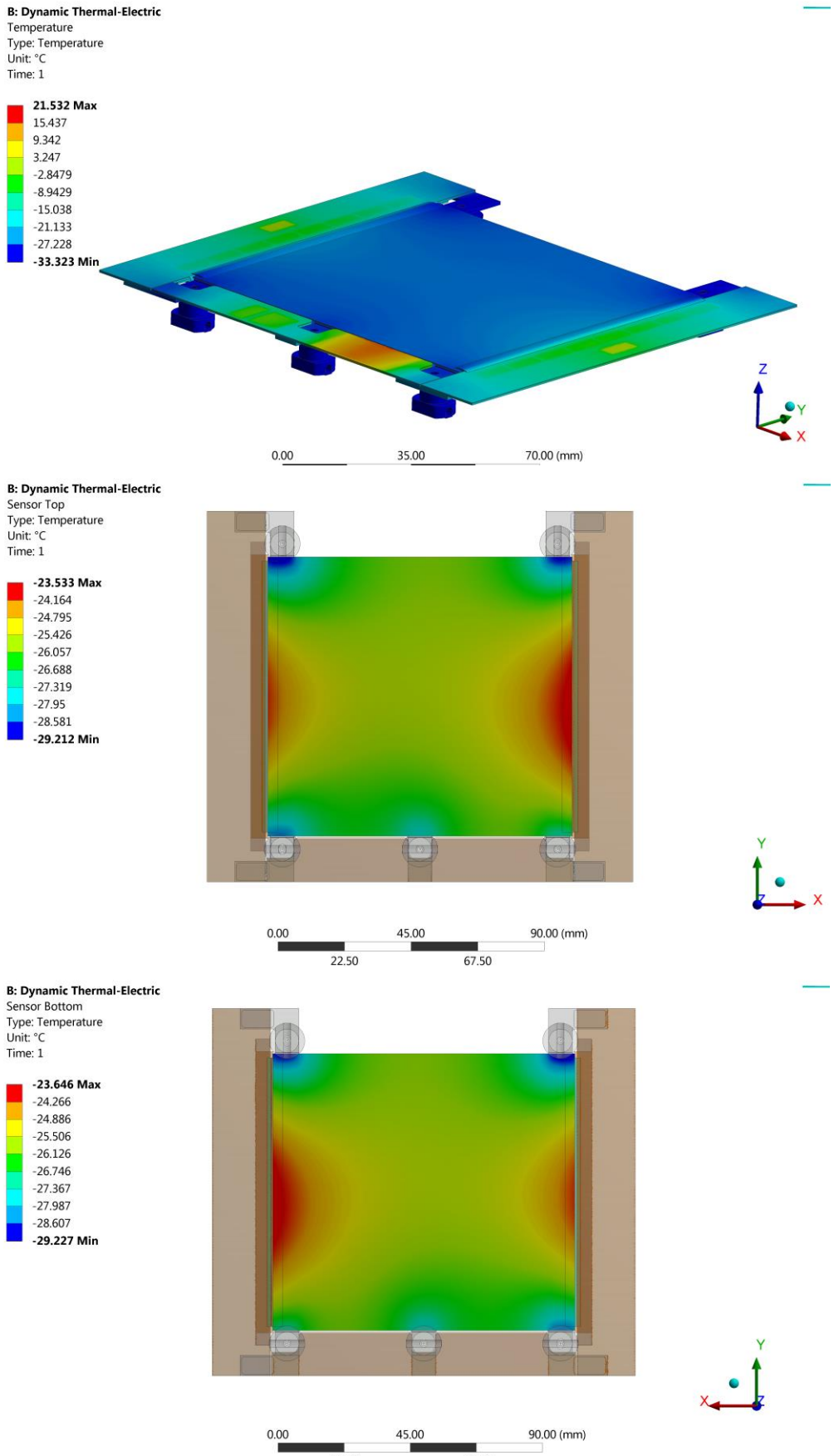

Appendix Figure 24: Temperature distribution (oC) on the total structure of the 2S 1.8mm Module and on the sensors, using laminates with stacking sequence [0,90]s and carbon fiber Nippon YSH 70A.

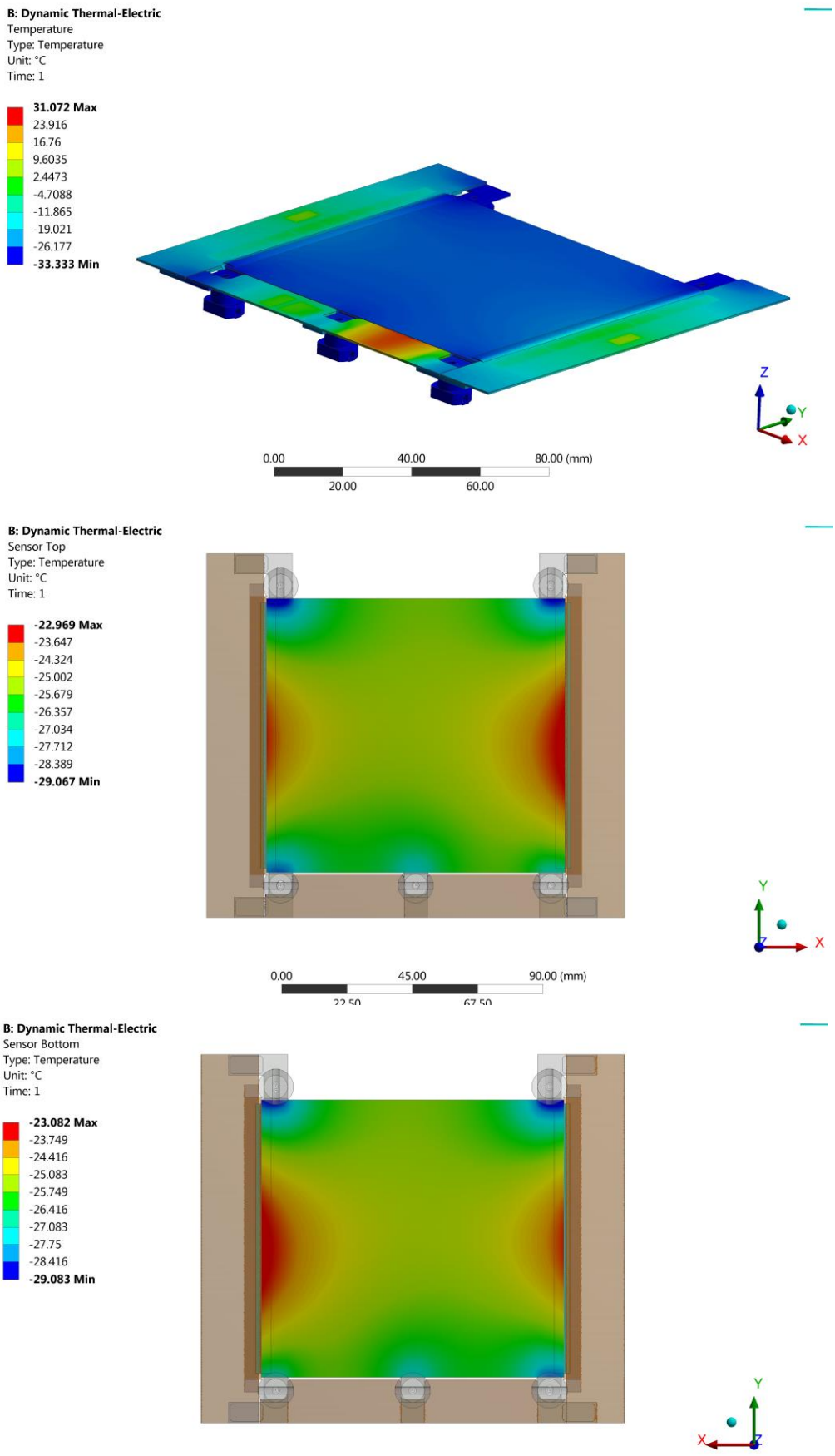

Appendix Figure 25: Temperature distribution (oC) on the total structure of the 2S 1.8mm Module and on the sensors, using laminates with stacking sequence [0,90]s and carbon fiber Nippon XN 60/ YSH 60A.

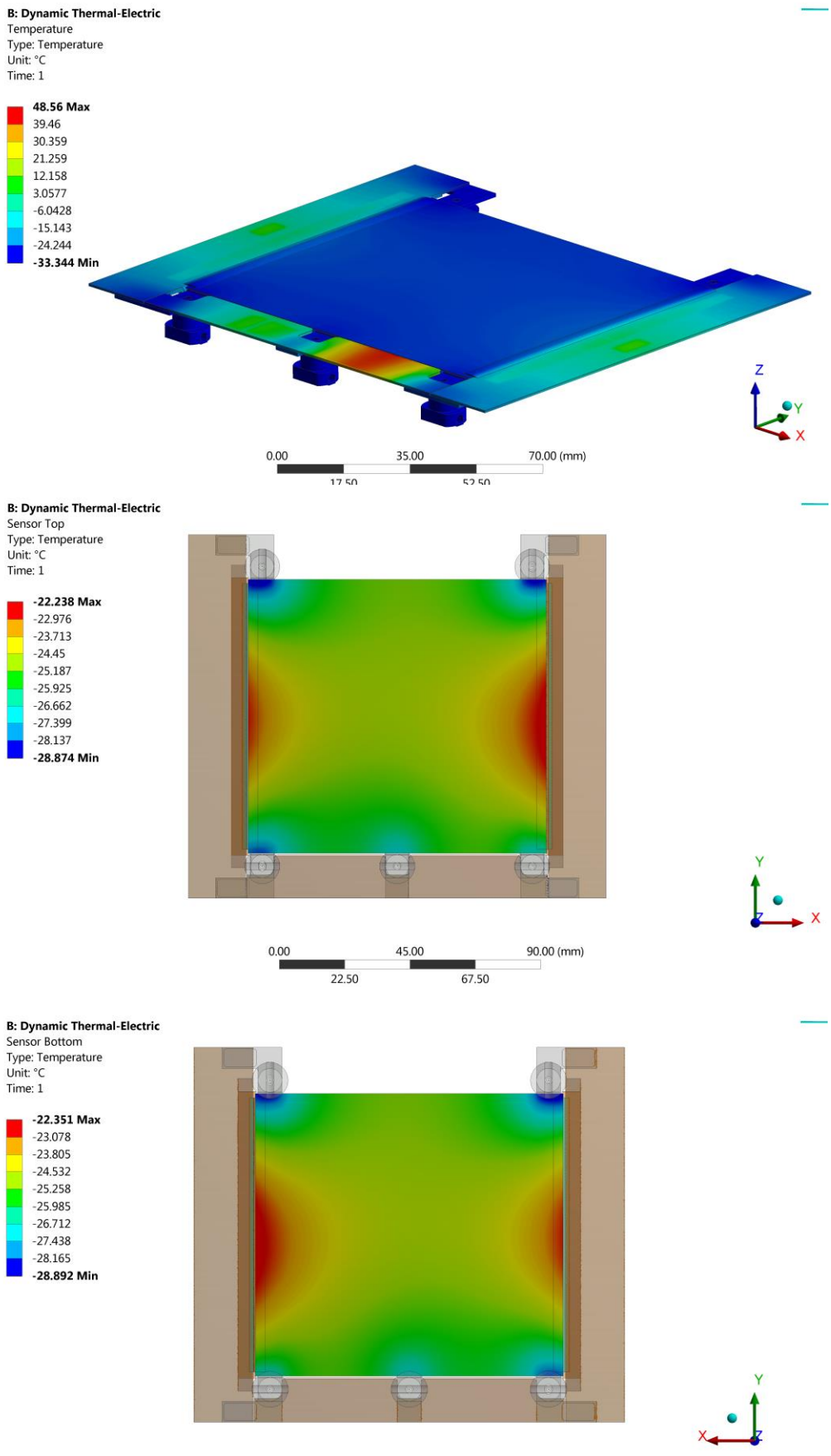

Appendix Figure 26: Temperature distribution (oC) on the total structure of the 2S 1.8mm Module and on the sensors, using laminates with stacking sequence [0,90]s and carbon fiber Nippon YSH 50A.

THERMAL RUNAWAY RESULTS USING 0/90/0/90/ 0 LAMINATES

Manufacturer	Carbon Fiber Name	Thermal Conductivity (W/mK)	Thermal Runaway Temperature (°C)
Mitsubishi	K13D2U	800	-20
	K13C2U	620	-20.2
	K13C6U	580	-20.4
	K63A12	220	-21.4
	K1392U	210	-21.4
	K13916	200	-21.4
	K63712/ K1352U	140	-22
	K13312	110	-22.2
Nippon (NGF)	YS-95	600	-20.2
	XN 90/ YS 90A	500	-20.4
	XN 80/YS 80A	320	-21
	YSH-70A	250	-21.2
	XN 60/YSH-60A	180	-21.6
	YSH-50A	120	-22.2

Table 5: Thermal runaway temperature of the 2S 1.8 Module, for different carbon fiber types of the laminate 0/90/0/90/0 with epoxy/polycyanate resin of thermal conductivity 0.2 W/mK.

The laminate was studied taking into account:

-Volume fraction of the fiber $V_f = 0.65$

-Transverse thermal conductivity of the fiber $k_{f2} = 2.4\ W/mK$

-Epoxy/polycyanate resin thermal conductity, $k_m = 0.2\ W/mK$

Manufacturer: Mitsubishi	Resin Type: Epoxy or Polycyanate Resin Thermal Conductivity: 0.2 W/mK
Carbon Fiber Name: K13D2U	**Fiber Thermal Conductivity: 800 W/mK**

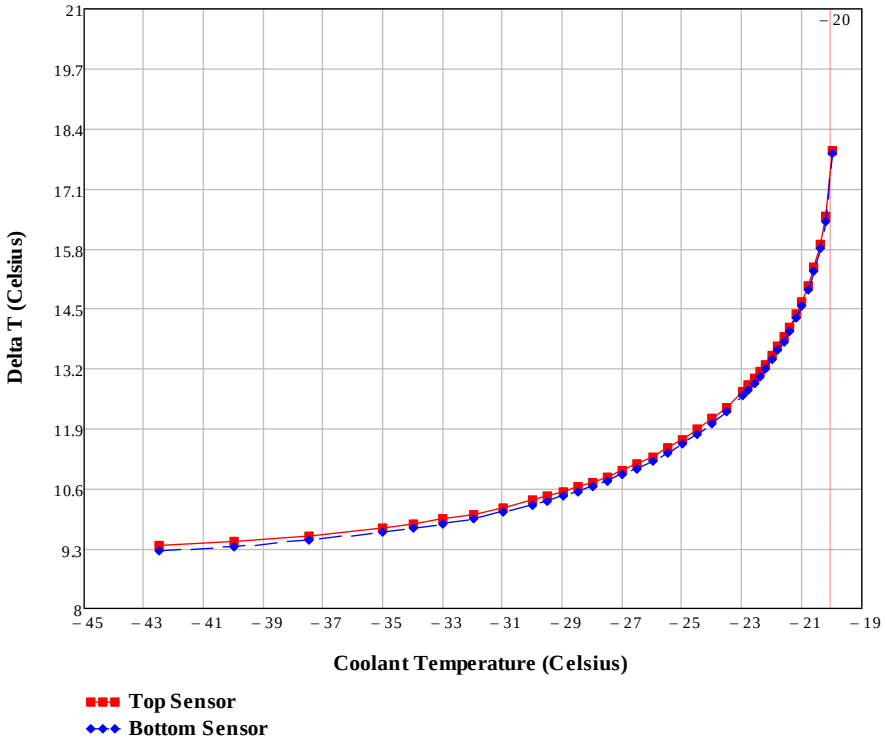

Figure 42: Differential temperature Vs Coolant temperature by using K13D2U carbon fiber.

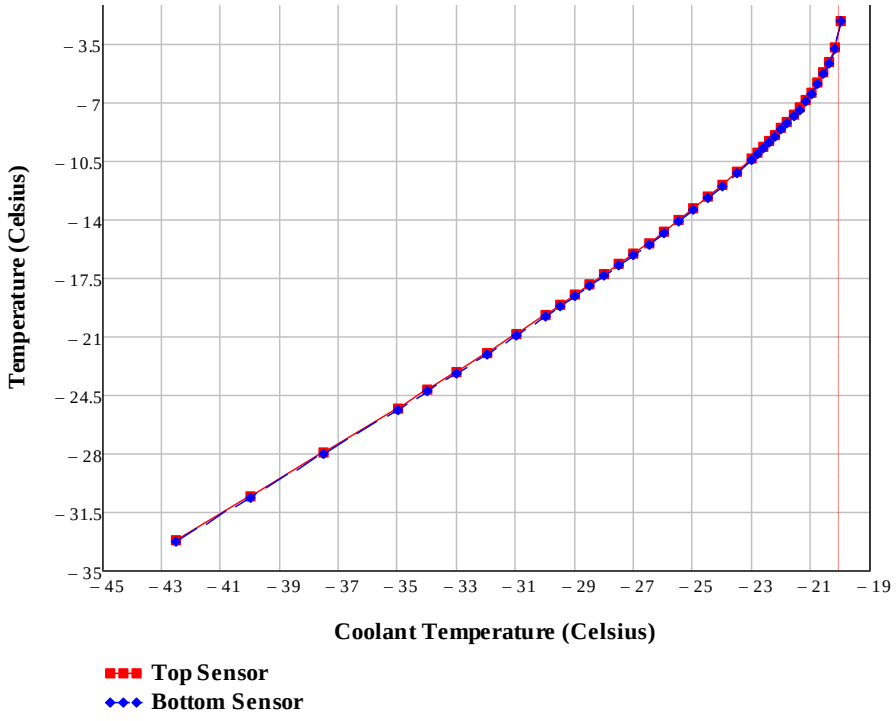

Figure 43: Maximum sensor temperature Vs Coolant temperature by using K13D2U carbon fiber.

Manufacturer: Mitsubishi	Resin Type: Epoxy or Polycyanate Resin Thermal Conductivity: 0.2 W/mK
Carbon Fiber Name: K13D2U	**Fiber Thermal Conductivity: 800 W/mK**

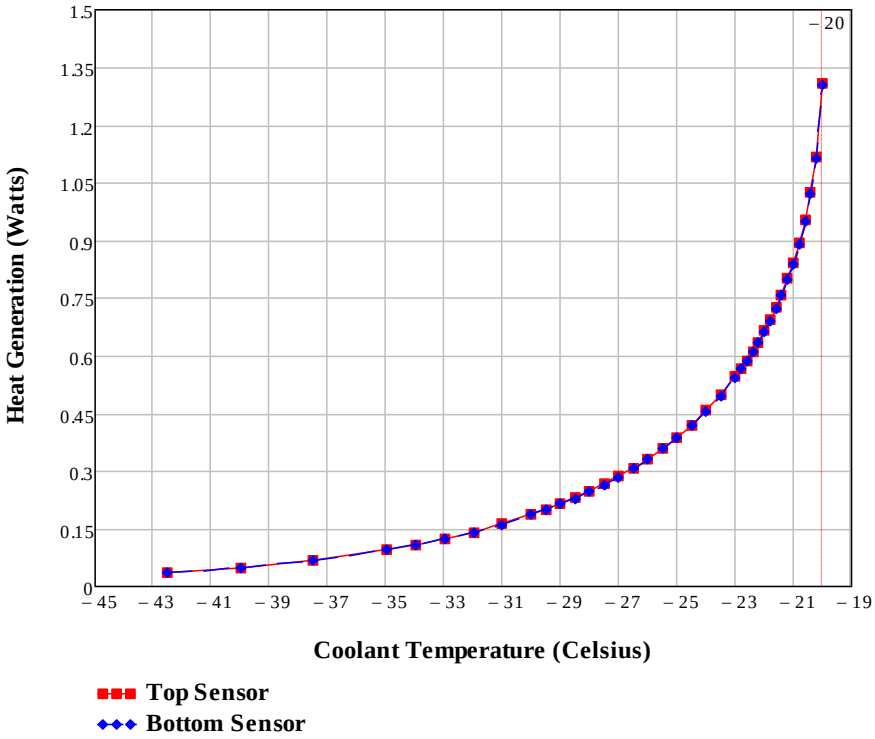

Figure 44: Heat generation of the sensor Vs Coolant Temperature by using K13D2U carbon fiber.

Manufacturer: Mitsubishi	Resin Type: Epoxy or Polycyanate Resin Thermal Conductivity: 0.2 W/mK
Carbon Fiber Name: K13C2U	**Fiber Thermal Conductivity: 620 W/mK**

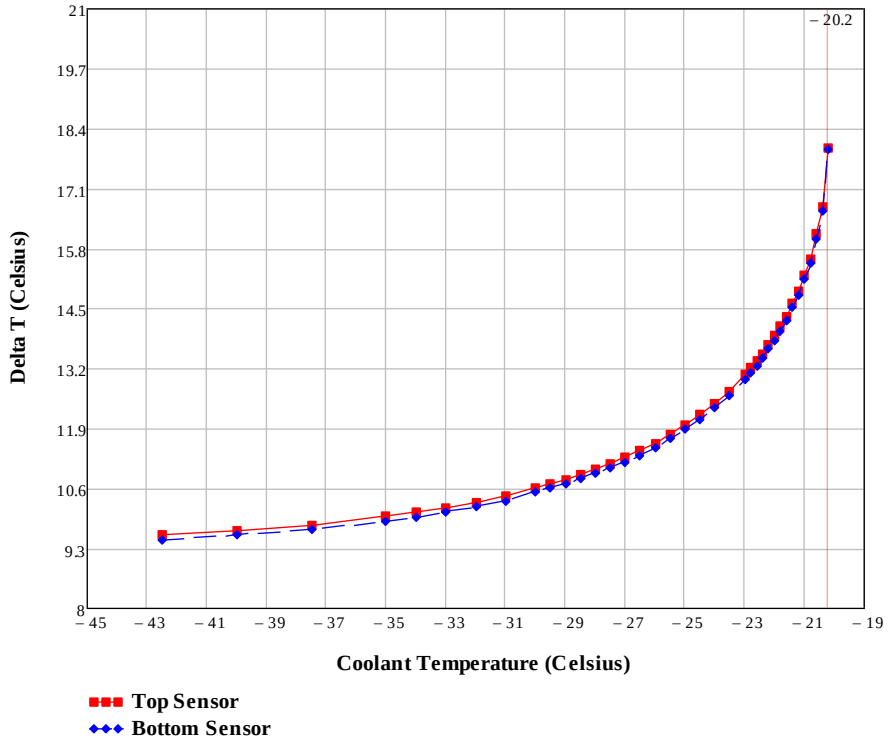

Figure 45: Differential temperature Vs Coolant Temperature by using K13C2U carbon fiber.

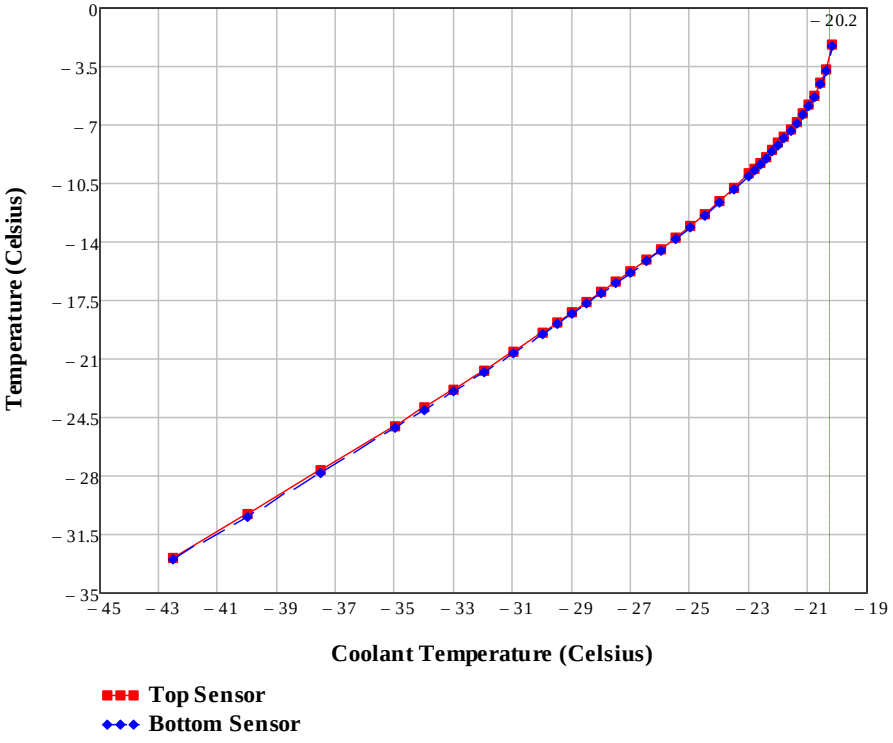

Figure 46: Maximum sensor temperature Vs Coolant Temperature by using K13C2U carbon fiber.

Manufacturer: Mitsubishi	Resin Type: Epoxy or Polycyanate Resin Thermal Conductivity: 0.2 W/mK
Carbon Fiber Name: K13C2U	**Fiber Thermal Conductivity: 620 W/mK**

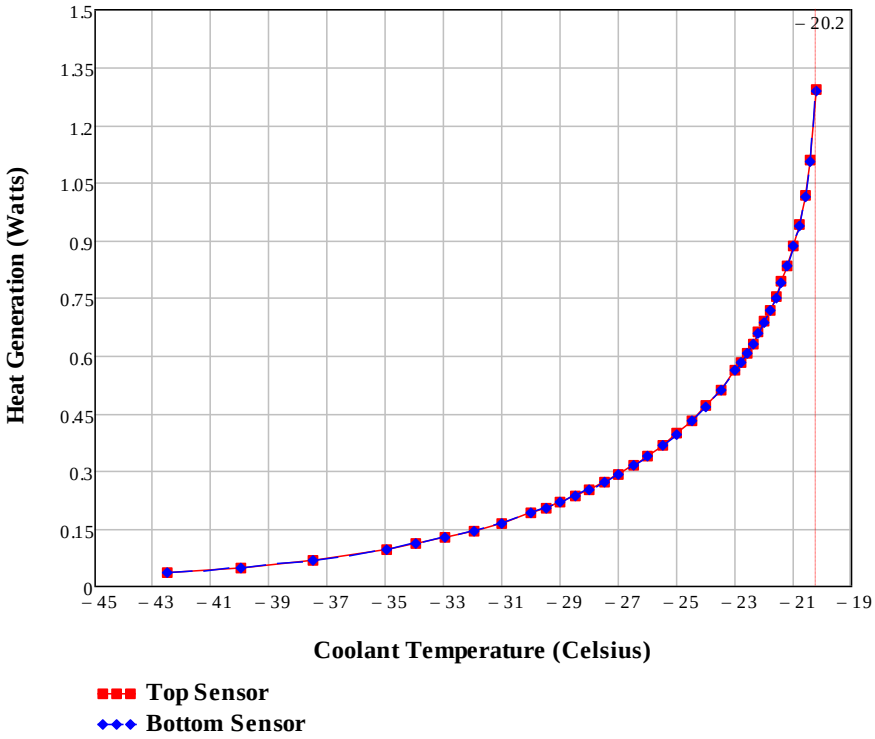

Figure 47: Heat generation of the sensor Vs Coolant Temperature by using K13C2U carbon fiber.

Manufacturer: Mitsubishi	Resin Type: Epoxy or Polycyanate Resin Thermal Conductivity: 0.2 W/mK
Carbon Fiber Name: K13C6U	**Fiber Thermal Conductivity: 580 W/mK**

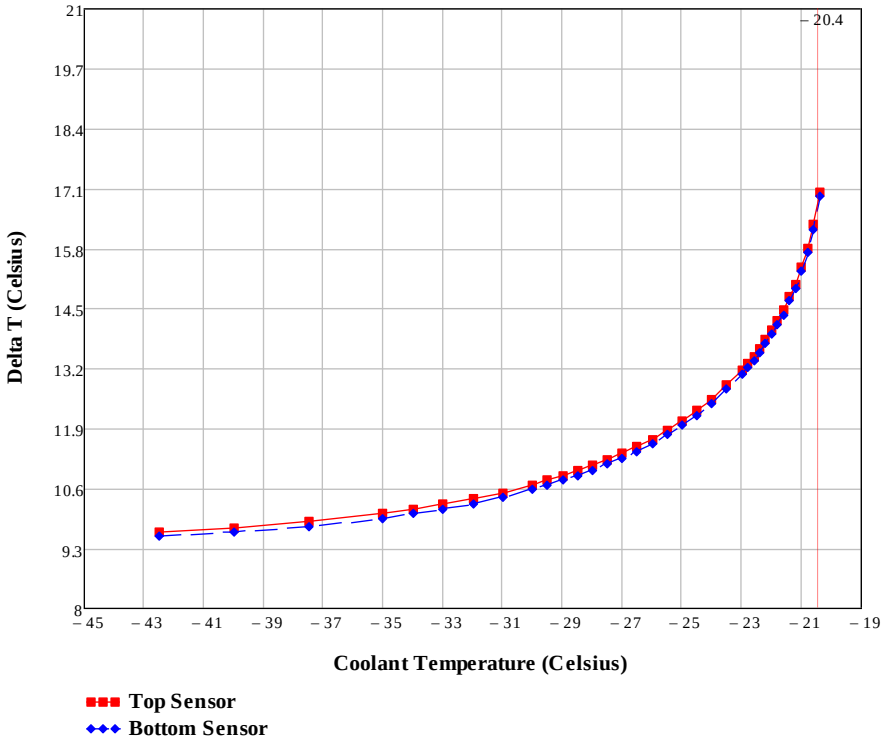

Figure 48: Differential temperature Vs Coolant Temperature by using K13C6U carbon fiber.

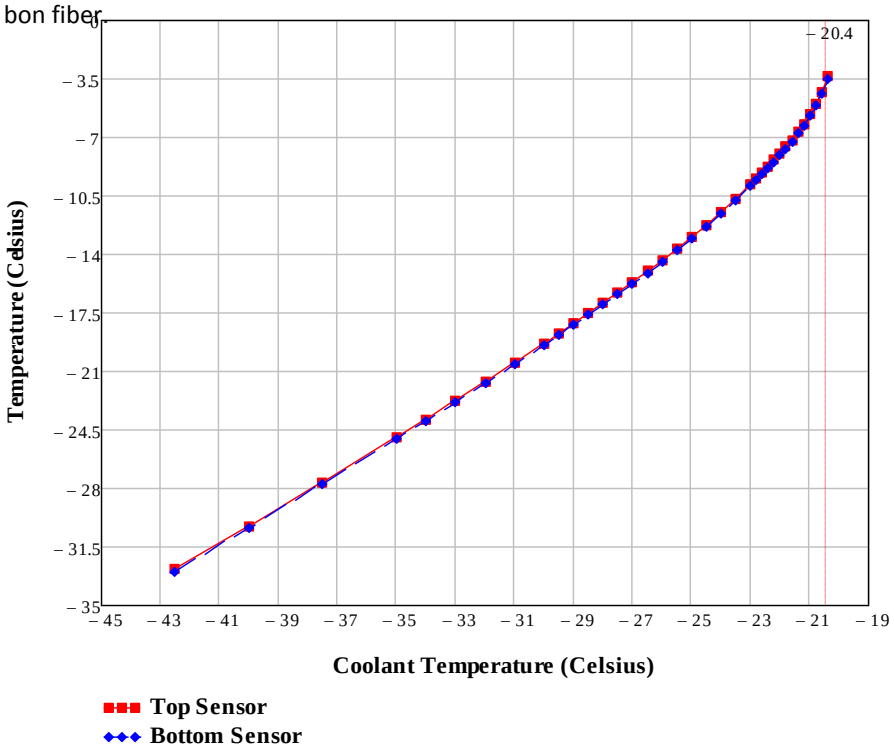

Figure 49: Maximum sensor temperature Vs Coolant Temperature by using K13C6U carbon fiber.

Manufacturer: Mitsubishi	Resin Type: Epoxy or Polycyanate Resin Thermal Conductivity: 0.2 W/mK
Carbon Fiber Name: K13C6U	**Fiber Thermal Conductivity: 580 W/mK**

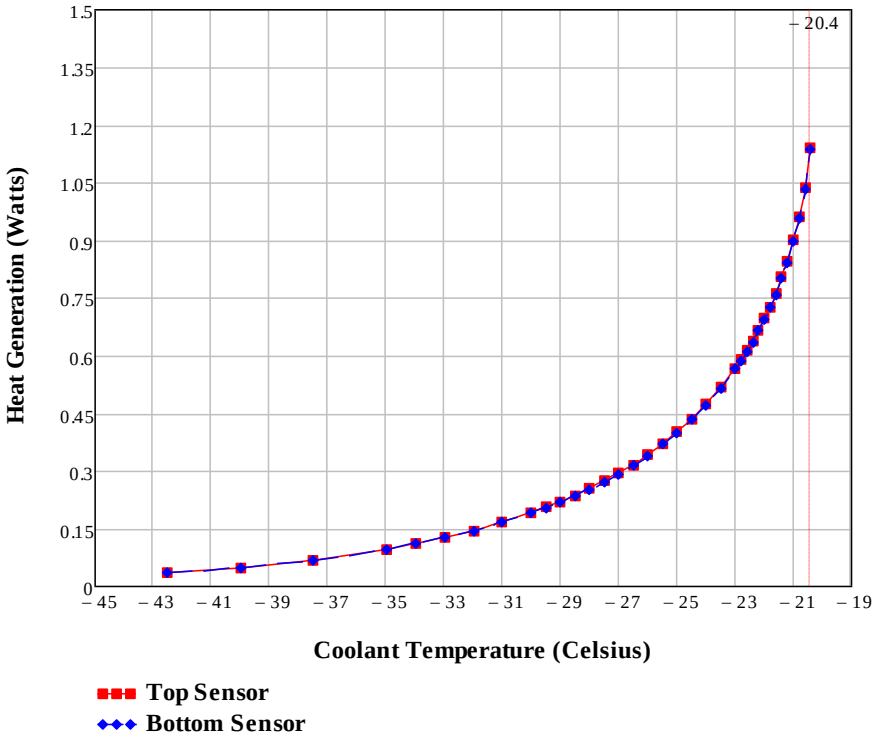

Figure 50: Heat generation of the sensor Vs Coolant Temperature by using K13C6U carbon fiber.

Manufacturer: Mitsubishi	Resin Type: Epoxy or Polycyanate Resin Thermal Conductivity: 0.2 W/mK
Carbon Fiber Name: K63A12	**Fiber Thermal Conductivity: 220 W/mK**

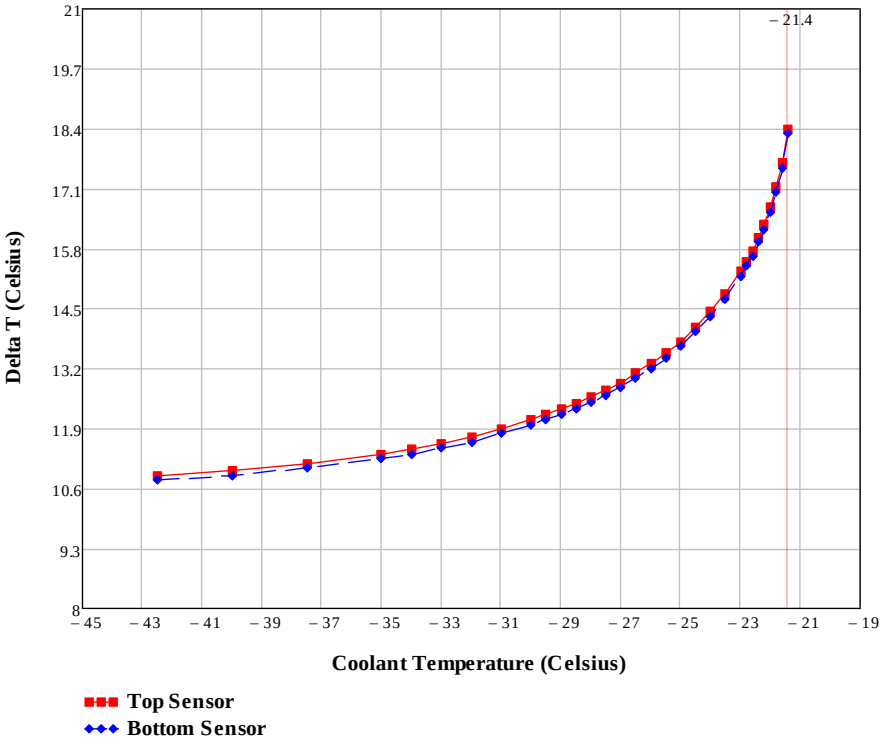

Figure 51: Differential temperature Vs Coolant Temperature by using K13A12 carbon fiber

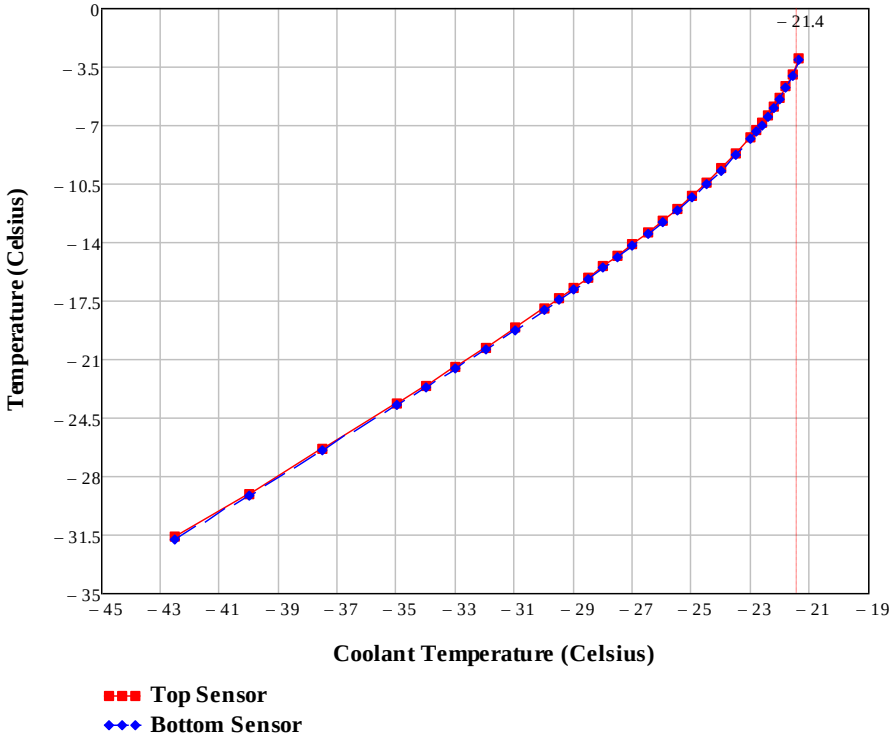

Figure 52: Maximum sensor temperature Vs Coolant temperature by using K13D2U carbon fiber.

Manufacturer: Mitsubishi	Resin Type: Epoxy or Polycyanate Resin Thermal Conductivity: 0.2 W/mK
Carbon Fiber Name: K63A12	**Fiber Thermal Conductivity: 220 W/mK**

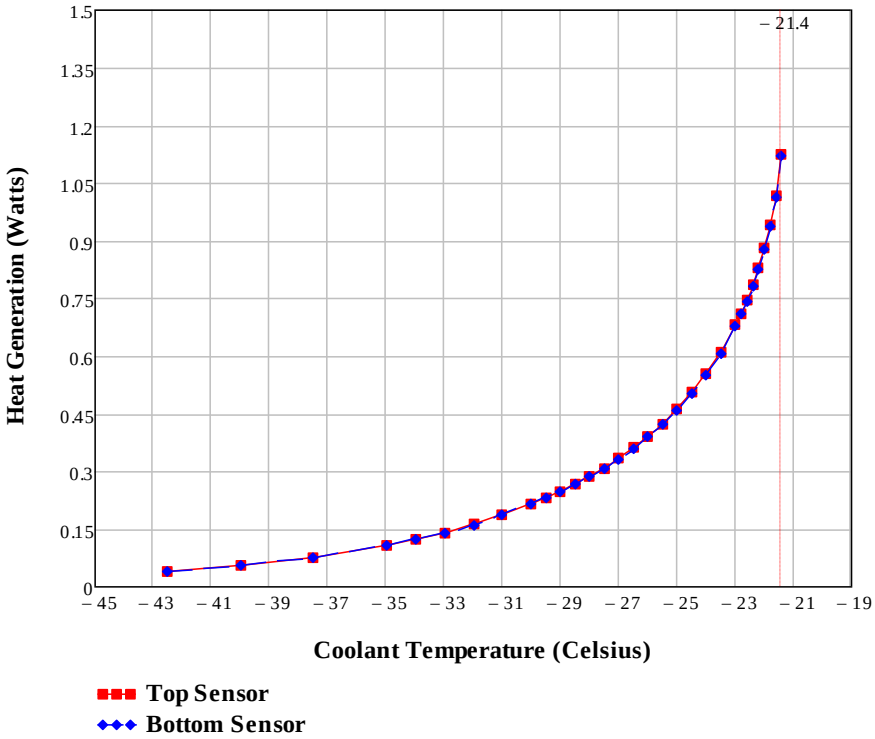

Figure 53: Heat generation of the sensor Vs Coolant Temperature by using K63A12 carbon fiber.

Manufacturer: Mitsubishi	Resin Type: Epoxy or Polycyanate Resin Thermal Conductivity: 0.2 W/mK
Carbon Fiber Name: K1392U	**Fiber Thermal Conductivity: 210 W/mK**

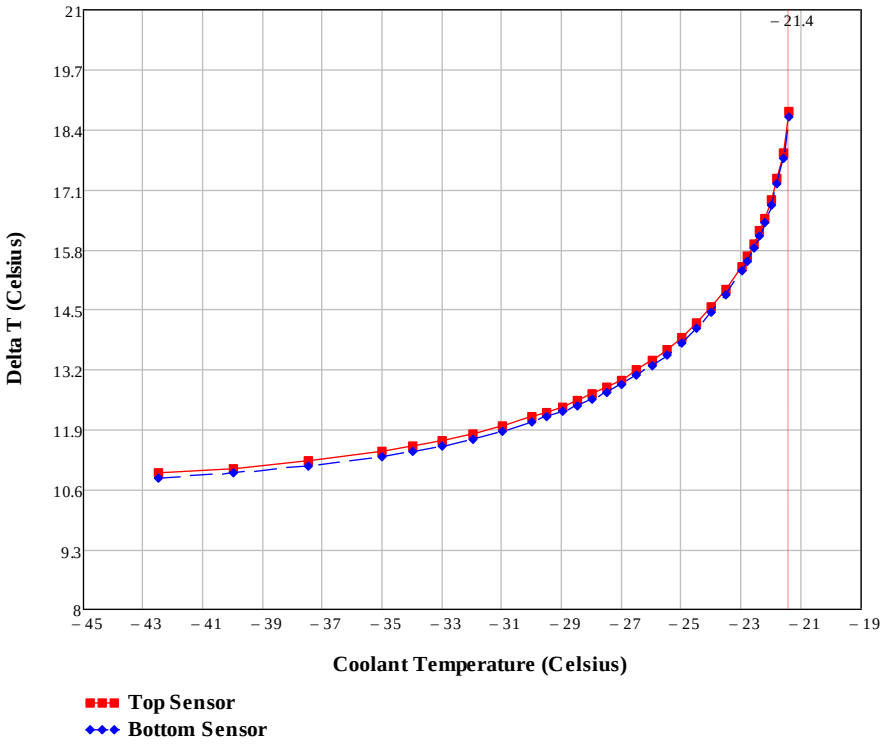

Figure 54: Differential temperature Vs Coolant Temperature by using K1392U carbon fiber.

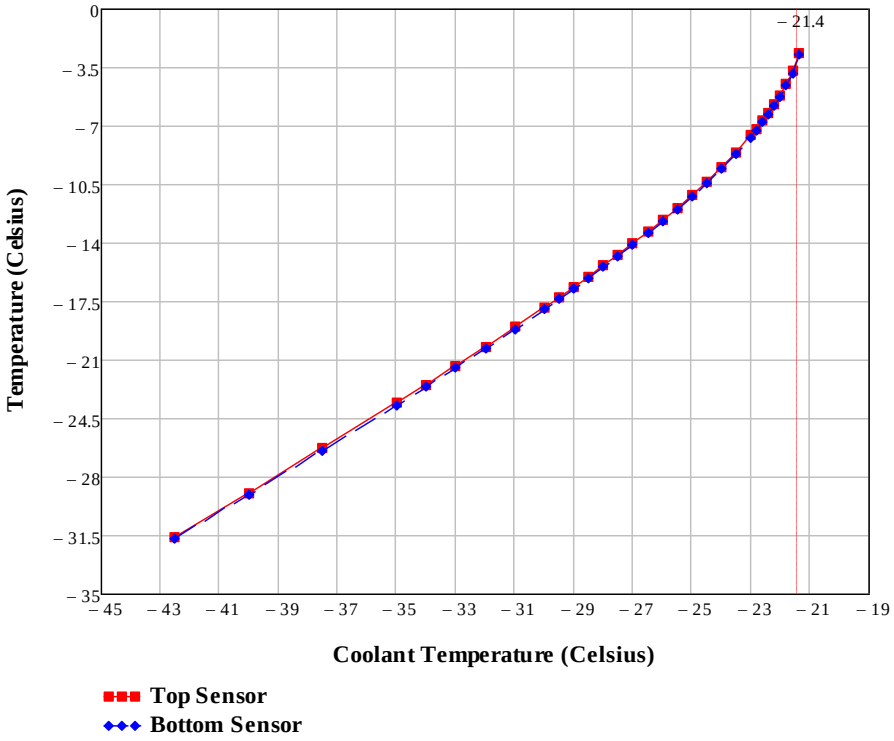

Figure 55: Maximum sensor temperature Vs Coolant temperature by using K1392U carbon fiber.

Manufacturer: Mitsubishi	Resin Type: Epoxy or Polycyanate Resin Thermal Conductivity: 0.2 W/mK
Carbon Fiber Name: K1392U	**Fiber Thermal Conductivity: 210 W/mK**

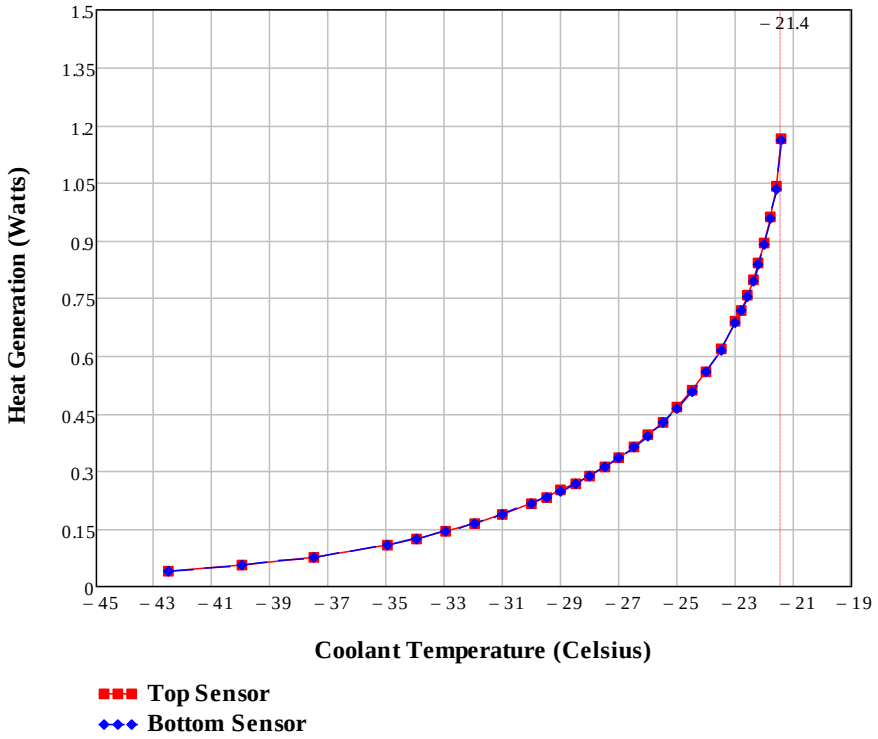

Figure 56: Heat generation of the sensor Vs Coolant Temperature by using K1392U carbon fiber.

Manufacturer: Mitsubishi	Resin Type: Epoxy or Polycyanate Resin Thermal Conductivity: 0.2 W/mK
Carbon Fiber Name: K13916	**Fiber Thermal Conductivity: 200 W/mK**

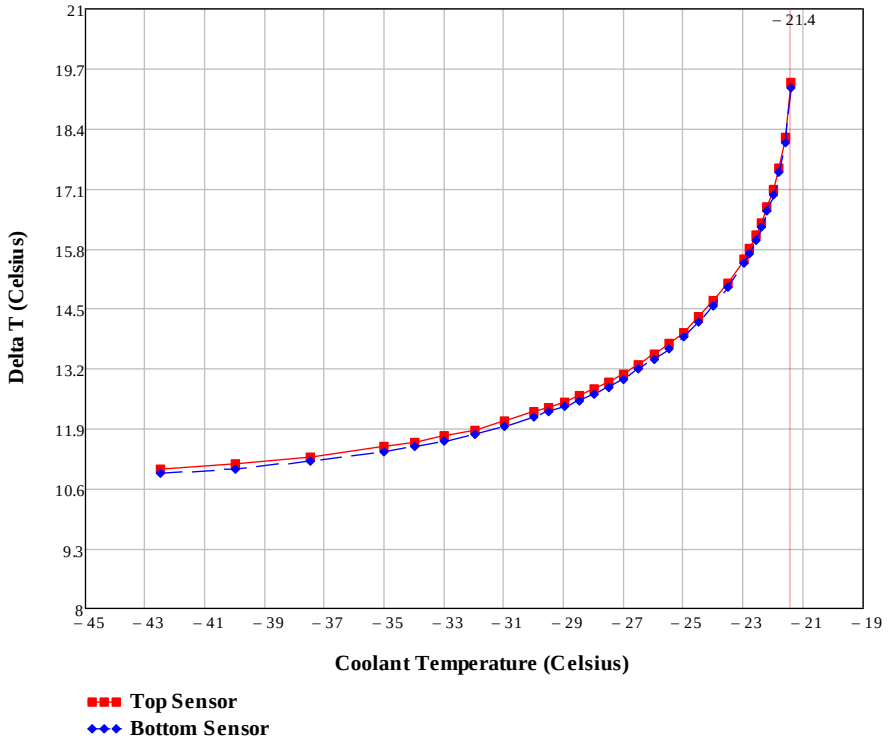

Figure 57: Differential temperature Vs Coolant Temperature by using K13916 carbon fiber.

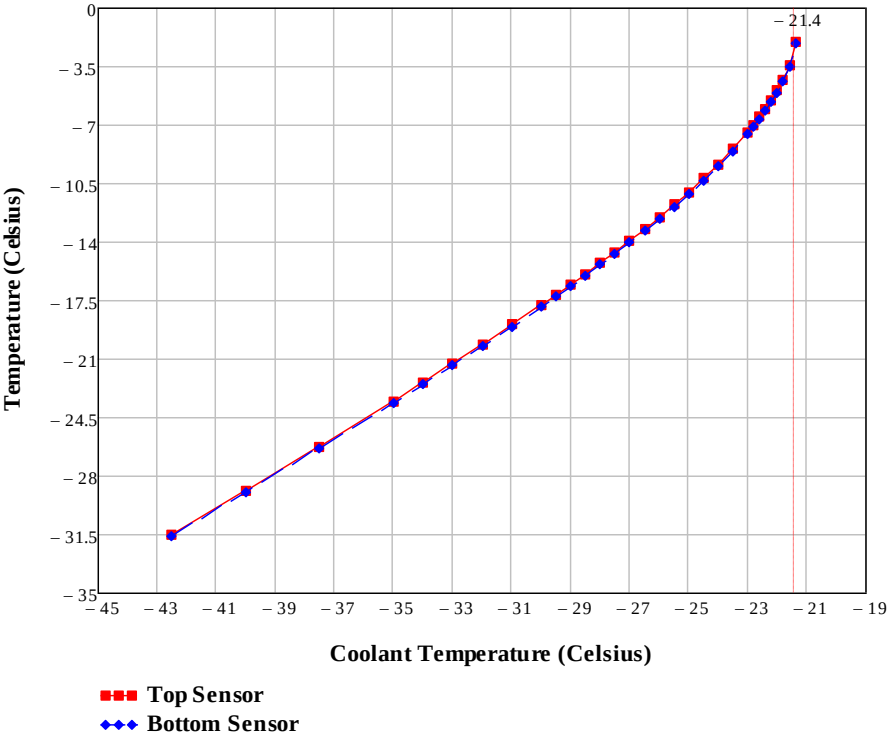

Figure 58: Maximum sensor temperature Vs Coolant temperature by using K13916 carbon fiber.

Manufacturer: Mitsubishi	Resin Type: Epoxy or Polycyanate Resin Thermal Conductivity: 0.2 W/mK
Carbon Fiber Name: K13916	**Fiber Thermal Conductivity: 200 W/mK**

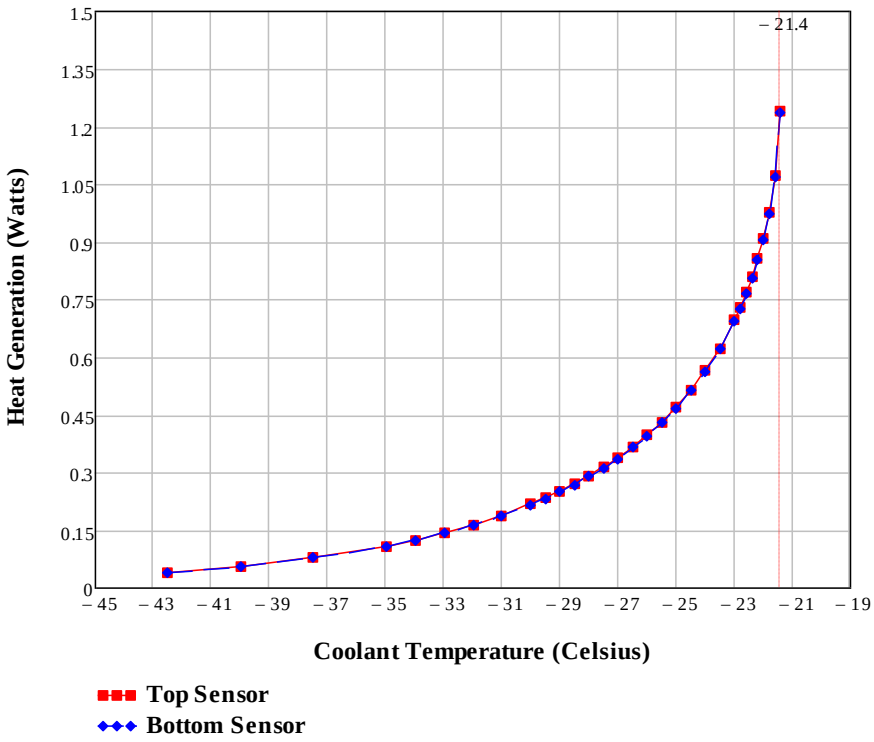

Figure 59: Heat generation of the sensor Vs Coolant Temperature by using K13916 carbon fiber.

Manufacturer: Mitsubishi	Resin Type: Epoxy or Polycyanate Resin Thermal Conductivity: 0.2 W/mK
Carbon Fiber Name: K63712/K1352U	**Fiber Thermal Conductivity: 140 W/mK**

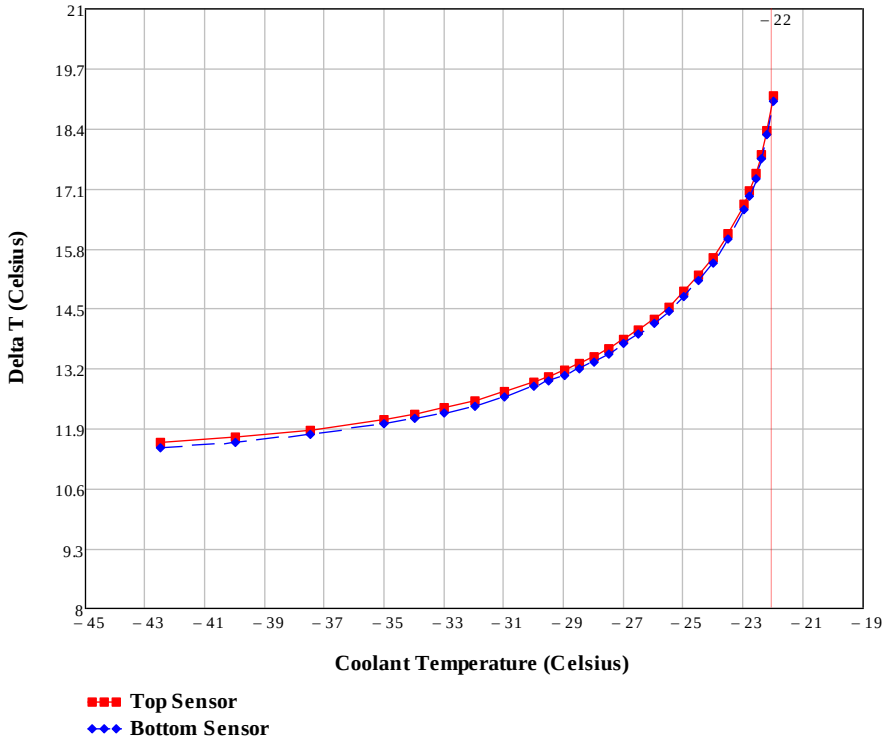

Figure 60: Differential temperature Vs Coolant Temperature by using K63712 or K1352U carbon fiber.

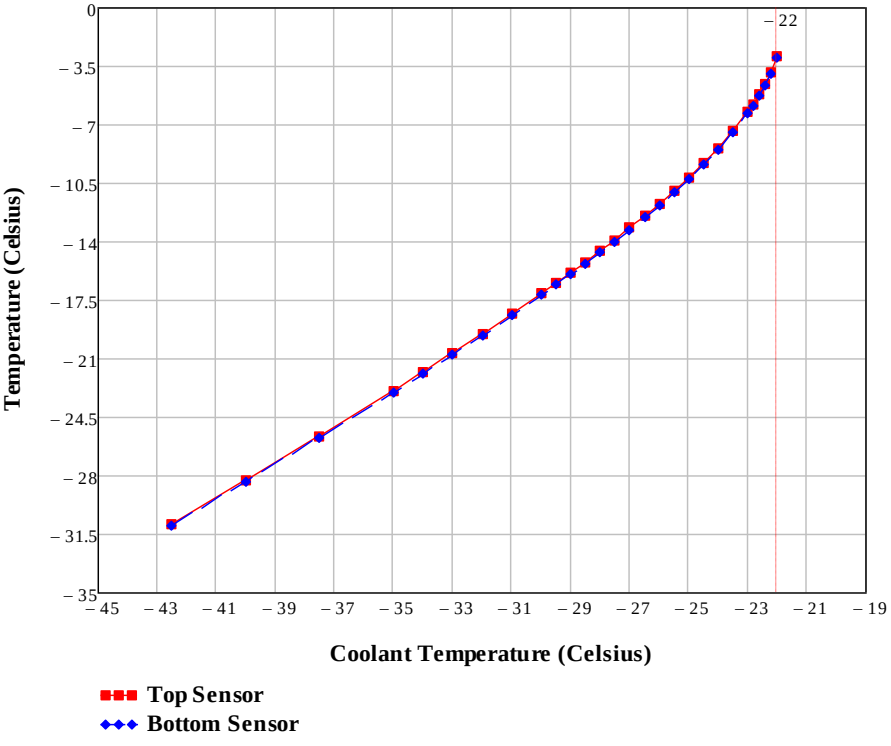

Figure 61: Maximum sensor temperature Vs Coolant temperature by using K63712 or K1352U carbon fiber.

Manufacturer: Mitsubishi	Resin Type: Epoxy or Polycyanate Resin Thermal Conductivity: 0.2 W/mK
Carbon Fiber Name: K63712/K1352U	**Fiber Thermal Conductivity: 140 W/mK**

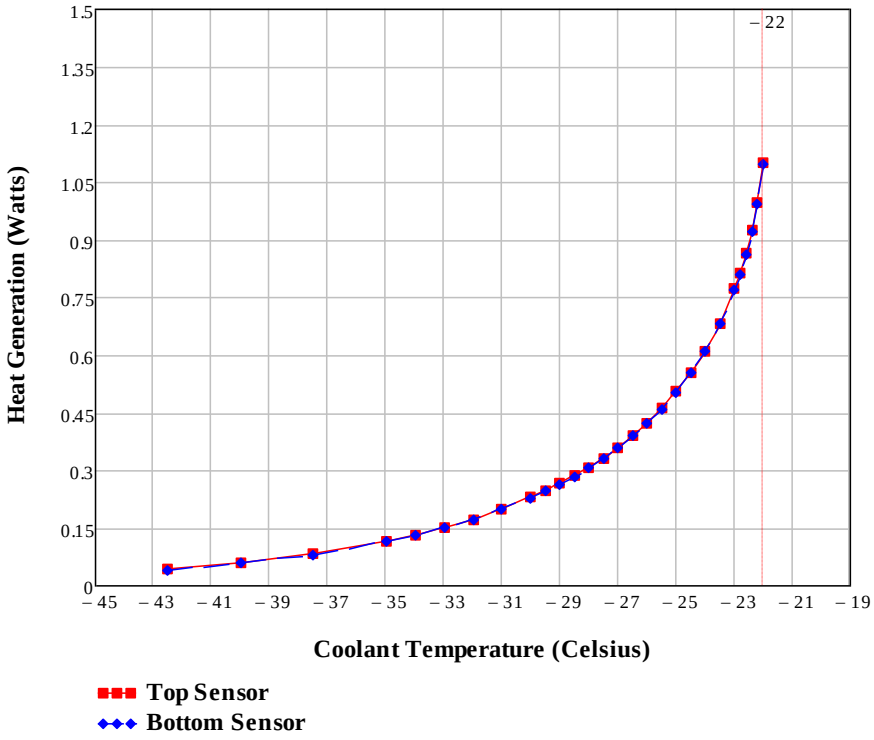

Figure 62: Heat generation of the sensor Vs Coolant Temperature by using K63712 or K1352U carbon fiber.

Manufacturer: Mitsubishi	Resin Type: Epoxy or Polycyanate Resin Thermal Conductivity: 0.2 W/mK
Carbon Fiber Name: K13312	**Fiber Thermal Conductivity: 110 W/mK**

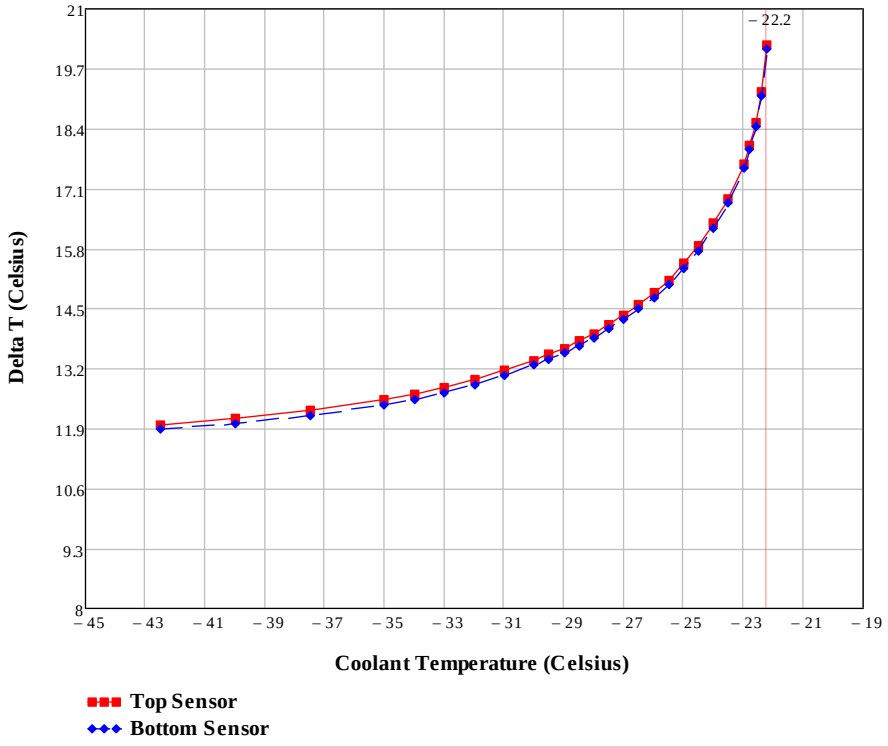

Figure 63: Differential temperature Vs Coolant Temperature by using K13312 carbon fiber.

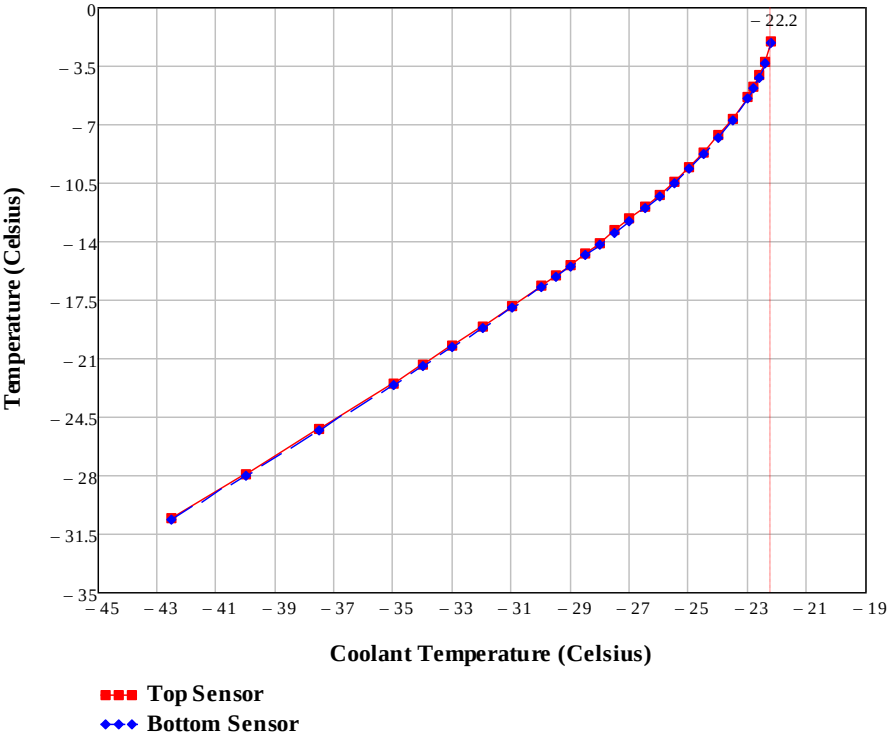

Figure 64: Maximum sensor temperature Vs Coolant temperature by using K13312 carbon fiber.

Manufacturer: Mitsubishi	Resin Type: Epoxy or Polycyanate Resin Thermal Conductivity: 0.2 W/mK
Carbon Fiber Name: K13312	**Fiber Thermal Conductivity: 110 W/mK**

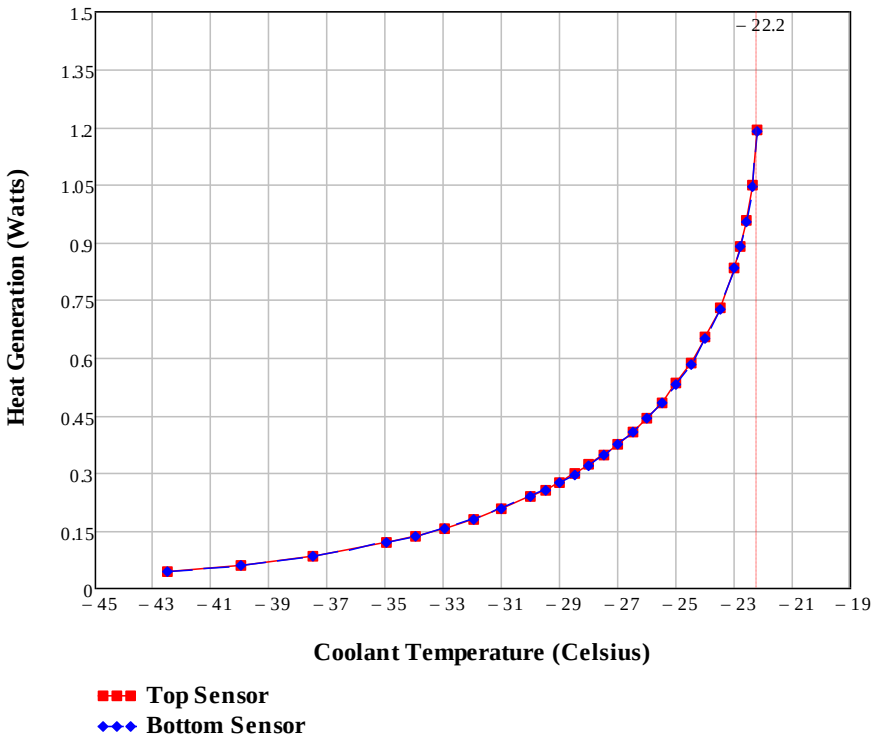

Figure 65: Heat generation of the sensor Vs Coolant Temperature by using K13312 carbon fiber.

Manufacturer: Nippon (NGF)	Resin Type: Epoxy or Polycyanate Resin Thermal Conductivity: 0.2 W/mK
Carbon Fiber Name: YS-95	**Fiber Thermal Conductivity: 600 W/mK**

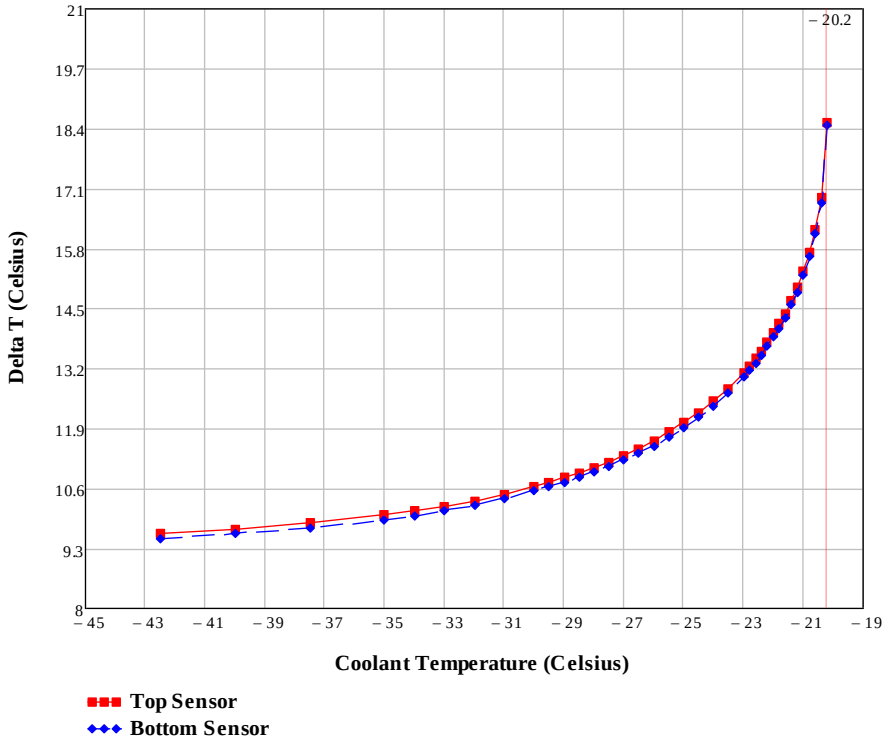

Figure 66: Differential temperature Vs Coolant Temperature by using Nippon YS-95 carbon fiber.

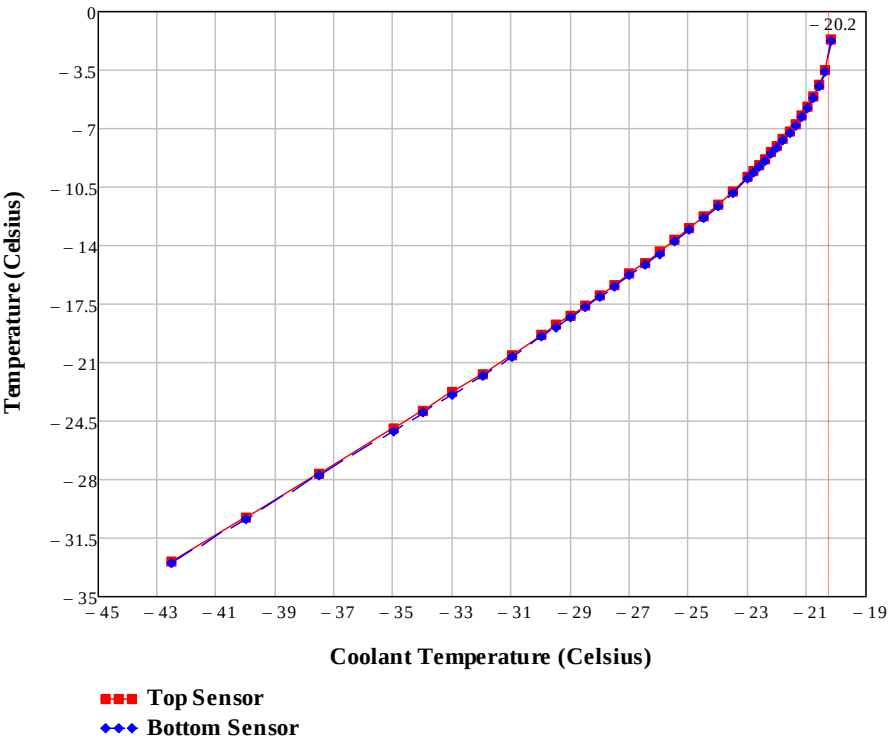

Figure 67: Maximum sensor temperature Vs Coolant temperature by using Nippon YS-95 carbon fiber.

Manufacturer: Nippon (NGF)	Resin Type: Epoxy or Polycyanate Resin Thermal Conductivity: 0.2 W/mK
Carbon Fiber Name: YS-95	**Fiber Thermal Conductivity: 600 W/mK**

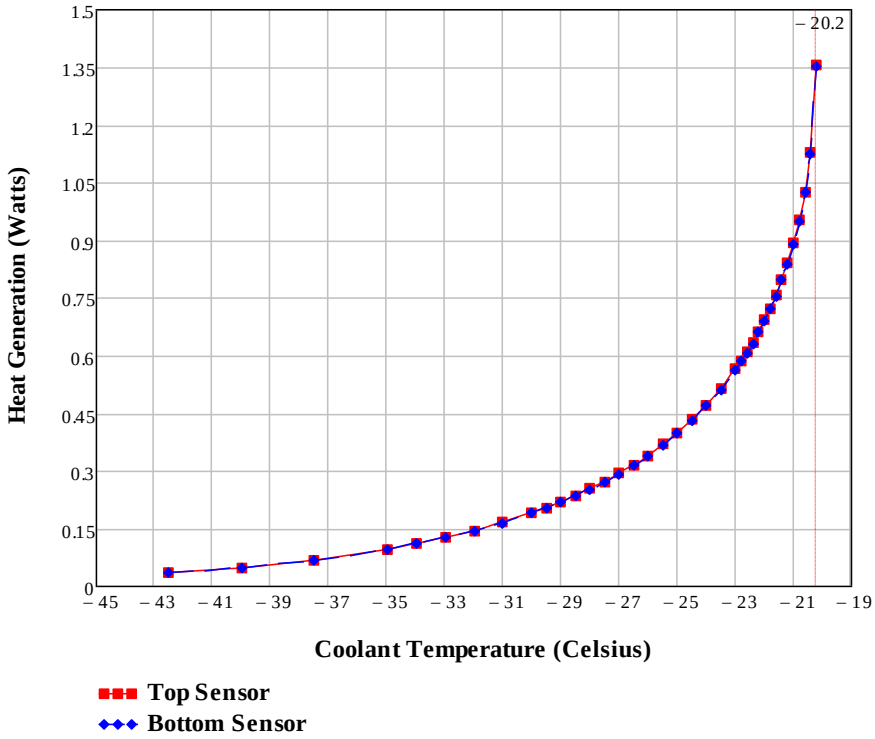

Figure 68: Heat generation of the sensor Vs Coolant Temperature by using Nippon YS-95 carbon fiber.

Manufacturer: Nippon (NGF)	Resin Type: Epoxy or Polycyanate Resin Thermal Conductivity: 0.2 W/mK
Carbon Fiber Name: XN-90/YS-90A	**Fiber Thermal Conductivity: 500 W/mK**

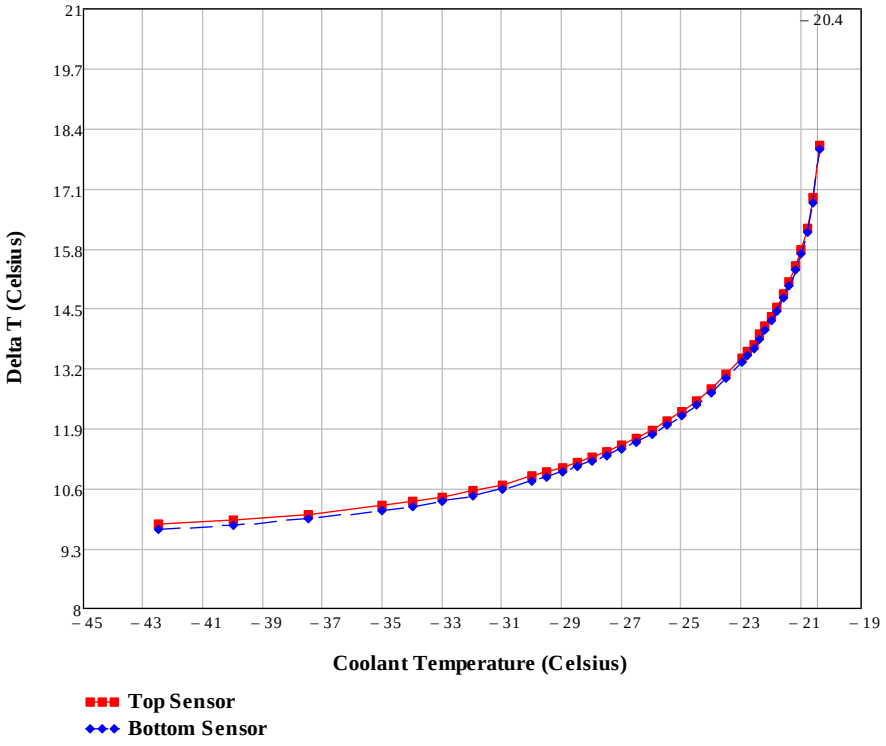

Figure 69: Differential temperature Vs Coolant Temperature by using Nippon XN-90 or YS-90A carbon fiber.

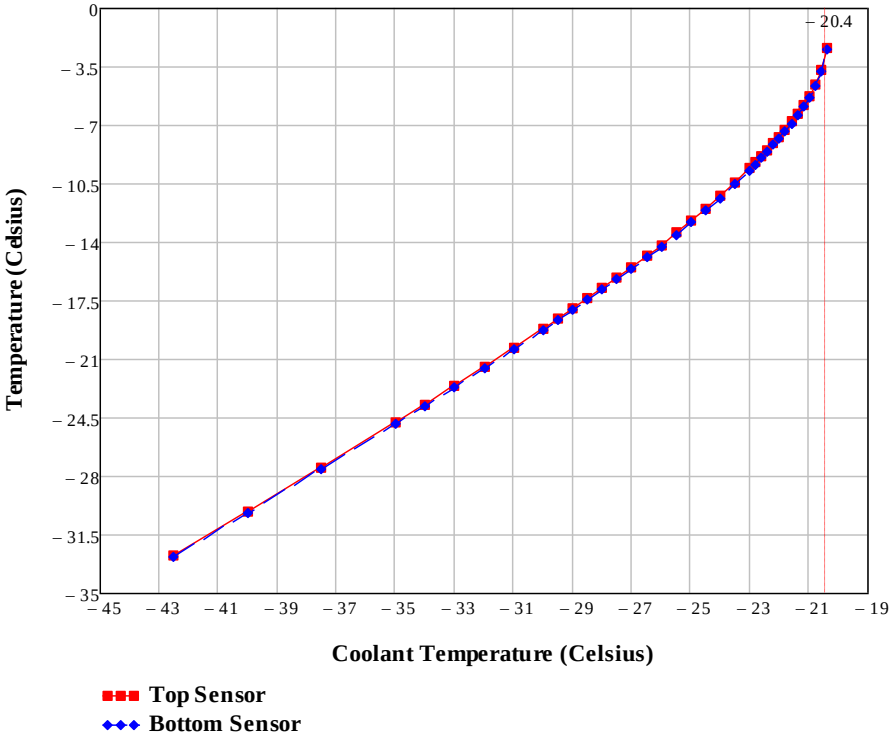

Figure 70: Maximum sensor temperature Vs Coolant temperature by using Nippon XN-90 or YS-90A carbon fiber.

Manufacturer: Nippon (NGF)	Resin Type: Epoxy or Polycyanate Resin Thermal Conductivity: 0.2 W/mK
Carbon Fiber Name: XN-90/YS-90A	**Fiber Thermal Conductivity: 500 W/mK**

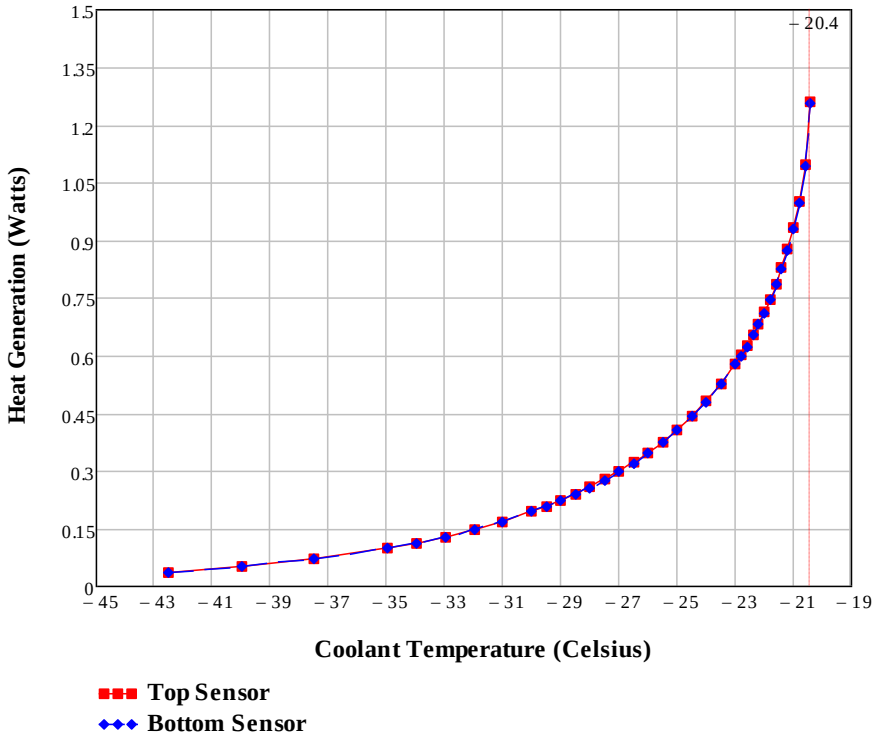

Figure 71: Heat generation of the sensor Vs Coolant Temperature by using Nippon XN-90 or YS-90A carbon fiber.

Manufacturer: Nippon (NGF)	Resin Type: Epoxy or Polycyanate Resin Thermal Conductivity: 0.2 W/mK
Carbon Fiber Name: XN-80/YS-80A	**Fiber Thermal Conductivity: 320 W/mK**

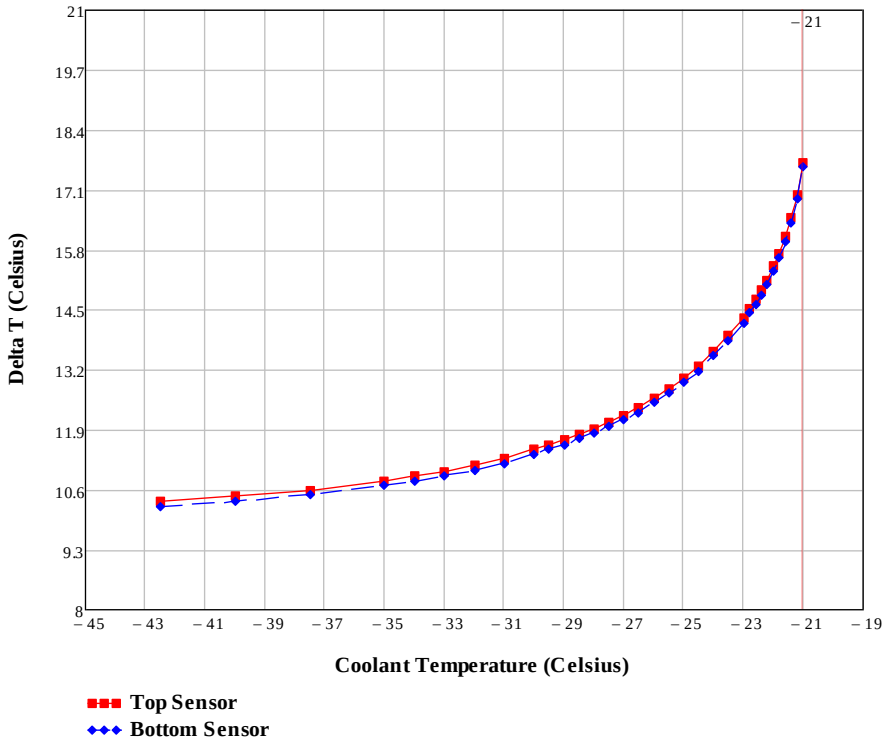

Figure 72: Differential temperature Vs Coolant Temperature by using Nippon XN-80 or YS-80A carbon fiber.

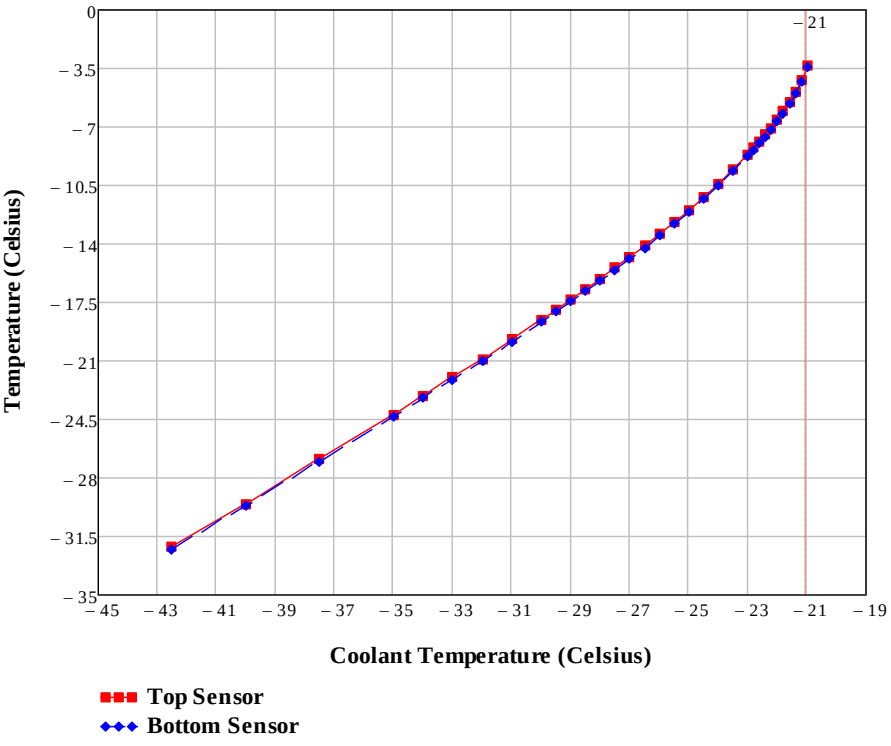

Figure 73: Maximum sensor temperature Vs Coolant temperature by using Nippon XN-80 or YS-80A carbon fiber.

Manufacturer: Nippon (NGF)	Resin Type: Epoxy or Polycyanate Resin Thermal Conductivity: 0.2 W/mK
Carbon Fiber Name: XN-80/YS-80A	**Fiber Thermal Conductivity: 320 W/mK**

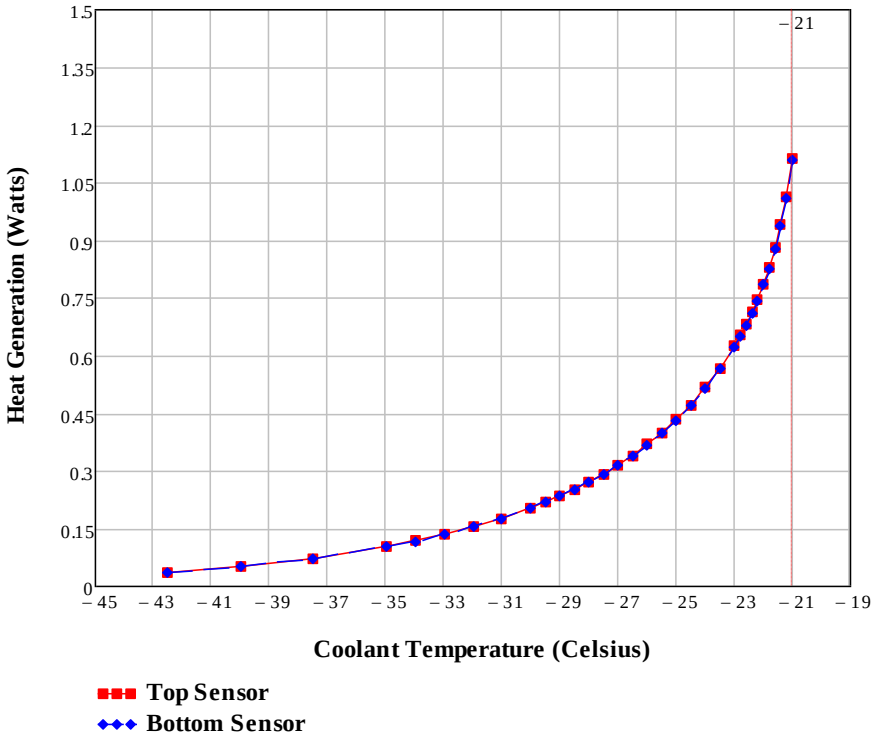

Figure 74: Heat generation of the sensor Vs Coolant Temperature by using Nippon XN-80 or YS-80A carbon fiber.

Manufacturer: Nippon (NGF)	Resin Type: Epoxy or Polycyanate Resin Thermal Conductivity: 0.2 W/mK
Carbon Fiber Name: YSH-70A	**Fiber Thermal Conductivity: 250 W/mK**

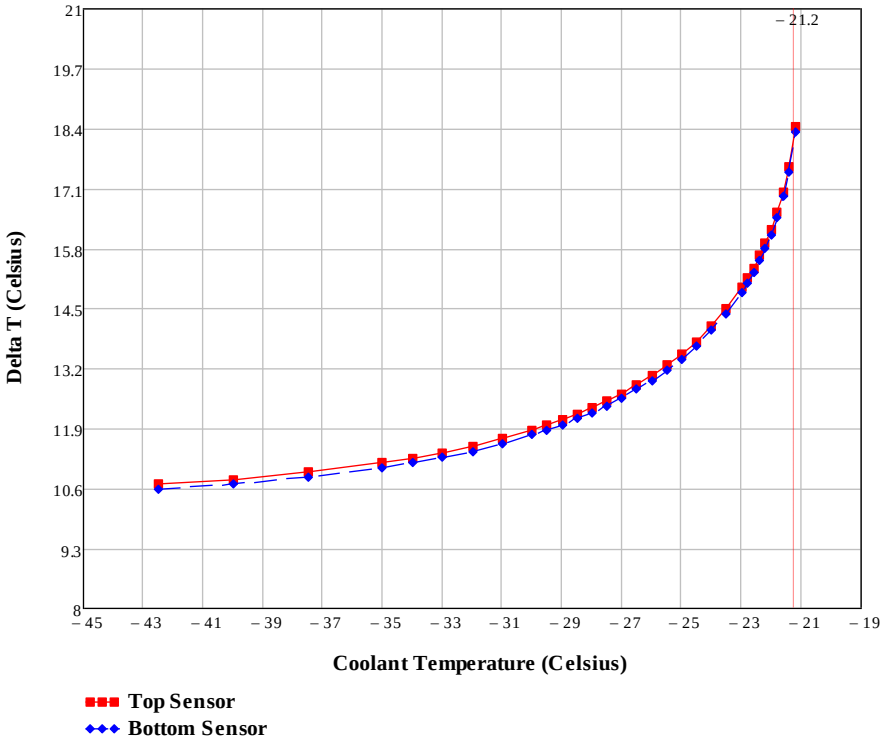

Figure 75: Differential temperature Vs Coolant Temperature by using Nippon YSH-70A carbon fiber.

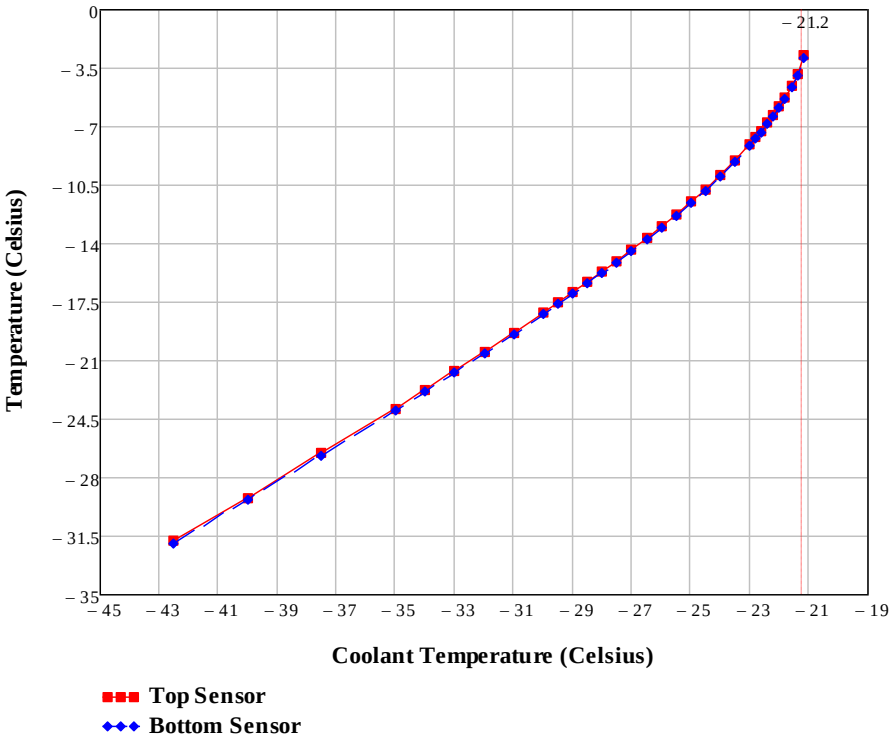

Figure 76: Maximum sensor temperature Vs Coolant temperature by using Nippon YSH-70A carbon fiber.

Manufacturer: Nippon (NGF)	Resin Type: Epoxy or Polycyanate Resin Thermal Conductivity: 0.2 W/mK
Carbon Fiber Name: YSH-70A	**Fiber Thermal Conductivity: 250 W/mK**

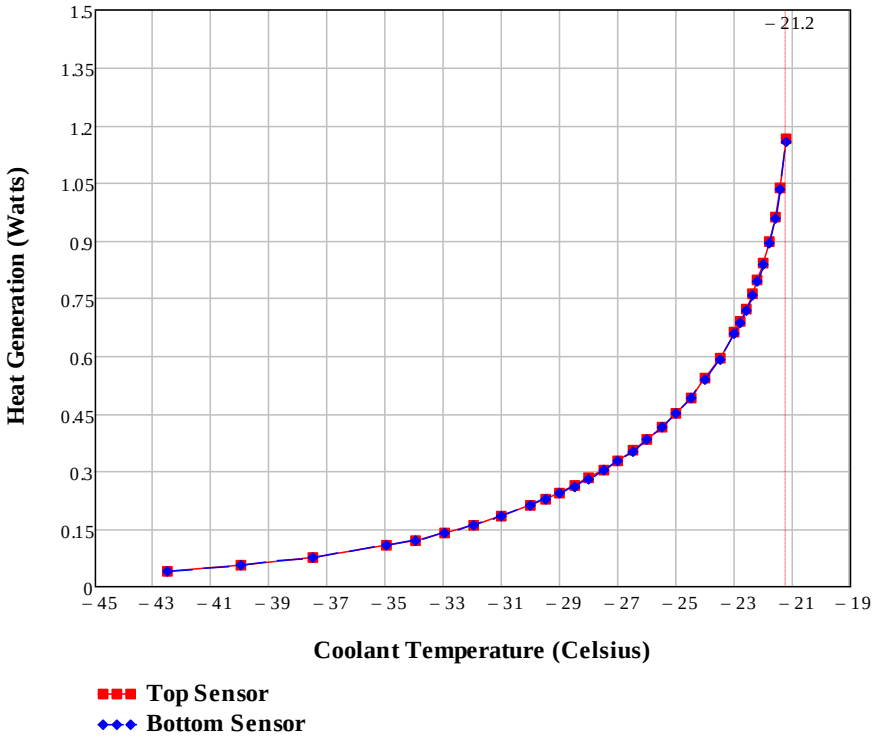

Figure 77: Heat generation of the sensor Vs Coolant Temperature by using Nippon YSH-70A carbon fiber.

Manufacturer: Nippon (NGF)	Resin Type: Epoxy or Polycyanate Resin Thermal Conductivity: 0.2 W/mK
Carbon Fiber Name: XN-60/YSH-60A	**Fiber Thermal Conductivity: 180 W/mK**

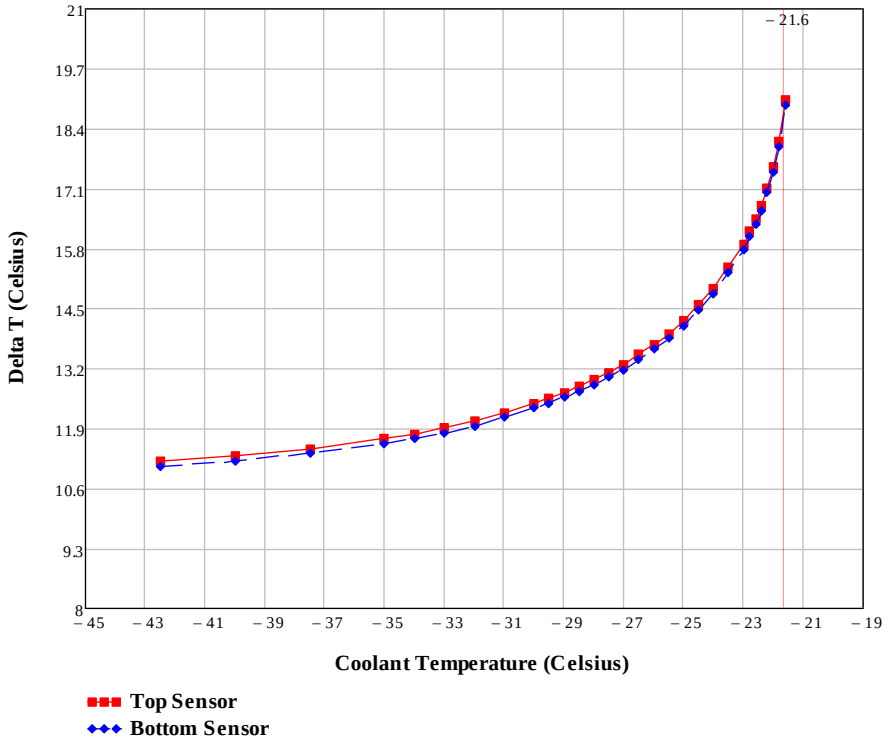

Figure 78: Differential temperature Vs Coolant Temperature by using Nippon XN-60 or YSH-60A carbon fiber.

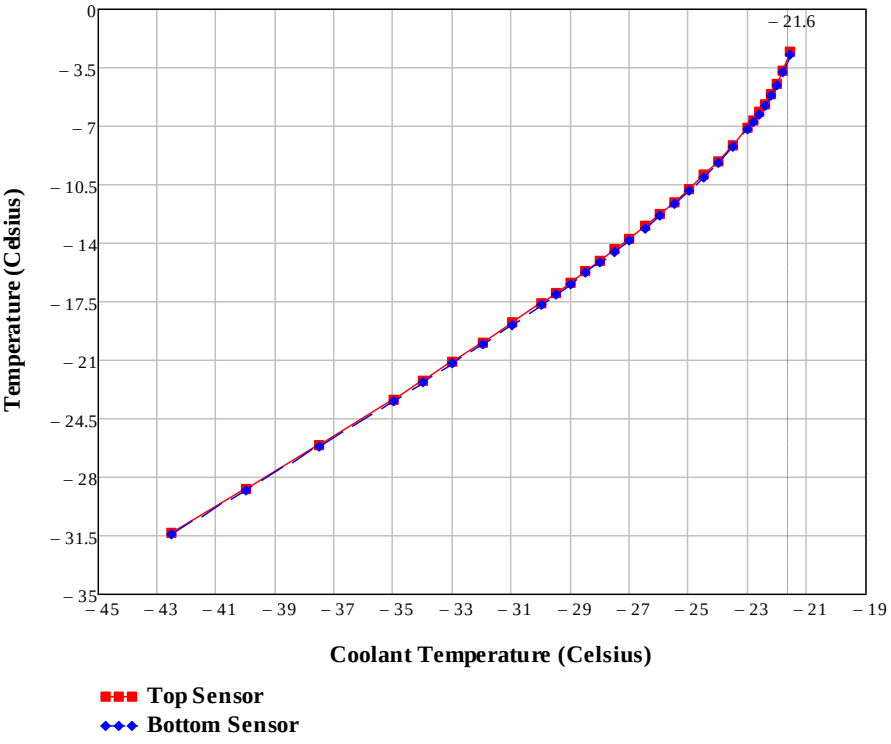

Figure 79: Maximum sensor temperature Vs Coolant temperature by using Nippon XN-60 or YSH-60A carbon fiber.

Manufacturer: Nippon (NGF)	Resin Type: Epoxy or Polycyanate Resin Thermal Conductivity: 0.2 W/mK
Carbon Fiber Name: XN-60/YSH-60A	**Fiber Thermal Conductivity: 180 W/mK**

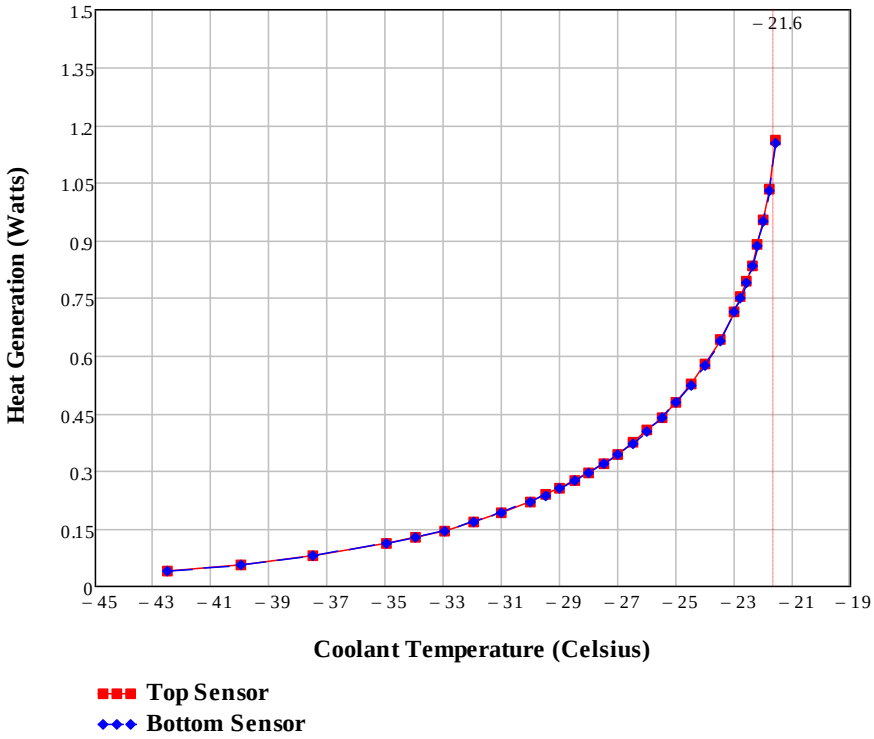

Figure 80: Heat generation of the sensor Vs Coolant Temperature by using Nippon XN-60 or YSH-60A carbon fiber.

Manufacturer: Nippon (NGF)	Resin Type: Epoxy or Polycyanate Resin Thermal Conductivity: 0.2 W/mK
Carbon Fiber Name: YSH-50A	**Fiber Thermal Conductivity: 120 W/mK**

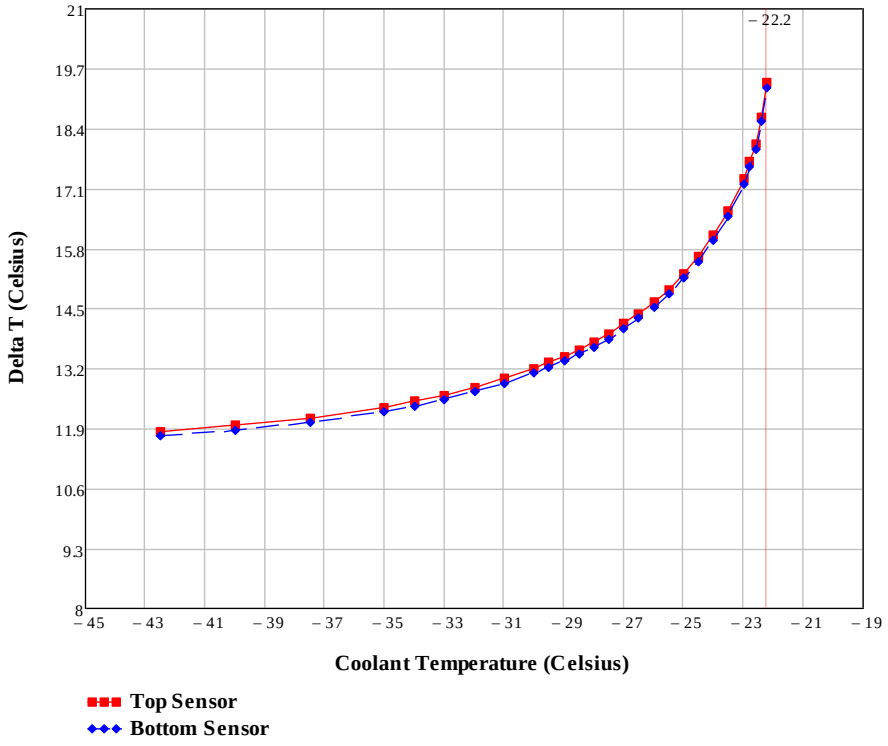

Figure 81: Differential temperature Vs Coolant Temperature by using Nippon YSH-50A carbon fiber.

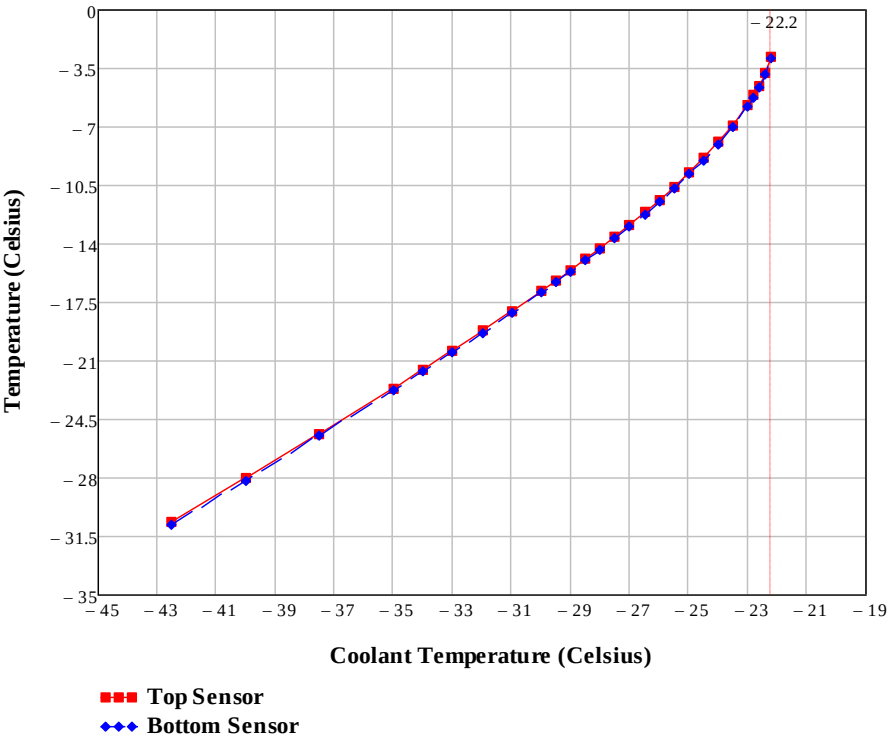

Figure 82: Maximum sensor temperature Vs Coolant temperature by using Nippon YSH-50A carbon fiber.

Manufacturer: Nippon (NGF)	Resin Type: Epoxy or Polycyanate Resin Thermal Conductivity: 0.2 W/mK
Carbon Fiber Name: YSH-50A	**Fiber Thermal Conductivity: 110 W/mK**

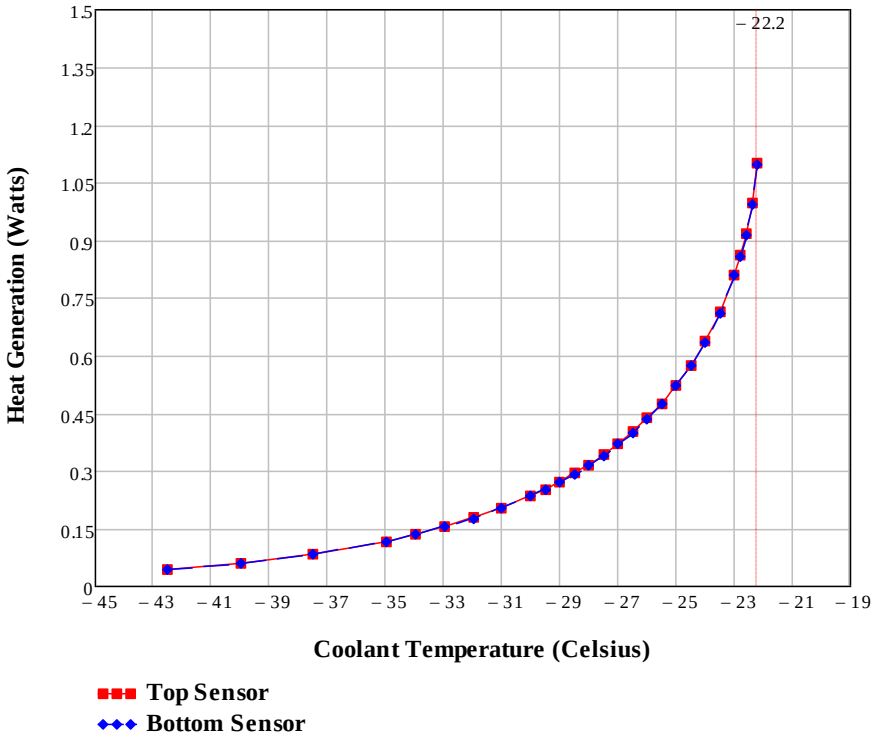

Figure 83: Heat generation of the sensor Vs Coolant Temperature by using Nippon YSH-50A carbon fiber.

THERMAL RUNAWAY RESULTS USING $[0/90]_s$ LAMINATES

Manufacturer	Carbon Fiber Name	Thermal Conductivity (W/mK)	Thermal Runaway Temperature (°C)
Mitsubishi	K13D2U	800	-20.2
	K13C2U	620	-20.4
	K13C6U	580	-20.4
	K63A12	220	-21.6
	K1392U	210	-21.6
	K13916	200	-21.6
	K63712/ K1352U	140	-22.2
	K13312	110	-22.6
Nippon (NGF)	YS-95	600	-20.4
	XN 90/ YS 90A	500	-20.6
	XN 80/YS 80A	320	-21.2
	YSH-70A	250	-21.4
	XN 60/YSH-60A	180	-21.8
	YSH-50A	120	-22.4

Table 6: Thermal runaway temperature of the 2S 1.8 Module, for different carbon fiber types of the laminate 0/90//90/0 with epoxy/polycyanate resin of thermal conductivity 0.2 W/mK.

The laminate was studied taking into account:

-Volume fraction of the fiber $V_f = 0.65$.

-Transverse thermal conductivity of the fiber $k_{f2} = 2.4\ W/mK$.

-Epoxy/polycyanate resin thermal conductity, $k_m = 0.2\ W/mK$.

Manufacturer: Mitsubishi	Resin Type: Epoxy or Polycyanate Resin Thermal Conductivity: 0.2 W/mK
Carbon Fiber Name: K13D2U	**Fiber Thermal Conductivity: 800 W/mK**

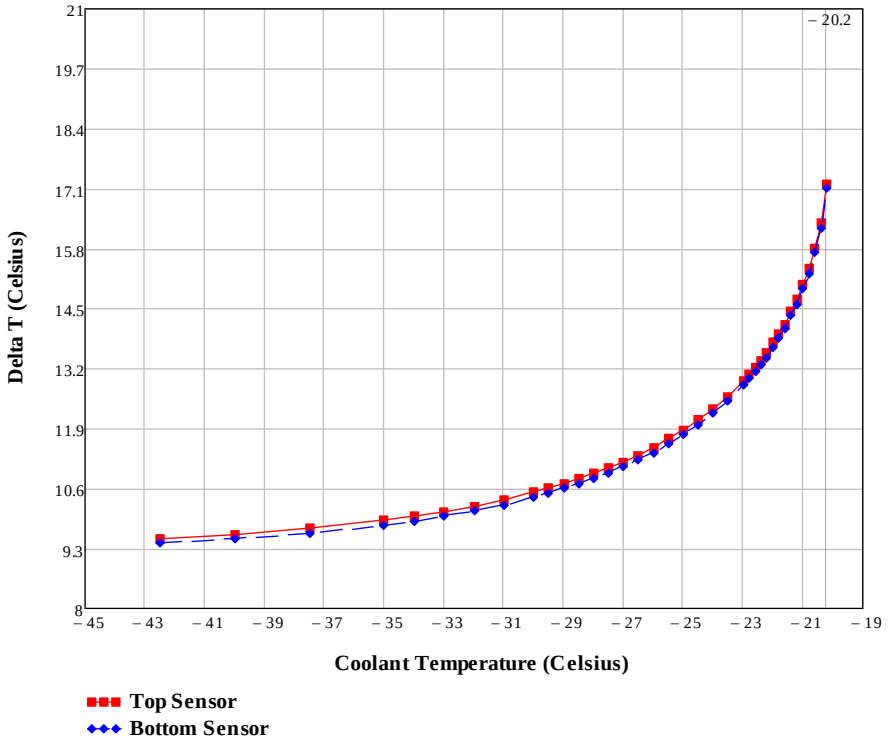

Figure 84: Differential temperature Vs Coolant temperature by using K13D2U carbon fiber.

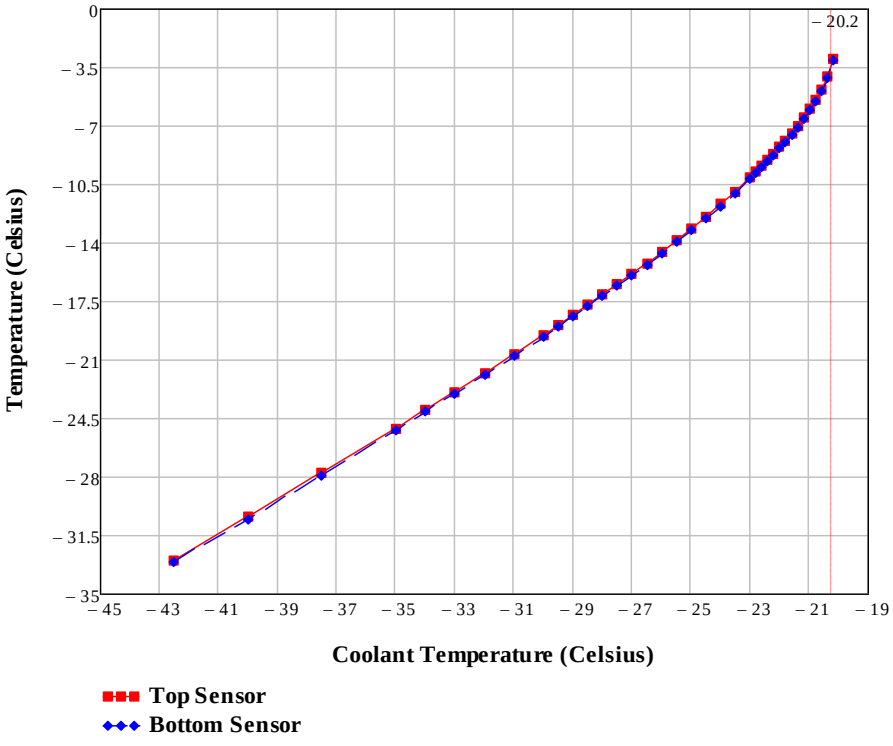

Figure 85: Maximum sensor temperature Vs Coolant temperature by using K13D2U carbon fiber.

Manufacturer: Mitsubishi	Resin Type: Epoxy or Polycyanate Resin Thermal Conductivity: 0.2 W/mK
Carbon Fiber Name: K13D2U	**Fiber Thermal Conductivity: 800 W/mK**

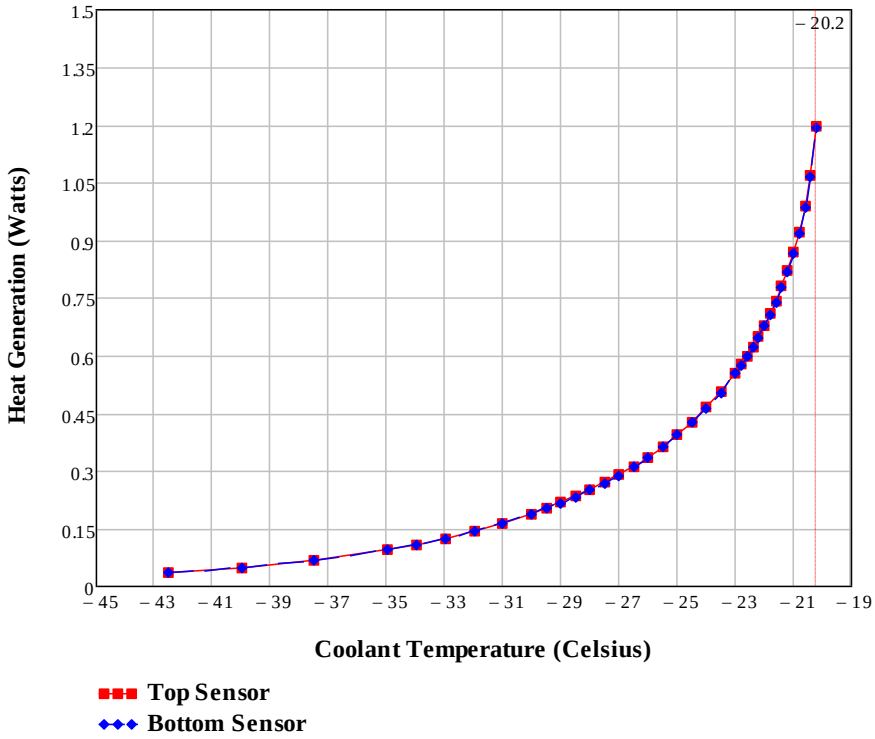

Figure 86: Heat generation of the sensor Vs Coolant Temperature by using K13D2U carbon fiber.

Manufacturer: Mitsubishi	Resin Type: Epoxy or Polycyanate Resin Thermal Conductivity: 0.2 W/mK
Carbon Fiber Name: K13C2U	**Fiber Thermal Conductivity: 620 W/mK**

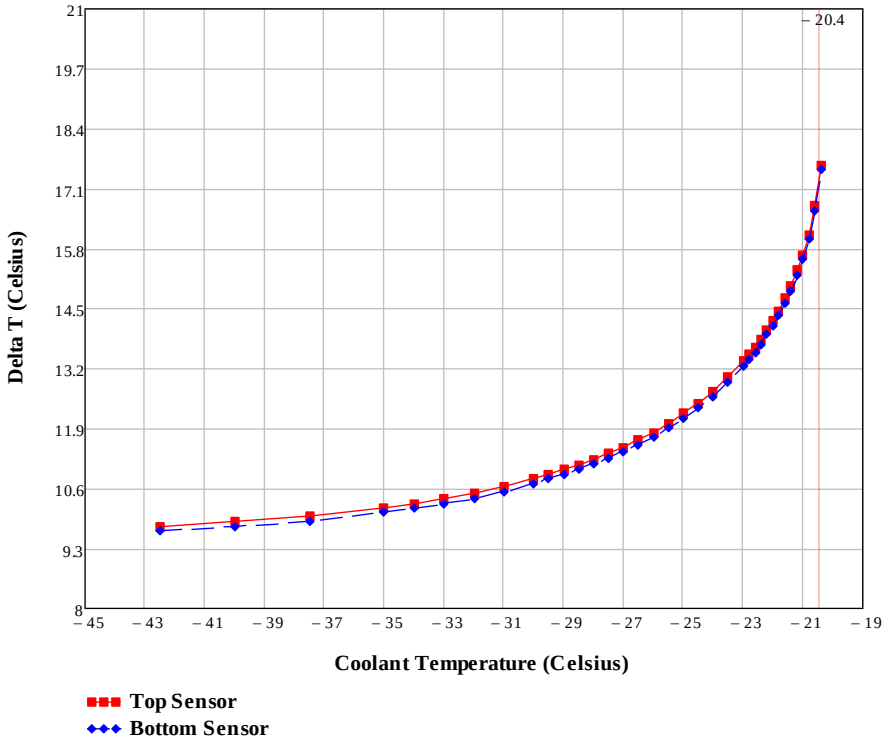

Figure 87: Differential temperature Vs Coolant Temperature by using K13C2U carbon fiber.

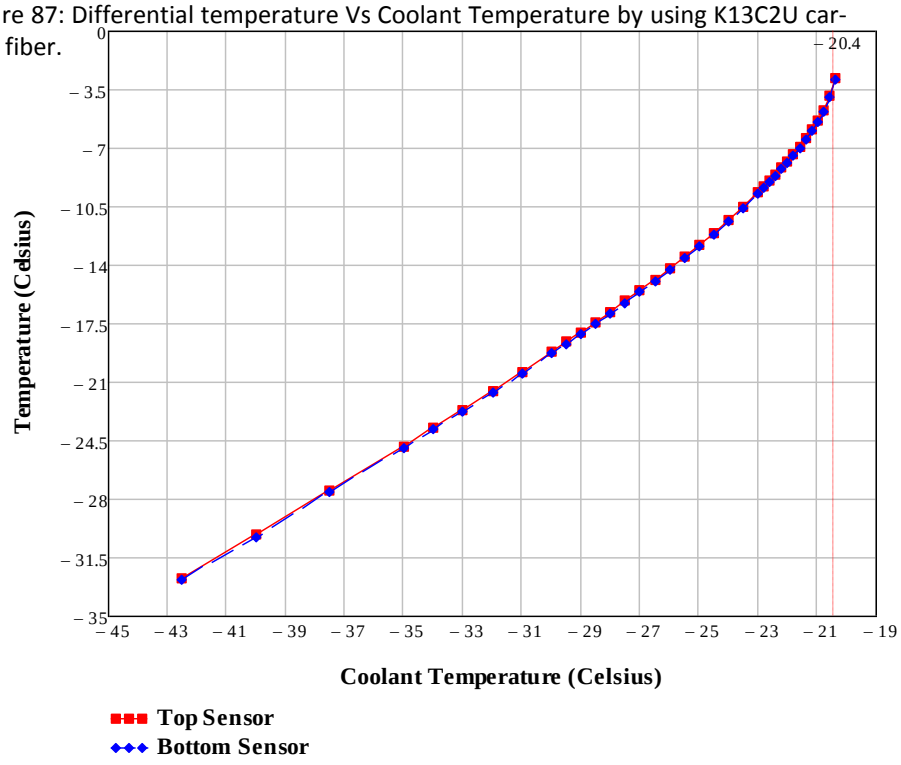

Figure 88: Maximum sensor temperature Vs Coolant Temperature by using K13C2U carbon fiber.

Manufacturer: Mitsubishi	Resin Type: Epoxy or Polycyanate Resin Thermal Conductivity: 0.2 W/mK
Carbon Fiber Name: K13C2U	**Fiber Thermal Conductivity: 620 W/mK**

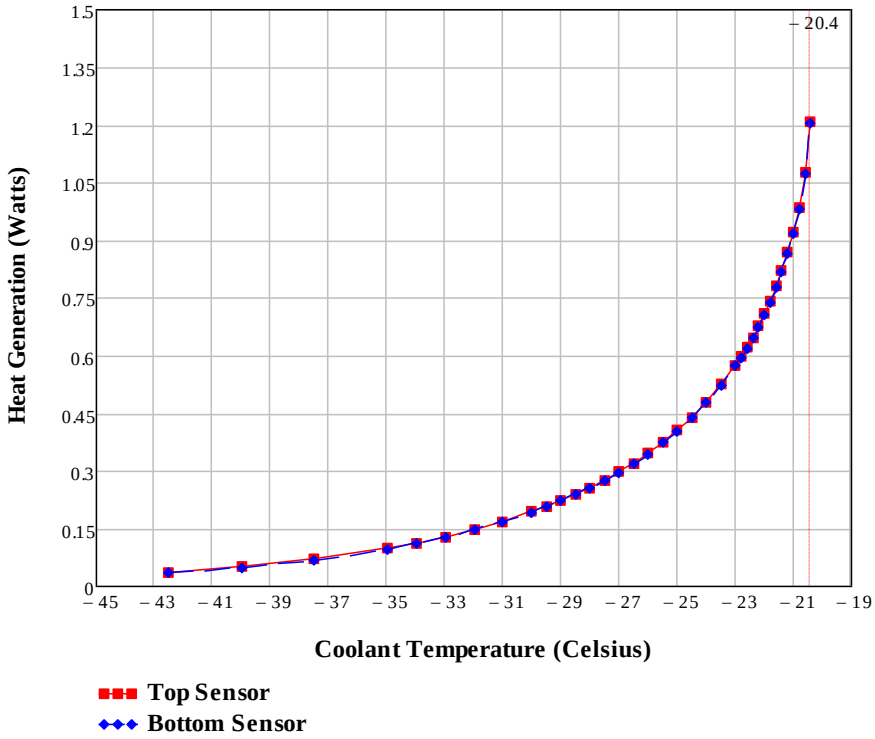

Figure 89: Heat generation of the sensor Vs Coolant Temperature by using K13C2U carbon fiber.

Manufacturer: Mitsubishi	Resin Type: Epoxy or Polycyanate Resin Thermal Conductivity: 0.2 W/mK
Carbon Fiber Name: K13C6U	**Fiber Thermal Conductivity: 580 W/mK**

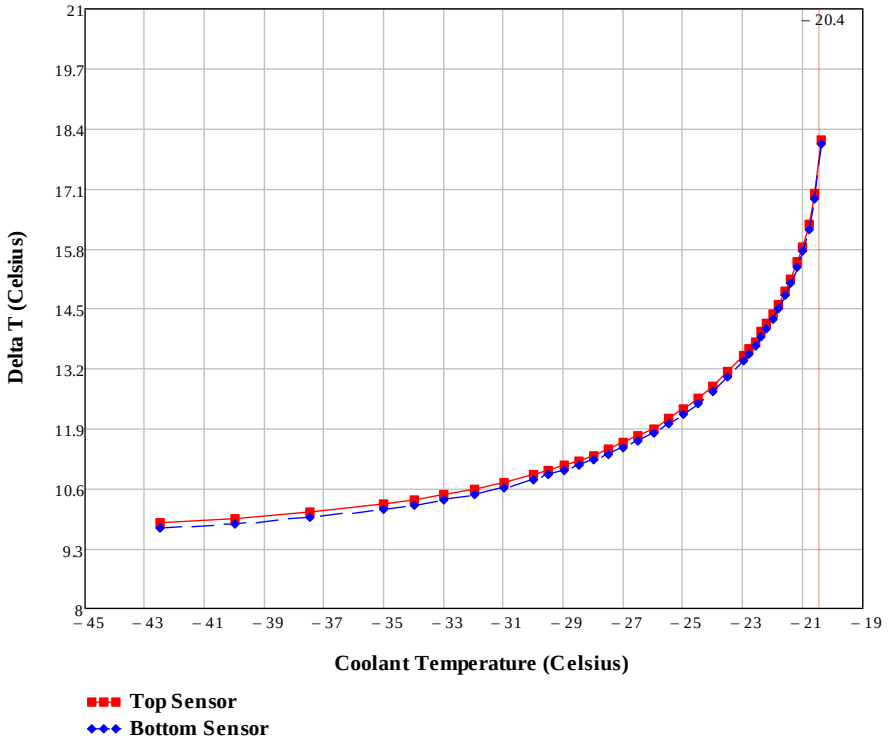

Figure 90: Differential temperature Vs Coolant Temperature by using K13C6U carbon fiber.

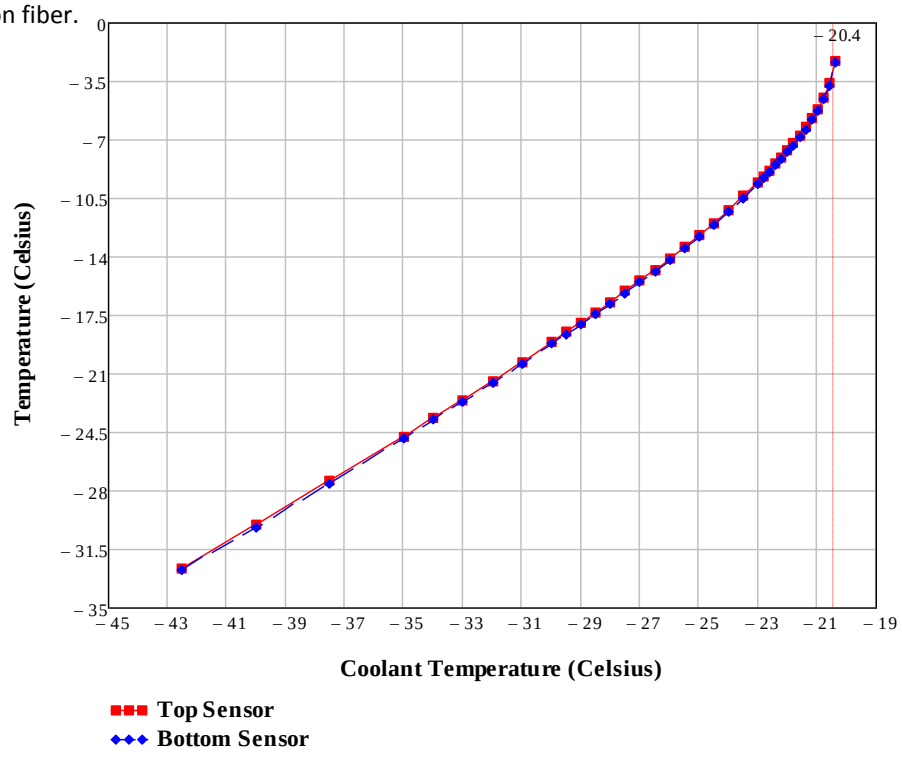

Figure 91: Maximum sensor temperature Vs Coolant Temperature by using K13C6U carbon fiber.

Manufacturer: Mitsubishi	Resin Type: Epoxy or Polycyanate Resin Thermal Conductivity: 0.2 W/mK
Carbon Fiber Name: K13C6U	**Fiber Thermal Conductivity: 580 W/mK**

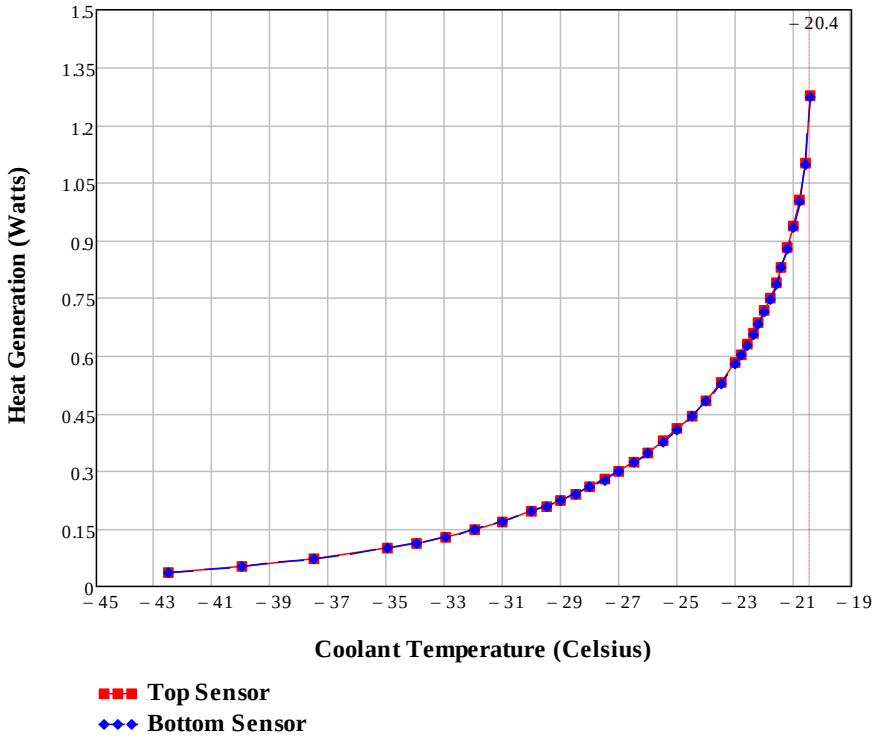

Figure 92: Heat generation of the sensor Vs Coolant Temperature by using K13C6U carbon fiber.

Manufacturer: Mitsubishi	Resin Type: Epoxy or Polycyanate Resin Thermal Conductivity: 0.2 W/mK
Carbon Fiber Name: K63A12	**Fiber Thermal Conductivity: 220 W/mK**

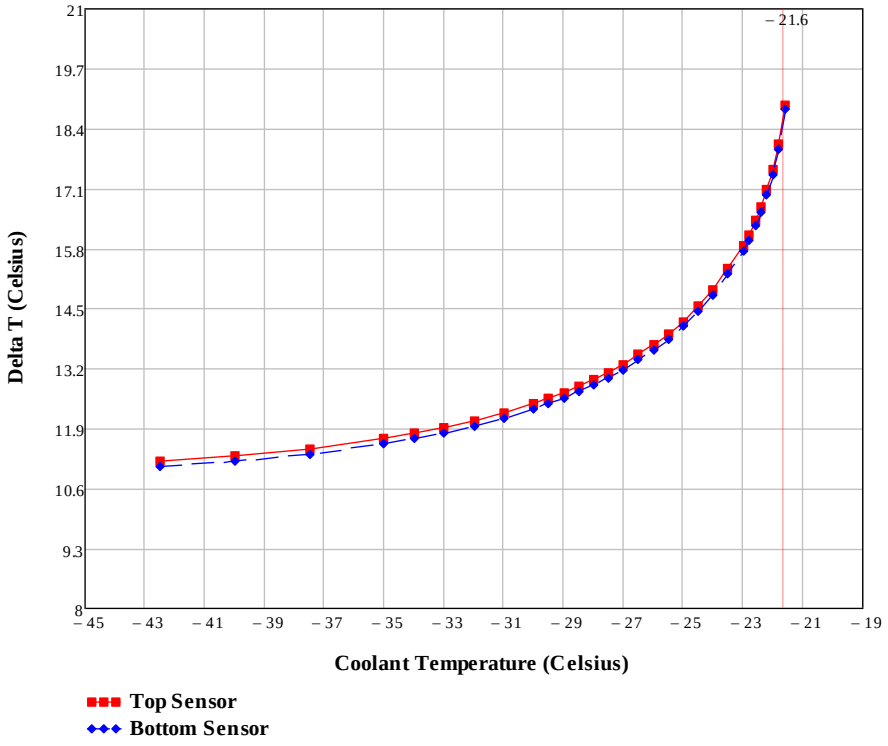

Figure 93: Differential temperature Vs Coolant Temperature by using K13A12 carbon fiber

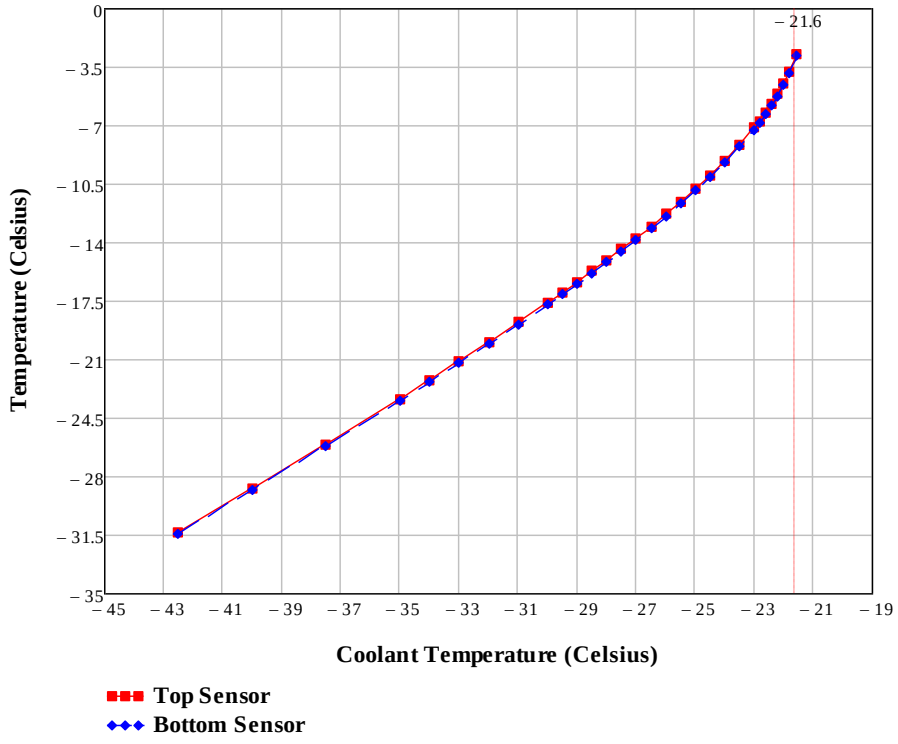

Figure 94: Maximum sensor temperature Vs Coolant temperature by using K13D2U carbon fiber.

Manufacturer: Mitsubishi	Resin Type: Epoxy or Polycyanate Resin Thermal Conductivity: 0.2 W/mK
Carbon Fiber Name: K63A12	**Fiber Thermal Conductivity: 220 W/mK**

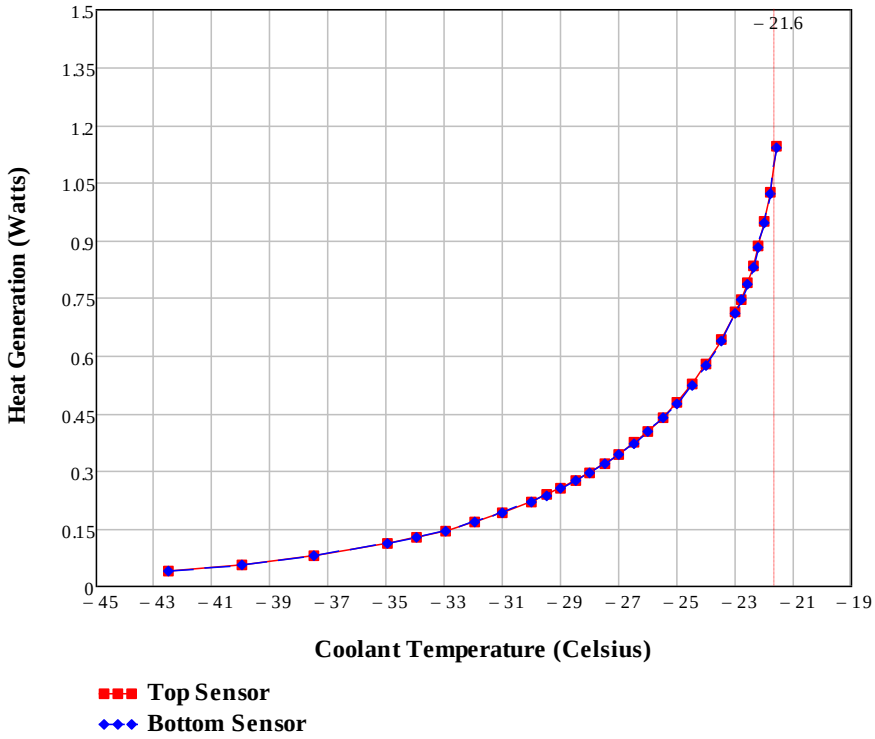

Figure 95: Heat generation of the sensor Vs Coolant Temperature by using K63A12 carbon fiber.

Manufacturer: Mitsubishi	Resin Type: Epoxy or Polycyanate Resin Thermal Conductivity: 0.2 W/mK
Carbon Fiber Name: K1392U	**Fiber Thermal Conductivity: 210 W/mK**

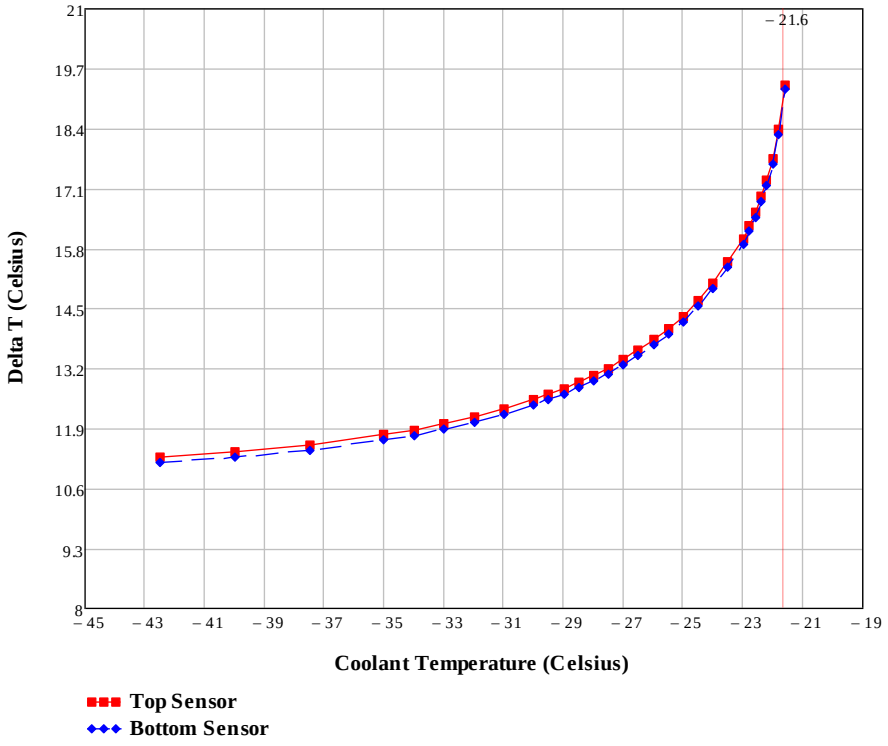

Figure 96: Differential temperature Vs Coolant Temperature by using K1392U carbon fiber.

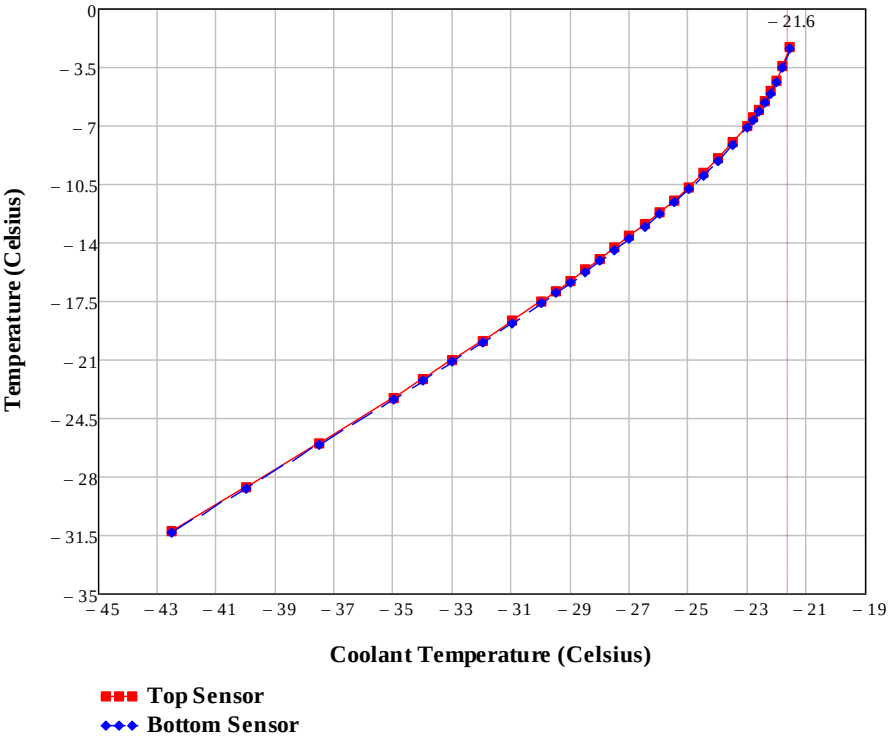

Figure 97: Maximum sensor temperature Vs Coolant temperature by using K1392U carbon fiber.

Manufacturer: Mitsubishi	Resin Type: Epoxy or Polycyanate Resin Thermal Conductivity: 0.2 W/mK
Carbon Fiber Name: K1392U	**Fiber Thermal Conductivity: 210 W/mK**

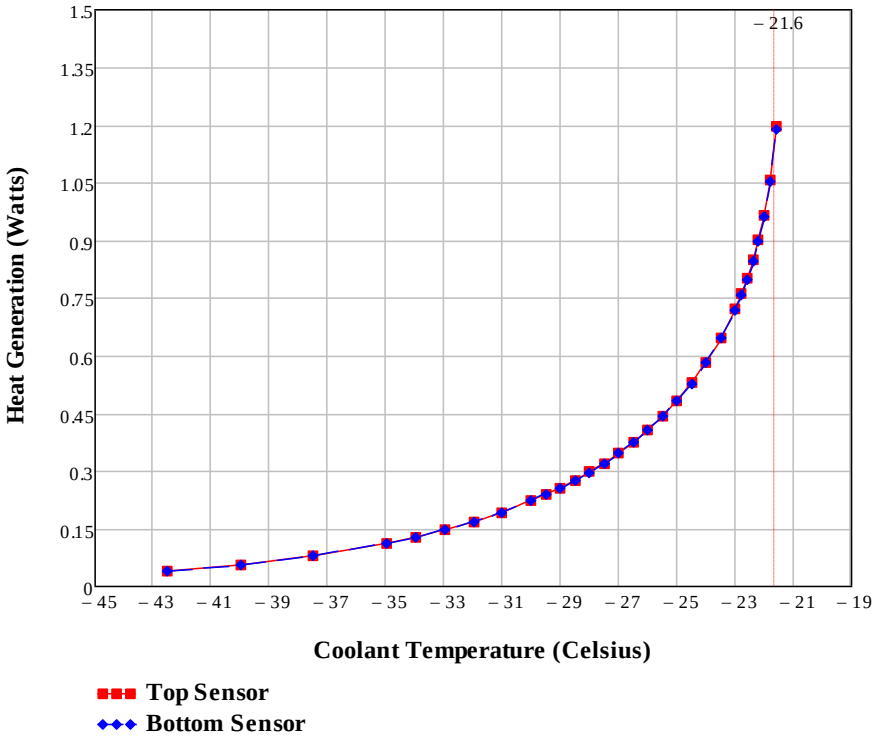

Figure 98: Heat generation of the sensor Vs Coolant Temperature by using K1392U carbon fiber.

Manufacturer: Mitsubishi	Resin Type: Epoxy or Polycyanate Resin Thermal Conductivity: 0.2 W/mK
Carbon Fiber Name: K13916	**Fiber Thermal Conductivity: 200 W/mK**

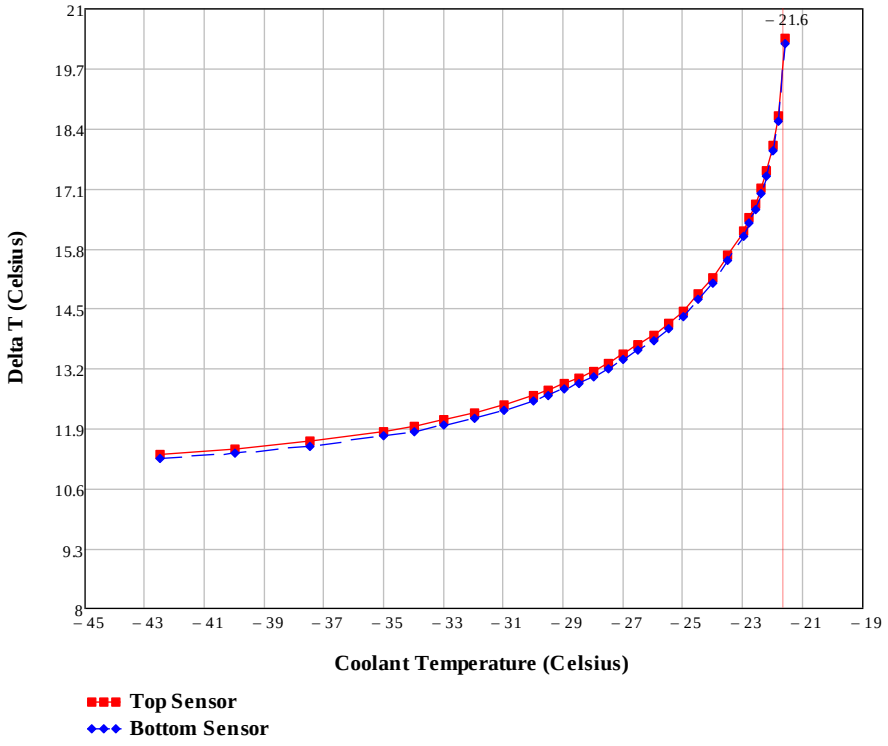

Figure 99: Differential temperature Vs Coolant Temperature by using K13916 carbon fiber.

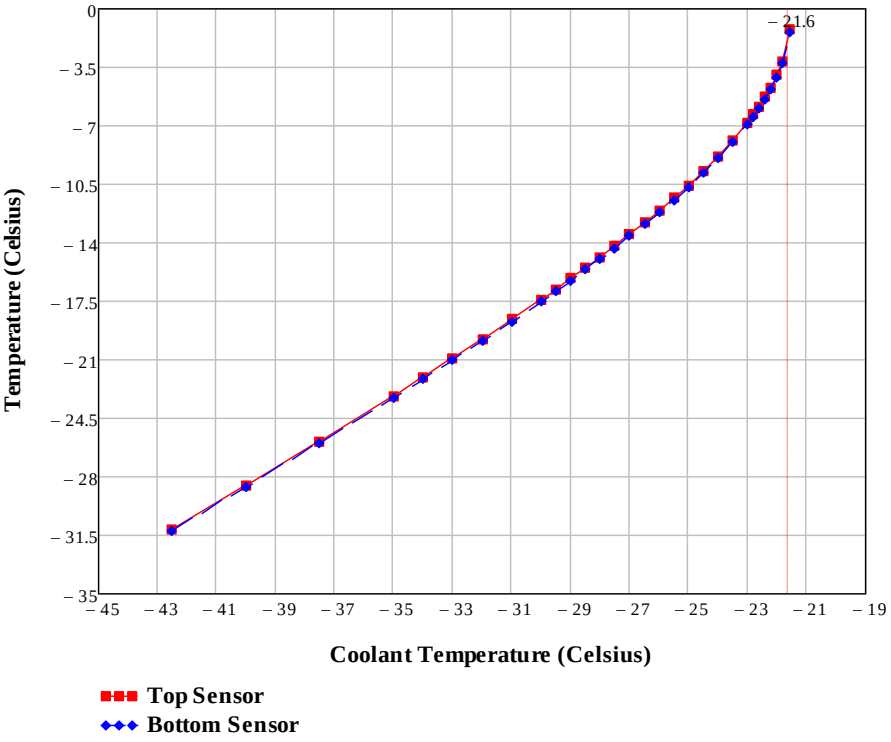

Figure 100: Maximum sensor temperature Vs Coolant temperature by using K13916 carbon fiber.

Manufacturer: Mitsubishi	Resin Type: Epoxy or Polycyanate Resin Thermal Conductivity: 0.2 W/mK
Carbon Fiber Name: K13916	**Fiber Thermal Conductivity: 200 W/mK**

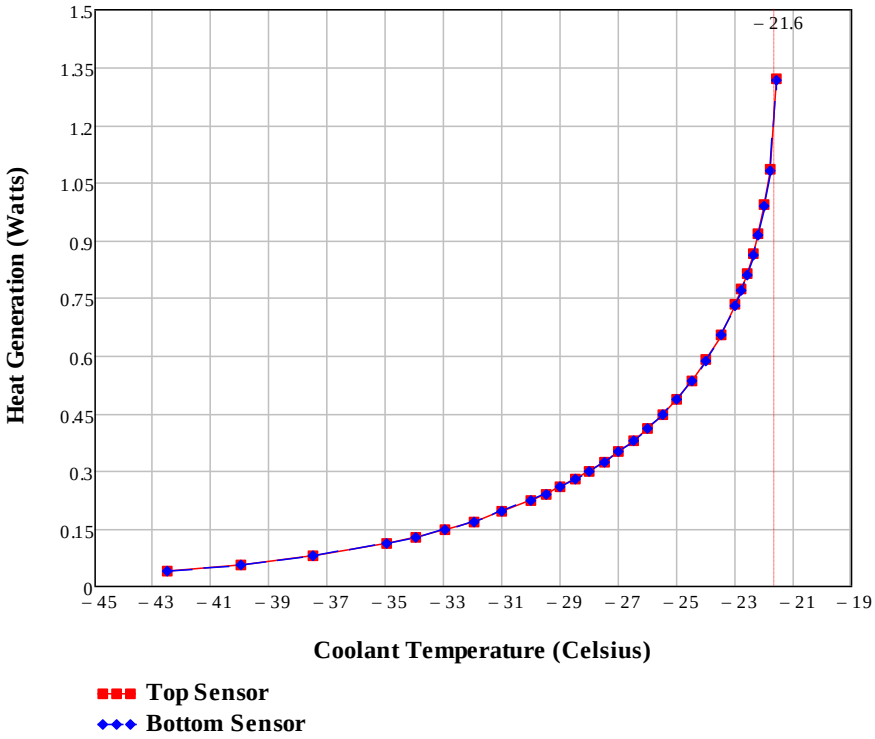

Figure 101: Heat generation of the sensor Vs Coolant Temperature by using K13916 carbon fiber.

Manufacturer: Mitsubishi	Resin Type: Epoxy or Polycyanate Resin Thermal Conductivity: 0.2 W/mK
Carbon Fiber Name: K63712/K1352U	**Fiber Thermal Conductivity: 140 W/mK**

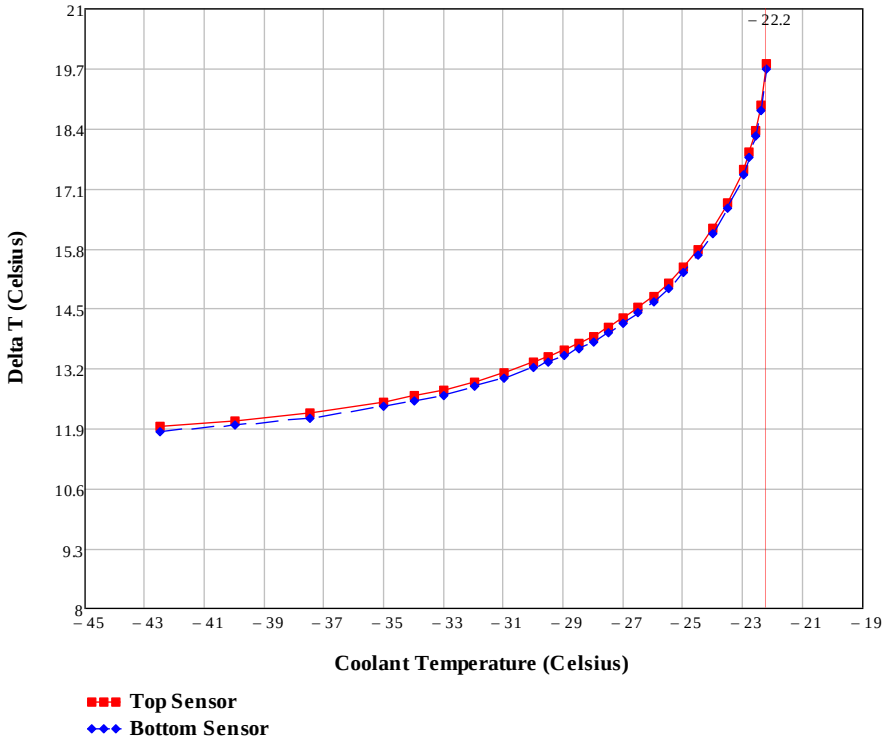

Figure 102: Differential temperature Vs Coolant Temperature by using K63712 or K1352U carbon fiber.

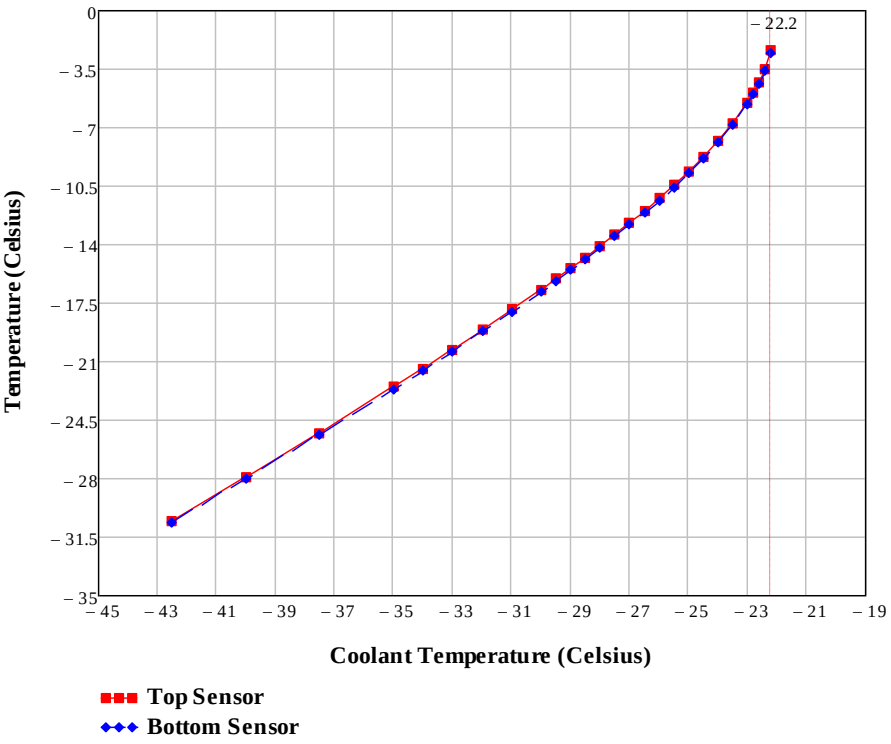

Figure 103: Maximum sensor temperature Vs Coolant temperature by using K63712 or K1352U carbon fiber.

Manufacturer: Mitsubishi	Resin Type: Epoxy or Polycyanate Resin Thermal Conductivity: 0.2 W/mK
Carbon Fiber Name: K63712/K1352U	**Fiber Thermal Conductivity: 140 W/mK**

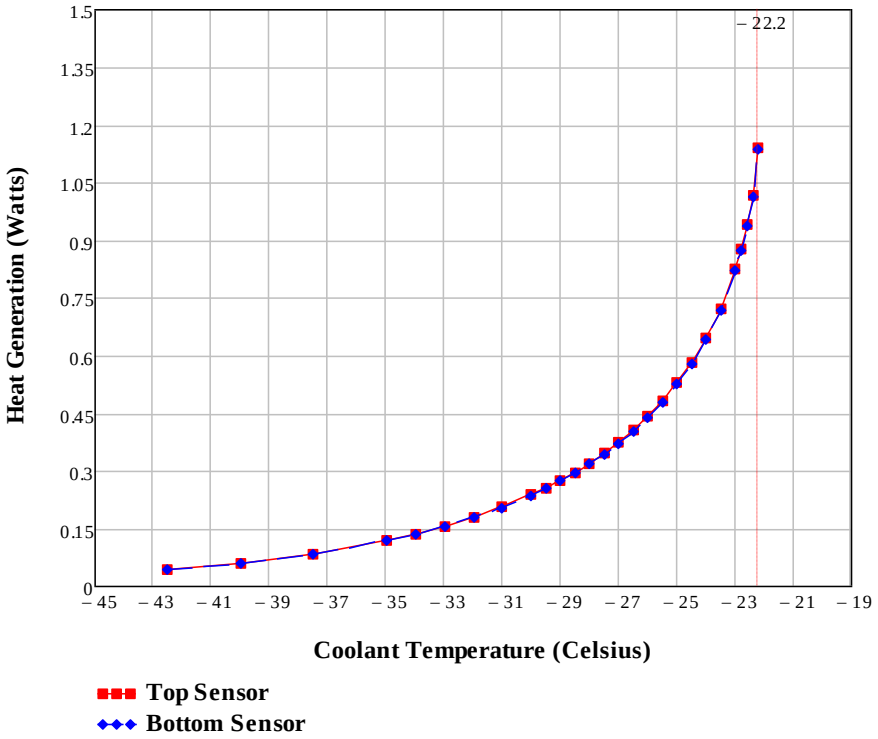

Figure 104: Heat generation of the sensor Vs Coolant Temperature by using K63712 or K1352U carbon fiber.

Manufacturer: Mitsubishi	Resin Type: Epoxy or Polycyanate Resin Thermal Conductivity: 0.2 W/mK
Carbon Fiber Name: K13312	**Fiber Thermal Conductivity: 110 W/mK**

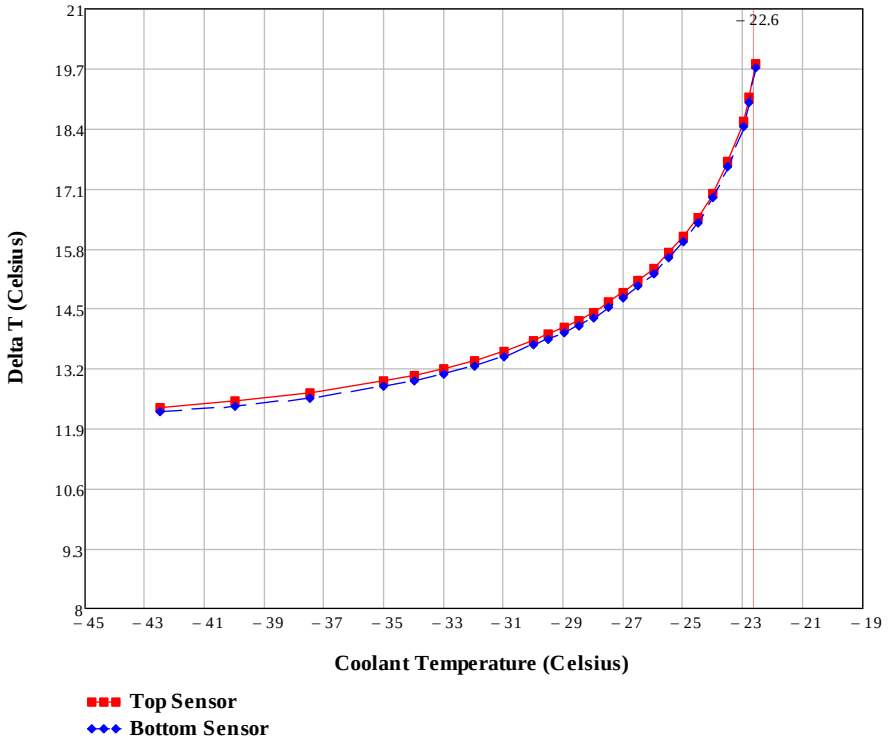

Figure 105: Differential temperature Vs Coolant Temperature by using K13312 carbon fiber.

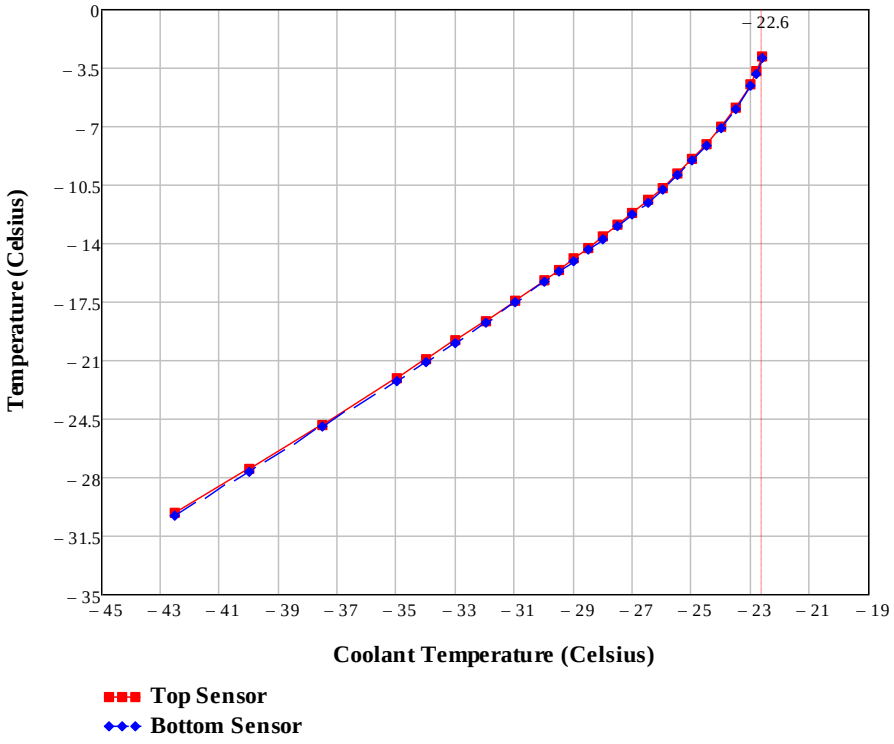

Figure 106: Maximum sensor temperature Vs Coolant temperature by using K13312 carbon fiber.

Manufacturer: Mitsubishi	Resin Type: Epoxy or Polycyanate Resin Thermal Conductivity: 0.2 W/mK
Carbon Fiber Name: K13312	**Fiber Thermal Conductivity: 110 W/mK**

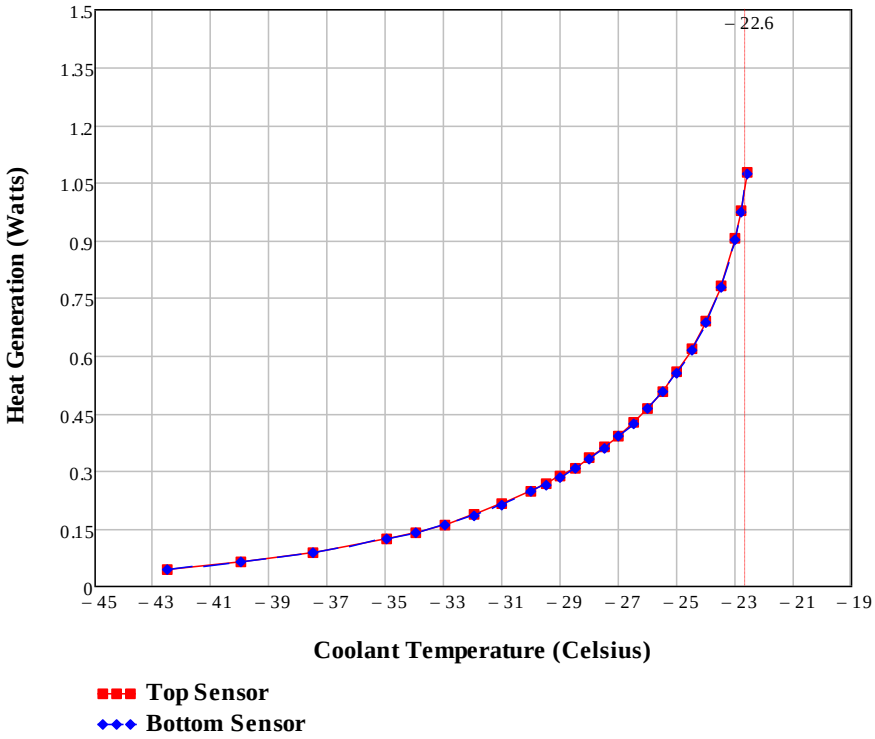

Figure 107: Heat generation of the sensor Vs Coolant Temperature by using K13312 carbon fiber.

Manufacturer: Nippon (NGF)	Resin Type: Epoxy or Polycyanate Resin Thermal Conductivity: 0.2 W/mK
Carbon Fiber Name: YS-95	**Fiber Thermal Conductivity: 600 W/mK**

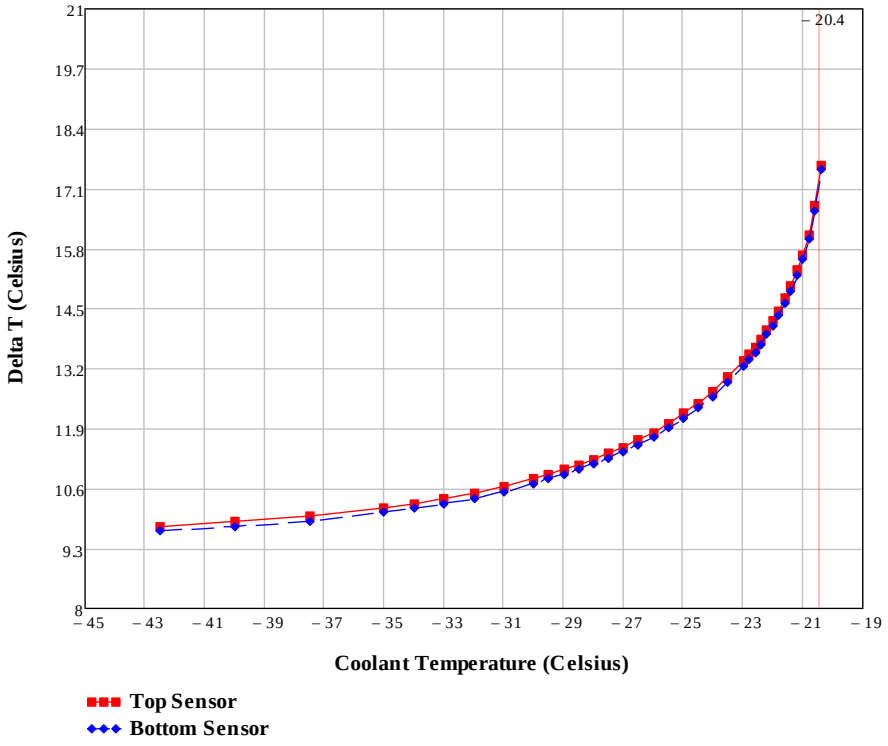

Figure 108: Differential temperature Vs Coolant Temperature by using Nippon YS-95 carbon fiber.

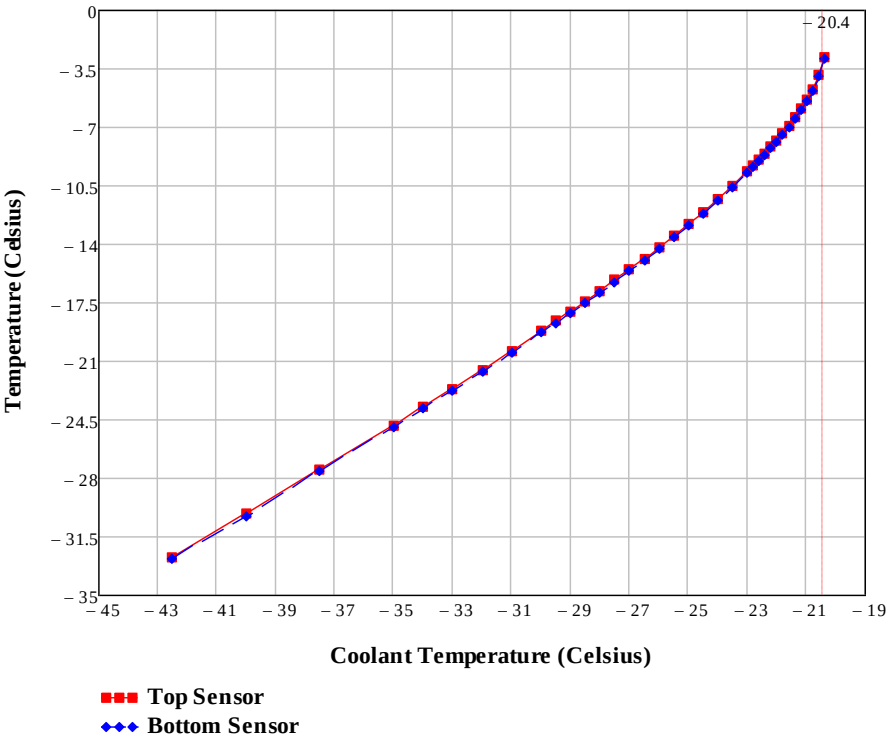

Figure 109: Maximum sensor temperature Vs Coolant temperature by using Nippon YS-95 carbon fiber.

Manufacturer: Nippon (NGF)	Resin Type: Epoxy or Polycyanate Resin Thermal Conductivity: 0.2 W/mK
Carbon Fiber Name: YS-95	**Fiber Thermal Conductivity: 600 W/mK**

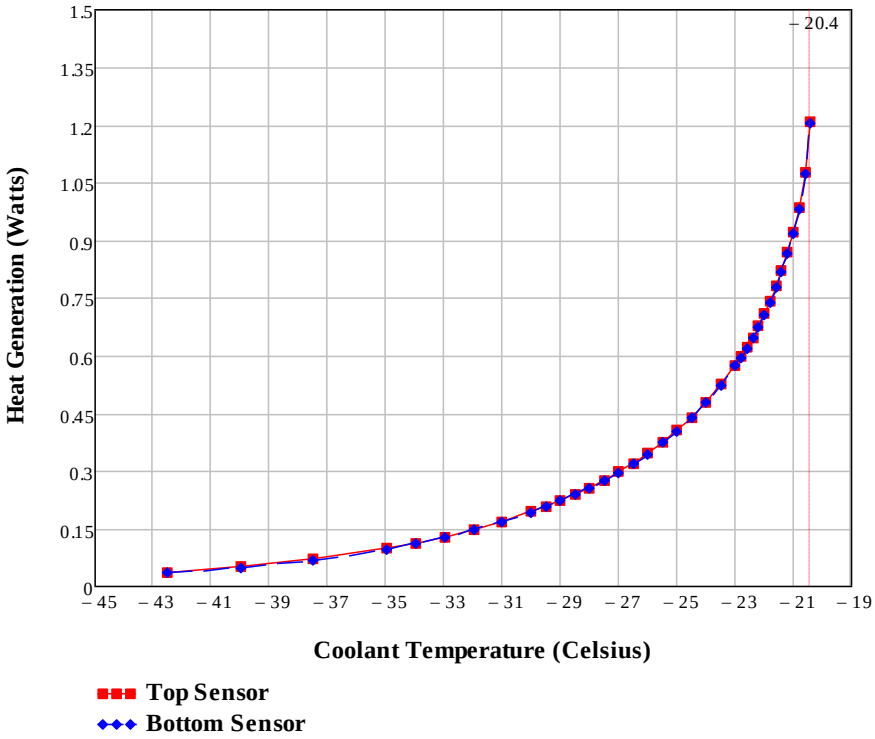

Figure 110: Heat generation of the sensor Vs Coolant Temperature by using Nippon YS-95 carbon fiber.

Manufacturer: Nippon (NGF)	Resin Type: Epoxy or Polycyanate Resin Thermal Conductivity: 0.2 W/mK
Carbon Fiber Name: XN-90/YS-90A	**Fiber Thermal Conductivity: 500 W/mK**

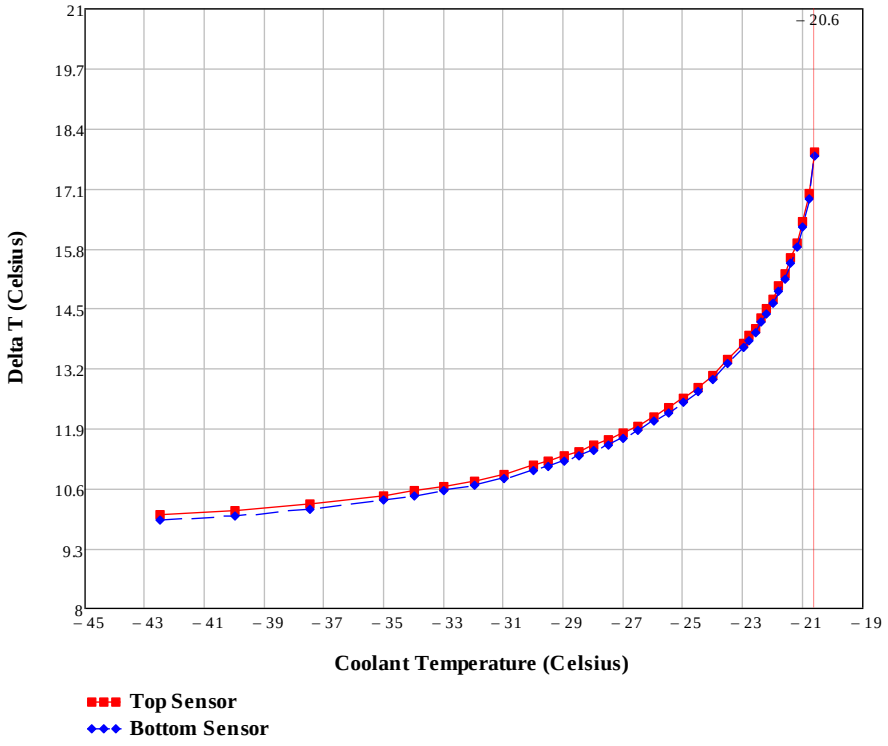

Figure 111: Differential temperature Vs Coolant Temperature by using Nippon XN-90 or YS-90A carbon fiber.

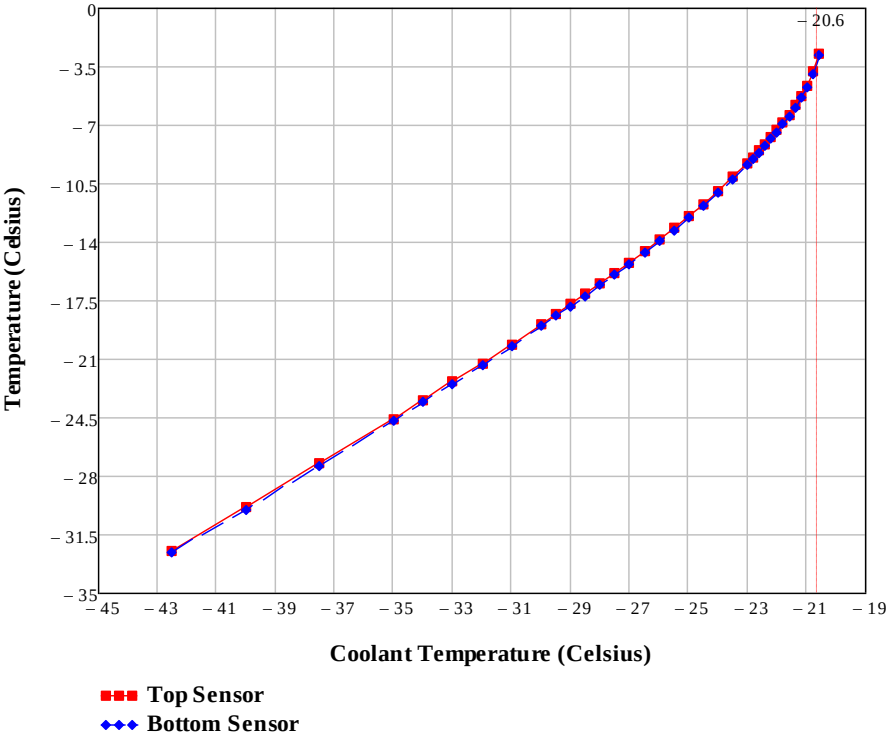

Figure 112: Maximum sensor temperature Vs Coolant temperature by using Nippon XN-90 or YS-90A carbon fiber.

Manufacturer: Nippon (NGF)	Resin Type: Epoxy or Polycyanate Resin Thermal Conductivity: 0.2 W/mK
Carbon Fiber Name: XN-90/YS-90A	**Fiber Thermal Conductivity: 500 W/mK**

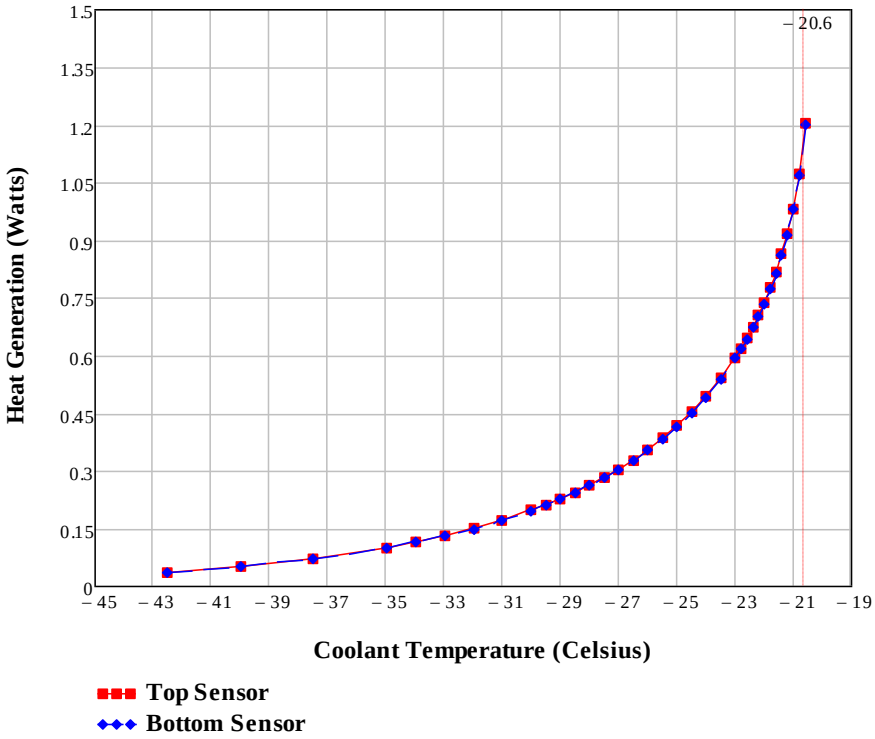

Figure 113: Heat generation of the sensor Vs Coolant Temperature by using Nippon XN-90 or YS-90A carbon fiber.

Manufacturer: Nippon (NGF)	Resin Type: Epoxy or Polycyanate Resin Thermal Conductivity: 0.2 W/mK
Carbon Fiber Name: XN-80/YS-80A	**Fiber Thermal Conductivity: 320 W/mK**

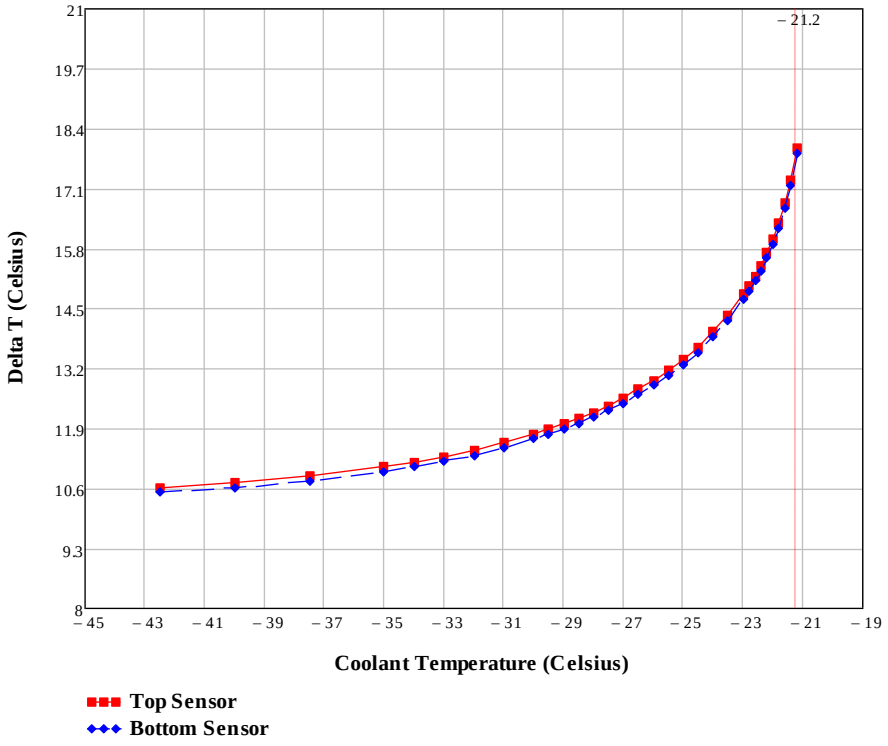

Figure 114: Differential temperature Vs Coolant Temperature by using Nippon XN-80 or YS-80A carbon fiber.

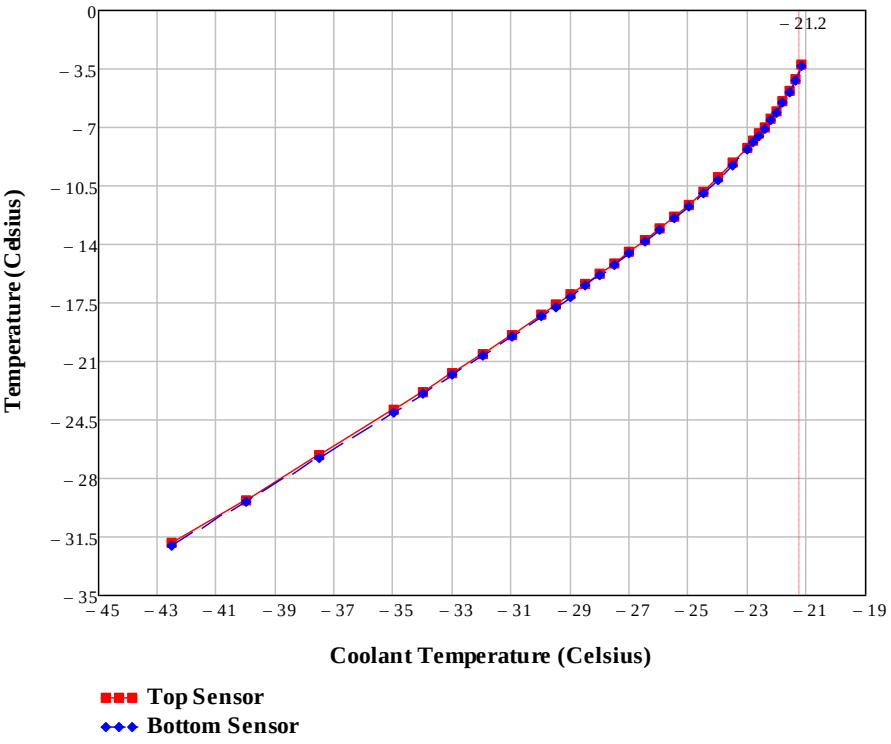

Figure 115: Maximum sensor temperature Vs Coolant temperature by using Nippon XN-80 or YS-80A carbon fiber.

Manufacturer: Nippon (NGF)	Resin Type: Epoxy or Polycyanate Resin Thermal Conductivity: 0.2 W/mK
Carbon Fiber Name: XN-80/YS-80A	**Fiber Thermal Conductivity: 320 W/mK**

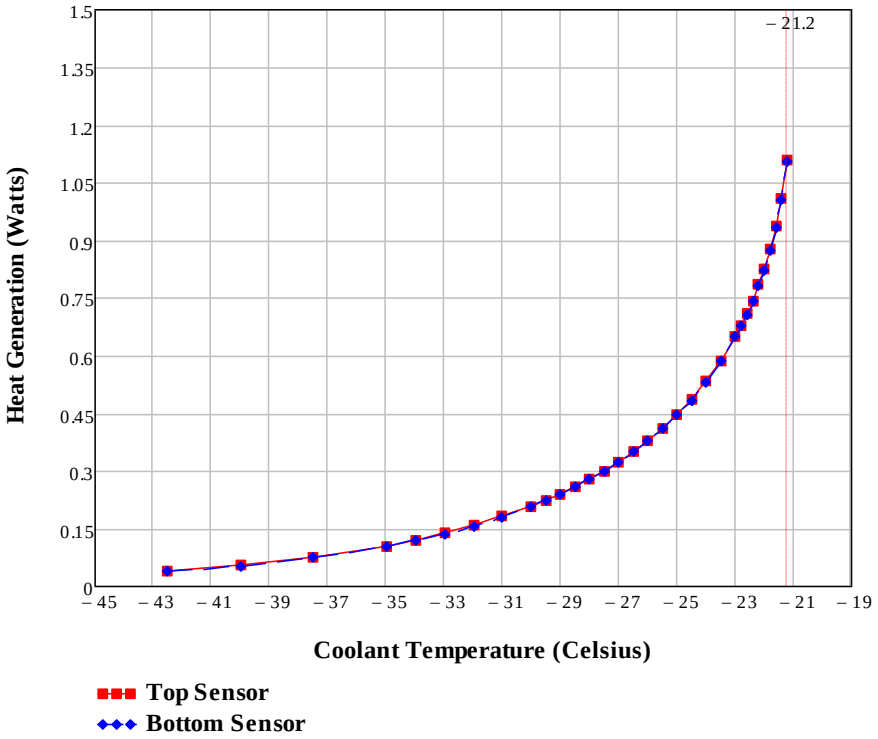

Figure 116: Heat generation of the sensor Vs Coolant Temperature by using Nippon XN-80 or YS-80A carbon fiber.

Manufacturer: Nippon (NGF)	Resin Type: Epoxy or Polycyanate Resin Thermal Conductivity: 0.2 W/mK
Carbon Fiber Name: YSH-70A	**Fiber Thermal Conductivity: 250 W/mK**

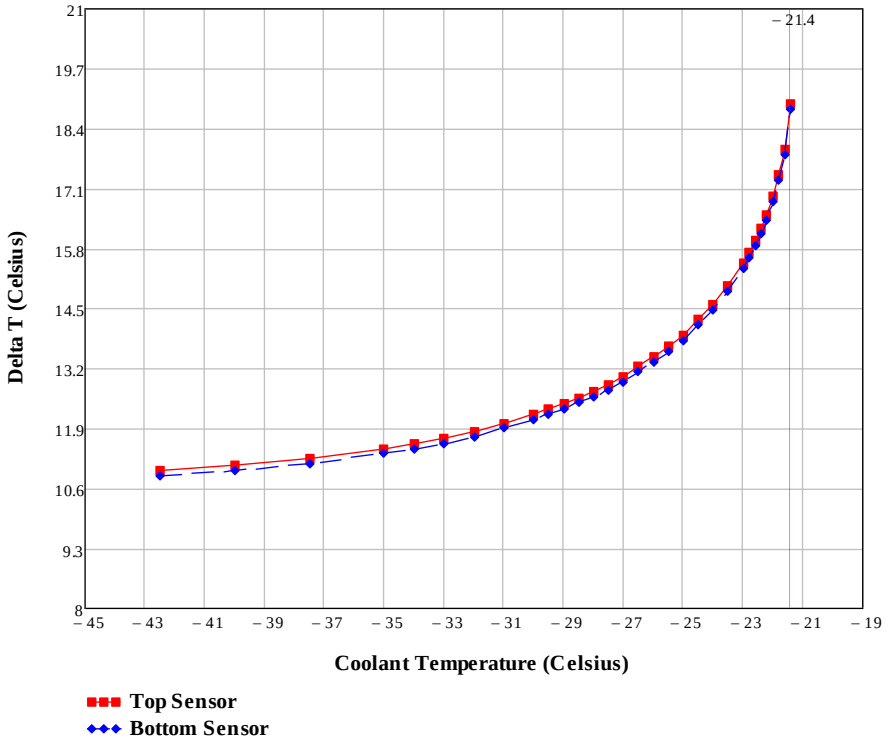

Figure 117: Differential temperature Vs Coolant Temperature by using Nippon YSH-70A carbon fiber.

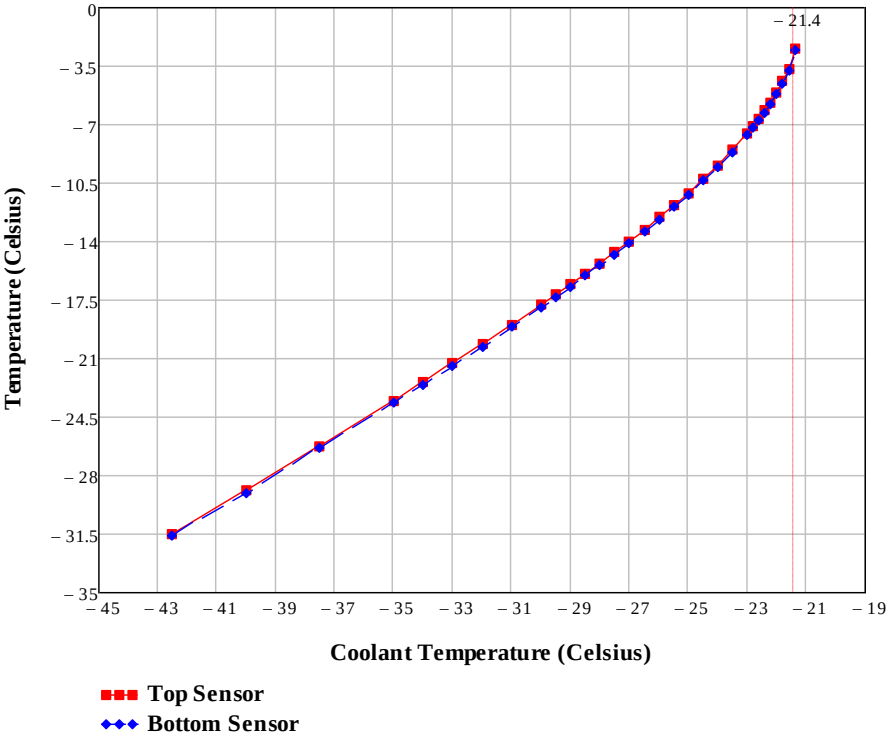

Figure 118: Maximum sensor temperature Vs Coolant temperature by using Nippon YSH-70A carbon fiber.

Manufacturer: Nippon (NGF)	Resin Type: Epoxy or Polycyanate Resin Thermal Conductivity: 0.2 W/mK
Carbon Fiber Name: YSH-70A	**Fiber Thermal Conductivity: 250 W/mK**

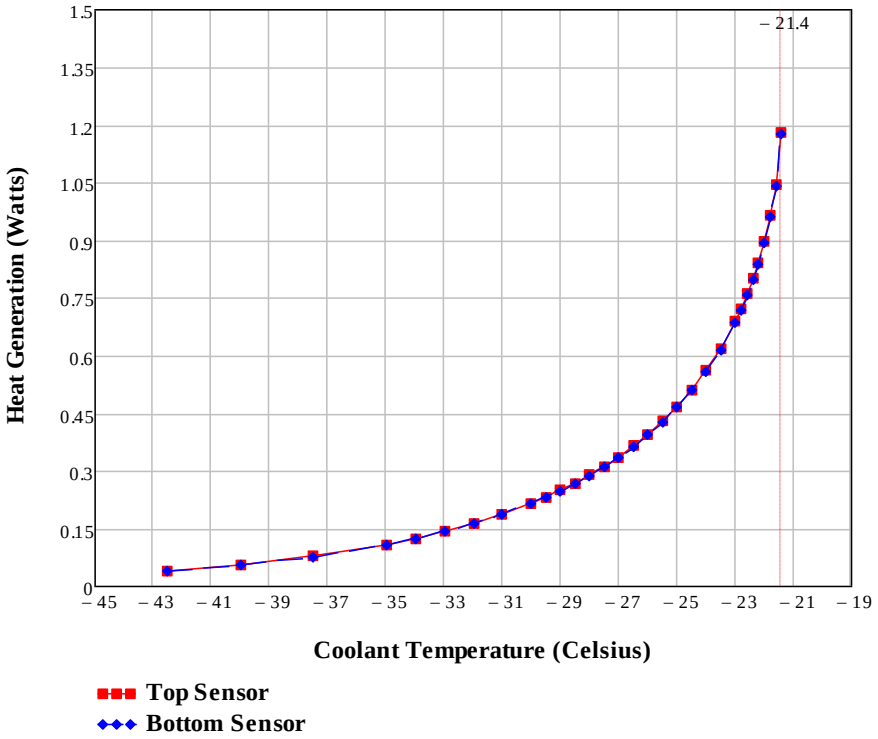

Figure 119: Heat generation of the sensor Vs Coolant Temperature by using Nippon YSH-70A carbon fiber.

Manufacturer: Nippon (NGF)	Resin Type: Epoxy or Polycyanate Resin Thermal Conductivity: 0.2 W/mK
Carbon Fiber Name: XN-60/YSH-60A	**Fiber Thermal Conductivity: 180 W/mK**

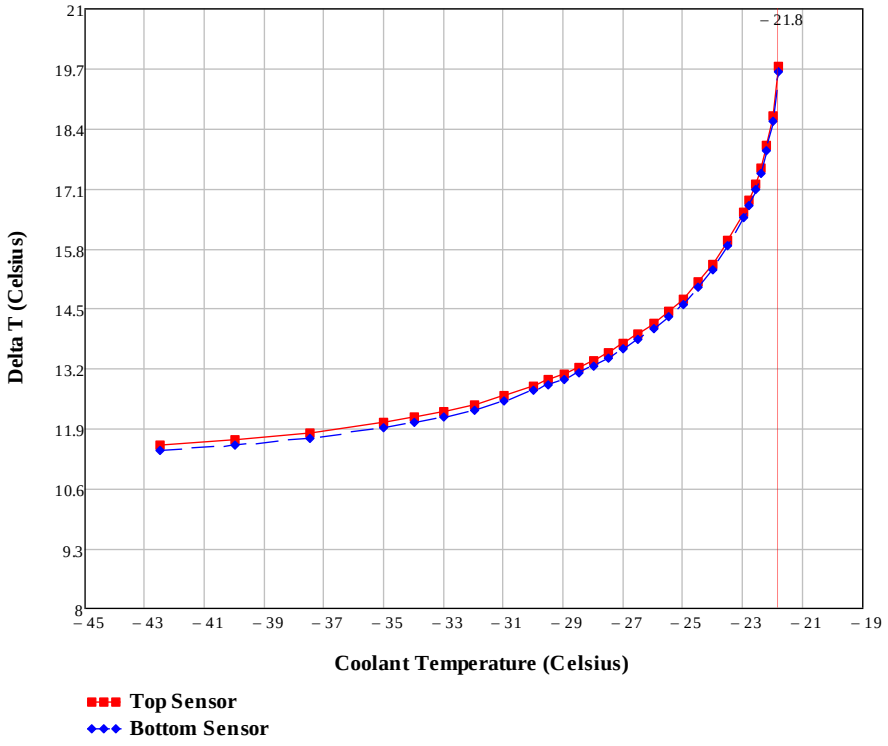

Figure 120: Differential temperature Vs Coolant Temperature by using Nippon XN-60 or YSH-60A carbon fiber.

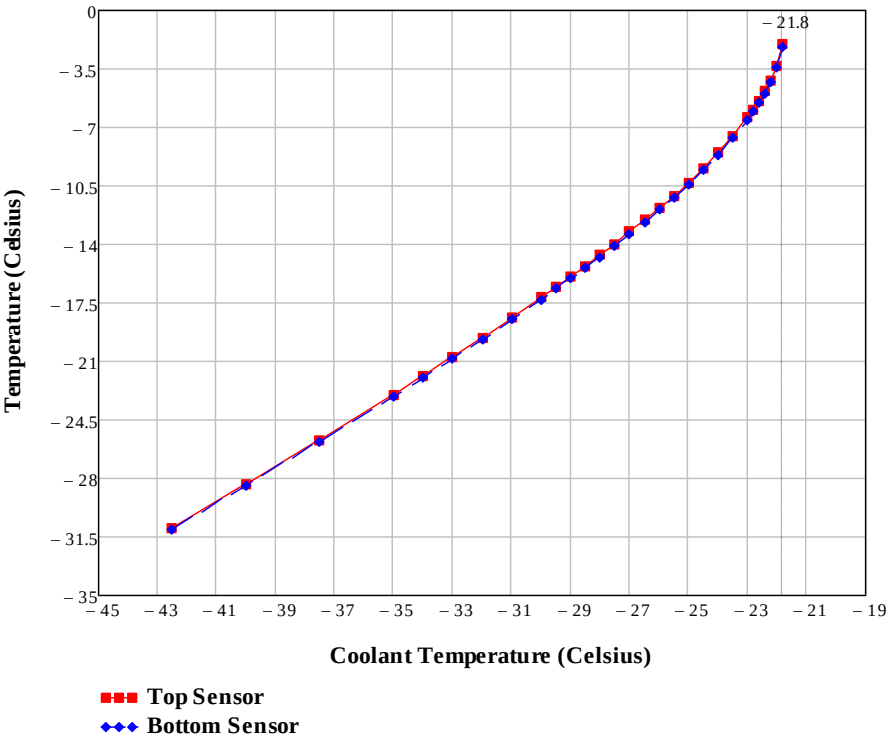

Figure 121: Maximum sensor temperature Vs Coolant temperature by using Nippon XN-60 or YSH-60A carbon fiber.

Manufacturer: Nippon (NGF)	Resin Type: Epoxy or Polycyanate Resin Thermal Conductivity: 0.2 W/mK
Carbon Fiber Name: XN-60/YSH-60A	**Fiber Thermal Conductivity: 180 W/mK**

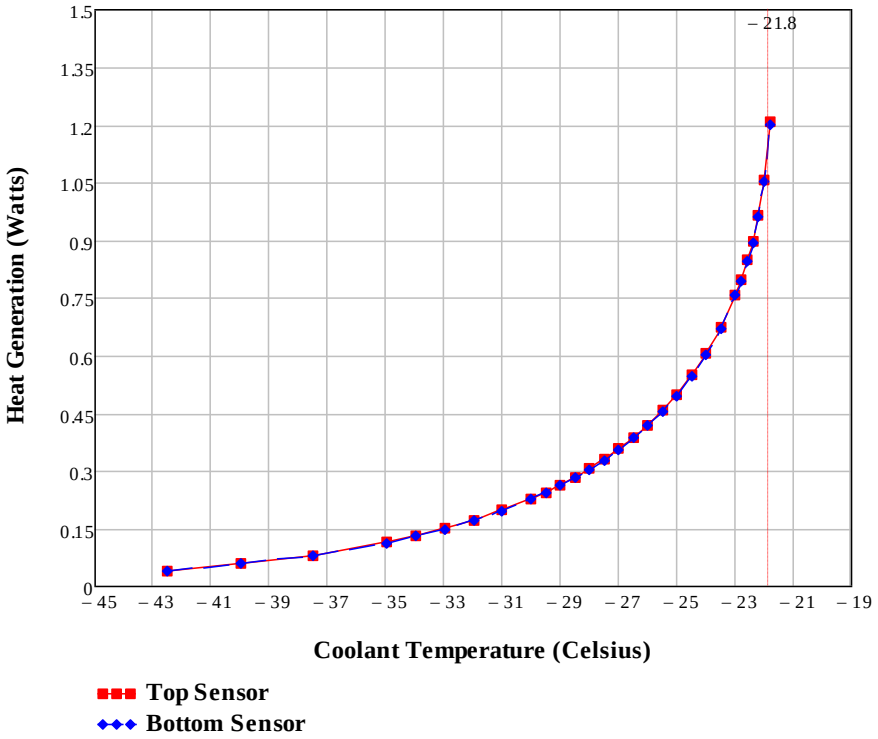

Figure 122: Heat generation of the sensor Vs Coolant Temperature by using Nippon XN-60 or YSH-60A carbon fiber.

Manufacturer: Nippon (NGF)	Resin Type: Epoxy or Polycyanate Resin Thermal Conductivity: 0.2 W/mK
Carbon Fiber Name: YSH-50A	**Fiber Thermal Conductivity: 120 W/mK**

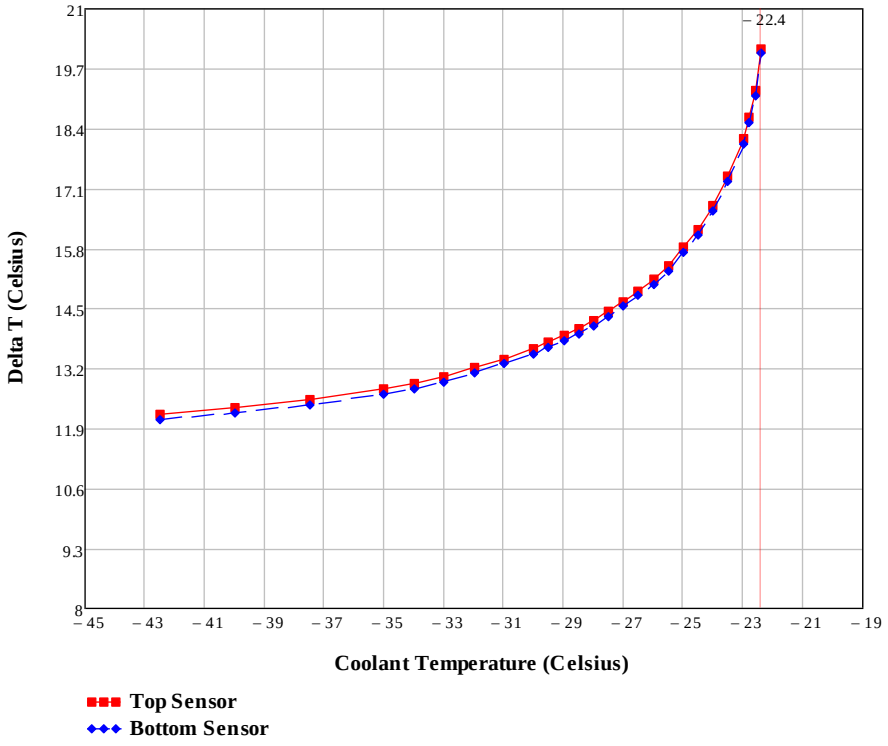

Figure 123: Differential temperature Vs Coolant Temperature by using Nippon YSH-50A carbon fiber.

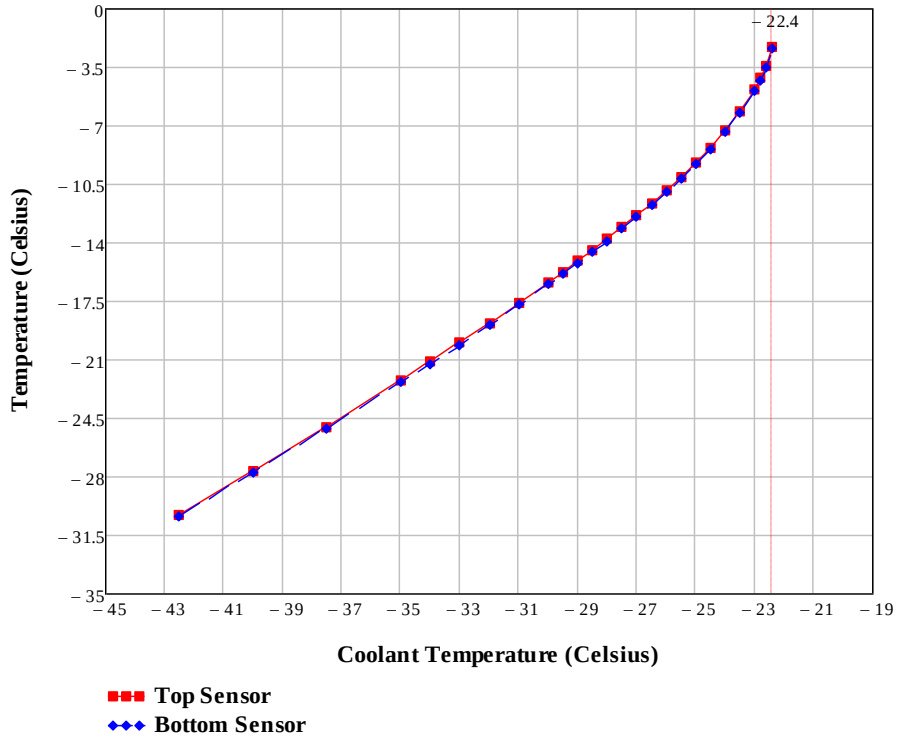

Figure 124: Maximum sensor temperature Vs Coolant temperature by using Nippon YSH-50A carbon fiber.

Manufacturer: Nippon (NGF)	Resin Type: Epoxy or Polycyanate Resin Thermal Conductivity: 0.2 W/mK
Carbon Fiber Name: YSH-50A	**Fiber Thermal Conductivity: 110 W/mK**

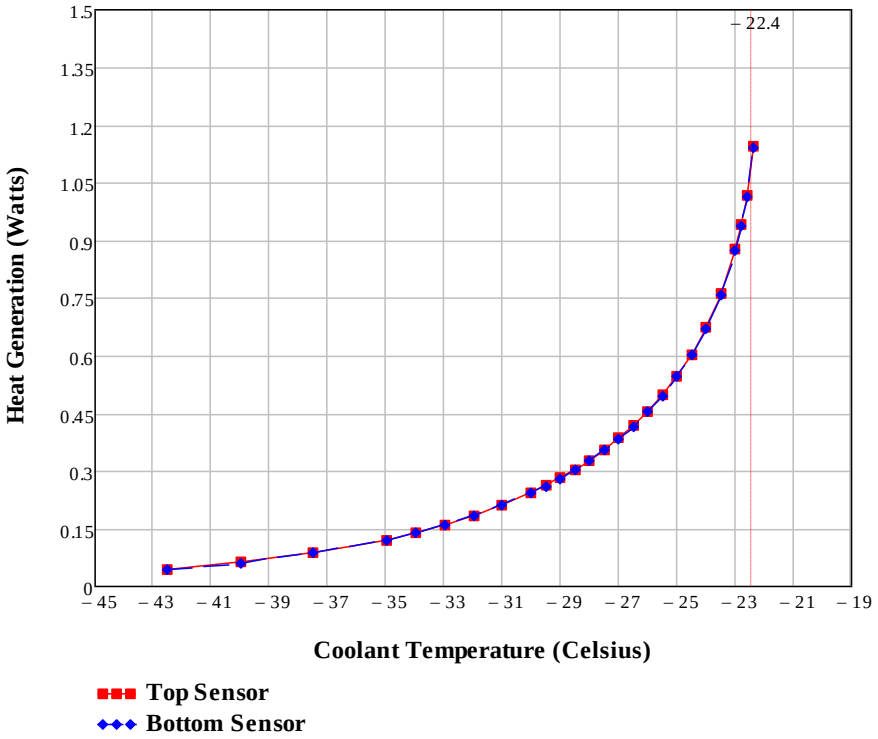

Figure 125: Heat generation of the sensor Vs Coolant Temperature by using Nippon YSH-50A carbon fiber.

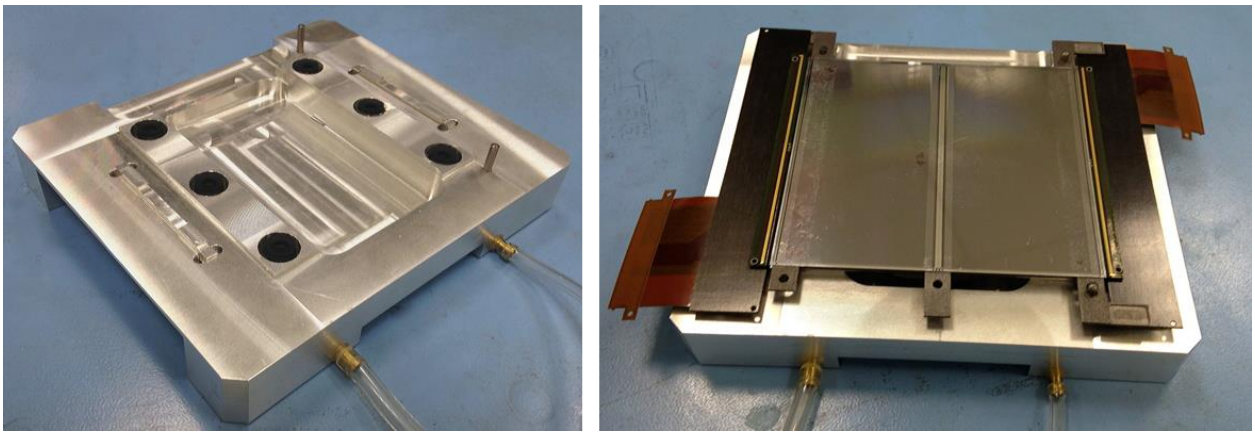

Appendix Figure 27: Photos of the 2S modules' wire bonding jig.

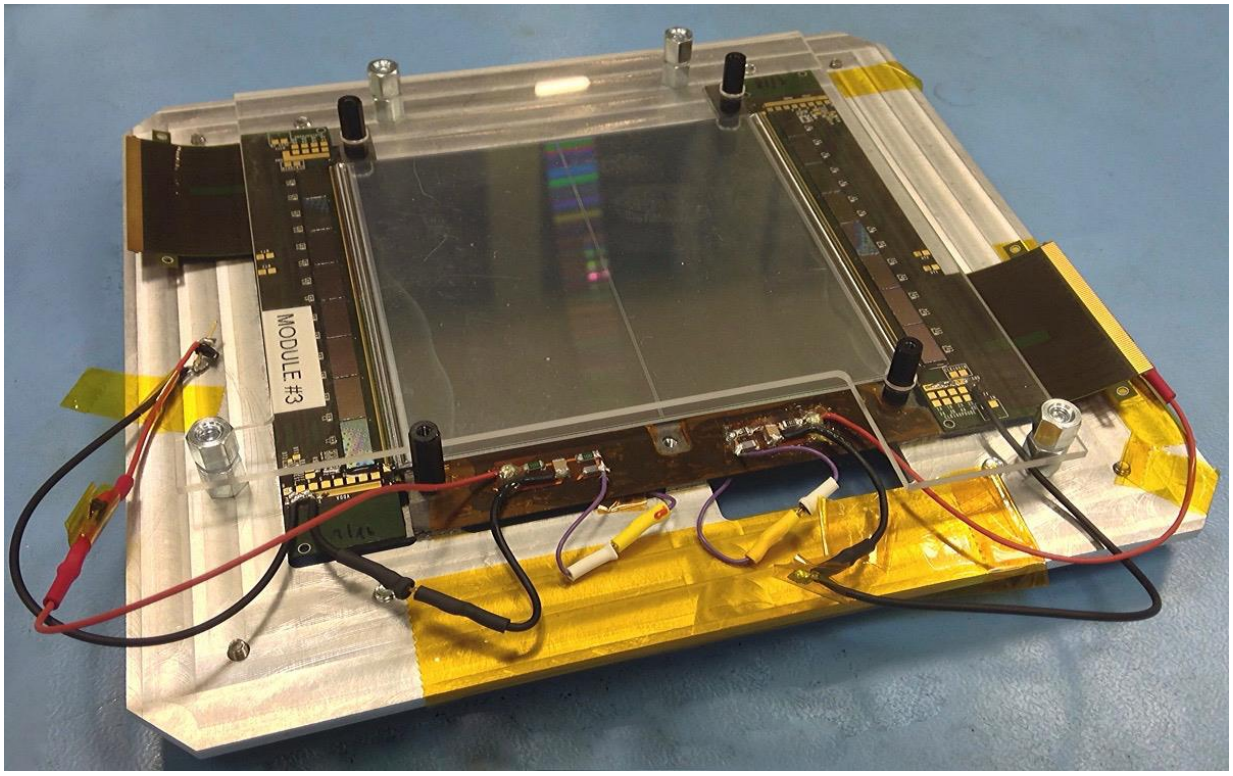

Appendix Figure 28: Photo of a 2S module on its carrier plate.

References

[1] Χαρακτηρισμός ανιχνευτών πυριτίου για την αναβάθμιση στη φάση 2 του ανιχνευτή Τροχιών του πειράματος CMS, Ασσιούρας Παναγιώτης, Εθνικό Μετσόβιο Πολυτεχνείο, Μεταπτυχιακή Εργασία, 2017

[2] The Phase-2 Upgrade of the CMS Tracker, 2017, CERN-LHCC-2017-009, CMS-TDR-014

[3] "HDI flexible front-end hybrid prototype for the PS module of the CMS tracker upgrade**"**, 2017, Kovacs M., Blanchot G., Gadek T., Honma A., Koliatos A., Journal of Instrumentation, *JINST* 12 (2017) C02029

[4] "Quality control considerations for the development of the front end hybrid circuits for the CMS Outer Tracker upgrade", 2018, Gadek Tomasz, Blanchot Georges, Bonnaud Julien Yves Robert, De Clercq Jarne Theo, Honma Alan, Koliatos Alexandros, Kovacs Mark Istvan, Luetic Jelena, Proceedings of Science, PoS TWEPP-17 (2017) 061

[5] http://mccfc.com

[6] http://www.ngfworld.com/en.html

[7] http://www.dupont.com/products-and-services/membranes-films/polyimide-films/brands/kapton-polyimide-film/products/kapton-mt.html

[8] A model of global thermal conductivity in laminated carbon/carbon composites, 1997, M.R.Kulkarni, R.P.Brady, Composites Science and Technology Volume 57, Issue 3

[9] Behrens E (1968) J Composite Mater 2:2

[10] Composite Materials: Science and Engineering, Krishan K. Chawla, 3rd Edition, 2012

[11] Z. Han and A. Fina, "Thermal conductivity of carbon nanotubes and their polymer nanocomposites: A review," Polym. Sci., vol. 36, no. 7, pp. 914–944, Jul. 2011

[12] G. S. Springer and S. W. Tsai, "Thermal conductivities of unidirectional materials," J. Composite Materieals, vol. 1, no. 2, pp. 166–173, Jan. 1967

[13] J. C. Halpin and J. L. Kardos, "The Halpin-Tsai Equa tions: A Review," Polymer Engineering and Science, Vol. 16, No. 5, 1976, pp. 344-352

[14] Hashin, Z. 1983, "Analysis of Composite Materials-A survey", J. Appl. Mech., 50:497

[15] W. A. Clayton, "Report: Thermal conductivity of phenolic-carbon chars," Boeing Co., pp. 1–181, 1969

[16] A. Dasgupta and R. K. Agarwal, "Orthotropic thermal conductivity of plain-weave fabric composites using a homogenization technique," J. Composite Materials, vol. 26, no. 18, pp. 2736–2758, Jan. 1992

[17] J. Strutt (Lord Rayleigh): On the influence of obstacles arranged in rectangular order upon the properties of a medium, Phil. Mag., vol. 34, pp. 481, 1892

[18] Karol Pietrak, Tomasz S. Wisniewski, "A review of models for effective thermal conductivity of composite materials", Journal of Power Technologies 95 (1) (2015) 14–24

[19] M. Zimmer, X. Fan, J. Bao, R. Liang, B. Wang, C. Zhang and J. Brooks, "Through-Thickness Thermal Conductivity Prediction Study on Nanocomposites and Multiscale Composites," Materials Sciences and Applications, Vol. 3 No. 3, 2012, pp. 131-138

[20] http://ecss.nl

[21] https://www.tencatecomposites.com/product-explorer/products/T3GL/EX-1515

[22] https://inis.iaea.org/collection/NCLCollectionStore/_Public/26/041/26041771.pdf

[23] https://www.ptc.com/en/products/mathcad

[24] Ansys Workbench 17.2, Academic Research

[25] Dassault Systemes, Catia V5